THE ROLE OF AEROTHERMOCHEMISTRY IN DOUBLE CONE AND DOUBLE WEDGE FLOWS

BY

ANDREW SWANTEK

DISSERTATION

Submitted in partial fulfillment of the requirements
for the degree of Doctor of Philosophy in Aerospace Engineering
in the Graduate College of the
University of Illinois at Urbana-Champaign, 2012

Urbana, Illinois

Doctoral Committee:

Professor Joanna Austin, Chair
Professor J. Craig Dutton
Professor Gregory Elliott
Professor Jonathan Freund

Abstract

In this work, hypervelocity flows over double cone and double wedge geometries are studied. The flow configurations established over the double cone/double wedge models are extremely sensitive to thermochemistry, and thus serve as ideal benchmarks for validating chemical models. The goals of this research are: i) to investigate the coupling between the fluid mechanics and thermochemistry in these flow fields by varying freestream flow composition and enthalpy, ii) to implement a diagnostic suite for time-resolved surface and freestream measurements, iii) to investigate the nature of flow field unsteadiness across various test conditions, and lastly iv) to extend the experimental database for shock wave boundary/layer interactions.

An expansion tube is used to generate flows with enthalpies ranging from 2.2-8.0 MJ/kg (2-4 km/s) and Mach numbers from 4-7. The expansion tube is a novel impulse facility for accelerating a test gas to these velocities, while maintaining a minimally dissociated freestream. Additionally, the facility allows variation of the freestream composition (between nitrogen and air), while maintaining freestream test parameters (Mach number, density, enthalpy) to within 0.5%. Two models are used: a 25°-55° double cone model and a 30°-55° double wedge.

There are four diagnostic components to this research which aim to enable a better understanding of these canonical flow fields. Single frame, high resolution schlieren photography is used to visualize various flow features including: the separation zone formed in the corner, the triple point interaction, and a supersonic shear layer. From these images, a separation zone length scaling parameter is determined. This parameter, derived for wedge geometries, is successfully applied to conical geometries by using a judicious choice of flow properties for scaling. In the wedge image series, nitrogen test conditions exhibit a distinct increase in bow shock standoff distance. Additionally, aft wedge

shock impingement in nitrogen occurs upstream, compared to air.

The second portion consists of heat transfer profiles taken over the double wedge model. Fast response ($\sim$1μs), coaxial thermocouples are used to measure average heat transfer values through the established test time. Differences in heat transfer profiles between air and nitrogen are seen at flow enthalpies as low as 3.6 MJ/kg. In all test conditions where a difference is seen, air exhibits augmented heating compared to nitrogen. This is limited to the region surrounding peak heating. Fluctuations in the established profile are quantified via the standard deviation of the signal. Fluctuations normalized by the mean are seen to be highest in regions of shock boundary layer interaction and separation.

The third part of the research consists of high speed schlieren imaging. High speed data (75-100 kHz framing rates) has been taken which visualizes the establishment process of the shock interactions, as well as of the separation zone. Distinct differences between nitrogen and air are observed, including: increased triple point establishment time in nitrogen, and the transient nature of shock waves. Establishment times of the shock configurations are compared with establishment times from the heat transfer traces, and experimental correlations from the literature. Normalized establishment times of 2-8 are observed, in agreement with historical data (5.5-11). Shock tracking algorithms are employed to trace and plot the profiles of the transient shock configurations for further analysis. Fast Fourier Transforms of shock location are computed and the frequencies are compared to frequency predictions for an acoustic wave traveling between the bow shock and shear layer.

The fourth and final part of this work investigates the nitric oxide (NO) emission spectrum in the ultraviolet band. Spectra are obtained at four locations behind the bow shock (0, 2, 4, 6 mm) in the highest enthalpy test condition. Simulated NO vibrational spectra are used to make estimates of the vibrational temperature at these four locations. The temperature is seen to peak at the 0 mm location, being similar in magnitude to the predicted frozen post shock temperature ($\sim$7700 K). A decrease in temperature is seen when traversing downstream, however temperatures do not approach the equilibrium temperature ($\sim$3900 K), indicating this region of the flowfield is in non-equilibrium.

An increase of temperature is seen in the furtherest downstream point (6 mm), and may be a result of viscous heating in the shear layer, which this interrogation point falls near.

Acknowledgments

I must first thank my advisor, Professor Joanna Austin. The opportunities and guidance she has provided me in my academic pursuits are unparalleled. Her enthusiasm for experimental work has made every day a pleasure working with her. She has given me such a high degree of control over my project and has sent me around the world to present about it. No student could ask for a better advisor.

Next, an enormous thanks to my parents, Nancy and Tony. For 27 years, they have been unwaveringly supportive of my endeavors and have always taken interest in what I do. A huge thanks to my brothers Al and Bo as well. Their visits have always been very welcomed and vacations at home would not be quite the same without bonfires, Call of Duty, and a few bottles of Spotted Cow. My aunt, godmother, and first doctoral recipient in the Steckiewicz family branch, Ellen Radel, has always been a source of advice and motivation as she knows the commitment of a doctoral pursuit. Thanks to all the extended family as well in the Garzino, Radel, Krupa, and Swantek branches for supporting me and humoring me at family events. Also a special thanks to Scarlett, Armstrong, Bam, and the late MacGyver. Despite the profuse amount of dog and cat hair, they were always the first ones at the door welcoming me home.

Many thanks to my committee consisting of Professors Greg Elliott, Craig Dutton, and Jon Freund. I am extremely grateful for the time they have invested in me, and the wonderful feedback they have provided to further augment this work.

A huge thanks goes out to various present and former graduate students of the group who I have had the pleasure of working with. Bill Flaherty has provided countless hours of collaboration and help with various aspects of my research, especially with the thermocouple instrumentation. He has

always be a supplier of good advice and consultation on research related issues. Dr. Manu Sharma trained me on the HET and set up a majority of the data collection/instrumentation infrastructure in the HET. Ryan Fontaine has always been helpful for research related discussions and opinions from a different perspective. Andrew Knisely has been a great source of coding/MATLAB/Cantera information. His role in setting up the the spectroscopy experiments was invaluable, and I feel very proud to leave my project in his hands. Dave Prisco provided experimental insight, as well, assistance implementing the SA-5. Lastly, Galina Shpuntova has been a wonderful office mate and given great advice on various research related topics. These people have not only made working a pleasure, but have been a great group of friends.

I must also thank several other students who have aided me along the way. Tommy Herges has been a terrific source of information for MATLAB and image processing, and helped with some of the light source construction. Todd Reedy helped with implementing the SA-5 and his experimental advice was always welcome. Brad DeBlauw has always provided useful insight into experiments and methods, and helped with the PI-Max setup. Heath Reising did a considerable amount of work with the laser light source and designing and manufacturing a model which will be used in future studies. Brad Sanders provided assistance with the UV-VIS light source and NO spectroscopy details. Lastly, the spectroscopy experiments would not have been possible without the help of David Allen from Prof. Nick Glumac's group in MechSE. The several hours he spent with me saved me weeks of work, and I must thank him greatly for it.

A huge thanks to a lot of my additional friends who have been down here during my stay including: Elizabeth Bozek, Nikki Ford, Corinne DiFonso, Chris Cirone, Dave Krause, and Jon Lange. Another thanks to my friends from Chicago and IIT who have come down to visit routinely: Chris Adams, Dave Poli, Brian Schiller, Anthony Cerra, Kevin Yokley, Shane Steward, Noel Wessely, Pat Bowles.

I have been very fortunate to maintain a line of communication with group alumnus Aaron Dufrene at CUBRC. His conversations have always been helpful. Prof. Hans Hornung and the Caltech T5 group very openly shared information about the thermocouple design and implementation.

Thanks to Greg Milner in the machine shop who has built nearly every component used for this research. He has always provided great input for model design, and his standard of work is beyond exceptional. I must extend an enormous thanks to Staci Tankersley and the rest of the administrative staff whom have helped me with countless questions about the degree requirements, scheduling, funding, and much more. They are truly invaluable to our department.

Lastly, in the Spring of 2006, Professor Hassan Nagib at IIT allowed me to work as an undergraduate in his research group. If it weren't for this opportunity and his compressible flow course, I would never have considered graduate studies.

This research was funded through the U.S. Air Force Office of Scientific Research (award FA 9550-11-1-0129) with Dr. John Schmisseur as program manager. I am deeply grateful for their continued support for my research and the Compressible Fluid Mechanics Lab.

Table of Contents

List of Tables

List of Figures

Chapter 1

Introduction and Background

In hypervelocity flight conditions, typical of sub-orbital and reentry trajectories, the coupling between the fluid mechanics and the thermochemistry of the flow becomes important. The use of "hypervelocity" indicates both a high Mach number, as well as a high velocity ($\mathcal{O}(2+$ km/s)), compared with "cold" hypersonic flows ($\mathcal{O}(500-1000$ m/s)). Double cone and double wedge flows have been identified sensitive test cases to use for benchmark aerothermochemistry studies. These models generate several features characteristic of high velocity flows, including: strong bow shocks, hypersonic boundary layers, separation zones, shock/boundary layer interactions, and shear layers. Predictions of peak heating loads, especially in the vicinity of shock boundary layer interactions, are crucial for vehicle design. This is evidenced by the well known failure of an X-15 space plane. A shock interaction on the vertical stabilizer caused augmented heating and resulted in both a catastrophic destruction of the vehicle, as well as the loss of test pilot Michael Adams' life. Another example is the phenomenon known as the "shuttle flap anomaly," where the flight moments and pitch differed from ground test measurements. High temperature, real gas effects were believed to cause this discrepancy [1].

In a 2006 review of high enthalpy research, Holden [2] notes that the focus of computational work has shifted to developing and validating models of surface and flow field chemistry. However, due to the aforementioned flow field sensitivity to thermochemistry, modeling has seen a halt because of improper characterization of facilities which generate a dissociated freestream (most notably shock tunnels). In a 2010 review Holden [3] states that accurate models of the free stream chemistry must be developed before the accuracy of shock layer chemistry can be assessed. Simulations of these flow fields in shock tunnels required a simulation of the facility to predict the freestream conditions, and

are considered to be inaccurate [4]. Currently there is a lack of well characterized, thermochemically "clean" experimental data. The unique gas acceleration process of an expansion tube can be used to generate a wide range of hypervelocity test conditions, while maintaining a minimally dissociated freestream. Thus, we can investigate the coupling the fluid mechanics, chemical processes, and thermal processes in the double cone and double wedge flow fields.

1.1 General Flow Field Description

A general flow field schematic of the two dimensional double wedge/axisymmetric double cone flow is shown in Figure 1.1. An incoming hypersonic flow travels from left to right and forms an oblique/conical shock off the leading edge. On the forebody, a boundary layer forms and develops until it detaches after the separation shock. Underneath the dividing streamline a separation zone forms, which may have a complex structure. Gaitonde *et al.* [5] show that there can, in fact, be three different structures within the separation zone. A schematic of this is shown in Figure 1.2 based on their numerical results. The separation zone is terminated with the reattachment shock on the aft body. Additionally, a triple point forms with the intersection of the bow shock and either the separation shock (most cone cases) or the oblique shock (most wedge cases). This triple point results in a transmitted wave and shear layer. Figure 1.1 shows one configuration where a second shear layer forms from the intersection of the reattachment shock and the transmitted shock. The shear layer will separate a relatively hot and slow flow (behind the bow shock) from a relatively cold and fast flow (behind the reattachment shock).

Nompelis [6] provides a description of regions where chemistry will be important in the flow. Dissociation reactions will be important behind the oblique/conical shock, the bow shock and potentially in the separation zone. There is also potential for recombination reactions within the separation zone. Additionally, there is the possibility of reactions occurring in the boundary layer. Throughout the entire flow field non-equilibrium thermochemisty can occur due to reduced collisions from low density. He also states that chemical reaction rates obtained from shock tube experiments can be inaccurate through expansion waves which may occur on the aft body of the geometry. Olejniczak *et*

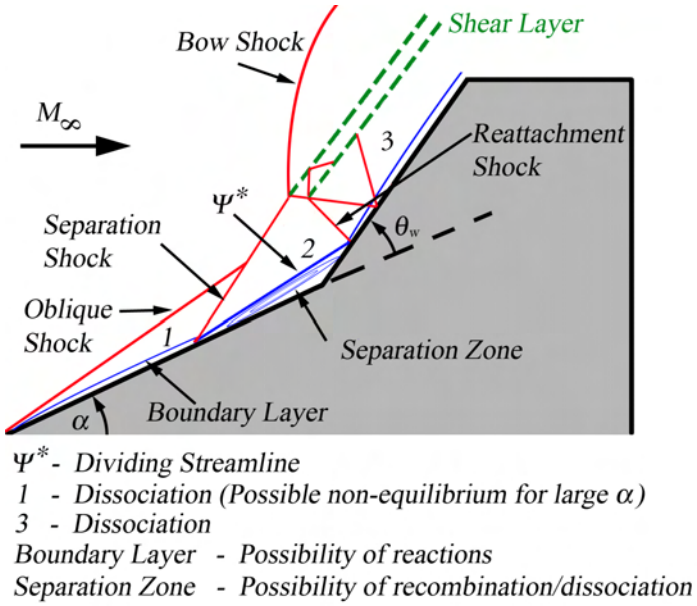

Figure 1.1: A schematic of the flow field is present, along with important features labeled. Flow is from left to right.

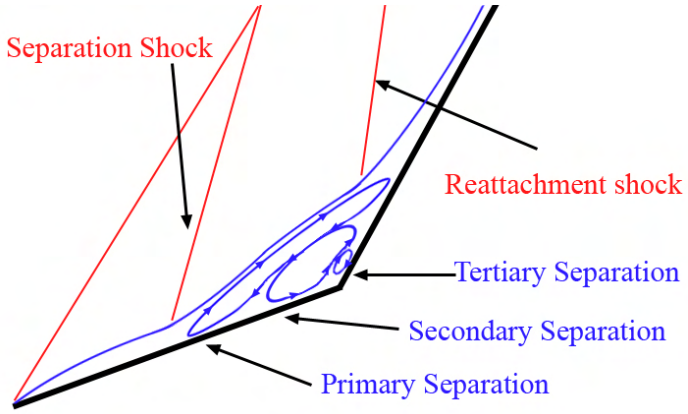

Figure 1.2: A schematic based on the observations of Gaitonde *et al.* is shown. Three distinct separations and corresponding structures are shown. Flow is from left to right. Drawing is not to scale.

al. [7] note that a feedback from the separation zone can exist. The separation zone may contain a non-Boltzman distribution of vibrational energy levels. Some of the molecules with high vibrational energy levels can be ejected back into the flow behind the oblique shock and cannot equilibrate with the bulk gas. These will dissociate faster than the bulk gas, and if enough are present can have a large impact on the flow field behavior.

1.2 Wedge Geometries

The double wedge geometry has evolved out of extensive work on two dimensional compression corner flows where an incoming boundary layer is exposed to a linear ramp. Davis [8] presents a review of this literature, mentioning that it had a tendency to focus on perfect gas flows. Specifically, he focuses on predictive methods for separation length and reattachment heating. More relevant to the current work are studies that have been done in high enthalpy flows. Davis provides a summary of the results of two dissertations from Rayner at Australian National University [9] and Mallinson at The University of New South Wales [10].

Mallinson *et al.* [11, 12, 13] have published several works regarding the single compression corner in high enthalpy nitrogen flows. In several studies, they investigate the laminar shock/boundary layer interactions on a flat plate followed by a single compression corner which varies from 0° to 24°. The research was performed in the T3 reflected shock tunnel at Australia National University at enthalpies of 2.8, 13.7, and 19.0 MJ/kg. They limit the study to laminar interactions, as they believe transitional and turbulent interactions can mask real gas effects. Heat transfer and pressure data are taken, as well as interferometry flow visualization [13]. To ensure two dimensional behavior, data are taken with and without side walls, and no differences are seen. They define the upstream influence, l_u, as the point where the pressure and heat transfer (on the flat plate portion) deviate from flat plate behavior due to the compression corner. Good agreement with the perfect gas laminar pressure plateau in the separation zone is achieved. The authors do not believe that real gas effects are present at these flow conditions, and state that the boundary layer is most likely frozen.

In another study [14], they provide a discussion about the effects on the interaction when real

gas effects become significant. Flow features that will affect the interaction include: a change in the incoming boundary layer thickness, a change in the shock strength, real gas effects in the separation zone, and a change in the reattachment boundary layer thickness, the last of which is not believed to affect the upstream influence. The boundary layer thickness (in both the incoming and reattachment boundary layers) will depend on the degree of non-equilibrium. Generally, dissociation boundary layers are thinned, while recombination boundary layers are thickened compared to a frozen boundary layer. Additionally, the upstream influence, l_u is reduced for dissociation dominated boundary layers, while it is increased for recombination dominated boundary layers. The authors note that for flows with an overall endothermic reaction, larger peak heating occurs due to boundary layer thinning. For flows with exothermic reactions, a thickening of the boundary layer should lead to a lower peak heating. This disagrees with the results of Grumet *et al.* [15], where peak heating is increased, and may be due to bulk flow heating.

Olejniczak and Candler [16] perform two dimensional Navier-Stokes simulations of a select set of these experimental conditions, focusing on turning angles of 10°, 18°, and 24°. In general, the agreement with the experimental data is poor downstream of reattachment. The heat transfer and pressure profiles do agree with the experimental data in the flat plate region of the flow field; however, the location and magnitude of peak heating do not agree with experiment. The authors do believe that the flow field has a moderate amount of non-equilibrium.

In two similar works Olejniczak *et al.* [17, 18] perform both experiments and simulations of a 15°-48° double wedge with variable angle of incidence. Experiments are performed in nitrogen at flow enthalpies ranging from 25.7-28.5 MJ/kg. The authors explain that differences in observables, in particular shock shape, surface heat transfer and surface pressure, will be able to distinguish differences between various vibrational-dissociation models. They explain the sensitivity of the vibrational-dissociation coupling in the flow field as follows. Non-equilibrium chemistry, in part, will dictate the shape of the bow shock. The shape of this shock will dictate the location of the transmitted shock impingement on the aft wedge. Large differences in the size of the separation zone will occur for small changes in the location of shock impingement, due to different amounts

of mass reversed into separation. This brings about the importance of using a double wedge rather than a compression corner for model validation. At low turning angles, the separation zone is small, and there is nearly no difference between vibration dissociation models. The flows in this study were all laminar and steady. Computations failed to reproduce the experimental data. In conditions with little dependence on vibration-dissociation coupling, separation zone size is under predicted; however, heat transfer data exhibit good agreement. For sensitive conditions, the model of Marrone and Treanor [19] matches the data slightly better than the model of Park [20] in the separation zone; however, overall agreement is still poor. The authors attribute these discrepancies to several sources: uncertainties in the equilibrium and non-equilibrium dissociation rates, the presence of a non-Boltzmann vibrational energy distribution in the T5 freestream, and lastly the failure of the continuum formulation in the strong interaction regions.

Perhaps two of the most comprehensive works come from Davis and Sturtevant [21] and Davis [8]. The authors perform a theoretical analysis of the separation zone using triple deck theory to derive a scaling parameter. They perform experiments over a 30°-55°, variable angle of attack double wedge. Hypervelocity nitrogen flows are generated with the T5 reflected shock tunnel at GALCIT and enthalpies range from 3.9-28 MJ/kg. Finally, they perform two dimensional, non-equilibrium RANS simulations using a code developed by Olejniczak [22] and Candler [23]. They authors separate real-gas effects into two groups: external mechanisms, which refer to effects in the external, inviscid flow, and internal mechanisms, which refer to the effects in the viscous regions of the flow. The authors found that their modified scaling parameter captured the behavior of the separation zone. The inclusion of a new term which relates the ratio of the temperature at the wall to the temperature at the edge of the boundary layer was seen to improve the scaling correlation. In addition, they note that some test conditions exhibited a transitional/turbulent boundary layer and indicate this may have an effect on the separation zone size. A significant increase in scaled separation length is observed for high enthalpy data when compared with low enthalpy data. Davis [8] mentions that the correlation may be able to be improved if flow properties are measured near separation and reattachment, rather than being estimated. He also provides insight into the behavior of the flow

field when dissociation occurs behind either the leading edge shock, reattachment shock, or both.

Recently, Hashimoto [24] performed a study of several wedge configurations: a 25°-40°, a 25°-50°, and a 25°-68°. A reflected shock tunnel is used to create an air test condition with an enthalpy of 4.8 MJ/kg. Single frame interferometry images, as well as high speed schlieren data are taken. The 25°-40° exhibited a very typical Edney type VI [25] shock interaction, with a small separation zone in the corner. The 25°-50° wedge exhibits an Edney type V interaction, including a larger separation zone and a standoff bow shock. In the the 25°-68° the separation shock transitions to interacting with the bow shock, rather than the leading edge shock. Additionally, the separation point is seen to move forward with increasing secondary wedge angle. Unsteadiness is investigated with high speed imagery. For the case of the 50° second angle, the authors did not observe any unsteadiness after the triple point's establishment. In the 68° second wedge case, the authors do report movement in the separation zone; however, they do not comment on potential unsteadiness of the flow field. Finally, they provide some images of the model, post test, which illustrated the heating damage to different parts of the model.

1.3 Conical Geometries

One of the first experimental studies of axial flow separation comes from Maull [26], who investigated the supersonic flow around blunt bodies with a pointed nose. Diagnostics include both shadowgraph and schlieren photography, including high speed imaging for unsteady cases. In all cases, the ratio of the spike length, l, to blunt body diameter, d, was kept below 4 to minimize any spike vibrations. Oscillatory behavior of the flow is seen for spike lengths in the range of $0.25 < l/d \leq 2.5$. As has been seen in a later study [21], the pressure ratio that causes separation is a function of Mach number and Reynolds number based on the distance from the spike nose; hence the separation angle will be a function of these as well.

An important feature of the study, relevant to the current work is the description of oscillation. The separation cycle begins when the boundary layer separates on the spike near the nose, with a conical dead air region. A detached shock is required to turn the flow around the blunt body outside

the separation region. The pressure ratio across this shock is too great for equilibrium with respect to the reversed flow/dead air region. Gas flows into the dead air region, enlarging it and pushing another detached shock out to the nose of the spike. This pattern is similar to that of a jet emanating from the blunt body tip. As the strong shock wave moves out, the feeding of air into the dead air region ceases due to a lower pressure ratio, resulting from a lower turning angle for the external flow to turn around the body. Flow from this zone begins to flow out over the shoulder and the dead air region collapses. Upon the escape of all the excess air, the cycle begins again. Non-dimensional frequencies are obtained, fd/u (Strouhal number), where f is the oscillation frequency, and u is the freestream velocity. The authors find this number to be 0.23, compared with 0.15 from the study of Mair [27], and go on to suggest that bodies which are not as blunt as hemispheres (ellipsoids for example) will be stable with a nose spike.

What could be defined as "modern" double cone studies (within the previous 15 years), seem to originate with a 1997 study by Olejniczak, Candler and Hornung [7]. In a combined numerical and experimental paper they investigate three models: a 25°-65°, a 25°-68°, and a 25°-70° at flow enthalpies ranging from 27-31 MJ/kg in nitrogen. This study is motivated by questions in the results of another study [17] where they investigated double wedges. Axisymmetric calculations are much less costly than wedge flow fields due to the necessity of computing the entire three dimensional flow. The authors describe why the double cone flow field separation zone size is sensitive to the choice of chemical model, and it is a nearly identical description as above in Section 1.2. A Mach-Zehnder interferometer is used to image the flow field, from which separation length and aft body shock impingement is measured. They find that three test conditions exhibit unsteadiness at the two highest aft cone angles. As in the double wedge studies, the simulations do not reproduce the experimental data. Agreement is better if a detailed transport and diffusion model is implemented; however most of the discrepancies are believed to be a result of the uncertainties in equilibrium and non-equilibrium dissociation rates.

In a related study [16] they investigated a blunted nose double cone, comparing with the data of Holden [28] in nitrogen and air at 10 MJ/kg. In addition to the failure to match pressure and heat

transfer in air (in this case, potentially due to a transitional shear layer), one of the most puzzling results is that the experiments indicate the flow is steady, while the computations predict it to be unsteady. Similar discrepancies are also seen in the transient behavior for the nitrogen test gas. The authors state that flow fields become unsteady on larger and solution adapted grids, and that they cannot attribute any one component of the study to the discrepancy. Holden [28] discusses some important aspects of these flows. The large variation in the levels of dissociated oxygen and NO can be used to provide a good experimental test environment for various diagnostics. Using thin film heat transfer instrumentation and pressure gauges, they found that real gases have a minimal effect on the pressure field, and air did exhibit higher heat transfer rates in interactions over a blunt nosed double cone. In this paper, Holden also goes over some phenomena associated with shock wave-turbulent boundary layer interactions. Although generally unsteady in nature, regions near these interactions can have gross characteristics and mean properties that are reasonably defined by correlation from experimental data. At hypersonic speeds these boundary layers are difficult to separate, requiring corners of at least 27°. He states that the separation region can be formed at the base of the turbulent flow, much akin to the laminar sublayer separating. The separation zone can even remain embedded within the original boundary layer. At the time of publication, the most advanced turbulence models had failed to predict the heat transfer and skin friction in these flows, with any sort of accuracy.

Further investigation of turbulent behavior took place in the study by Wright *et al.* [29]. Comparison of low enthalpy ($\sim$0.75 MJ/kg) experiments with simulation was performed with data obtained in the Princeton University Mach 8 Wind Tunnel. Models included 25°-35° and 25°-50° double cones instrumented with pressure ports. They are tested at two free stream Reynolds numbers. Turbulent simulations were performed using the κ-ϵ model. The comparisons for the 25°-35° with respect to the schlieren images and pressure distribution were found to agree for both run conditions (Re_D = 3.7 and 6.1 x 10^5), with the laminar and turbulent simulations being nearly identical. In the case of the 25°-50° double cone, the lower Reynolds number (Re_D = 2.7 x 10^5) condition saw good agreement with the experimental data on the forward cone, while having some discrepancy on the

aft cone. Laminar and turbulent simulations were nearly identical however. In the case of the higher Reynolds (Re_D = 4.8 x 10^5), laminar and turbulent simulations differed significantly in both the shock shapes, separation zone size, and pressure distributions. The experimental data exhibit slightly better agreement with the turbulent simulation. The qualitative trends disagree with a previous study [30]: for transitional interactions the separation zone size decreases with increasing Reynolds number, while it increases for fully laminar or turbulent boundary layers. The authors observed a decrease in separation zone size for increasing Reynolds number for the 25°-50° cones. The experimental and numerical data indicate that the reattachment shocks can cause a transition to turbulence.

In three related studies Nompelis *et al.* [31, 32, 33] perform simulations and experiments over a 25°-55° double cone to investigate real gas effects with an emphasis on the role of vibration non-equilibrium. The authors present a summary of low enthalpy (3.83 MJ/kg) results from their previous works, and conclude that nearly no chemical reactions happen; however, the test gas is predicted to vibrationally freeze near the throat conditions of the LENS I reflected shock tunnel. Heat transfer to the double cone was reduced due to a reduction of kinetic energy flux. This was able to be accounted for in the simulations with a vibrational energy slip model. They propose two test conditions: a single 5.43 MJ/kg case for which there was already nozzle data to compare with, and an 11.3 MJ/kg test condition, for which they can vary the reservoir pressure to examine the effects of reactions (as collision rate increases with increasing reservoir pressure). They discuss the importance of the vibration-dissociation coupling which governs oxygen and nitrogen dissociation. The molecules are vibrationally excited by the vibration-translation exchange of energy. These excited molecules have the highest probability of dissociating and the effective dissociation rate is lowered through the "ladder-climbing process." This is the cause for what they call an incubation time, also known as a relaxation time, behind strong shock waves. Understanding of this coupling is key in capturing the flow physics. The authors mention the creation of the LENS X expansion tube as an alternative to generating high enthalpy flows without highly stagnating and then expanding the test gas. Several comparisons [32] between simulation and experiment are performed for air and

nitrogen conditions at enthalpies of 7.5-8.8 MJ/kg. Agreement between simulation and experiment in nitrogen is good; however, the air simulations fail to match peak heating and separation zone size.

In the previous two studies the authors have used nominal freestream conditions in their analysis. In the third of these studies, they compute the entire reflected shock tunnel nozzle flow and apply a non-uniform inflow condition to the numerical simulation of the flow over the double cone. This is indeed seen to improve agreement with the peak heating and separation zone size at an enthalpy of 3.7 MJ/kg, along with the inclusion of vibrational non-equilibrium and slip in vibrational energy at the wall. They discuss grid convergence, which is beyond the scope of this work, but warn that spurious agreement can be caused by poor grid resolution and inadequate models of the flow physics. This reiterates how the sensitivity of the double cone flow field model to grid resolution and chemical models makes it a rigorous CFD validation test case. More data and details can be found in Nompelis' dissertation [6].

Nompelis *et al.* [34] employ new models for vibrational-translation (V-T) and vibration-vibration (V-V) relaxation rates for expanding highly stagnated flows in a nozzle. The hope was to achieve a better inflow condition for the simulations of the double cone flow. They find that the free stream conditions are not sensitive to the choice of model employed and that the standard single harmonic oscillator model (SHO) with the classic Landau-Teller model is adequate. After being unable to identify continued discrepancy between experiment and simulation, they believe reservoir conditions for the facility may not be accurate.

Nompelis and Candler [35] build on previous work with respect to modeling thermochemical reactions in air over the 25°-55° double cone. Agreement is increasingly poorer in test conditions going from 5 to 15 MJ/kg. Their modeling techniques assume that non equilibrium can exist for different energy modes, but all the states for a given energy mode are in equilibrium, following a Boltzmann distribution. When simulating the nozzle flow, they compare the amount of NO with spectroscopic measurements done by Parker [36] in the exit plane. NO levels are predicted to be over 3.5 times larger than measured, and with that the simulations give a lower velocity and higher temperature than measured. This is an indication that the CFD is predicting more energy storage

in vibration and chemical energy modes. As this discrepancy is significant, the authors believe that this is a potential reason for disagreement of historical data in high enthalpy air. They go on to investigate several processes which may be important to NO destruction, including: NO production destruction, oxygen recombination, Zeldovich reaction rates, and the role of excited electronic states. One conclusion common to all of these is the lack of experimental data (especially in the case of the role of excited electronic states) or large scatter in the measured rates from different sources. Even by varying rates through the scatter, the changes on NO mass fraction were minimal.

Recently, Nompelis *et al.* [4] presented experimental and computational data with nitrogen, oxygen, and oxygen-argon mixtures. The series of tests was designed to investigate chemical reactions by making direct comparisons with simulations. Argon is used as a third body because it as an inert gas and participates in the dissociation/recombination reactions without storing a significant amount of electronic energy. Fourteen experiments were tested to perform parameter sweeps (i.e. Reynolds number, composition, and pressure) at enthalpies from 3.48-10.17 MJ/kg. In a discussion of time to steady state in the simulations, they define a flow time as the time it takes a particle moving with the freestream velocity to traverse the length of the geometry, and state that it can take 100 flow times for the simulation to reach steady state. They believe that there is inadequacy in characterizing the freestream when operating at conditions where chemical reactions are important. This seems to be a result of modeling the oxygen, as at high enthalpies disagreement between simulation and experiment is severe. Failed prediction of the separation zone size appears to be independent of the amount of argon added. Additionally, they note that surface catalysis must be considered when there is a significant amount of freestream dissociation. A related study by Candler *et al.* [37], in part, looks at the role of electronically-excited states in the modeling of oxygen recombination. While the study mostly focused on the role in carbon dioxide modeling, they point out that oxygen has two low-lying electronic states, in which a substantial amount of recombination may occur. The transition from these states to the ground state is spin forbidden, and as a result the collisional quenching rate will be slow compared to the nozzle flow time.

The NATO Research and Technology (RTO) Applied Vehicle Technology (AVT) Panel 136

Subtopic Number 2 was created to focus on the assessment of CFD for shock interactions and control surfaces in non-equilibrium laminar flows [38]. One of the model flow fields investigated was the double cone, for which three total conditions at two different enthalpies (5 and 9 MJ/kg, with two stagnation pressures for the 5 MJ/kg) were used as test conditions based on runs in the LENS I facility. The purpose of the group was to select several researchers to employ codes using different numerical schemes, grid refinement, and thermochemisty models, with the goal of assessing what the state of the art was for simulating these flows using nitrogen as a test gas. Perhaps the best summary of the work is provided by Knight and Longo [39], who present details and analysis of simulation results for all six codes, as well as experimental data. In general, agreement with simulation is reasonable for all three cases, with respect to the pressure and heat transfer. Perhaps the most interesting result from this study is that of flow steadiness on the model. In the high enthalpy case, and the low enthalpy/high density run condition, simulations and experiments are seen to be steady. For the case of the low enthalpy/low density, the experiment is seen to be steady while **all six codes observe significant unsteadiness in the flow field**. This cannot be attributed to a particular grid or flux algorithm, as each code is entirely different. In the full AVT 136 report [40], data from the simulations of the unsteady case universally exhibit aft body pressure and heat transfer peaks which travel downstream in time. The reason for this discrepancy between simulation and experiment is currently unknown, and its resolution is critical in understanding the flow physics.

1.4 Establishment and Steadiness Considerations

Several works have investigated the establishment of structures in various hypersonic flow fields both experimentally and numerically. Mallinson *et al.* [13] present a summary of the body of literature examining the establishment of viscous structures in various planar flows. Results include the relationship given by Davies and Bernstein [41] $\Delta t_{fp} = 3.33L/U_\infty$ (Identical to the relationship given by Gupta [42] for a flat plate, with L being the length of the plate and U_∞ being the freestream velocity. The establishment time for a compression corner from Holden [43] is also present as $\Delta t_{sep} = l_{sep}/\overline{a}_\delta$. $\overline{a}_\delta$ is the average sound speed in the boundary layer evaluated at the Eckert

reference temperature. The authors present experimental data on the establishment of compression corner flow. When converted to characteristic flow times, $t_{est}/(L_{model}/U_{\infty})$ (where L_{model}/U_{∞} is the flow residence time over the model) values ranging from 5.5 to 11 are found for flow enthalpies of 3-20 MJ/kg in the reflected shock tunnel facility.

Druguet, Candler, and Nompelis [44] present results for the number of flow times required to reach steadiness in numerical simulations of nitrogen over a double-cone. They find that computing 150 characteristic flow times are required to reach a steady state laminar solution. This value agrees with what Gaitonde *et al.* [5] who found that 100 characteristic flow times were required to establish a steady state solution. Druguet *et al.* do mention that time accuracy is known to be lost with implicit integration (which they perform) due to large time steps and incomplete convergence of the non-linear update in each time iteration. It should be noted now that between these numerical studies and the previous experimental studies, there is a discrepancy between the time required to establish the flows over these geometries which is **over one order of magnitude**. Currently the reason for this discrepancy is unknown, however it may be linked to discrepancies seen by the NATO AVT Panel 136 results discussed in section 1.3.

Two similar studies by Jagadeesh *et al.* [45] and Hashimoto [24] use high speed schlieren imaging to study shock behavior over a double cone and double wedge respectively. Research is conducted in the free piston shock tunnel at the Shock Wave Research Center, at Tohoku University. Both studies use a M=6.99, H_0=4.8 MJ/kg test condition for testing the models. Facility test time is listed at 300 μs.

In the first study, four different cones were used. All have a first semi-apex angle of 25°, while the aft semi-apex angles are 50°, 65°, 68°, and 70°. High speed imaging was performed with a HADLAND IMACON 468 camera at 33.3 kHz. The authors note that for secondary angles from 65° to 70° there are severe shock oscillations and movement of the transmitted shock location on the second cone's surface. These cases exhibited a Type IV interaction, whereas the case with a secondary angle of 50° exhibited a Type V, and is described by the authors as being "steadier." Establishment times are not listed, and oscillations are not quantified. This may be due to the

limited images presented during the test time (8 for all cases).

In the Hashimoto study, three double wedge models were used; all with a first wedge angle of 25°, and second wedge angles of 40°, 50°, and 68°. Only the latter two are investigated with high speed imaging. An IRIS Shimadzu Co. high speed camera capable of a 1 MHz imaging rate (312 pixels x 260 pixels) was used to record the image sequence. The 25°-50° exhibits a Type V interaction and significant flow fluctuations are not observed. In the 25°-68° model, the separation point is seen to move upstream. There is also reported movement in the triple point for this case. The flow for this case is described as "unsteady and complex," and the authors note that the transmitted shock from the triple point impinges normal to the wall surface which increases unsteadiness.

Marineau and Hornung [46] investigated bow shock unsteadiness in the T5 facility as a result of reservoir fluctuations. Unsteadiness in the freestream may have an effect on laminar/turbulent transition as well as stagnation point heating augmentation. The authors mention that there has been no assessment as of the publication of the paper. Experimental data are collected with a Vision Research Phantom camera at 97.5 kHz and 63 kHz over an Apollo shaped capsule along with pressure traces in the reservoir. Frame rates are estimated using frequency of acoustic waves resonating from the shock to the body in the shock layer. Boundary tracking is used to collect information about the transient shock location. The authors provide two spectra of the reservoir showing the dominant frequencies in the reservoir before and after the rupture of the diaphragm. Post-rupture spectra display the same peaks as the pre-rupture spectra, indicating the diaphragm rupture introduces additional fluctuations into the reservoir. The noise in the flow is very distinct to the facility the research is performed in, and is dependent on the location of the piston as well as the diaphragm. From linear theory the authors predict that the frequency of shock oscillations should match the frequency of the incident flow disturbances. This is observed in comparison of the pressure and shock location spectra, which match to a reasonable degree. The authors also perform simulations using an Euler solver. They simulate freestream simulations by using transient sinusoidal variations in pressure at the inflow. The ratio of wavelength to cylinder radius (λ/R) is varied from 1/4 to 2. They observe that shock oscillations occurs at the frequencies of the disturbances and are

proportional to the amplitude of the oscillations.

Lind and Lewis have two related publications [47, 48] which investigate an oblique shock impinging on a cylinder via numerical simulations. The flow field is quite similar to the that of Sanderson [49] and Sanderson *et al* [50]. They use conditions from Holden *et al.* [51, 52]: M=8.033, T_∞=404.6, and Re/m=4.911x10^6 for the first study, and M=8.144, and Re/m=12.43x10^6 in the second study. In the first work, the authors discuss establishment of the flow on the surface of the cylinder in terms of the surface pressure traces. These traces exhibit a low frequency establishment process, followed by higher frequency fluctuations in the "steady state." These fluctuations appear for shock locations impinging higher on the cylinder, and a direct relationship between oscillation frequency and shock location is observed. In all cases a decay in the magnitude of the fluctuations appears to occur; however, the long time behavior is not observed due the limited time the simulation was carried out. The authors describe an inherent unsteadiness associated with the Type IV interaction. Unsteady configurations were observed when the supersonic impinging jet was either perpendicular to the surface of the cylinder, or it was oriented such that flow was deflected downward. Additionally, unsteadiness in shock motion can be caused by an unsteady separated region on the cylinder surface. In the second of the works, they extend their analysis about some of the interaction behavior and physical mechanisms. They notice that for certain impingement angles the flow field can transition between a Type IV and Type V interaction. A physical mechanism for the bow shock oscillations is presented in terms of vortex formation. Peak pressure occurs when the shocks are their farthest from the body. A vortex will form near the jet impingement on the body. This reduces the local pressure and the outer shock moves toward the body. The expansion region will bend toward the lower portion of the shear layer resulting in a a small separated region. As the vortex moves along the shear layer (and around the body), it dissipates. An increase in local pressure associated with the vortex dissipation moves the shock back away from the body.

1.5 The State of the Art and Current Work's Contributions

To motivate the present study, there are several major points which should be summarized about these flows. First, nitrogen experiments and simulations have been seen to agree up to ∼9 MJ/kg flow enthalpies [32]. However, simulations fail to reproduce experimental data above ∼5-6 MJ/kg in air [35]. Currently, simulations are limited to laminar predictions for these flow fields. There are several factors which have been attributed to this disagreement. The modeling of NO (specifically production and destruction mechanisms) and molecular oxygen are inadequate at higher enthalpies, as summarized in Section 1.3. Vibration-dissociation coupling is still under investigation, as are the effects of surface catalysis.

Improperly characterized freestream conditions may play a role in the discrepancy. The LENS I facility has generated a large database of double cone/wedge data. The facility, which operates as a reflected shock tunnel, produces a high temperature stagnated gas, and then expands it through a conical nozzle. The flow in the stagnation chamber will be subject to chemical reactions, as will the flow through the expansion. The test conditions will most likely contain dissociated species and may even be in thermochemical non-equilibrium. Although this has been simulated, it is still a concern that the predictions of the freestream may have inaccuracies.

Lastly, as illustrated in both Sections 1.3 and 1.4, there are drastic discrepancies between experiment and simulation with respect to the time required to achieve a steady state, as well as, predictions of the existence of a steady state. Extensive work has not been performed (experimentally and numerically) examining the establishment of all the different flow structures in the double cone/wedge flow field. The diagnostics currently employed for detailed investigation of these flow fields are (to the author's knowledge): single frame schlieren photography, and surface measurements of heat transfer (coaxial thermocouples/thin film gauges) and pressure. Heat transfer gauges have typically been used to quantify flow establishment. Limited spectroscopic diagnostics have been applied, and only for characterization of the freestream, rather than as a tool for investigating the flow field. This is not surprising, as these diagnostics can be challenging to implement, and will not yield nearly as much data as surface measurements.

In the current work, there are several goals set to contribute to the literature. First, **the coupling between thermodynamics and fluid mechanics is investigated.** To do this, a systematic sweep of flow enthalpy and freestream composition is performed. Various Reynolds numbers are investigated. Second, **flow field establishment and unsteadiness is investigated.** A high speed schlieren photography setup is implemented to visualize the establishment process, and any potentially oscillatory behavior of the flow field. An edge detection code is used to extract shock configurations and locations for further analysis. This is complemented by thermocouple data which show the establishment process of the heat transfer profiles, as well as fluctuations in the established profiles. Lastly, **the experimental database for shock/boundary layer interactions is extended with the current data set.** The expansion tube provides thermochemically "clean" inflow conditions for validation of numerical models, and comparison with other types of ground test facilities. A brief, spectroscopic investigation of the ultraviolet emission from the NO radical is conducted to yield post shock NO vibrational temperatures. To the author's knowledge, this is the first comprehensive study of double wedge/cone flows to be performed in an expansion tube, and the first study to interchange air and nitrogen as test gases while maintaining nearly identical freestream conditions.

Chapter 2

Experimental Setup

2.1 The Hypervelocity Expansion Tube

Experiments are performed in the Hypervelocity Expansion Tube (HET) at the University of Illinois. The HET is a 9.14m long expansion tube facility, consisting of a driver, driven, and accelerator section, all with an internal diameter of 150mm. Facility capabilities include: operating at Mach numbers of 3.5-7.5 and achieving stagnation enthalpies of 2-8.8 MJ/kg. The use of an expansion tube offers several advantages, along with disadvantages, over other types of high enthalpy facilities. A good review of hypersonic testing facilities, as well as requirements for different types of vehicles/weapons systems is provided by Lu and Marren [53]. Trimpi [54] was the first to propose the idea of attaching a third section to a shock tube and using an unsteady expansion to further accelerate shocked gas, and increase the enthalpy. In contrast with the steady expansion of a diverging nozzle, an unsteady expansion fan will increase stagnation enthalpy. This can be seen mathematically in Equation 2.1, which is given by Anderson [55].

$$\rho \frac{Dh_0}{Dt} = \frac{\partial p}{\partial t} \tag{2.1}$$

D is a total derivative given by $\frac{D}{Dt} = \frac{\partial}{\partial t} + \overline{u} \cdot \frac{\partial}{\partial \overline{x}}$, ρ is the density, h_0 is the stagnation enthalpy, and p is the pressure. It is quite obvious that if $\frac{\partial p}{\partial t} \neq 0$, as it is through an unsteady expansion, then h_0 is not a constant. Heating the test gas with only a single shock, maintains a thermochemically "clean" test gas with low levels of freestream dissociation and non-equilibrium. As mentioned above in Section 1.3 for reflected shock tunnels, not only can these exist, but they can have significant effects on the freestream. A thermochemically clean free stream is important to maintain when simulating

the flight environment, as flight vehicles do not travel through dissociated air. The expansion tube also has the benefit of being able to access a wide range of Mach numbers and flow enthalpies merely by varying the gas fill pressures and compositions in each of the three sections, rather than using individual nozzles. The HET has some specific benefits compared with other facilities. The facility can be operated by a single person, with a turnaround time of approximately 2 hours. Additionally, it has a relatively low operational cost, due to its smaller scales.

These advantages do not come without certain trade offs however. One of these is that in general expansion tubes have much shorter test times than other facilities. Typical HET test times are on the order of 100-500 μs. Another major drawback is the increased viscous effects in the test gas. The test gas in a reflected shock tunnel will be immediately behind the reflected shock, where in an expansion tube it must travel the length of the third section to reach the test section. This dictates the core flow, and, in general, how large models can be. Typical HET core flows range from 38-100mm. Smaller models limit both the number of gauges that can be instrumented, as well as reduced resolution in surface measurements. Finally, flow disturbances resulting from propagating acoustic waves [56] and contact surface instability [57] create large amplitude flow disturbances in the test gas.

2.1.1 Gas Dynamic Processes of the HET

The nature of the processes that govern the expansion tube operation are inherently three dimensional complex interactions, among which include: wave-wave interactions, wave-contact surface interactions, shock-boundary layer interactions, fluid-structure interactions, and thermochemistry. The problem can, however, can be reduced to an unsteady, one dimensional, perfect gas flow. Theoretical test conditions can then be solved for including: Mach number, temperature, pressure, and test time. The description of the facility operation is best described using a position-time diagram, otherwise known as an $x-t$ diagram. A typical HET $x-t$ diagram is shown in Figure 2.1 courtesy of Sharma [57], calculated with the code of Dufrene [58].

The expansion tube is comprised of three sections denoted by the vertical dashed lines, and from

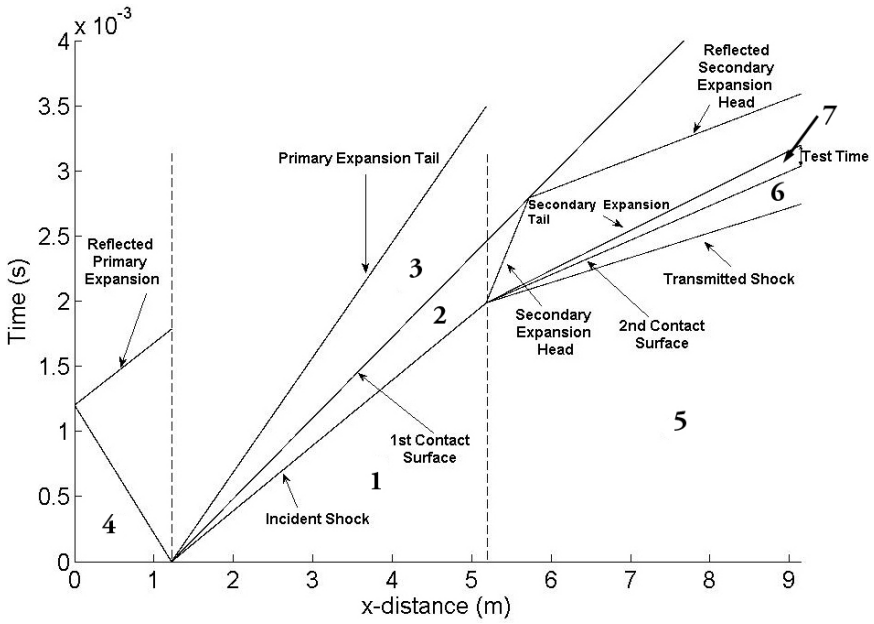

Figure 2.1: An example of an $x-t$ diagram of the the Air-5 run condition with a test gas Mach number of 7.42. Fill pressures are p_4=2500 kPa (helium), p_1 = 1.5 kPa (air) and p_5=175 mTorr (helium).

left to right are the driver (State 4) , the driven (State 1), and the expansion (State 5) sections. The driver and driven section operate identical to a shock tube. Upon the rupture of an aluminum diaphragm separating the two sections, the right-running, incident shock is transmitted into the gas at State 1. This heats the gas, and induces mass motion bringing it to state 2. At the same time, the left running primary expansion wave propagates into the driver gas, creating State 3. Although different gases and temperatures, States 2 and 3 must have the same velocity and pressure to satisfy shock polar requirements. Their interface is designated as the 1^{st} contact surface.

A thin mylar diaphragm separates States 1 and 5 initially. Upon the incident shock arriving at the interface, the transmitted shock is sent forward into the accelerator section, while the secondary reflected expansion wave propagates into the test gas at State 2. While the wave is left running, due to the fact that the flow is supersonic throughout, the entire wave moves to the right in the lab frame. A second contact surface is formed between the shocked accelerator gas (State 6) and the test gas at test conditions (State 7), as a result of this wave interaction. As shown in Figure 2.1, the test time for this specific run condition is the time between the arrival of the second contact surface, and the arrival of the secondary expansion tail.

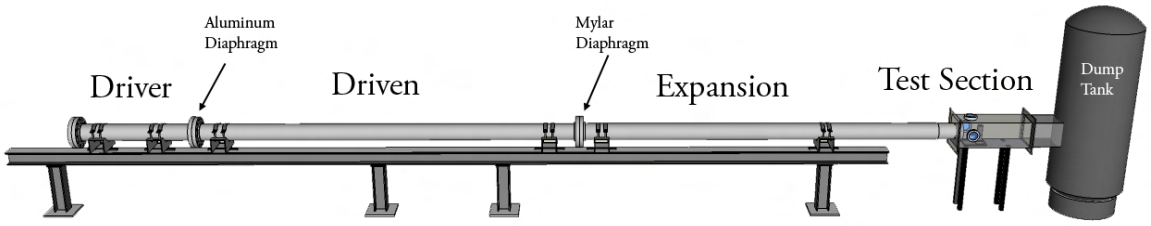

Figure 2.2: A schematic of the HET with important features labeled.

The secondary expansion tail is one of three flow features that can terminate the test time. The second is the reflected secondary expansion head. When the secondary expansion head reaches the first contact surface, it will by necessity reflect and create a non simple region. Dufrene *et al.* [59] solve for the trajectory of the reflected expansion head with an ordinary differential equation. The third, is the arrival of reflected primary expansion head. Due to the dimensions of the HET, this case is extremely unlikely, and is not considered when estimating test time.

2.1.2 HET Facility Description

The HET design process is described in detail in several works [58, 60, 59], and certain aspects are summarized here. Each of the three sections is manufactured with 152 mm (ID) honed 304/304L stainless steel and has a wall thickness of 9.5 mm. The test section is a square channel with three 100 mm windows for optical diagnostic access. Downstream of the test section is a 1.060 m^3 dump tank, which is used to trap the spent gas and keep the facility at a pressure below atmosphere post-experiment. The tube is designed to tolerate fill pressures of 5.5, MPa and a vacuum of 75 mTorr can be drawn. The length of the sections is as follows: the driver is 1.22 m and the driven and accelerator sections are 3.96 m each. These dimensions have been optimized to maximize test times. Each of the three sections is connected with flanges that attach with twelve 3/4" bolts. The tube is mounted on linear bearings for operator access. A schematic of the HET can be seen in Figure 2.2.

The aluminum diaphragm separating the driver and the driven sections is made of 5052-H32 aluminum. Two thicknesses are used in this study: 1.27 mm to yield a burst pressure of $\sim$2.5 MPa, and 0.813 mm to yield a burst pressure of 1.65 MPa. A knife cross, redesigned by Sharma [57],

maintains burst pressure repeatability, and prevents aluminum shrapnel from traveling down the tube. The secondary diaphragm is made of 12.7μm mylar sheet. This diaphragm, in effect, is invisible to the incident shock wave. Physically this means that transmitted and reflected waves are due to gas dynamics only, not fluid-structure interaction. A wire cross is used to maintain diaphragm integrity while evacuating the driven and expansion section. Unlike the primary diaphragm, shrapnel from this diaphragm does travel down the tube and can cause damage to the model.

The HET itself is instrumented with various sensors to monitor the state of the tube and performance. Along the span of the tube, four PCB 113A26 piezoelectric pressure transducers measure post wave static pressures and time of arrival, and can be used for triggering. Additionally, these sensors can be mounted in a housing normal to the flow and placed in the test section for pitot measurements and triggering. During evacuation the pressures in the driven and expansion sections are monitored by MKS Piezo+ A900-02 (0 to 1 atm) transducers. Additionally, an MKS Baratron 626A capacitance manometer (0-2000 mtorr) is used to monitor the accelerator section during the descent to its final pressure. Lastly, a Setra 206 gauge is used to measure the burst pressure of the driven section.

All data are acquired using a National Instruments PXI-1031 chassis, with two 8 channel BNC-2100 DAQ blocks. A Windows computer fitted with a 14-bit PXI-6133 parallel data acquisition module is used to collect data via the NI LabVIEW software package. Both the tube and model instrumentation data are recorded at a rate of 1 MHz for 30 ms, yielding 12000 data points before the trigger signal, and 18000 after the trigger signal.

2.1.3 Sting Mounting Modifications

In order to facilitate the visualization of a broader range of models, the current sting mounting [58] is redesigned to allow a variable mounting position in the axial direction of the HET. The new design includes counter sunk bolts to allow the sting to move forward on the plate. The new base plate and window mount are shown in Figure 2.3.

The lower piece is made of 1018 steel to allow it to be welded to the window flange. The top

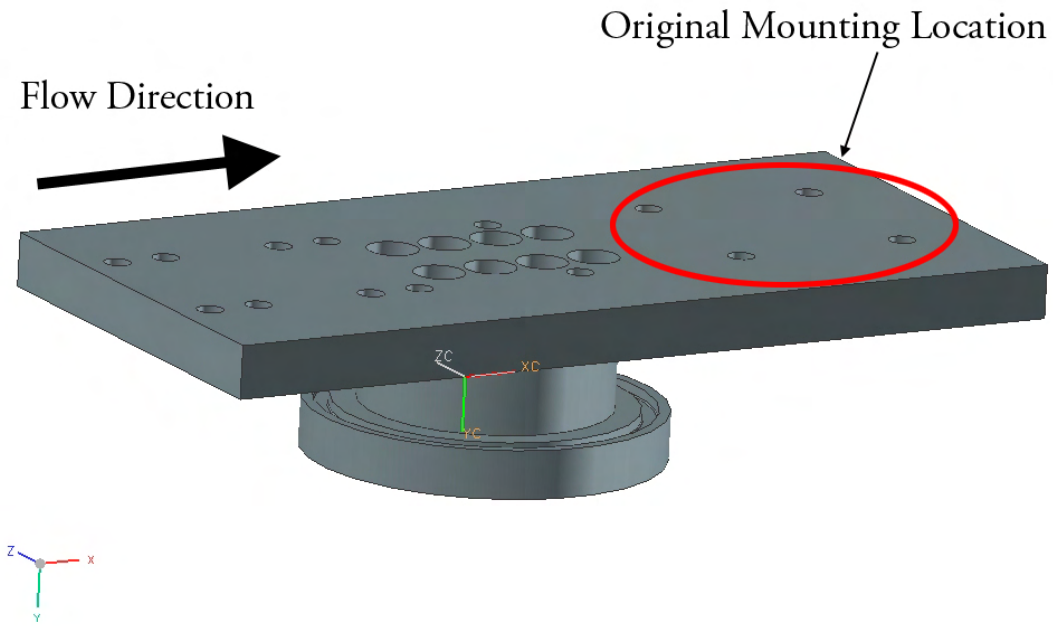

Figure 2.3: A three dimensional drawing of the new sting mounting. The original mounting location is labeled, along with flow direction.

plate is made of 4140 steel as originally designed by Dufrene [58]. The new design allows models to be moved 273 mm forward, which has the potential to aid in visualizations of longer flat plate/wedge models. Figure 2.4 shows an image of the plate installed in the test section.

2.2 Model Geometries

Two models are used in this study: a two dimensional double wedge geometry, and an axisymmetric double cone geometry. Both models are designed based on historical designs, which have been shown to be useful for studying shock/boundary layer interactions. Both geometries are modeled in Unigraphics (NX 6.0), and Nastran is used to simulate the loads experienced during tube operation to ensure model failure does not occur.

Figure 2.4: An image of the base plate mounted in the test section. The front flange is off, and the view is facing downstream in the facility

2.2.1 Double Wedge Model

We utilize a double wedge model ($\alpha = 30°$, $\theta = 25°$, $L = 50.8$ mm, and $b = 101.6$ mm) machined from A2 tool steel. It is composed of two separate pieces to allow access to the internal areas for instrumentation The model is dimensioned according to the criteria summarized by Davis and Sturtevant [21], and is designed as a one half scale version of theirs. One of the critical parameters is that the wedge width should be 85 times greater than the boundary layer thickness at separation (δ_1), to minimize the effects of three dimensionality on the separation zone. For the present work, the minimum δ_1/b value is found to be $\sim$125 which exceeds the recommended minimum. Side fences are not included as they have potential for increasing the separation zone size, as well as optical interference. An image of the double wedge model is shown in Figure 2.5

The model is instrumented with 19 coaxial thermocouples at 16 different streamwise locations along the model face. Three locations have 2 gauges, to assess any three dimensional behavior. The locations for each gauge are shown in Table 2.1. Gauges are clustered around areas of interest in the flow such as: separation, reattachment, and shock impingement. These locations are determined from single frame schlieren imaging.

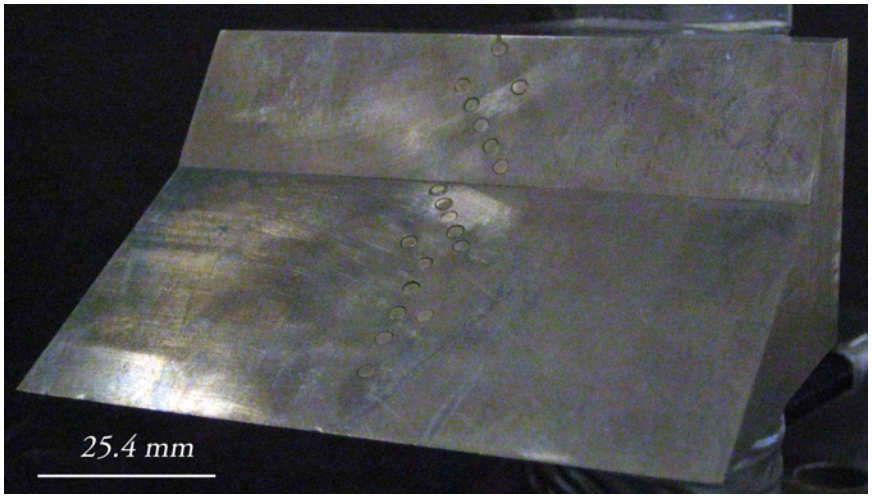

Figure 2.5: An image of the double wedge model is shown with a scale. Coaxial thermocouples are mounted in the model

Table 2.1: Location of coaxial thermocouples on the double wedge model.

	Gauge	x, in	z, in	x/L_1	z/W
	A	0.4	0	0.2	0
	B	0.7	0	0.35	0
	C	0.9	0	0.45	0
	C1	0.9	0.162	0.45	0.0405
	D	1.1	0	0.55	0
Fore End	E	1.3	0	0.65	0
	F	1.468	-0.162	0.734	-0.0405
	F1	1.468	0.162	0.734	0.0405
	G	1.584	0.081	0.792	0.02025
	H	1.7	0	0.85	0
	I	1.816	-0.081	0.908	-0.02025
	J	1.932	-0.162	0.966	-0.0405
	K	2.119	0.185	1.0595	0.04625
	L	2.251	0.092	1.1255	0.023
	M	2.383	0	1.1915	0
Aft End	N	2.515	-0.092	1.2575	-0.023
	O	2.647	-0.185	1.3235	-0.04625
	O1	2.647	0.185	1.3235	0.04625
	P	2.897	0	1.4485	0

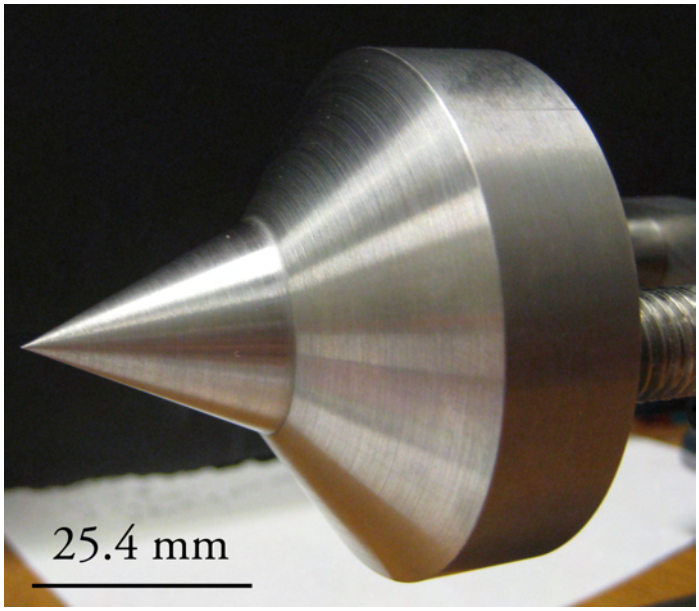

Figure 2.6: An image of the double cone model is shown with a scale.

2.2.2 Double Cone Model

The double wedge model is designed based on a schematic provided by Nompelis *et al.* [35]. The model is a 25°-55° geometry, with the first diameter being 25 mm, and the second diameter being 63.5 mm. This geometry allows for a large separation zone, and has the benefit of creating a standoff bow shock, which ensures high temperatures. The model is manufactured from A2 tool steel, and is created in two sections for alignment purposes. An image of the double cone model is shown in Figure 2.6

2.3 Diagnostics Techniques

2.3.1 Schlieren Imaging

A Z-type schlieren setup is used to image density gradients in the flow. Settles [61] gives a thorough description of the fundamentals behind schlieren imaging, as well as practical implementation, thus they will not be addressed here. A schematic of the setup used in for this study is shown in Figure 2.7

Four light sources are available, three of which have been used for this work. A Xenon spark gap is used for the single frame schlieren, and has an effective pulse width of ∼20 ns. For high speed

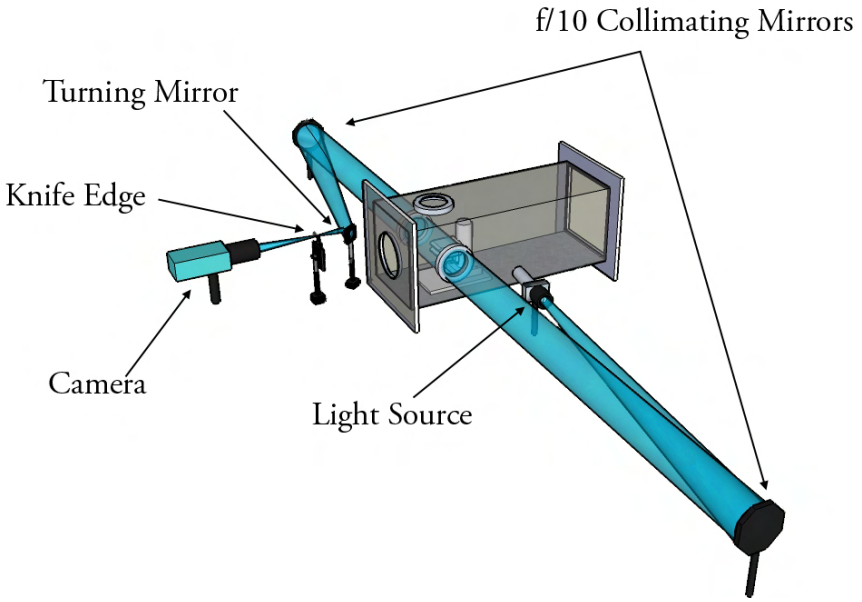

Figure 2.7: The Z-type schlieren system used in this study is shown, along with key components labeled.

imaging, two continuous wave light sources are used. A Thor Labs high intensity (1W) broadband LED is used for imaging at 10 μs exposure time. A custom built, 5W light source is used for imaging at 1μs in the later stages of this work. This light source is a 5W LED (Thor Labs) mounted to a Corsair water CPU cooler via Arctic Silver Thermal Compound. Using the CPU cooler, the stock max current of $\sim$1 Amps can be overdriven to $\sim$2 Amps. A low ripple, variable power supply from McMaster-Carr is used to provide power without the 60 Hz noise of typical wall transformers.

The mirrors used are $\lambda/4$, 108 mm, f/10 parabolic mirrors. A standard 50.8 mm turning mirror is used to align the light with the camera. After passing over the knife edge, the image is recorded with one of two cameras, both equipped with a Nikon zoom lens (f = 70-300 mm). The camera used for the single frame is a PCO 1600 camera. With sensor size of 1600 x 1200 pixels, it yields high resolution images for measuring flow features. The second camera used is a Photron Fastcam SA-5 high speed digital camera. Two framing rate settings are used for this study: 75,000 frames per second (13.33 μs inferframe time) at 320 x 264 pixels and 100,000 frames per second (10 μs interframe time) at 320 x 192 pixels. Framing settings have used both a 10 μs and 1 μs shutter time to allow an ample signal level for a given light source. Although these frame areas are over an order of magnitude smaller than the PCO, each shot in the expansion tube can be visualized in its

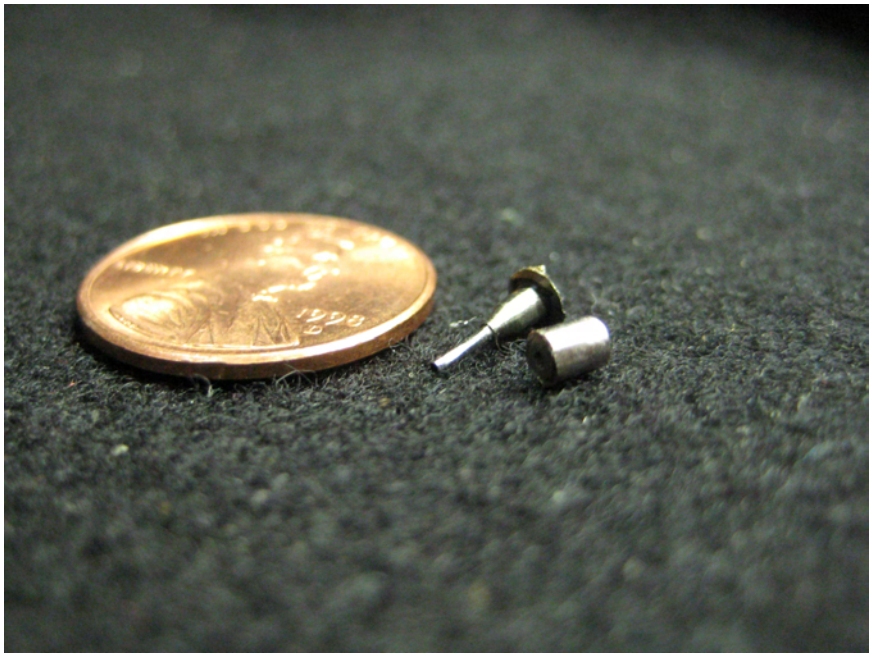

Figure 2.8: The inner and outer electrodes are shown along with a penny for scale. Image is courtesy of Flaherty.

entirety, as the camera records at these rates for ∼3 seconds. Typically 20-35 images are obtained within the test time.

2.3.2 Fast Response Thermocouples

Surface heat transfer is measured via coaxial fast response thermocouples. The gauges are designed based on the work of Sanderson [49] and have been implemented for the HET by Flaherty [62]. The gauges are Type E (constantan-chromel) thermcouples, 2.4 mm in diameter and are flush mounted to the surface of the model. An inner electrode and outer electrode are epoxied together to form the sensor. A junction of ∼1 μm in depth is formed at the interface of the two materials, yielding a response time of $\sim 1\mu$s. An image of the gauges is shown in Figure 2.8

As the signal is on the order of millivolts, amplifiers (nominal gain of 1000) manufactured by Flaherty are used to prior to recording the signal to increase the signal level. Individual calibration is not performed, as the response of these gauges is well known. The NIST reference tables are used to convert the output voltages to temperatures. Heat transfer is deconvolved from the temperature traces using a Fourier method described by Sanderson. The temperature is defined using

Equation 2.2.

$$\Delta T(x,t) = \int_0^t g(x,t-\tau)\dot{q}(\tau)d\tau \tag{2.2}$$

ΔT is the change in temperature, and $g(x,t)$ is an impulse function, given by Equation 2.3

$$g(x,t) = \frac{\partial \Delta T(x,t)}{\partial t} = \sqrt{\frac{\alpha}{\pi k^2 t}} \exp \frac{-x^2}{4\alpha t} \tag{2.3}$$

α is the thermal diffusivity and x is the thermocouple junction depth. The heat flux is then solved for by taking the Fourier transform of the equation, and then using Equation 2.4.

$$\dot{q}_n = FFT^{-1}\left[\frac{S_n}{G_n}\right] \tag{2.4}$$

In Equation 2.4, S_n is the Fourier Transform of the temperature signal, and G_n is the Fourier Transform of the Impulse function shown in Equation 2.3.

2.3.3 Emission Spectroscopy

NO vibrational spectra are obtained in the M7_8 air test condition, on the double wedge using a setup based on the work of Sharma [57]. The NO A-X band is interrogated in the ultraviolet (UV) portion of the spectrum from 220 to 255 nm. NO is the dominant species emitting in the region, thus it is ideal for temperature fitting. Light from the emission is collimated with an f/4 (f=200 mm) UV coated lens. The collimation lens passes the light to an identical lens that focuses it onto the slit of the spectrometer. The spectrometer used in this experiment is an f/4 (f=0.270 m) SPEX 270M. The slit width is 43 μm ,and a 1200 groove/mm diffraction grating (200 nm blaze wavelength) is used, which gives approximately 35 nm across the 12.4 mm intensified CCD (ICCD) chip. The resolution based on the slit width and the diffraction grating is 1.56 Angstroms. The camera used for detection is a Princeton Instruments PI-Max 512 intensified camera. Due to low signal levels, the PI-Max is set to a gain of 255 and an exposure of 110 μs. A delay of 90 μs is added from the

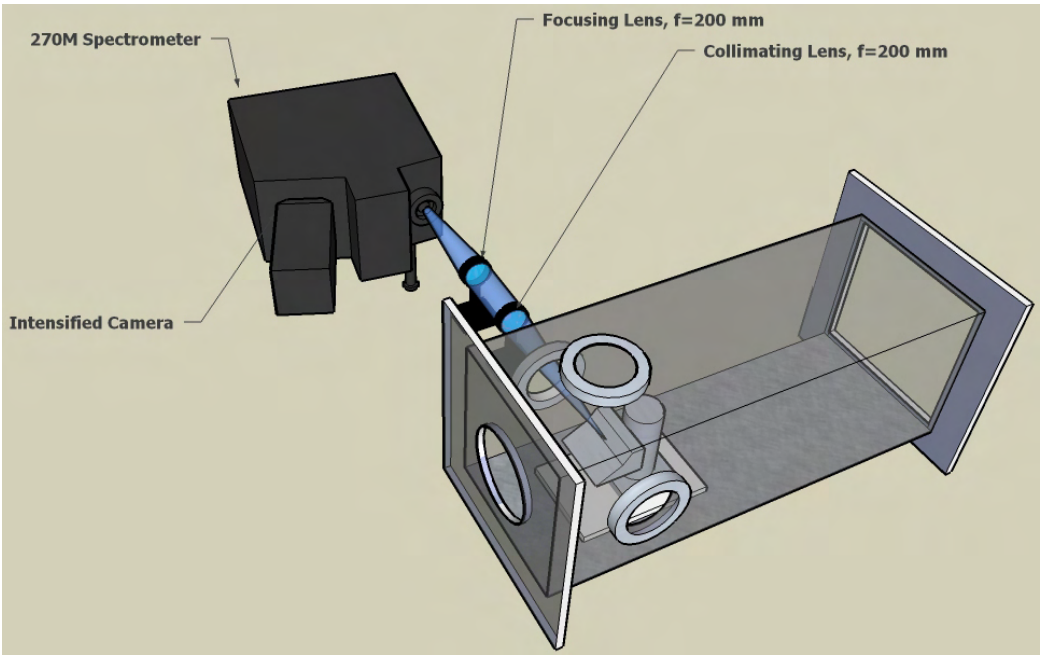

Figure 2.9: The NO emission spectroscopy setup is shown.

start of the test gas to allow for flow establishment. A three dimensional schematic of the setup (modified from Sharma's [57]) is shown in Figure 2.9.

Spatial alignment of the optics is performed with a guide plate cut to the contour of the double wedge model. The plate is aligned with a custom piece assembled from a lab jack (for vertical adjustment) and a translation stage (for streamwise adjustment). Images of the plate and the alignment unit are shown in Figures 2.10(a) and (b). Single frame schlieren images and the high speed imaging results have been used to determine bow shock location. 4 holes at 2mm spacing are drilled in the plate, starting at the nominal location of the bow shock, 6.1 mm above the nominal location of the triple point.

Wavelength calibration is performed with a hollow cathode Fe lamp, and intensity calibration is performed with a Hamamatsu UV-VIS Deuterium lamp. A UV transmissive fiber optic cable with SMA905 couplers is routed from the guide plate to the light sources. This allows the calibration piece to be aligned once, while both light sources are kept on the exterior of the expansion tube and the fiber optic is switched between the two. This eliminates any uncertainties from moving each source individually into the tube, as was previously done. Losses through the fiber optic cable

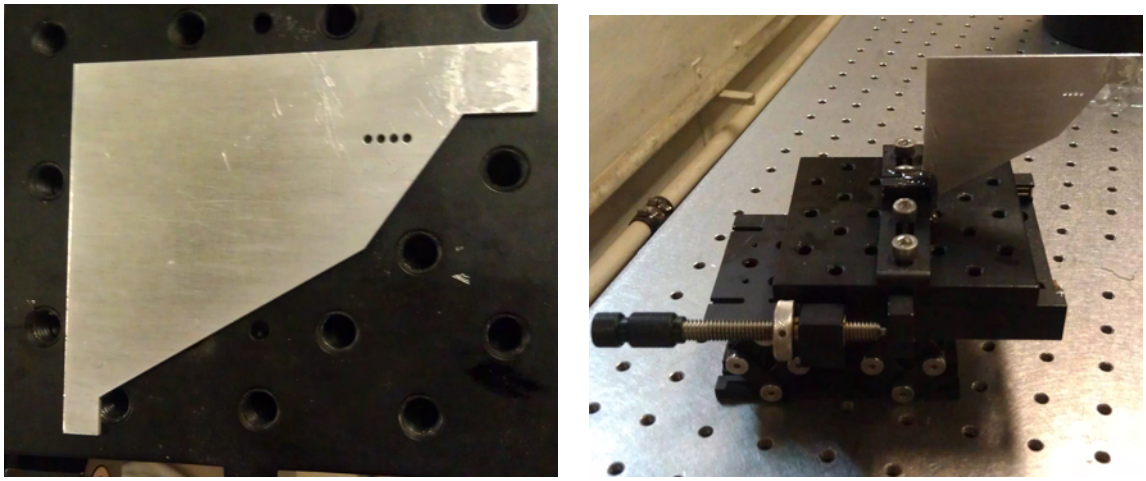

(a) (b)

Figure 2.10: The (a) alignment piece with calibration holes and (b) alignment unit are shown.

are non-negligible, thus a separate calibration of the component is performed. An image of the alignment unit with the optical assembly is shown in Figure 2.11.

The slit width is determined by measuring the fringe spaceing created by a laser of known wavelength. Two lasers, a 405 nm and 650 nm, are passed through the slit, and the fringe pattern is projected 750 mm away. Using the relation given in Equation 2.5 (for small divergence angles) the slit width is adjusted until the fringes appear at the desired spacing.

$$m\lambda = a\frac{y_m}{L_p} \tag{2.5}$$

This equation determines the location, y_m, of the m^{th} minimum away from the center fringe. a is the slit width, λ is the wavelength of light, and L_p is the length from the slit to the projection. The fourth minimum away from the center is used and measurements are made with a caliper. Accuracy in the y_m value is approximately 1mm (2% of the measurement), and accuracy in the laser wavelength is 1.5%. This results in a net error of approximatly 2.5% in the estimation of slit width.

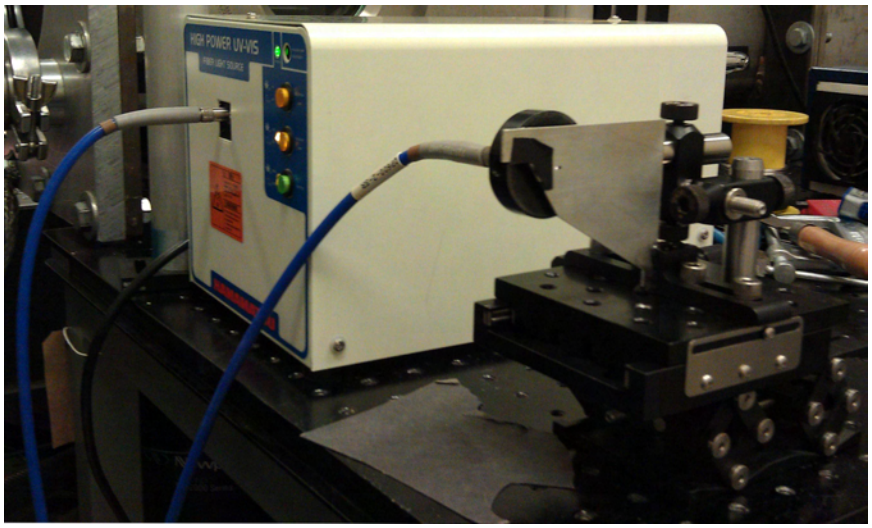

Figure 2.11: The alignment piece is shown affixed with the Deuterium light source and fiber optic coupling.

Table 2.2: Theoretical parameters for HET run conditions, for the current experiments.

Freestream Parameters	M7_2	M4_3.6	M5_4	M7_8
Mach Number	7.11	4.01	5.12	7.14
Static temperature, K	191	853	676	710
Static pressure, kPa	0.391	18.3	8.13	0.78
Velocity, m/s	1972	2340	2664	3812
Density, kg/m^3	0.0071	0.0747	0.042	0.0038
Test Time, μs	327	562	361	242
Unit Reynolds Number, $10^6/m$	1.10	4.64	3.42	0.435
Stagnation Enthalpy, MJ/kg	2.1	3.6	4.2	8.0
Initial Pressures, kPa				
Driver Section	1350(Air)	2500(He)	2500(He)	2500(He)
Driven Section	4.5	6.0	6.0	1.2
Expansion Section	0.037(He)	0.16(CO_2)	0.080(Air)	0.023(He)

2.4 Run condition selection

In this section a discussion of run conditions for the study is provided. There are two goals in selecting run conditions: 1.) to span the largest range of stagnation enthalpies as allowed by tube operation parameters and 2.) to span a range of Reynolds numbers. Sweeping stagnation enthalpy effectively allows control over the role of chemistry in the flow, while spanning Reynolds number allows control over the state of the boundary layer. Four run conditions are created using Dufrene's gas dynamics code, the parameters of which are listed in Table 2.2.

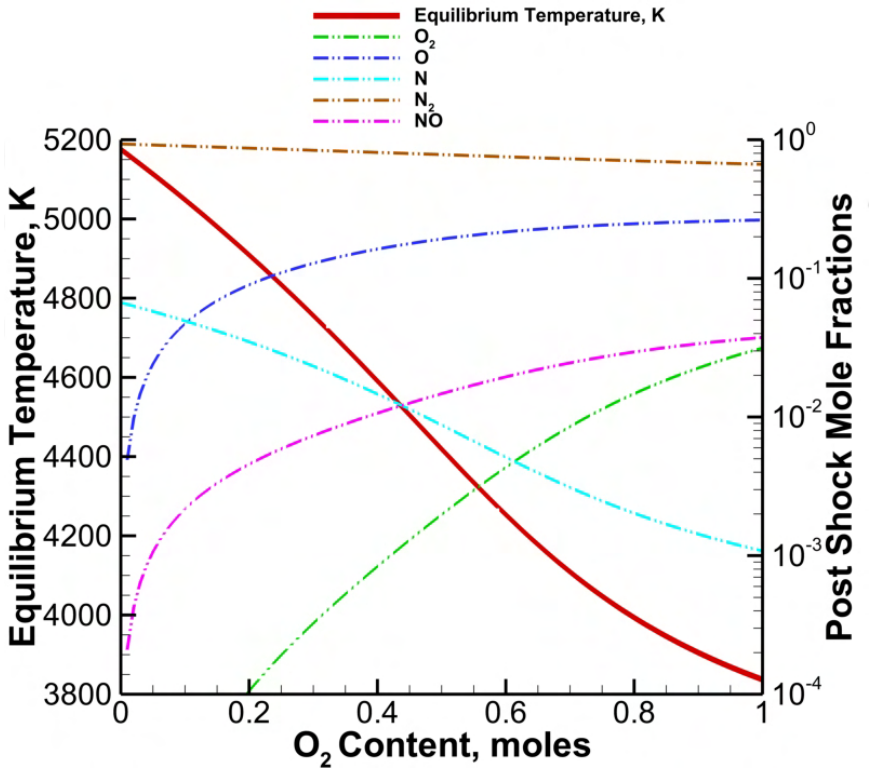

Figure 2.12: An equilibrium calculation using the Cantera software package for conditions behind a normal shock with the M_∞=7.14, T_∞=710 K, and P_∞=0.78 kPa.

These run conditions span enthalpies ranging from 2.1 MJ/kg up to 8 MJ/kg, nearly the entire HET operational range. Additionally, the unit Reynolds number spans over an order of magnitude ranging from 0.435 x $10^6 m^{-1}$ to 4.64 x $10^6 m^{-1}$. One feature unique to this study is that each of these run conditions can utilize either air or molecular nitrogen as a test gas. Due to the fact they have extremely similar gas properties, substituting gases yields negligible change in the freestream quantities ($< 0.5\%$). To the author's knowledge there is no study that has exploited an expansion tube's acceleration process to make direct comparisons of nitrogen and air in this manner. As an example of what is expected behind a normal shock in the M7_8 condition, a calculation of the equilibrium species concentration and temperature is plotted in Figure 2.12 with the Cantera software package [63]. The calculation is done such that the nitrogen content is kept constant at 3.76 moles and the moles of oxygen are varied from 0 to 1 (pure nitrogen to atmospheric composition).

Figure 2.12 illustrates that the inclusion of oxygen in the freestream decreases the equilibrium temperature by over 20%. It also has the effect of creating NO which is considered to be a very

important species in these types of flows, as mentioned in Section 1.3.

Chapter 3

Single Frame Schlieren and Separation Scaling Results

In this section, the results from the single frame schlieren imaging are presented for analysis. A brief summary of the theory behind two dimensional separation length scaling for these flows is presented followed by the methodology used to apply this body of work to axisymmetric geometries. Scaling results are presented for the current double cone data, as well as the current double wedge data and are compared with historical data. Shock polars are calculated for the triple point interactions on the wedge flow and compared with experimental measurements.

3.1 Theory of Separation

The separation of a flow occurs because the low speed flow in the boundary layer cannot negotiate the imposed pressure rise due to the corner. Glick [64] proposed one model for the process based on momentum transfer. A fluid particle starting at the separation point, S in Figure 3.1 has total pressure, P_{total}, equal to the static pressure, P_{static}, and $u = 0$. At reattachment, R , the fluid particle must have reattachment pressure, $\mathrm{P}_r > \mathrm{P}_s$. This is due to a mechanical energy increase by viscous transport of momentum from the outer flow towards the dividing streamline. As θ_w increases the length of the separation zone must increase, because the shear layer must be longer to impart the necessary momentum associated with the pressure rise.

The model used by Davis and Sturtevant's [21] analysis is based on the work by Sychev [65] and Roshko [66]. In its basic form, the model is a balance of momentum between the shear forces acting on ψ^* and the pressure rise at reattachment. Equation 3.1 shows this mathematically. Numbers reference the regions in Figure 1.1.

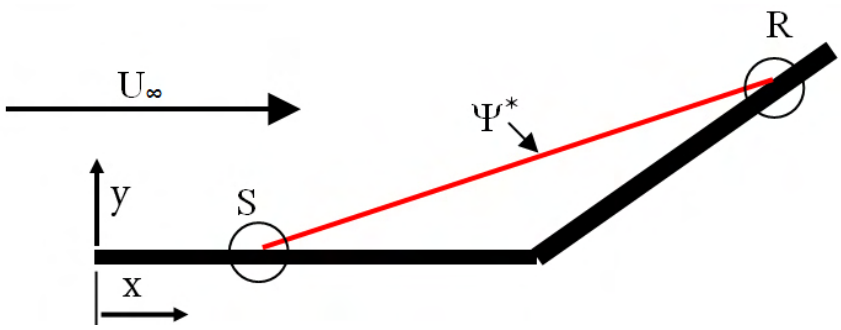

Figure 3.1: A diagram to illustrate the separation model. S is the separation location, ψ^* is the dividing streamline of the flow.

$$\int_0^{y_R} (p_{\psi^*} - p_2)dy = \int_{x_1}^{x_R} (\tau_{\psi^*})dx \tag{3.1}$$

The analysis of Davis and Sturtevant is based on the triple-deck formulation of Stewartson and Williams [67]. Flow coordinates are written for each of the three decks: $Y_L = \epsilon^{-5}y$ for the lower deck (viscous, incompressible), $Y_M = \epsilon^{-4}y$ for the middle deck (inviscid, compressible), and $Y_U = \epsilon^{-3}y$ for the upper deck (supersonic, isentropic). ϵ=$\mathrm{Re}_{x_1}^{-1}$ is a small parameter used to expand flow variables. To facilitate analysis, scaled variables are introduced and given in Equations 3.2, 3.3, and 3.4 . Variables a, b, and d are functions of the Mach number in Region 1, the wall conditions and the skin friction of the undisturbed boundary layer.

$$\tilde{x} = \frac{x - x_1}{a\epsilon^3} \tag{3.2}$$

$$\tilde{y} = \frac{y}{b\epsilon^5} \tag{3.3}$$

$$\tilde{u} = \frac{bu}{d\epsilon} \tag{3.4}$$

For a large scaled distance downstream of separation, an asymptotically matched solution is found for the flow near ψ^*, which matches the flow near separation. The leading-order term for scaled velocity is found to be $\tilde{u} \sim \tilde{x}^{1/3}F_0'(\tilde{\eta})$, with $\tilde{\eta} = (\tilde{y} - A(\tilde{x}))/\tilde{x}^{1/3}$. $A(\tilde{x})$ is a function which is

linear for large $\tilde{x}$ such that $\tilde{\eta} = 0$ along ψ^*. The prime indicates differentiation with respect to $\tilde{\eta}$. Substituting this result into Equation 3.1, using perfect gas relations for sound speed and further manipulation yields

$$\frac{L_{sep}}{x_1} \propto \frac{1}{\gamma_1^{3/2} M_1^3} \left(\frac{u_e}{x_1 U_0'(0)} \right)^2 \left(\frac{\rho_e}{\rho_w} \right)^{1/2} \left(\frac{\mu_e}{\mu_w} \right) \left(\frac{p_3 - p_2}{p_1} \right)^{3/2} \tag{3.5}$$

Further manipulation, and the incorporation of the Blasius solution with a reference temperature correction gives the final result Davis and Sturtevant found for separation scaling shown in Equation 3.6

$$\frac{L_{sep}}{x_1} \propto \frac{\Lambda_1}{\gamma^{3/2} M_1^3} \left(\frac{p_3 - p_2}{p_1} \right)^{3/2} \tag{3.6}$$

Λ_1 is a parameter unique to the work of Davis and Sturtevant which describes the effect of wall to boundary layer edge temperature ratio. It is defined as,

$$\Lambda = \left(\frac{\mu_w}{\mu^*} \right) \left(\frac{T^*}{T_e} \right) \left(\frac{T_w}{T_e} \right)^{1/2} \tag{3.7}$$

It is important to note at this point that this scaling **offers no predictive capability**. Scaling can only be performed *a posteriori* with measurements obtained from experiment, due to the fact it is based on an asymptotic theory for large Re_{x_1}.

3.2 Shock Interaction Background

Other phenomena investigated in this portion of the study are shock-shock interactions and triple point behavior. The first study to classify shock interactions was Edney [25], who investigated an oblique shock impinging on a hemisphere. Although the main goal of his work was the investigation of heating augmentation due to shock impingement, the Edney interaction classification is perhaps the most notable piece of this work, and is widely referenced in the literature. Sanderson [49] provides an extensive description of each of these types of interactions including polars and example

schlieren images. In a related work, Sanderson *et al.* [50] investigate the jetting resulting from a type IV Edney interaction, and its effect on the heat transfer on a cylinder in a hypervelocity nitrogen flow. Expanding on this, Sanderson *et al.* [68] go on to apply polar calculations to an unsteady detonation front. They make a connection between jetting in two flows: a steady flow with endothermic reactions, and an unsteady flow with exothermic reactions. Olejniczak *et al.* [69] have also done work looking at shock interactions on a double wedge geometry, and specifically the difference between viscous and inviscid simulations. They note that some viscous flows are difficult to classify in the Edney scheme, as the interactions are affected by the separation zone.

3.2.1 Edney Type IV Interaction

In this work, the most common interaction observed is the Edney Type IV interaction. The system of classification is based on the location of impingement of an oblique shock on a blunt body, and the form the resulting wave pattern takes. A Type IV interaction occurs at the intersection of a weak oblique wave (supersonic post shock flow) with a strong oblique wave (subsonic post shock flow). A single transmitted shock is formed along with a resultant shear layer. The flow on either side of the shear layer must have both the same direction as well as the same static pressure. Reflected waves can then propagate through the resultant flow field. This is visualized in Figure 3.2, which is based on a schematic by Sanderson [49].

In addition to the description above, a secondary triple point pattern can be seen at the intersections of regions 3, 4, and 5. These create a supersonic jet, which Sanderson observed to cause a jump in heat transfer. An example of a pressure polar of this type of flow is shown in Figure 3.3. Although depicted in the polar and the schematic as States 2 and 3 having a negative deflection, these can be positive and still be classified as an Edney IV interaction. This is, in fact, what is observed in the current study.

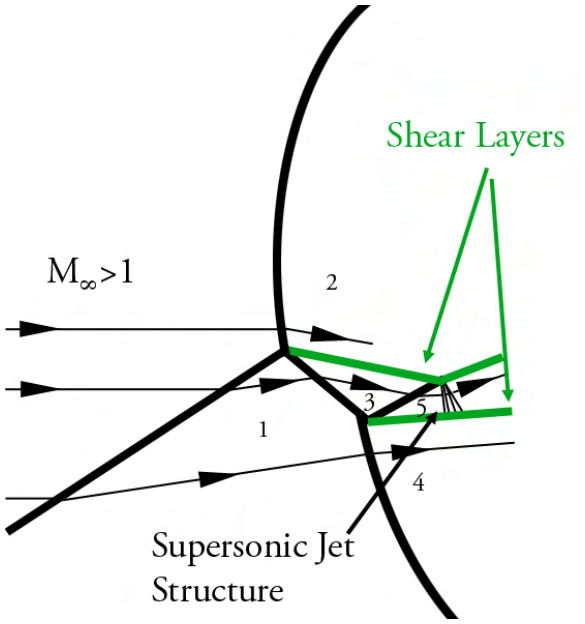

Figure 3.2: A schematic of the Edney type IV shock-shock interaction is shown. Flow is from left to right, and streamlines are drawn. Note: the image is not to scale.

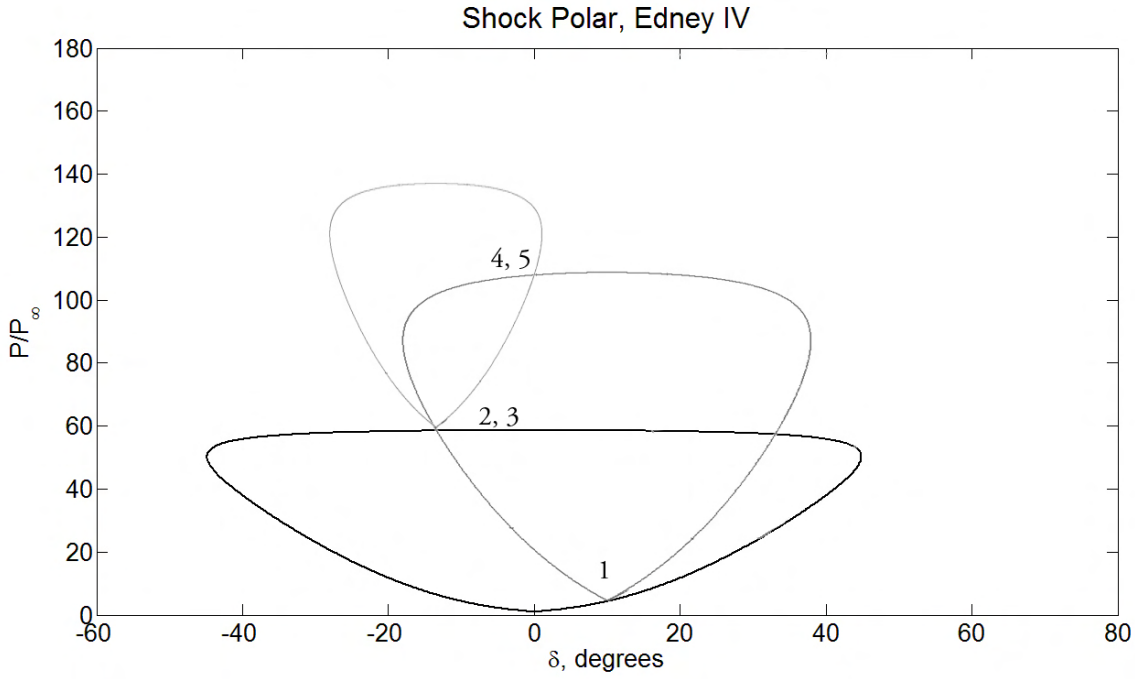

Figure 3.3: A pressure deflection polar for the Edney type IV shock-shock interaction is shown. Units are not to scale.

3.3 Double Wedge Schlieren Images

In this section example schlieren images are presented for each of the four test conditions in both nitrogen and air. The double cone and double wedge models are both included. Figure 3.4 shows the double wedge model data arranged in order of increasing enthalpy, with the location of the thermocouples indicated.

For the low enthalpy data in Figures 3.4(a) and (b), there are no noticeable differences in the nitrogen and air conditions that cannot be attributed to shot-to-shot variation. The flow appears to separate in between gauges B and C. As it travels downstream, the behavior of the diving streamline departs from what would be expected for a laminar separation zone. Impingement of the transmitted shock from the first triple point occurs near gauge M. Additionally, the triple point is not created by the leading edge shock, but rather the separation shock. This is an example of a case where triple point behavior and viscous behavior are coupled, and potentially the location of peak heating. Of the eight test conditions this is the only one that exhibits the creation of the triple point via the separation shock.

The next test condition is the M4_3.6 condition, which also has the highest unit freestream Reynolds number, shown in Figures 3.4(c) and (d). In general the flow field appears to have a more complex structure, which may be an indication of unsteadiness. The waves near what may be separation are numerous, and the location is not consistent from shot to shot. The transmitted wave from the triple point seems to bend down toward the first wedge forming a Mach stem. At this enthalpy there are some differences between the nitrogen and air test conditions. One of the most noticeable is that the standoff distance of the bow shock is further forward for the nitrogen case compared with the air case. This may result in the observed wave interaction just below the triple point. In the nitrogen case, what may be a Mach stem is formed just below the triple point, while in the air case, the interaction appears to be a normal reflection.

Perhaps one of the most interesting test conditions is the M5_4 condition, shown in Figures 3.4(e) and (f). The flow field has a more distinct structure than the previous case, exhibiting a triple point with reflected shock and shear layer. Both cases exhibit some distortion in the bow shock and

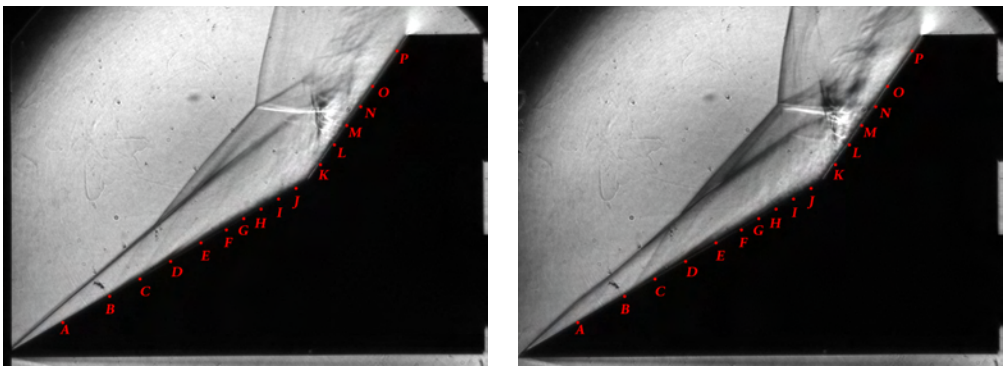

(a) M7_2 N_2

(b) M7_2 Air

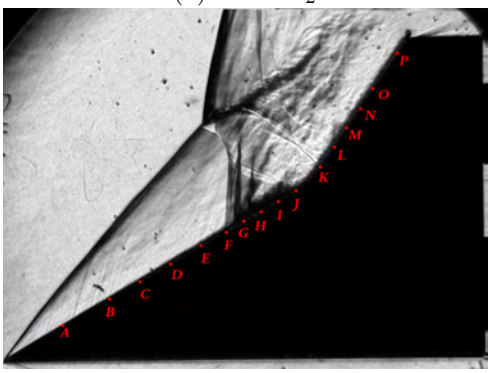

(c) M4_3.6 N_2

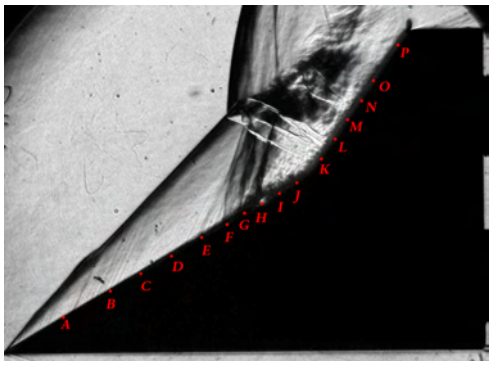

(d) M4_3.6 Air

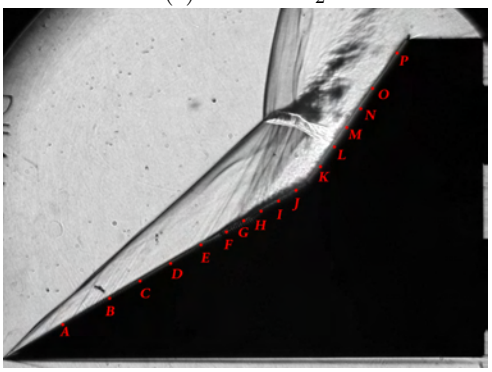

(e) M5_4 N_2

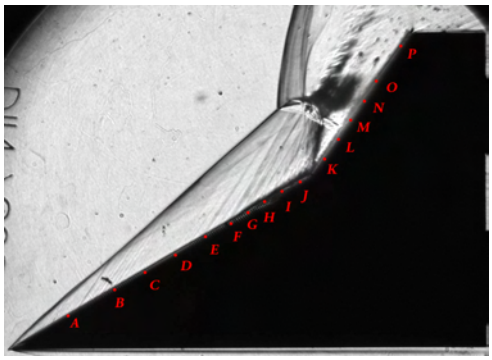

(f) M5_4 Air

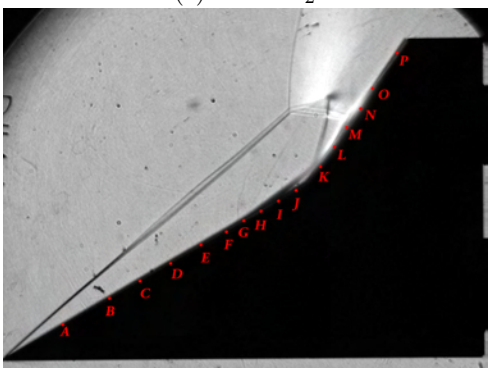

(g) M7_8 N_2

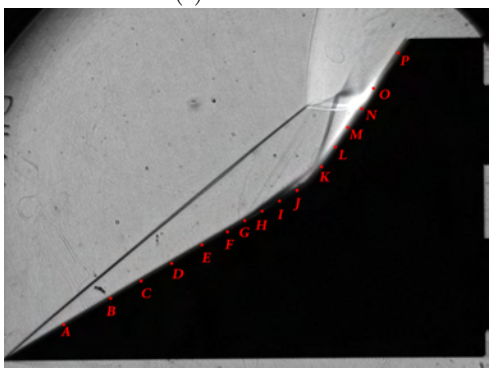

(h) M7_8 Air

Figure 3.4: Example images of the wedge flow for four different test conditions are shown. Thermocouple positions are also indicated on these images, referenced from Table 2.1

leading edge oblique shock. This is mostly likely due to shock curvature, and could be caused by either the edges of the model being outside the core flow, or the shock "bending" around the model near the edges. What is very unique about this condition is the behavior of the boundary layer and the mechanism for turning the flow up the second wedge. Both air and nitrogen exhibit a laminar boundary layer formed and developed on the first wedge. At a certain point downstream, waves emanate from the boundary layer, and a departure from laminar behavior is observed. The boundary layer thickens rapidly and the edge of the boundary layer exhibits structure. At this point the behavior of the flow is drastically different for the nitrogen and the air. A shock originating near the corner turns the flow upward, and a thinning of the boundary layer is seen. In the nitrogen flow, no wave is observed turning the flow. Instead, what appears to be a large region of subsonic flow (due to the lack of Mach waves traveling through it) merely turns up the corner. The boundary layer, again, is seen to thin on the second wedge. The lack of turning wave is another indication of this being a region of subsonic flow. The triple point is seen to form further forward on the model in the nitrogen flow than in the air flow, which agrees with the observations of the M4_3.6 condition. Interestingly enough, this does not appear to have an effect of the location of shock impingement on the aft body. For both gases, impingement appears to occur between gauges L and M. In this region, both images exhibit a noticeable amount of flow luminescence, most likely due to high gas temperatures.

Lastly, the M7_8 test condition is shown in Figure 3.4(g) and (h). Both flow fields exhibit laminar interaction, which is expected at this test condition, as it has the lowest unit Reynold's number. In both images, a boundary layer forms at the leading edge of the of the forward wedge, encounters a separation shock, forms a separation zone and then reattaches on the aft wedge. In both cases, the reattachment point is just upstream of gauge K. As in both previous cases, the standoff distance of the bow shock is seen to be larger for the nitrogen compared with the air. However, in contrast to the M5_4 test condition, the location of the shock that impinges on the surface is affected. For the nitrogen condition, the impingement occurs near gauge M, while for the air condition the impingement occurs near gauge N. Another major difference is the considerable

amount of illumination that occurs behind the bow shock in the nitrogen condition. This is a result of the high temperatures of the nitrogen, due to the lack of exothermic reactions created by the dissociating oxygen, thus more energy is stored in higher vibrational and electronic levels which emit photons when transitioning to lower levels. An equilibrium calculation of the post shock conditions, using the SDToolbox and Cantera software package [70, 63], indicates a post shock temperature of ∼5200 K, while for air it has a value of ∼3900 K.

3.3.1 Triple Point Calculations

Triple point calculations of each test condition are made and compared with experimental data. A triple point interaction between the leading edge oblique shock, and the bow shock is made. The interaction these shocks results in a shear layer and a transmitted shock. The transmitted shock is required turn the supersonic, post-oblique shock flow to match angle of the subsonic, post-bow shock flow. Two examples of these plots are shown in Figure 3.5 for the M7_2 and the M7_8 test conditions. Both frozen and equilibrium solutions are presented. The states are labeled as the "ramp condition", after the thirty degree turn, and the "shear layer", which is the post normal shock and post transmitted wave flows. In Figure 3.5b, there is a mismatch between the two polars at the ramp point in the equilibrium calculation. This is due to an error in the SD tool box calculation for low shock strengths.

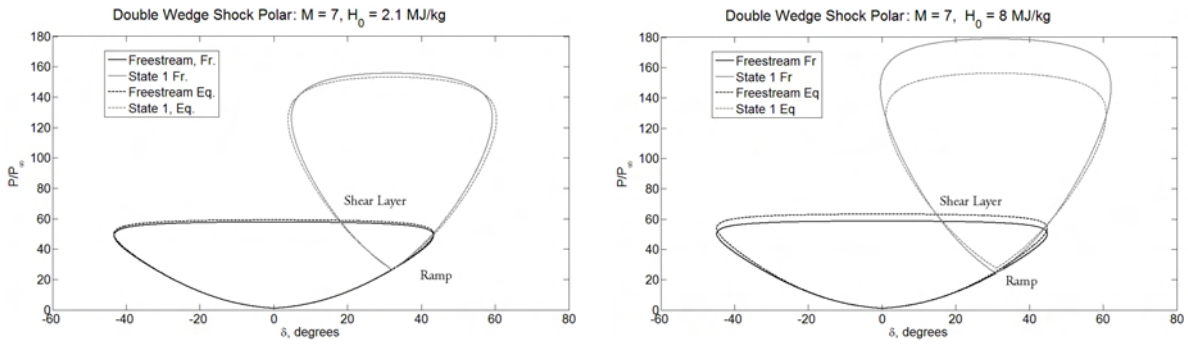

(a) M7_2 (b) M7_8

Figure 3.5: Example plots of polar calculations for the primary triple points. Calculations are performed for air conditions.

Not surprisingly, the equilibrium calculation and the frozen calculations do not differ significantly

at the 2 MJ/kg enthalpy condition. The equilibrium effects seen in the 8 MJ/kg case influence the polars in two ways. First, on the second polar, they reduce the pressure for strong shocks. With respect to geometrical considerations, equilibrium chemistry has the effect of reducing the shear layer angle, compared with the frozen calculations. Calculations like these have been done for every schlieren data set. The three features calculated from the triple point are the bow shock angle, the transmitted shock angle, and the shear layer angle. These are compared with the experimental measurements.

In general, the best agreement between theory and experiment across all test conditions is with nitrogen as a test gas. Of all the test conditions the best agreement with theory is the M7_2 test condition. The most disagreement between theory and experiment is the M4_3.6 test condition. Errors in the calculation of the transmitted shock angle are seen up to ∼50%, while at most for any other test condition they are ∼15%. Errors in the bow shock angles are minimal, at 1-4% across all test conditions. Lastly, errors in the shear layer angle are highly dependent on the test condition. For the M7_2, M5_4, and M7_8 conditions the error is 20% at most, with the mean being closer to 10%. For the M4_3.6 condition, the error climbs as high as 34%. The larger errors in the M4_3.6 condition may be a result the unsteady behavior which we believe to be seen in the schlieren images. This test condition also has the largest disagreement with the calculation of the shear layer angle as well. The results are summarized in Appendix F.

3.4 Double Cone Schlieren Images

As in the case of the double wedge, schlieren images of the double cone are shown in Figures 3.7 and 3.8. The double cone model offers the benefit of having two data points per each image (one on the top and bottom of the cone) and experiencing no three dimensional effects other than natural flow occurrences; however, due to the axisymmetric nature of the model the schlieren signal is weaker than the double wedge as there are fewer gas molecules for the light to interact with. In this study two types of interactions of the dividing streamline with the reattachment shock are observed. The first, shown in Figure 3.6(a), is the classical interaction where the dividing streamline terminates at

the base of the reattachment shock. The second, shown in Figure 3.6(b), is a new type of interaction where the dividing streamline intersects the reattachment shock. The presence of this second type of interaction indicates the separation zone may not be a simple recirculation zone, but contains various vortical structures akin to the schematic in Figure 1.2. As shown in Figure 3.6, the separation length, L_{sep}, is measured from the point of separation to the point where it interacts with the reattachment shock. For Interaction 1, this is at the base of the reattachment shock, and for Interaction 2, this is at a location above the base of the shock. This measurement of L_{sep} is used for calculation of the scaled separation length. When Interaction 2 configurations are present this causes a reduction in the separation zone length (compared with extending the dividing streamline to where it would interact with the aft cone surface. This reduction is approximately 15% for the M7_2, 50% for the M4_3, and 15% for the M5_4 test conditions. The M7_8 test conditions exhibits a dividing streamline which terminates at the base of the reattachment shock.

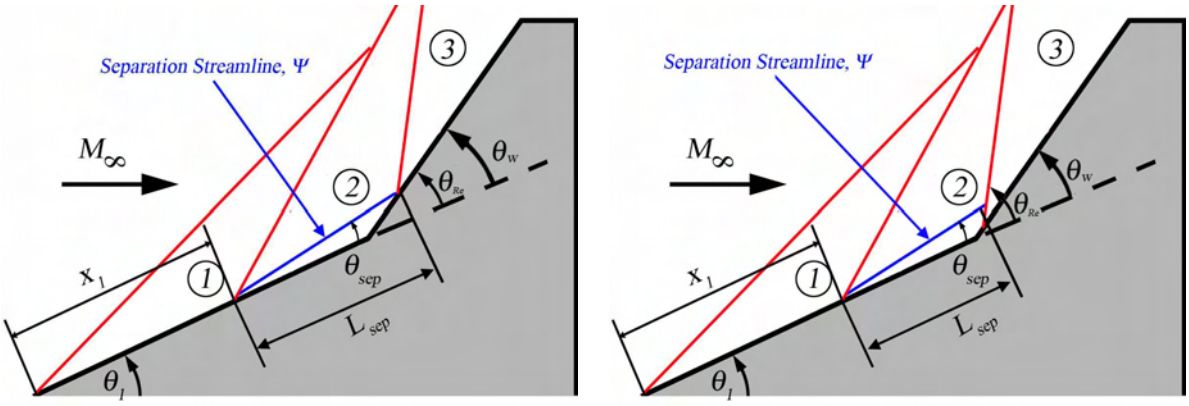

(a) Interaction 1 (b) Interaction 2

Figure 3.6: The two types of interactions observed in this study are illustrated above.

In Figures 3.7(a) and (b) the data for the M7_2 test conditions are presented. Both test conditions are seen to exhibit very similar flow features. A very thin boundary layer forms at the nose and separates nearly half way up the first cone. The dividing streamline exhibits a type 2 interaction (as in Figure 3.6(b)) wherein the dividing streamline intersects the reattachment shock. As in the case of the double wedge at this condition, the primary triple point is created by the separation shock. A shear layer and transmitted shock are also observed in both images. The reattachment shock forms up the aft cone, rather than at the corner.

Sample images for the M4_3.6 condition are shown in Figures 3.7(c) and (d). The flow field in these cases is more complex than for the M7_2.2 test condition. Again a boundary layer is seen to form in both images and separates. In contrast to the previous test condition, the dividing streamline deviates from laminar behavior quickly, and several Mach waves are seen to form off of it in both cases. The interaction type is most like the type 2 interaction described above. The primary triple point is created by the separation shock rather than the leading conical shock. The bow shock is considerably farther forward upstream than for all other cases, most likely due to the low Mach number. An interesting jet pattern is seen in both images just downstream of the primary triple point, being reminiscent of the pattern formed by an underexpanded jet. Due to variations between schlieren images in bow shock standoff distance and shape, it is believed this test condition may exhibit unsteady motion in the bow shock and separation zone. In this condition the reattachment shock occurs on the forward cone.

The M5_4 test condition is shown in Figures 3.8(a) and (b). The images are reasonably well structured, and as in the previous set of images, a boundary layer forms and separates, with a type 2 interaction happening at the reattachment shock. This, however is the first case where a distinct difference between nitrogen and air is seen. The nitrogen case in Figure 3.8(a) has a dividing streamline that appears to depart from laminar behavior before interacting with the reattachment shock, while the air case in Figure 3.8(b) is seen to remain closer to laminar behavior. This behavior is seen in several schlieren images. This phenomenon might be related to the behavior of the flow on the double wedge at the same test conditions. Although it is beyond the scope of this work, a full stability analysis may shed light on this phenomenon, as it has previously been seen by Massa *et al.* [71] that chemical reactions can have a significant effect on the stability of viscous layers. The triple point is formed by the separation shock and the reattachment shock, which for this case originates at the corner between the two cones. The shear layer formed by the triple point, in both cases lies very close to the body. Lastly, both images exhibit streaks of luminescence on the aft body. These structures may be an instability known as Goertler vortices, which are known to form on curved surfaces. The shape of the shear layer may create an "artificial" form of curvature allowing

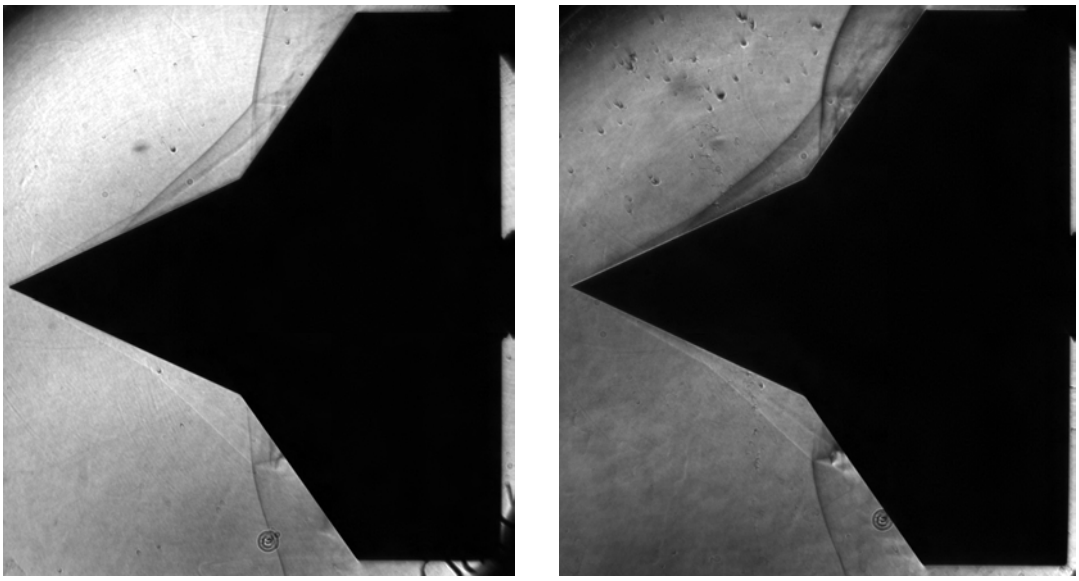

(a) M7_2 N_2 (b) M7_2 Air

(c) M4_3.6 N_2 (d) M4_3.6 Air

Figure 3.7: Example images of the double cone flow for the two lower enthalpy test conditions are shown. Note: pieces of diaphragm are visible in (c) and (d).

these structures to form.

Lastly, the M7_8 condition is shown in Figures 3.8(c) and (d). Due to the low density of these test conditions, shocks and other structures are faint compared to the other images. Both of these conditions exhibit the type 1 interaction, as the shear layer terminates at the base of the reattachment shock. In this case the reattachment shock occurs on the aft cone. The triple point, again, is created by the separation shock, rather than the leading edge conical shock. The bow shock has a slightly larger standoff distance in the nitrogen than it does in the air.

3.5 Scaling Parameter Results

To perform the calculation of the scaling parameter, a *MATLAB* code which utilizes the *SD Toolbox* [70] and *Cantera* [63] is implemented. States are determined using equilibrium shock calculations. The wedge parameter is calculated first, as no other assumptions are made beyond those of Davis and Sturtevant. The M7_8, nitrogen test condition is a similar test condition to their "B2" test condition (h_0=8.3 MJ/kg); thus this will be used as a validation test case. Quantities measured from the images include: x_1, θ_{sep}, L_{sep}, and θ_{Re}.

The physics of an axisymmetric conical flow are fundamentally different from those of two dimensional wedge flows. Streamlines will curve rather than stay straight; and properties are constant along rays rather than throughout the entire region. In the current modeling, it is estimated that the flow immediately behind the conical shocks will have the same deflection (and thus the same properties) as a two dimensional wedge with the same shock angle and freestream Mach number, based on arguments from Anderson [55]. Therefore, scaling is performed with the properties which lie along the ray an infinitesimally small distance behind the shocks in the system. The data for both the double cone and the double wedge are presented in Figure 3.9. Data from Davis and Sturtevant are also presented here for their low (red open symbols), mid (blue open symbols), and high (black open symbols) enthalpy data as well as their curve fits.

The agreement between the double wedge M7_8 nitrogen test condition with Davis and Sturtevant in Figure 3.9 serves as validation that the current code used for calculation is appropriate. In addition

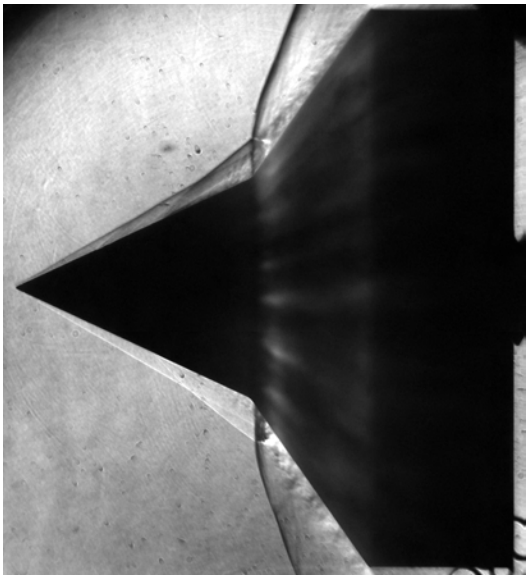

(a) M5_4 N_2

(b) M5_4 Air

(v) M7_8 N_2

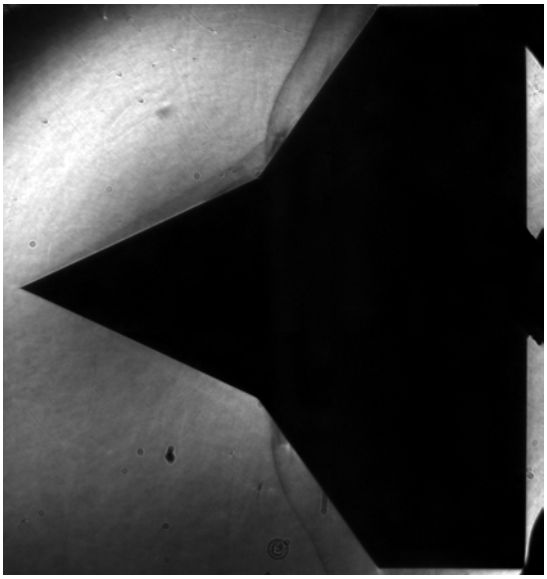

(d) M7_8 Air

Figure 3.8: Example images of the double cone flow for the two highest enthalpy test conditions are shown.

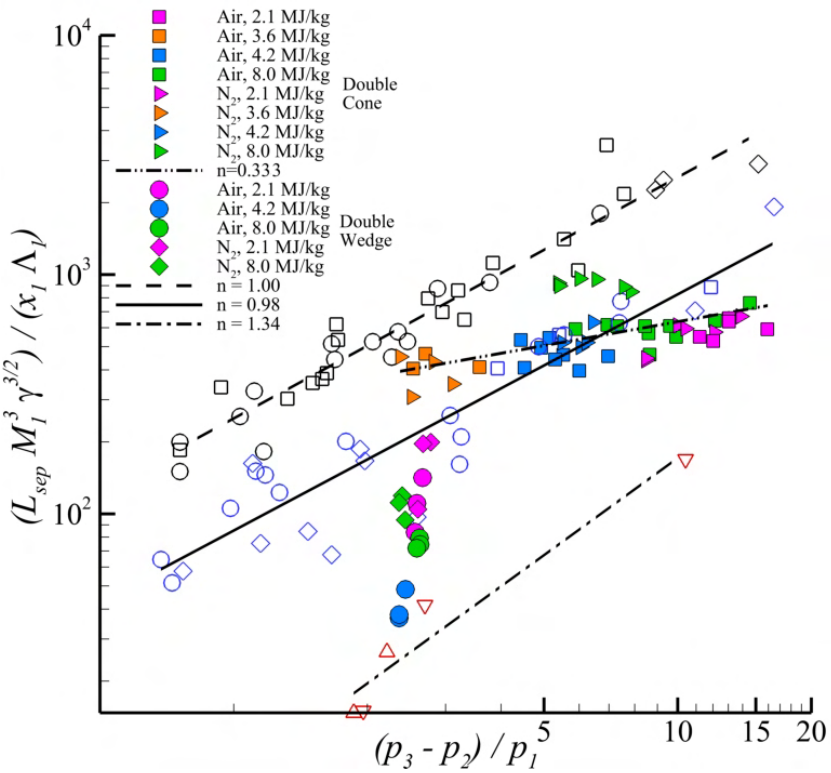

Figure 3.9: The scaling parameter is plotted versus shock system pressure ratio for double wedge data and double cone data. The ––,–, and –· are Davis and Sturtevant's fits to the high, mid-range and low enthalpy data. The 8.0 MJ/kg data are in agreement with Davis and Sturtevant (open blue diamonds), as at this test conditions our studies and theirs are similar.

to this data set, the M5_4 air conditions, which are similar to their "A1" (3.9 MJ/kg), test condition are also in agreement. The M7_2 condition does not agree with the other low enthalpy data, which will be addressed later.

With respect to the double cone model, the data lie along a single curve fit with a power law exponent of 0.823, with no distinct separation in enthalpy range. This value is lower that of the double wedge fits of Davis and Sturtevant, and physically indicates that in conical flows the separation zone size is less sensitive to changes in pressure than the double wedge. This may, in fact, be a manifestation of conical flow physics. The body allows for pressure relief due to its inherent symmetry about the streamwise axis, which will potentially limit the size of the steady separation zone that can form around the body. Additionally, all of the double cone data fall near the mid enthalpy range of data from Davis and Sturtevant. For the current double cone curve fit, Mach number increases as $(p_3 - p_2)/p_1$ increases. Curve fits for the current double wedge data are not performed, as there is an insufficient variation in $(p_3 - p_2)/p_1$ to produce a meaningful fit.

To further investigate the behavior of these flow fields, a plot of the scaled separation length versus Reynolds number is shown in Figure 3.10, which serves to quantify the effects of Reynolds number. The Reynolds number for the M5_4 double wedge flow is comparable to the low enthalpy data of Davis and Sturtevant and the data agree with theirs. Davis and Sturtevant noted that the boundary layer for these conditions appeared to be turbulent, and Figures 3.4(f) show a departure from laminar behavior. It is now apparent why the M7_2 double data does not fall with the rest of the low enthalpy data of Davis and Sturtevant. The Reynolds number is approximately an order of magnitude smaller than the "turbulent" conditions. While the dividing streamline does appear to depart from laminar behavior in the M7_2 case (Figures 3.4(a) and (b)), separation occurs while the boundary layer is laminar. This contrasts the behavior of the M5_4 case where the boundary layer has already deviated from a laminar profile.

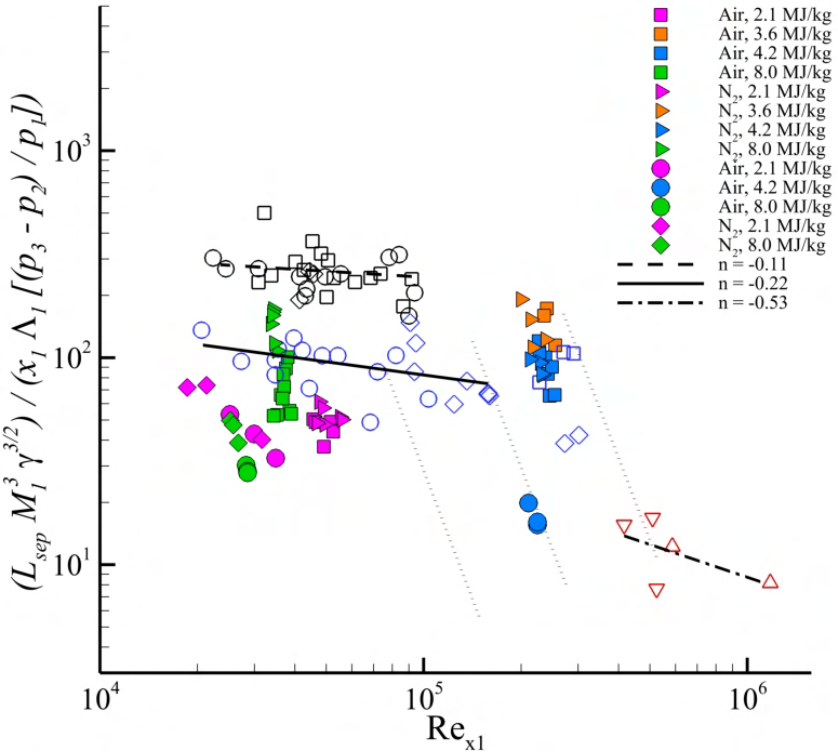

Figure 3.10: The scaling parameter is plotted versus Reynolds number based on the separation location for the double wedge and double cone data. The $--$,$-$, and $-\cdot$ are Davis and Sturtevant's fits to the high, mid-range and low enthalpy data. Dotted lines indicate possible transition paths indicated by Davis and Sturtevant. Symbols for the current data are the same as in Figure 3.9.

3.5.1 The Effect of Λ_1 on the Double Cone Scaling Parameter

The constant Λ_1 was derived to include the effects of the wall to edge temperature ratio on the scaled separation length, as previous scalings had not utilized it. The data in Figure 3.9 are shown without the inclusion of Λ_1 in Figure 3.11. From visual inspection, it can be seen that the cone data deviate father from the curve fit than in Figure 3.9. To quantify this, the root square deviation is defined in Equation 3.8, and is calculated at each data ordinate.

$$d = \sqrt{\left(\frac{\mathcal{L} - \mathcal{L}_{fit}}{\mathcal{L}_{fit}}\right)^2} \tag{3.8}$$

$\mathcal{L}$ is the scaled value of L_{sep} and $\mathcal{L}_{fit}$ is the value of the fit at that location. Without including Λ_1 the mean, $\bar{d}$, and standard deviation, σ, are 0.25 and 0.54 respectively. Including Λ_1 reduces these values to $\bar{d} = 0.19$ and $\sigma = 0.20$. This is in agreement with the results of Davis and Sturtevant, who observed an increase in correlation when including Λ_1. Davis and Sturtevant found that the inclusion of Λ_1 recovered the linear dependence of separation length on pressure. In the current double cone experiments, it is observed that the inclusion of Λ_1 drives the scaled separation length away from a linear dependence on pressure (changing the exponent from 0.823 to 0.33 with its inclusion). Additionally, there is no separation of enthalpy range as observed by Davis and Sturtevant.

3.6 Separation Scaling Conclusions

Hypervelocity flow over double cone and double wedge geometries has been observed . Single frame schlieren imagery is used to measure the separation zone length. A new type of interaction is observed in which the dividing streamline terminates on the shock from the secondary cone, and thus we define a different L_{sep} for this type of interaction. Scaled separation length data are compared with the results of Davis and Sturtevant for a double wedge for a similar inflow boundary layer condition. It is seen that the theoretical framework for the double wedge configuration can successfully be applied to double cones, by assuming the properties along the rays immediately behind the conical shocks. The inclusion of the Λ_1 parameter is seen to improve the scaling correlation, by taking

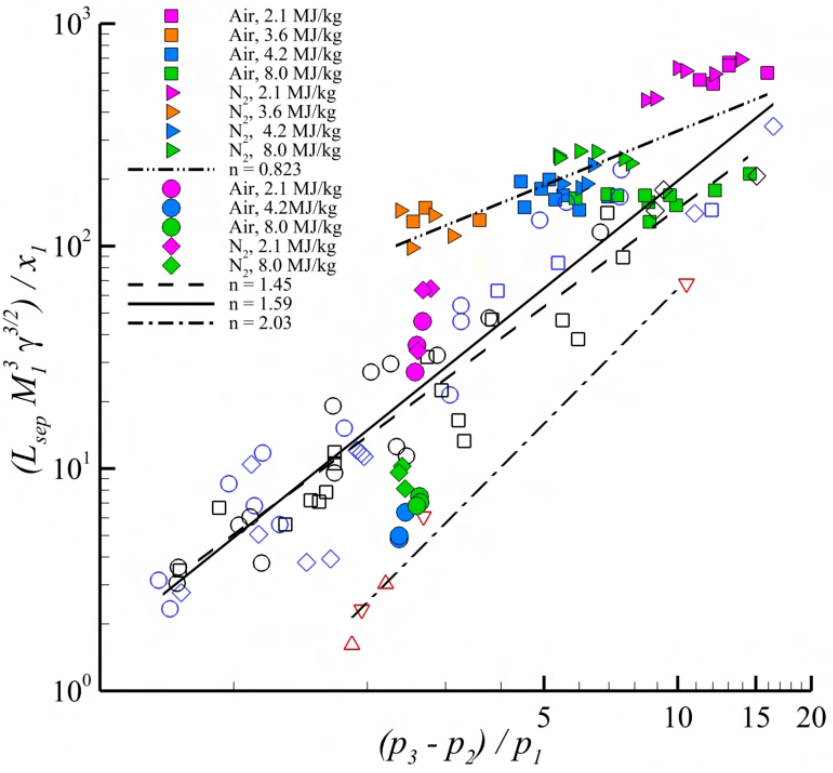

Figure 3.11: The scaling parameter is plotted versus shock system pressure ratio for double wedge data and double cone data without the inclusion of Λ_1. Symbols for the current data are the same as in Figure 3.9.

into account the ratio of the wall temperature to the edge of the boundary layer temperature. It has also been shown that this scaling is appropriate for air flows, in addition to nitrogen flows. An equilibrium solver is used to calculate the separation parameter, and is found to be appropriate. This does not necessarily imply that the flow is entirely in equilibrium, but that scaling can be done via equilibrium states. Lastly, it is observed that in addition to the flow enthalpy, as expected, the nature of incoming boundary layer also has an effect on the separation zone scaling. Plots of separation length versus Reynolds number illustrate the difference between test conditions which span over an order of magnitude in Reynolds number.

Chapter 4

Heat Transfer Measurements as a Comparison of the Thermochemical Differences Between Air and Nitrogen Flows

Using the fast response thermocouples discussed in Section 2.3.2, heat transfer profiles are constructed over the double wedge model for each of the 8 different test conditions. Current capabilities limit data acquisition to 10 channels. As there are 19 gauges on the model, two shots are required to capture all the points. At least three full data sets are obtained for each model to assess repeatability. In total ∼60 shots are taken to establish working gauges, as well as to profile all of the test conditions. Heat transfer values are averaged after the flow has been established; thus each transient heat transfer profile must be inspected individually to determine the useful test time. In addition to averages, the standard deviation of heat flux is also recorded with the goal of quantifying the fluctuations. An example of gauge establishment is shown in Figure 4.1. Averaging is done through period of time after establishment, before the end of the test gas. Toward the leading edge of the model (Gauge A) nearly no establishment is observed, thus the average is taken through the entire test gas. This is typical of gauges in the laminar, flat plate region of the flow. Heat transfer traces exhibit a mean value with a fluctuating component as well.

4.1 Mean Heat Transfer Profiles

In this section each set of heat transfer profiles is presented along with the schlieren images seen in Section 3.3. The error bars on the heat transfer values are ±8% of the absolute value. The location of the hinge is shown by a vertical dashed line, and x location is normalized by the length of the first wedge face. A laminar calculation of heat transfer on the forward wedge is performed based on the work of Hayne *et al.* [72]. This method uses the Young-Janssen reference temperature, at which flow properties are evaluated. The post-oblique shock properties are used for the calculation.

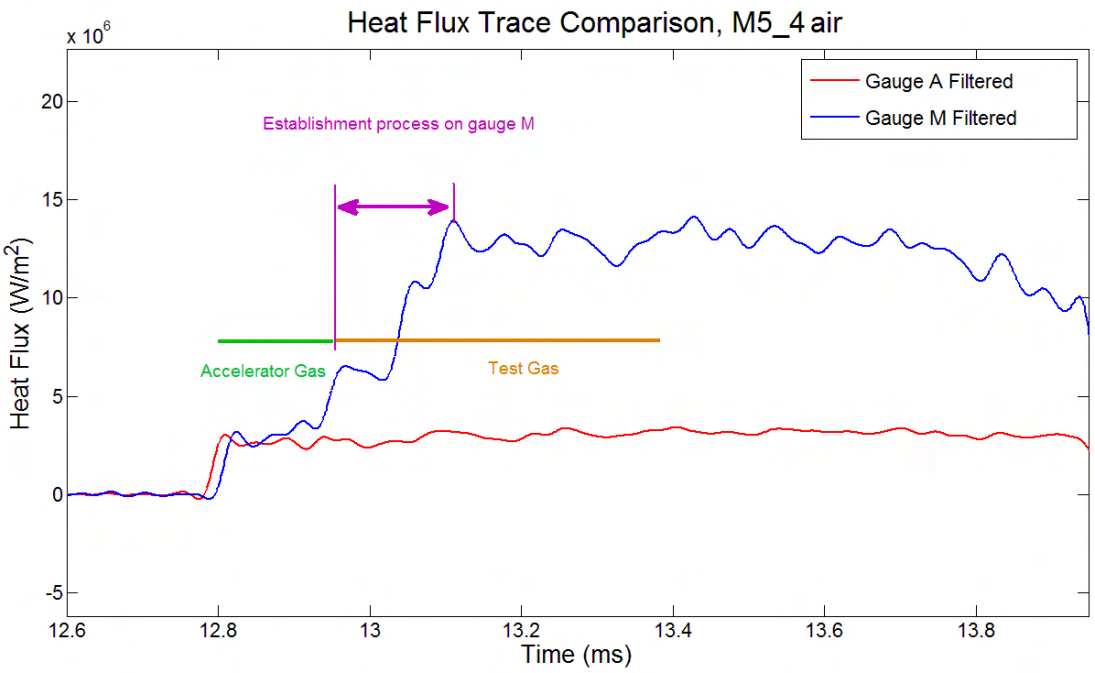

Figure 4.1: Two heat transfer traces for the M5_4 air test condition are shown. The two gauges are located toward the leading edge of the forward wedge (Gauge A), and near shock impingement on the aft wedge (Gauge M). Accelerator gas time, test gas time, and establishment time are all labeled.

Predictions exhibit reasonable agreement where the experimental data exhibit laminar behavior.

4.1.1 M7_2 Test Condition

Figures 4.2(a) and (b) show the heat transfer for the nitrogen and air along with the corresponding schlieren images. In Figure 4.2(c) both heat transfer profiles are overlaid. The forward wedge experiences laminar heat transfer behavior on the section upstream of separation. Due to low signal to noise ratio (nearly an order of magnitude smaller than any other test condition), the heat transfer experiences large scatter in the separation zone. On the aft cone there is a jump in heat transfer, and peak values are $\sim$1.3 MW/m^2 at gauge M. This corresponds with roughly the location of shock impingement on the aft cone. The combined overlay of both test conditions in Figure 4.2(c) shows that, as expected, the heat transfer does not differ significantly between the two test conditions.

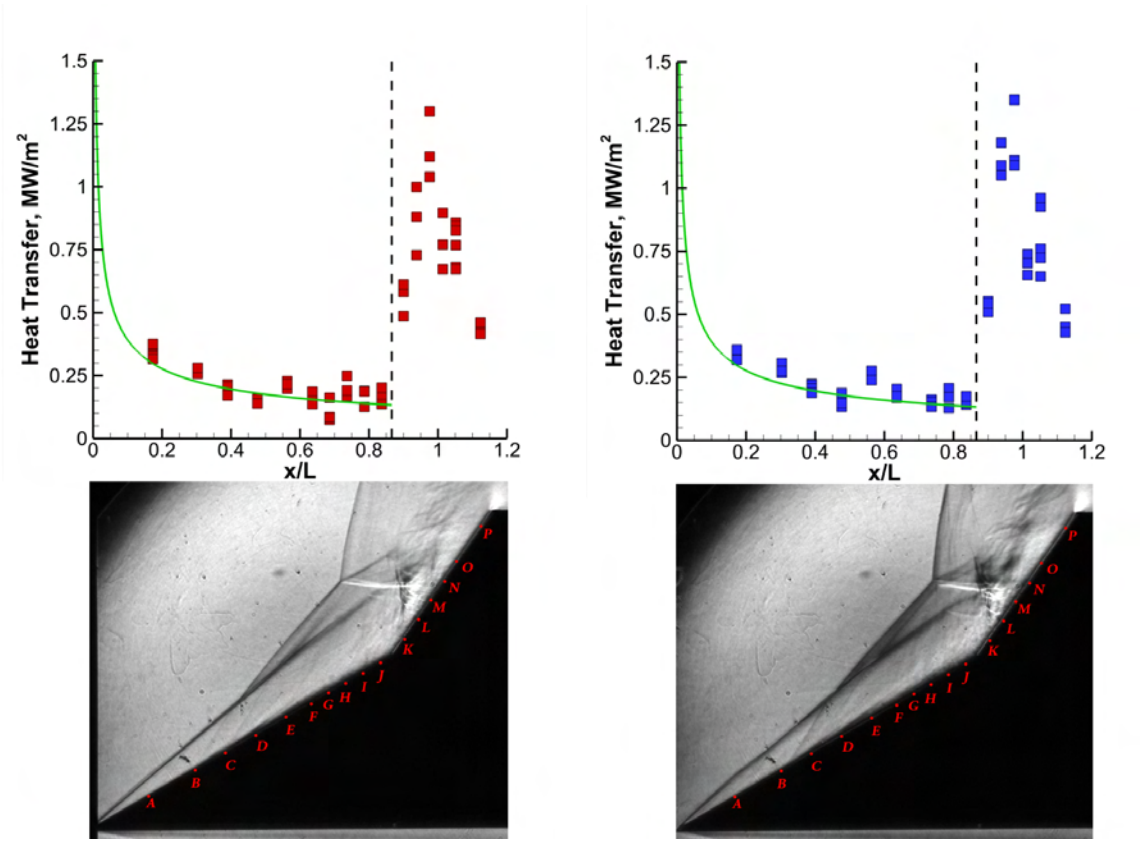

(a) M7_2, N_2

(b) M7_2, air

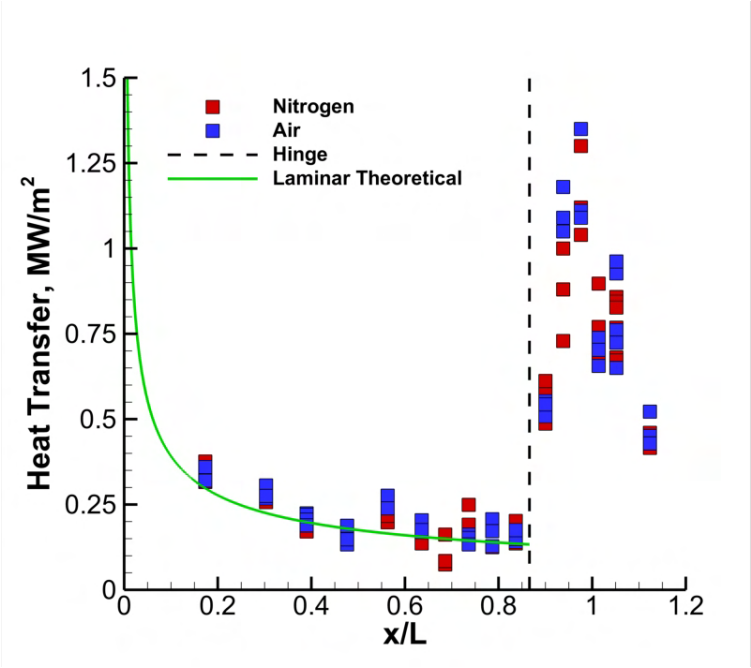

(c) Combined profiles

Figure 4.2: Heat transfer profiles for the M7_2 test condition in (a) N_2, and (b) air. An overlay of the two profiles is shown in (c). The green line is the laminar heat transfer prediction of Hayne *et al.* Note: These test conditions experience low signal to noise ratio.

4.1.2 M4_3.6 Test Condition

Figures 4.3(a) and (b) show the heat transfer for the nitrogen and air along with the corresponding schlieren images. In Figure 4.3(c) both heat transfer profiles are overlaid. On the forward wedge, there is an immediate departure from laminar heating profiles. Gauge G is missing from the traces due to damage. In both figures, between gauges F and H, there is a large differential between the heating values (an increase of approximately 2 times). This may be due to the the shock interactions that are seen to occur in this area in the images. On the forward wedge, very little difference is seen between the two test conditions. Peak heating on the aft wedge is seen to be approximately 13 MW/m^2 for the nitrogen, and approximately 14 MW/m^2 for air. These both occur at gauge M. In general on the aft wedge, the heat transfer rates in air are slightly higher than those in nitrogen. This is especially true in the area of peak heating. Augmented heating was discussed in Section 1.2 for a "reacting" gas over a "non-reacting" gas. Even at this lower enthalpy, this phenomenon is beginning to be seen.

4.1.3 M5_4 Test Condition

Figures 4.4(a) and (b) show the heat transfer for the nitrogen and air along with the corresponding schlieren images. In Figure 4.4(c) both heat transfer profiles are overlaid. On the forward wedge, laminar heat transfer behavior is seen on the upstream side in both gases. As the boundary layer behavior deviates from the laminar condition in the images, the heat transfer is seen to increase as expected. As the Reynolds number is smaller than the M4_3.6 case, this behavior occurs further downstream. Interestingly, the nitrogen experiences a much larger heating value at gauge G, when compared with the air. This may be due to two things: a lack of gauge resolution may not be detecting the actual peak heat transfer (for which the location may have moved for air), or some sort of interaction between the shock and boundary layer unique to nitrogen may be occurring. It is important to note that the open red symbols in Figures 4.4(a) and (c) are a result of two different behaviors seen during the test time for that location. During the first portion of the test time ($\sim$80% into the test gas), the heating values are seen to be laminar, while the last portion ($\sim$20% at the

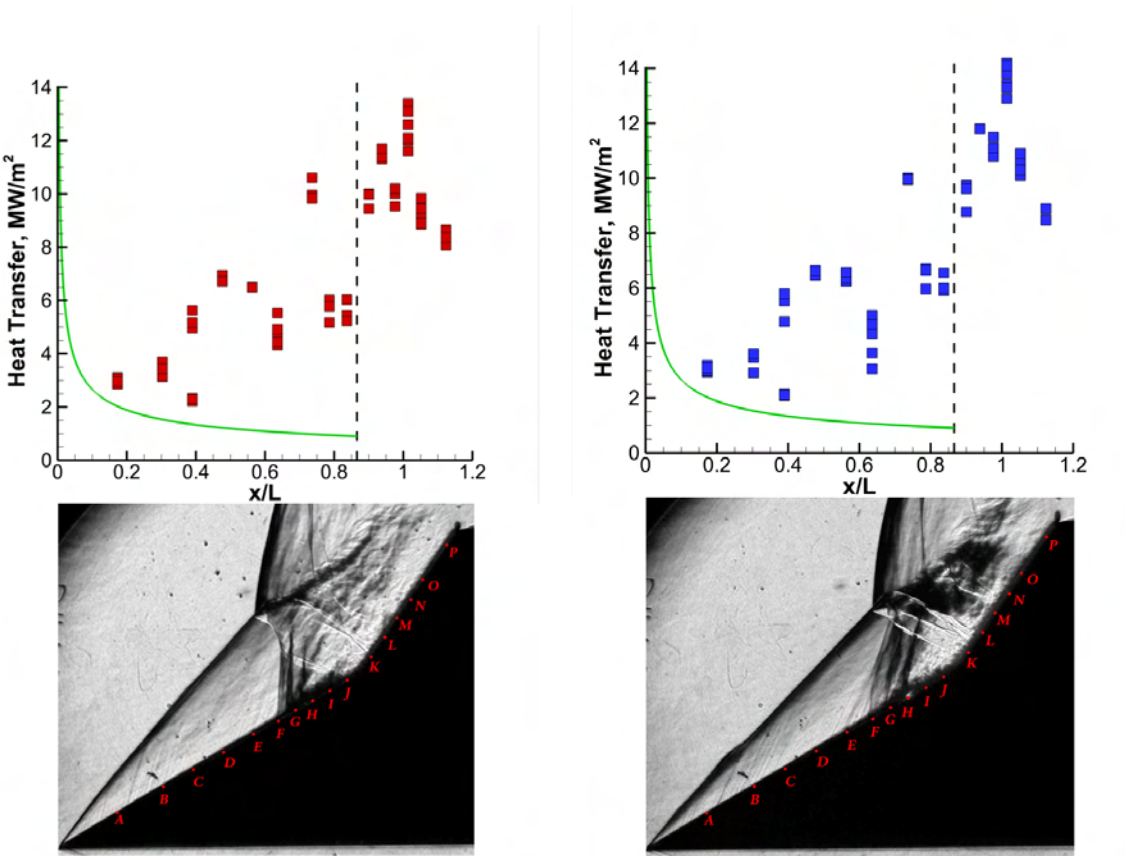

(a) M4_3.6, N_2

(b) M4_3.6, air

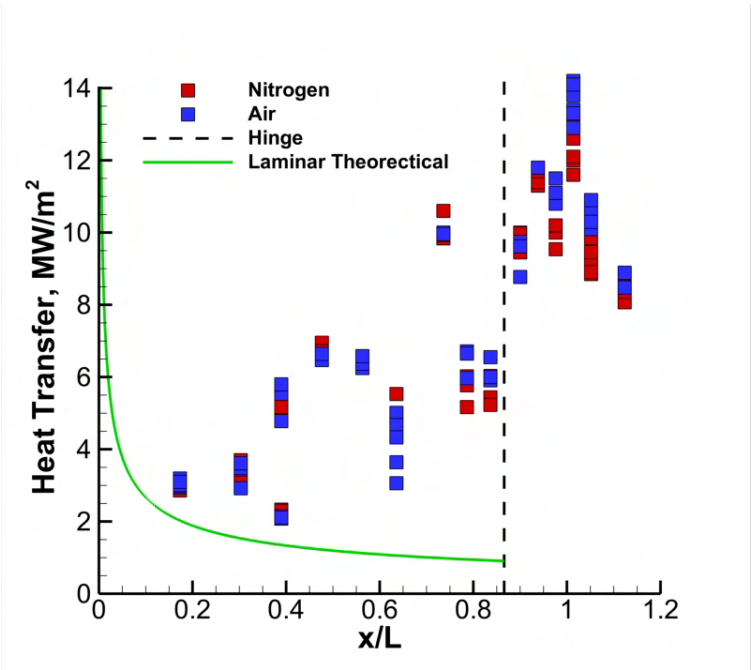

(c) Combined profiles

Figure 4.3: Heat transfer profiles for the M4_3.6 test condition in (a) N_2, and (b) air. An overlay of the two profiles is shown in (c). The green line is the laminar heat transfer prediction of Hayne *et al.*

end of the test gas) of the test time exhibits higher heating rates; therefore, both are reported. On the aft end of the wedge, peak heating for the nitrogen is seen to occur at gauge M and have a value of ∼10.5 MW/m^2, and in air is ∼13 MW/m^2. As in the M4_3.6 case, slighly higher heating values are seen in the case of the air on the aft cone in the vicinity of shock interaction with the surface. From the images it is observed that the shock interaction occurs just downstream of gauge L, which is in agreement with the heat transfer profiles.

4.1.4 M7_8 Test Condition

Figures 4.5(a) and (b) show the heat transfer for the nitrogen and air along with the corresponding schlieren images. In Figure 4.5(c) both heat transfer profiles are overlaid. On the upstream end of the forward wedges, laminar heat transfer behavior is seen. This is the only case where a slight difference is seen with respect to the two gases for laminar heating rates. The air values are consistently higher than the nitrogen, but are still within the error bars of the measurements. A distinct separation zone is seen in each plot as a dip in heat transfer after x/L=0.6. In the nitrogen case, the separation zone appears to begin at gauge F, and in the air case at gauge G. Perhaps the most noticeable difference between the two cases is the level of peak heating of the aft wedge. In nitrogen, the peak heating value is ∼8.5 MW/m^2, while in air it is ∼13.5 MW/m^2. An interesting behavior in air is seen, where just prior to the peak heating a dip in heat transfer is observed. This may be the result of a secondary recirculation zone that lies upstream of the shock impingement, although this is hard to discern, due to the luminescence in the image. There is a considerable amount of scatter in the results, not unexpectedly in the area of shock impingement on the aft wedge.

4.2 Heat Transfer Fluctuations

This section examines the standard deviation of the heat transfer traces in order to quantify the fluctuations. During processing of the data, an unbiased standard deviation ($n-1$ method) is taken when the heat transfer traces have established. Figures 4.6(a)-(d) show these data for each of the test conditions. Nitrogen and air data are combined for each test condition.

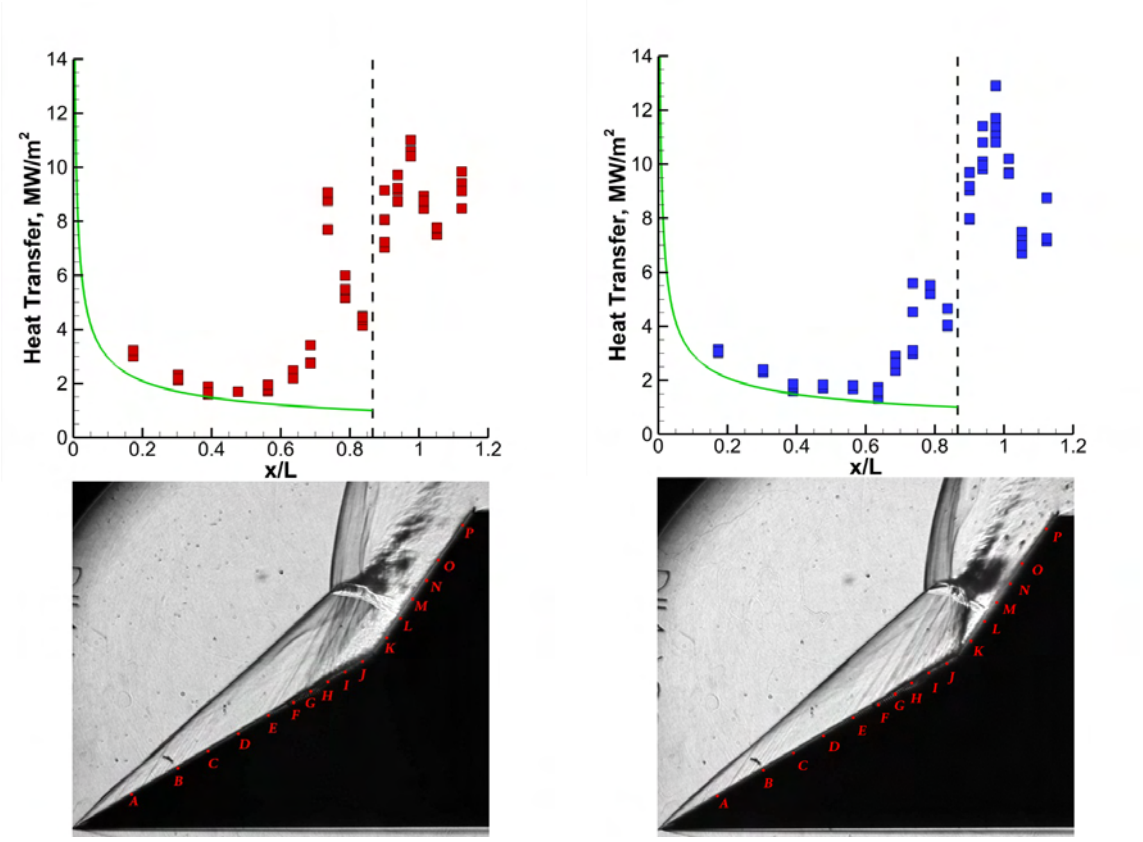

(a) M5_4, N_2

(b) M5_4, air

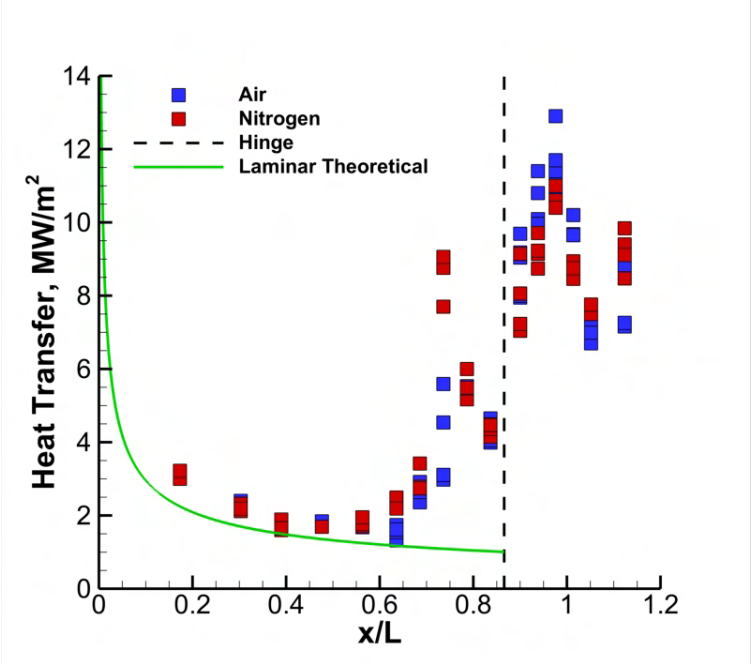

(c) Combined profiles

Figure 4.4: Heat transfer profiles for the M5_4 test condition in (a) N_2, and (b) air. An overlay of the two profiles is shown in (c). The green line is the laminar heat transfer prediction of Hayne *et al.*

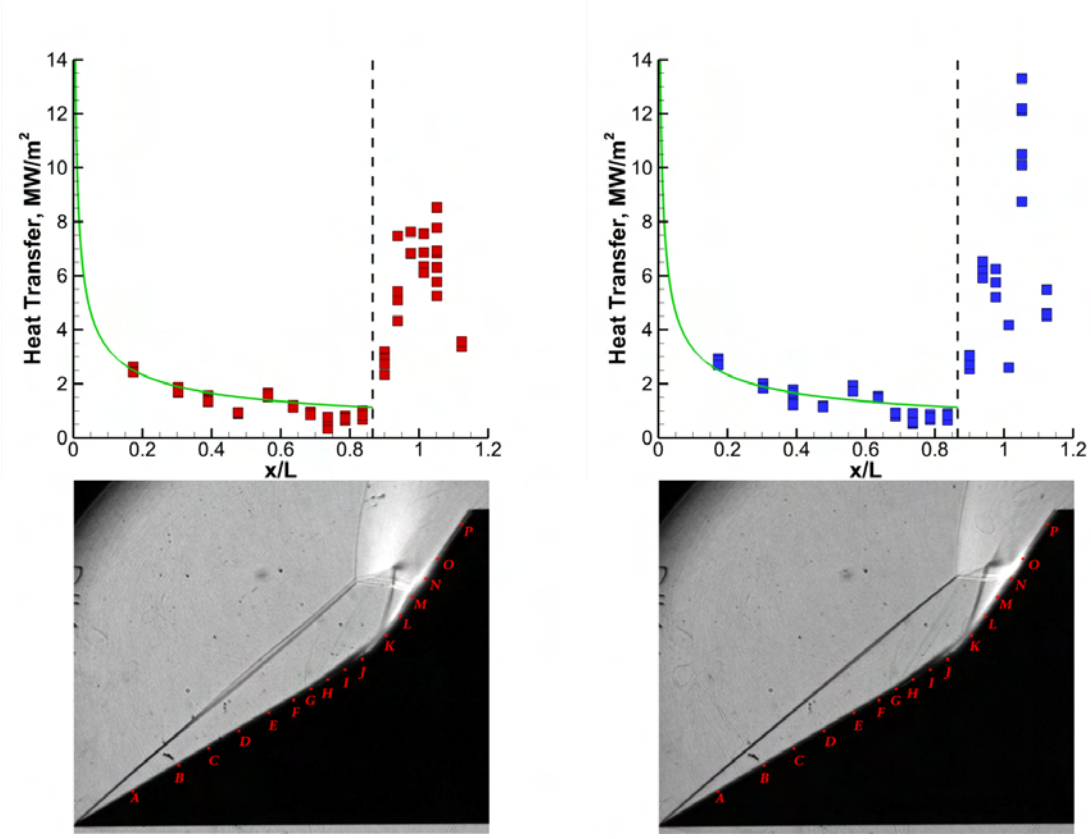

(a) M7_8, N_2

(b) M7_8, air

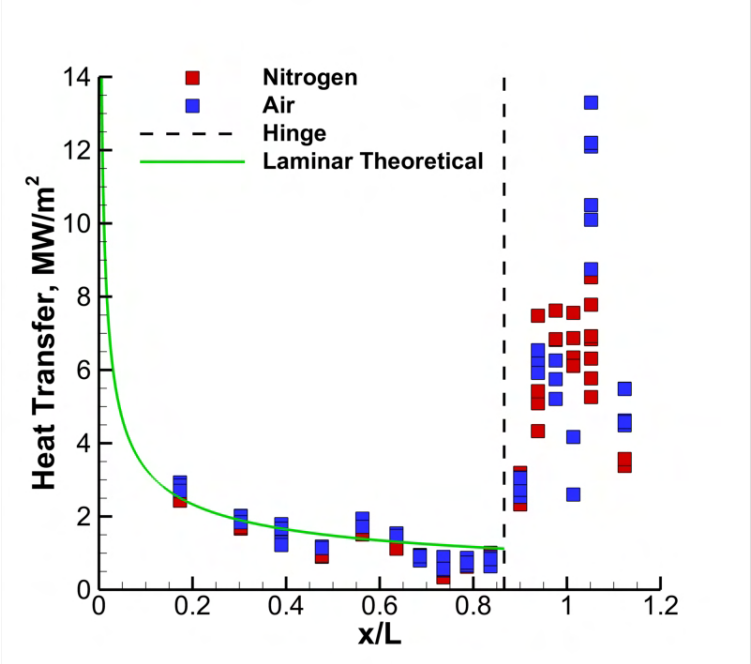

(c) Combined profiles

Figure 4.5: Heat transfer profiles for the M7_8 test condition in (a) N_2, and (b) air. An overlay of the two profiles is shown in (c). The green line is the laminar heat transfer prediction of Hayne *et al.*

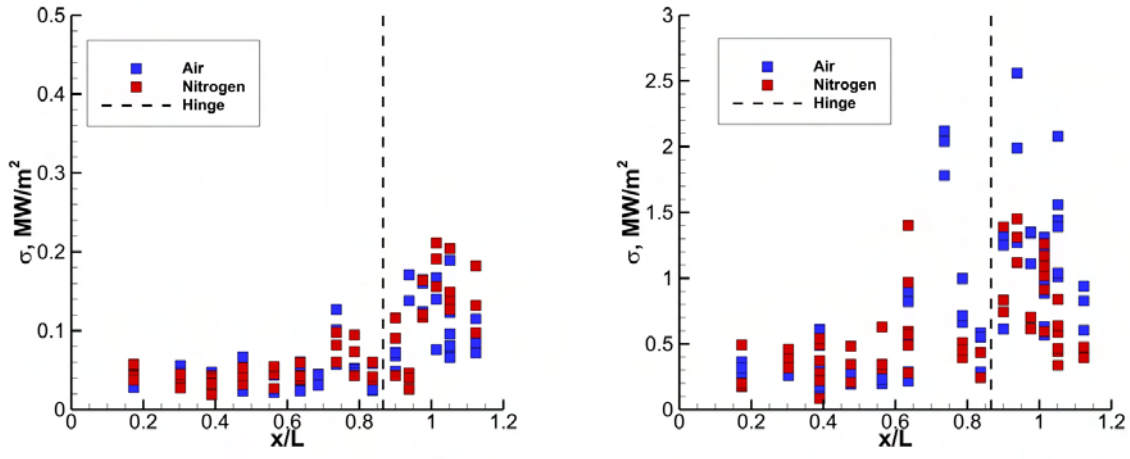

(a) M7_2

(b) M4_3.6

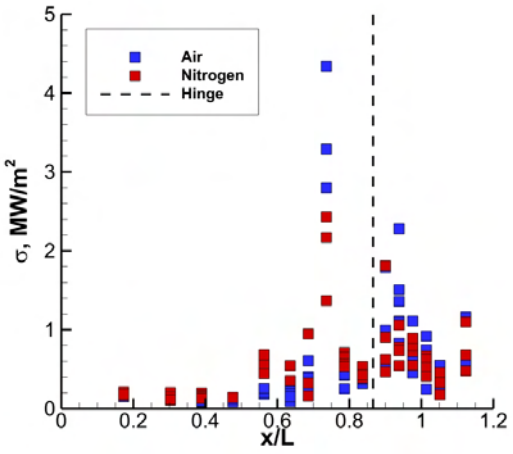

(c) M5_4

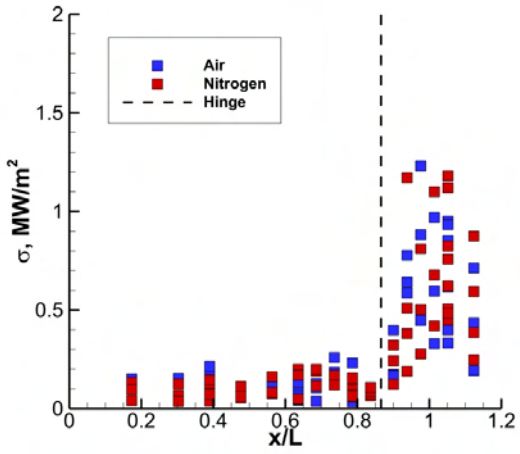

(d) M7_8

Figure 4.6: Fluctuations in the heat transfer profiles for the (a) M7_2,(b) M4_3.6, (c) M5_4, and (d) M7_8 test conditions are presented. Air and nitrogen data are combined for each test condition.

As a general observation, the profiles of the fluctuations are similar in shape to the mean profiles. The amplitude of the fluctuations is lower on the forward wedge, increases near regions of transitional behavior (if they exist), and peaks near shock impingement on the aft wedge. In addition to this behavior, the scatter of the fluctuation data is larger on the aft wedge, in agreement with the mean data.

Figure 4.6(a) illuminates the M7_2 case. The mean profiles for air and nitrogen in Figure 4.2 would suggest that there is no departure from laminar behavior. There is, however, a noticeable increase in the fluctuations just prior to the hinge location. This may indicate a more complex behavior of the flow over that region of the model. There are indications of this in the schlieren images as well. The schlieren image of the boundary layer behavior deviates from what would be considered a laminar profile in Figures 4.2(a) and (b).

Figures 4.6(b) and (c) both exhibit large spikes in the fluctuations at gauge H. This may be a result of a localized increase in heating due to the shock/boundary layer interactions in those regions. Another possibility is that there is gauge damage and thus the response is altered.

In the M7_8 case seen in Figure 4.6(d) (which is the only case exhibiting completely laminar behavior), there is nearly no increase of the fluctuations on the forward wedge continuing through the separation zone. Interestingly, in all of the four different cases there does not appear to be a distinct dependence of the fluctuations on the test gas as in the the mean profiles.

In order to compare the fluctuations across all test conditions, the percentage of the mean of the fluctuations is shown in Figures 4.7(a)-(d). In general it is seen that the the largest peaks in the normalized fluctuations occur just upstream of the hinge location on the forward wedge. For the test conditions in the present work, this is a region of either shock/boundary layer interaction, transitional flow, or a combination of the two. The peaks in this region are between 30 % and 60 % for most test conditions. For the other areas of the flow, peaks are typically 5% to 20%.

In Figure 4.7, the M7_2 case exhibits higher normalized fluctuations than the other cases over much of the surface. This test conditions (as has been noted) suffers from low signal condition which may be a contributing factor. The region where the normalized fluctuations peak is in the same area

where an increase was seen in Figure 4.6(a). On the aft wedge, normalized fluctuations appear to increase while moving downstream.

The M4_3 case exhibits similar behavior on the forward wedge, seen in Figure 4.7(b). Normalized fluctuations remain nearly constant until the location of the shock interaction. On the aft wedge they appear to slightly decrease moving downstream, although the change is small.

Figure 4.7(c) shows the M5_4 test conditions. This case exhibits very large spikes in the normalized fluctuations at $\sim x/L = 0.8$ (Gauge H), where they peak at over 100%. This, as speculated before may be due to gauge damage. On the aft wedge a slight decrease is observered in the fluctuations moving downstream, with a distinct increase in the last gauge.

Lastly, in Figure 4.7(d) the M7_8 test case is shown. Peaks occur in the same region as the separation shock and the separation zone. On the aft wedge there is no distinct change in the normalized fluctuations. Scatter in the data does seem to be higher than the forward wedge.

4.3 Conclusions

The heat transfer rates for nitrogen and air over a double wedge configuration at eight test conditions with stagnation enthalpies of 2 to 8 MJ/kg have been presented. Distinct differences between the air and nitrogen flows are apparent as low as 3.6 MJ/kg, indicating that thermochemistry plays a role in flows at these enthalpies. For all cases, thermochemistry effects seem to be minimal toward the leading edge of the front wedge where a laminar boundary layer is observed. For the two highest Reynolds number conditions, a departure from laminar heating behavior is seen on the forward wedge. In all cases, heating rates on the aft wedge are higher in air than in nitrogen. In the highest enthalpy flow, a very distinct separation zone exists in both the schlieren and heat transfer data and are in reasonable agreement. On the aft body, considerable differences are present in the heat transfer profiles, most notably with the location of peak heating. Scatter in the aft heat transfer data may be due to flowfield unsteadiness from a large second wedge angle, or variation in the shock configurations due to facility shot to shot variation. Augmented heating in air compared to nitrogen has been seen experimentally by Holden [28], who reported that both experiments and simulations

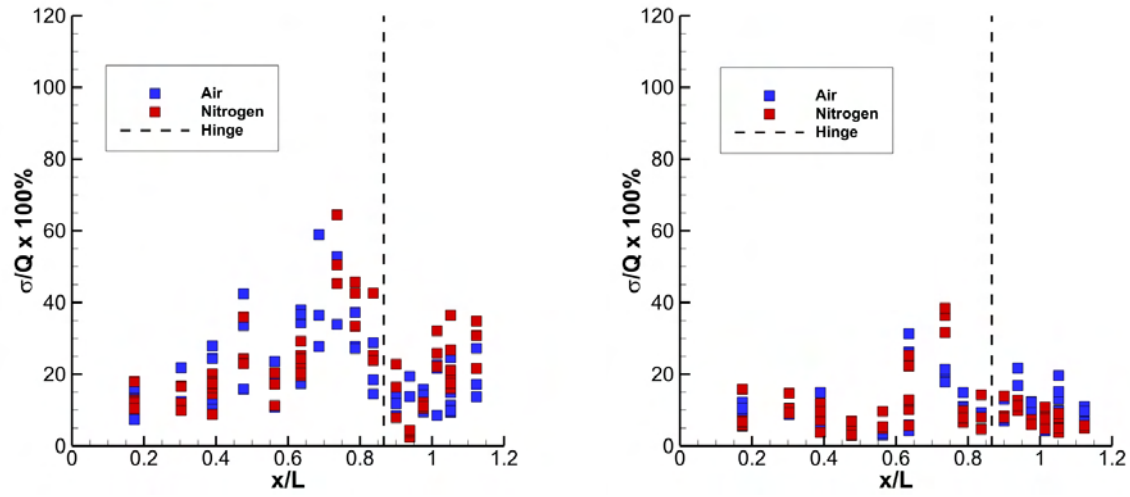

(a) M7_2 (b) M4_3.6

(c) M5_4 (d) M7_8

Figure 4.7: Normalized fluctuations in the heat transfer profiles for the (a) M7_2,(b) M4_3.6, (c) M5_4, and (d) M7_8 test conditions are presented. Air and nitrogen data are combined for each test condition.

indicated that real gas effects augment heating.

Although peak heating location is recorded for each test condition, it must be noted that this measurement can have dependacines on both gauge size and spacing. Knight *et al.* [73] state that for surface measurements, peak properties may occur between gauges and thus may not be resolved. Additionally, the finite size of the gauges effectively integrates the signal over the width of the gauges' sensing element (0.762 mm). Schlieren images indicate a difference in the location of aft body shock impingement between freestream compositions of air and nitrogen. However, the difference in impingement location (0.69 mm in the M5_4 condition and 2.30 mm in the M7_8 condition) is on the order of the gauge spacing in this region (3.35 mm). In these two test conditions, nitrogen impingement occurs upstream of air impingement. This agrees with the behavior of the bow shock's increased standoff distance in nitrogen compared to air. The finite gauge size should be accounted for if the experimental data are compared with simulations. Knight *et al.* note that a similar behavior occurs in their measurements, however agreement for the low enthalpy cases is still reasonable. The test condition with the most noticeable difference between the air and nitrogen is the M7_8 condition. In addition to a large difference in peak heating values, the shape of the aft wedge profile is different. A simulation would provide further insight to the current experimental data set. The current data set, however, is not believed to suffer large inaccuracies due these effects.

Fluctuations in the established heat transfer traces are calculated via the unbiased standard deviation. Profiles are presented both in units of MW/m^2, as well as normalized by the mean. The shape of the profiles in raw units resembles the mean profiles. When normalized, the profiles indicate that the largest fluctuations generally occur near the location of shock/boundary layer interaction, and/or transitional boundary layer behavior.

Chapter 5

High Speed Imaging Experiments for Investigation of Flow Establishment and Unsteadiness

In this section, the results from the high speed imaging experiments are presented for all test conditions on the double wedge and double cone models. Data have been acquired with the Photron Fastcam SA-5 detailed in Section 2.3.1. High speed image sequences for each test condition are presented to illustrate the transient nature of the flow field. Establishment times for the triple points are measured for all test conditions, and compared with the establishment times measured from the heat transfer traces presented in Section 4, as well as the laminar boundary layer prediction from Gupta [42].

An image tracking code has been implemented to extract the shock surface location. Image tracking is done in several steps. First, using *ImageJ*, a Gaussian blur of 0.8 pixels is applied to the images to aid in the edge detection process. Next, *ImageJ*'s built-in edge detection is used to enhance the shock surfaces. Lastly, a MATLAB code has been written which utilizes the *edge()* subroutine to locate and extract the shock surfaces. Edge threshold parameters must be tuned for each image set to properly capture the edge. For each test condition, all shock surface data are plotted in a single figure to show the establishment process, as well as oscillations in the shock. The frequency content of the shock motion is extracted via a Fast Fourier Transform taken of the position of the shock at a single vertical location.

5.1 High Speed Image Sequences

Data are presented in this section for each model and each run condition in air. Differences are observed between air and nitrogen as a test gas; however, the general behavior for each test condition is similar. Nitrogen data are presented in Appendix E. Specific difference between gases will be

illustrated. Data are presented during the test gas only; the accelerator gas is omitted. Each image sequence is broken into two parts: the establishment of the triple point, and the behavior of the established flow.

5.1.1 Double Wedge Image Sequences

The establishment process of the M7_2 flow is 110μs $\pm$ 10 μs and is visualized in Figure 5.1. At the earlier times, from 0 to 70 μs, the triple point is formed by the bow shock and oblique shock emanating from the tip of the wedge. From 80 to 110 μs the triple point is formed by the separation shock originating from the surface of the forward wedge. Although difficult to see (due to the low density of the run condition), the separation shock traverses upstream along the face of the forward wedge. Throughout the establishment process there is minimal movement in the location of the triple point in the streamwise direction, when compared with other run conditions (as will be shown in this section).

Figure 5.2 presents several post-establishment frames. There are evident oscillations in the shock structures of the flow field. Some streamwise motion is observed in the bow shock, and in turn, slight movement in the location of the impinging shock on the aft wedge surface. Mild movement in the lead oblique shock indicates a degree of freestream fluctuations in the run condition. Aft wedge flow structures are difficult to visualize due to low density of the flow field, although they do appear to be complex in nature. The boundary layer and separation zone do appear to deviate from laminar behavior. In the nitrogen test condition, no noticeable differences are seen (compared to air) in either the flow field, or establishment time.

The establishment process of the M4_3.6 triple point is shown in Figure 5.3 and occurs over 170 μs $\pm$10 μs. A bow shock/triple point structure is already observed in the first frame of the test gas. The triple points moves downward and up stream over the course of the establishment. Correspondingly, the impinging shock on the aft wedge moves upstream along the face of the model. As the triple point structure moves forward, a complex series of shock interactions can be seen between the waves originating from the wedge corner and the triple point. The shear layer which results from the triple

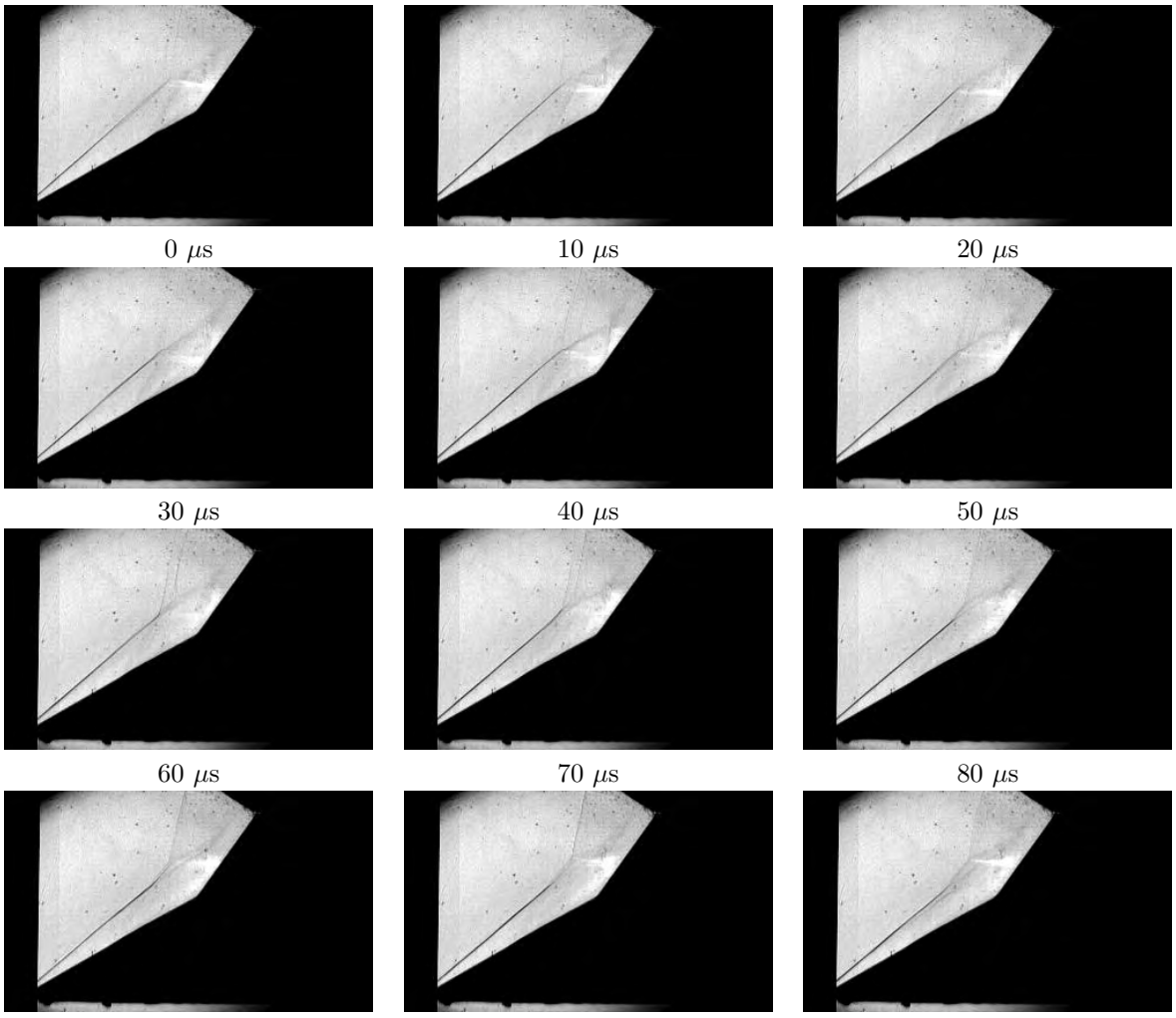

Figure 5.1: The establishment process of the triple point is shown for the M7_2 test condition in air. The interframe time is 10 μs, and the exposure time is 1 μs. Flow is from left to right.

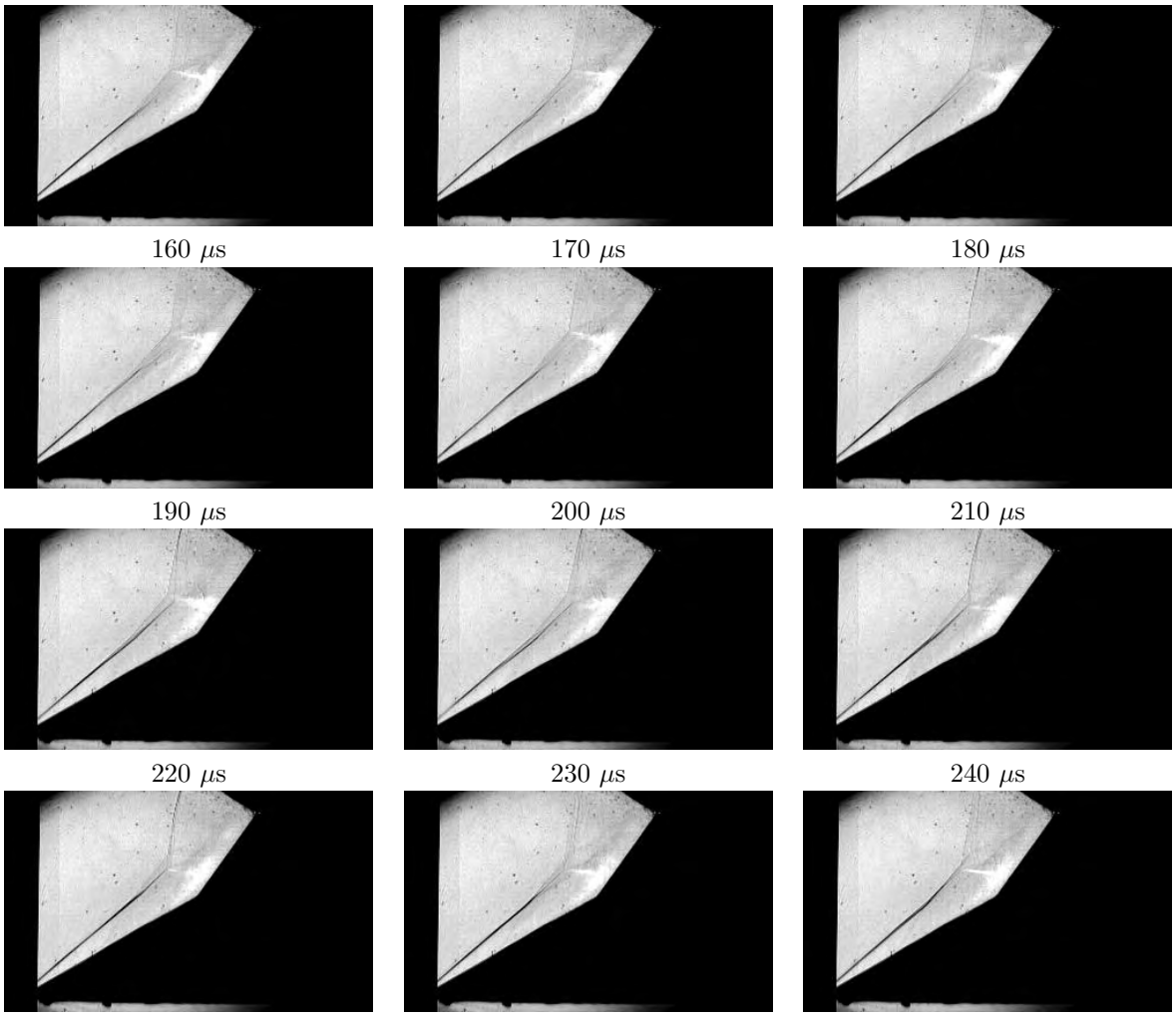

Figure 5.2: Movement in various parts of the flow field is shown for the M7_2 test condition in air. The interframe time is 10 μs, and the exposure time is 1 μs. Flow is from left to right.

point is visualized and appears to turn upward when it interacts with the shock structure below it. In some frames, including 70 and 80 μs, structure in the shear layer can be observed. This is not visible in all frames, as the schlieren effect is very strong (due to high density and high gradients) and obscures these finer details. A distinct turning wave is observed at the wedge corner until 120 μs, although break up of the wave happens progressively starting at about 90 μs. Upon breaking up, this wave structure is seen to traverse upstream and down stream in oan scillatory pattern. As this happens, the shape of the transmitted wave is seen to change as the interaction evolves. Although this has been deemed the test time based on pressure and heat transfer traces, the smearing of shock surfaces in the first 30 μs may be a result of contact surface/accelerator gas contamination.

The established behavior of the flow field is shown in Figure 5.4. Oscillations in the shock foot are seen throughout all the frames, which appear to alter the geometry of the shock with the transmitted shock from the triple point. Behind these, the boundary layer exhibits departure from laminar behavior. These oscillations may, in fact, be from a single shock foot which varies in shape in the spanwise direction. The boundary layer in this run condition is almost unnoticeable upstream of the shock foot, however a rapid thickening is seen near it. Detecting a specific frequency from this motion is difficult as tracking the individual entity from the two dimensional visualization is difficult. In some frames there is a wave normal to the surface of the aft cone (roughly half way up) that runs between the surface and the shear layer. As in the M7_2 case, there is mild oscillation in the lead shock indicating some freestream unsteadiness. Although the run conditions do no vary greatly, the establishment time observed in the nitrogen case is 180 μs. Additionally, the break up of the turning wave at the corner takes approximately 150 μs.

The establishment of the M5_4 test condition is shown in Figure 5.5 and occurs over 110 μs $\pm$10 μs. At 0 μs the flow is seen to exhibit a two oblique shock pattern before the formation of the triple point. As the sequence of images progresses, a shock originating from just upstream of the corner is maintained, and both the angle and origin of the shock remain constant. There are several consequences of the triple point moving upstream. First, as can be seen in the images, the location of the shock which impinges on the model moves up the face of the aft wedge. Thus it

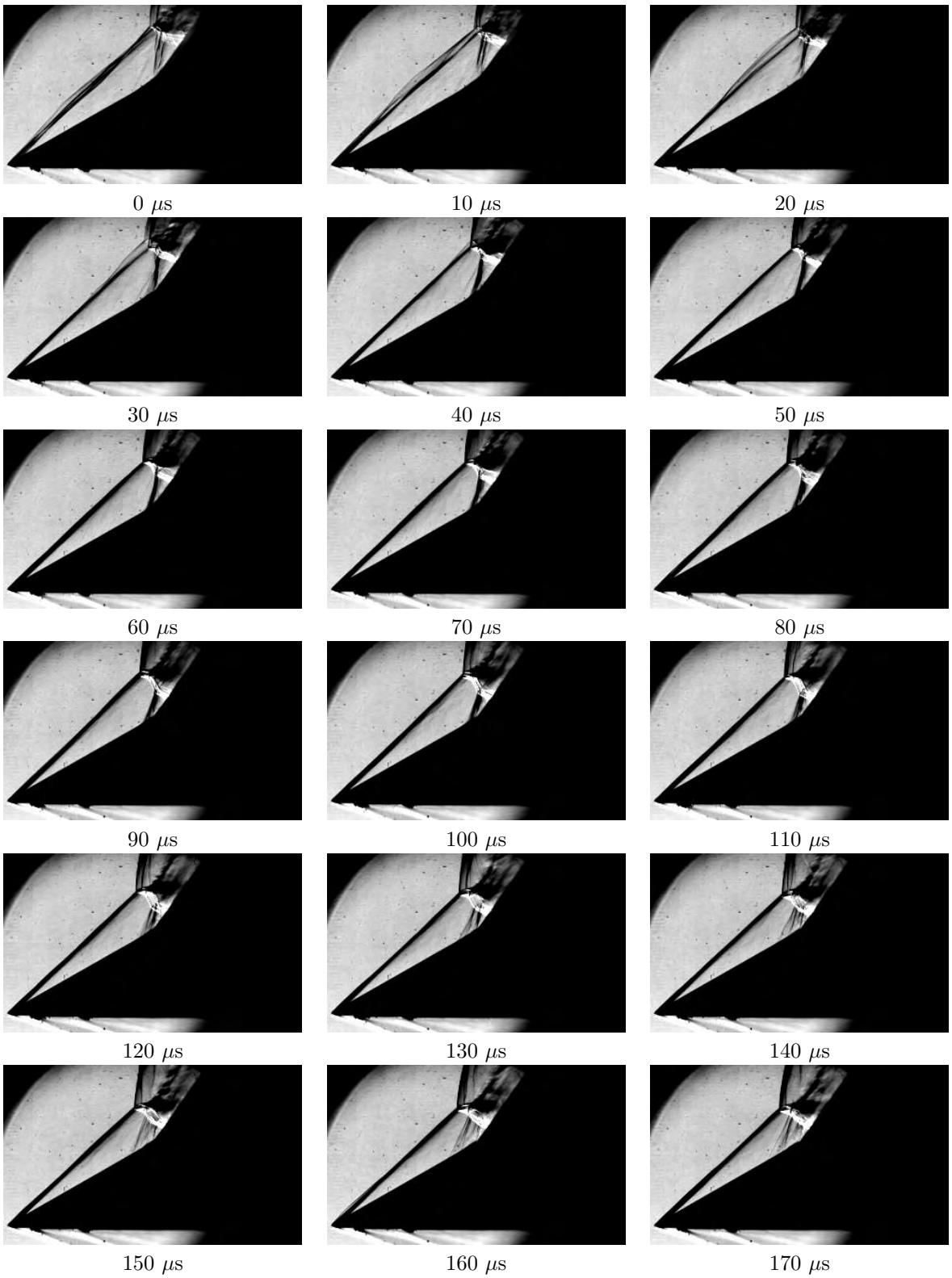

Figure 5.3: The establishment process of the triple point is shown for the M4_3.6 test condition in air. The interframe time is 10 μs, and the exposure time is 1 μs. Flow is from left to right.

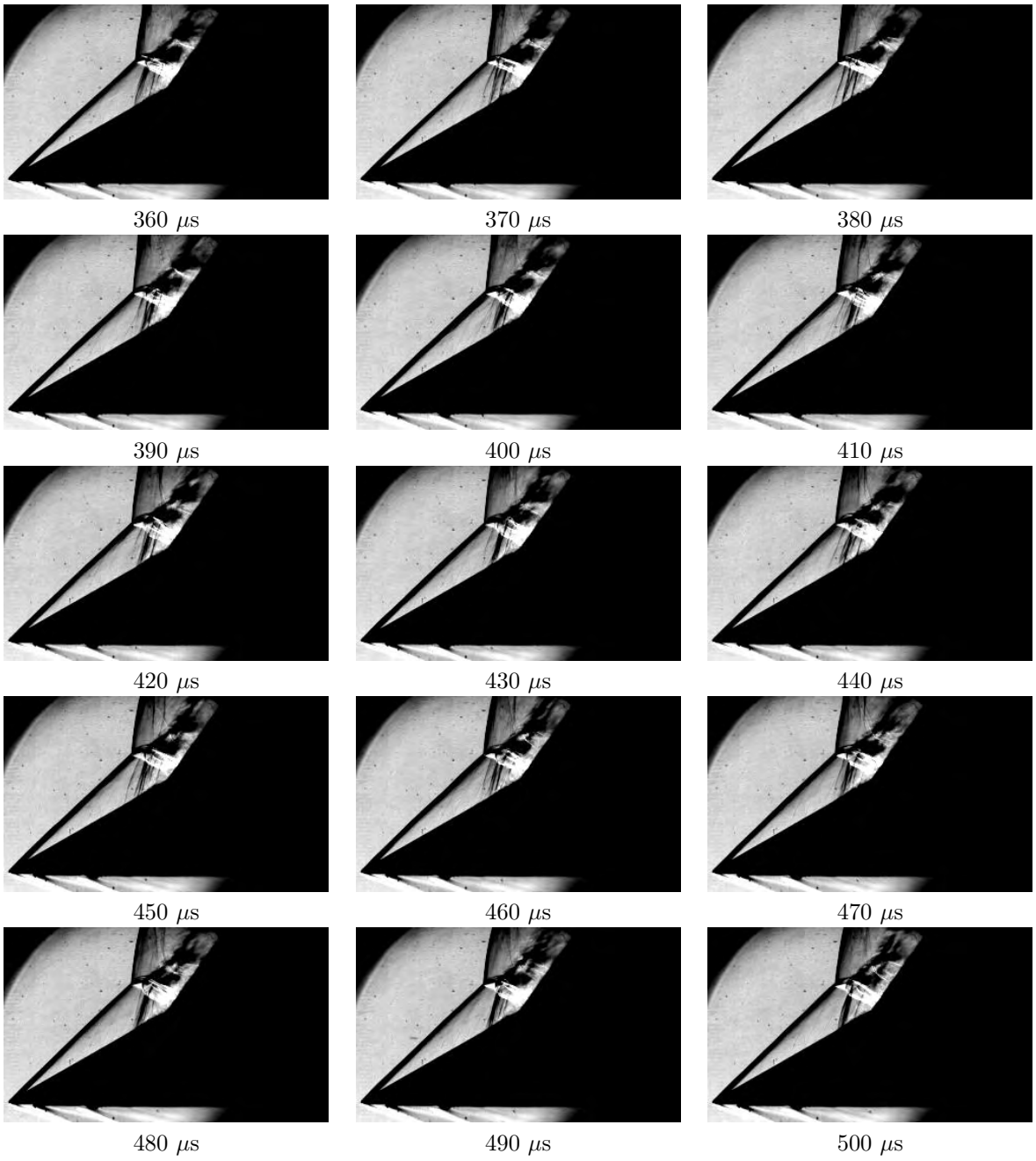

Figure 5.4: Movement in various parts of the flow field is shown for the M4_3.6 test condition in air. The interframe time is 10 μs, and the exposure time is 1 μs. Flow is from left to right.

is expected that the location of peak heating will also move. Second, as the triple point moves upstream, the transmitted shock and shear layer begin to interact with the shock emanating from the corner. Lastly, the bow shock location is seen to move with the triple point, thus the moving bow shock will be stronger than a stationary one, as it has a larger relative velocity with respect to the freestream flow. The flow behind the bow shock exhibits considerable luminescence; however, as the sequence progresses, two layers are seen to form on either side of the shear layer. The relatively hot gas behind the bow shock is separated from the relatively cold gas on the other side of the shear layer.

In Figure 5.6 the motion of the shock on the forward wedge is seen. This is best seen through the luminescence as it traverses up the wedge face, reaching a maximum forward distance at 260 μs (80 μs after the first frame shown). At that point, the shock begins retreating back up the wedge face. There is also some indication of spanwise variation in the front, as there is higher frequency motion seen in the Mach waves upstream of the front. Throughout this series of images the location of the leading edge shock and triple point are seen to remain relatively constant in location, indicating a steady incoming flow. In the case of the nitrogen, flow structures are similar and establishment time is seen to be 105 μs.

Another series of data has been collected in the M5_4 test condition with a reduced exposure time of 1 μs to reduce flow luminescence and visualize structures on the aft wedge. Similar to the single frame series of schileren images, a complex system of wave interactions is observed over the aft cone. An interesting behavior occurs in the evolution of the turning wave in the corner when comparing between air and nitrogen as the test gas. Figure 5.7 shows image sequences of a zoomed in region near the corner. The air test condition is shown on the top, while the nitrogen test condition is shown on the bottom. In this sequence of images, the shock wave at the corner is seen to be present in both the air and the nitrogen until approximately 80 μs. The wave in nitrogen begins to break down at this point and eventually disappears at 110 μs. This same process is observed in the air, however it doesn't begin until 250 μs. The wave is gone by 270 μs. These behaviors agree with the schlieren images shown in Figure 3.4(e) and (f), both of which correspond to 200 μs into the test

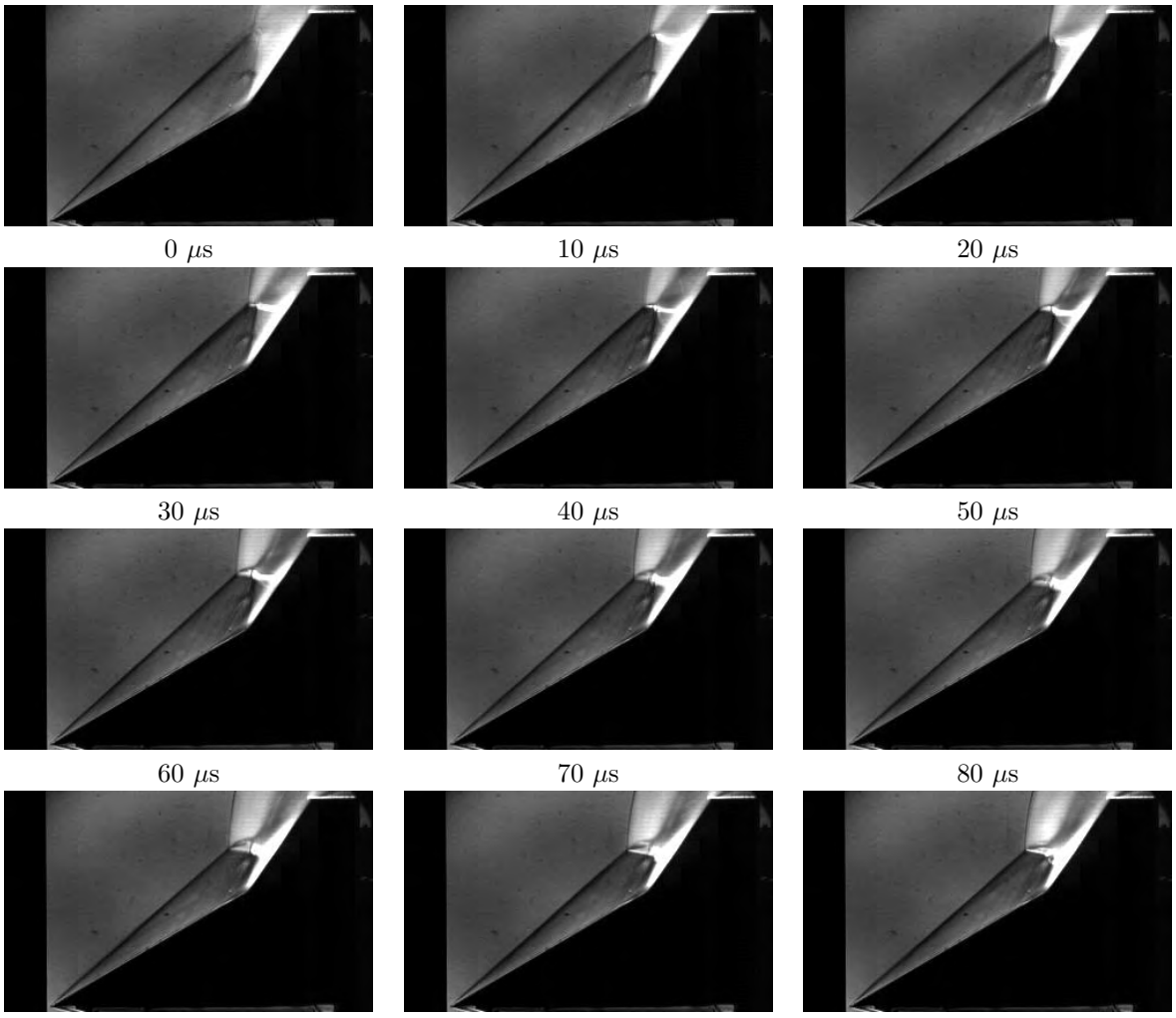

Figure 5.5: The establishment process of the triple point is shown for the M5_4 condition in air. Both interframe and exposure times are 10μs. Flow is from left to right.

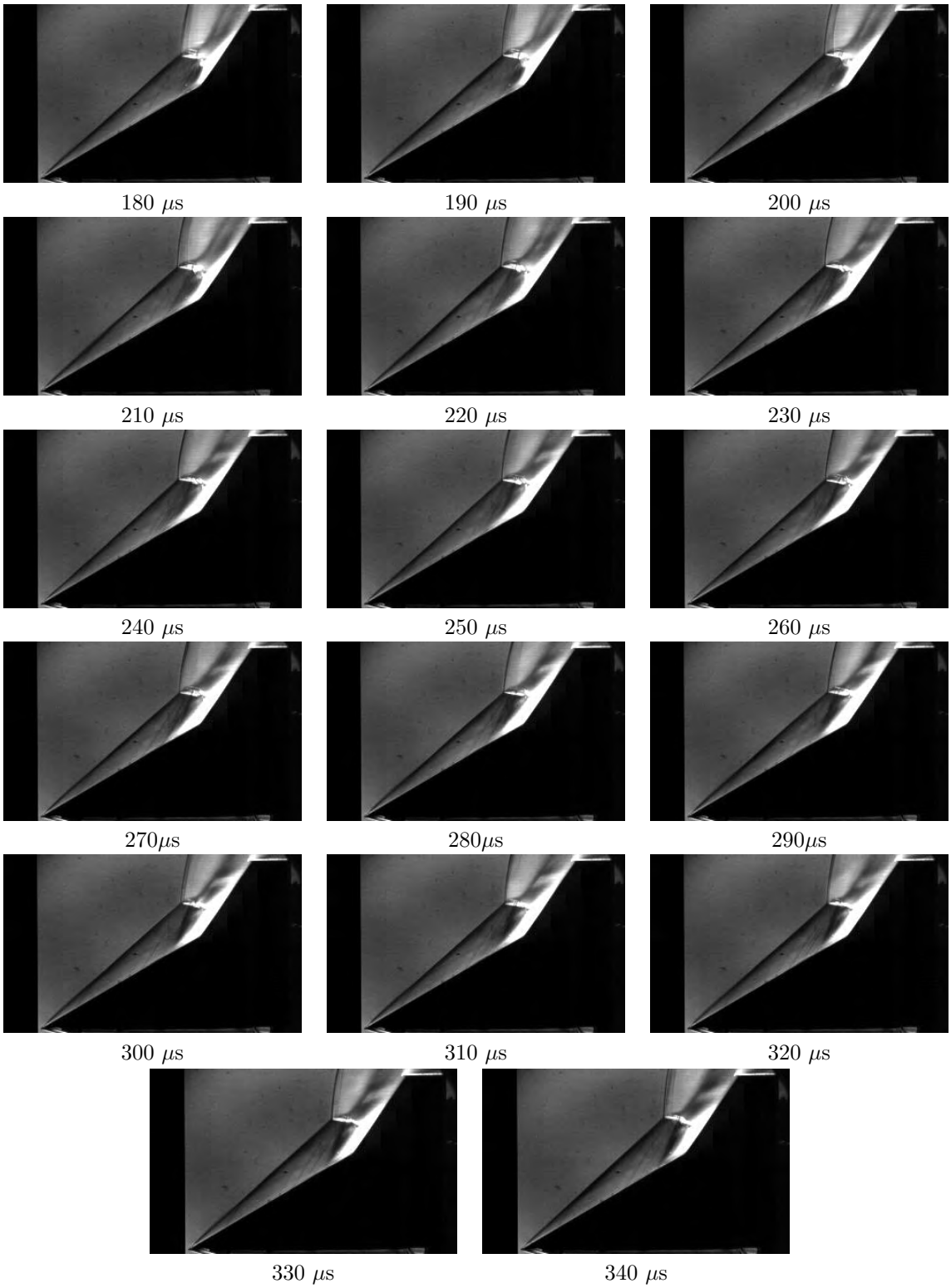

Figure 5.6: Movement in various parts of the flow field is shown for the M5_4 test condition in air. Both interframe and exposure times are 10μs. Flow is from left to right.

gas.

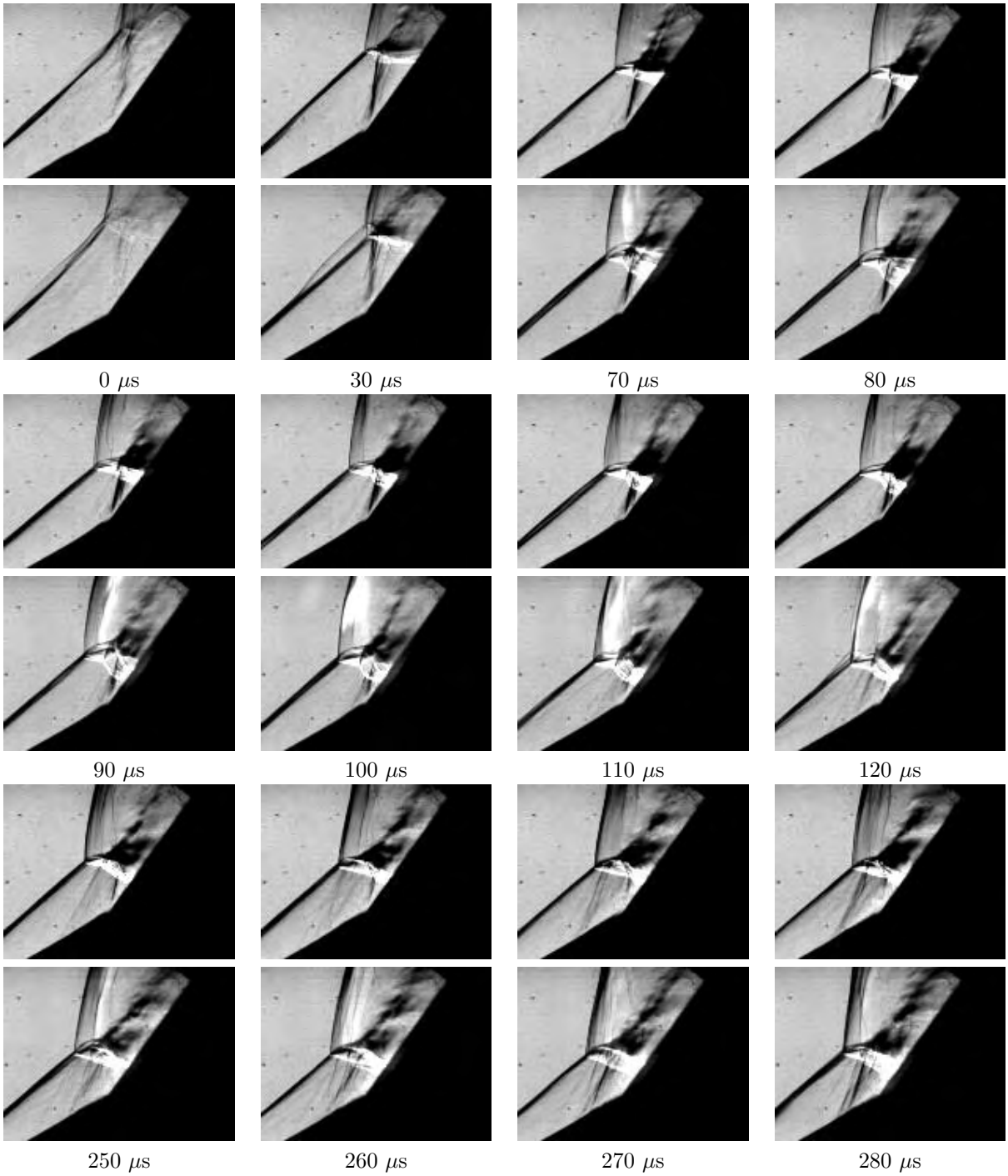

Figure 5.7: A comparison of the transient behavior of the M5_4 flowfield near the corner is shown for air (top) and nitrogen (bottom). The interframe time 10μs is and exposure times is 1μs. Flow is from left to right.

The establishment process of the triple point for the M7_8 test condition is 80 μs $\pm$10 μs, and

is shown in Figure 5.8. Similar to the M5_4 condition in Figure 5.5, at 0 μs, the shock structure resembles a two oblique shock system. The triple point moves upstream and downward in time. There is considerable luminescence (larger than the M5_4 case) behind the bow shock and the reattachment shock due to a combination high temperatures in those regions, as well as a long exposure time. Nearly all of the shock structure is obscured by this luminescence. At the start of the test gas, a small separation zone is already present. The separation shock, although faint, can be seen moving upstream from the wedge corner along the forward wedge face throughout this part of the image sequence.

The continued behavior of the flow field is seen in Figure 5.8. Triple point and bow shock movement are minimal; however, the separation shock continues to traverse upstream on the forward wedge until approximately 170 μs. A light strip occurs above the dividing streamline which is reasonably thick. This is mostly likely luminescence from the heating in the viscous layer, as this feature is not present in the single frame imaging in Figure 3.4(h) for air. Shock structure is still obscured by the large amount of flow luminescence on the aft wedge. The nitrogen establishment time is measured to be 100 μs, and is the only test condition with the two times outside the $\pm$10 μs uncertainty.

As in the case of the M5_4 flow, a second series of images wass taken with a 1 μs exposure time to illustrate the flow structures on the aft wedge. These are shown in Figure 5.10, where the air condition is on top and the nitrogen condition is on the bottom.. At 0 μs, the interactions are very similar between air and nitrogen and the location of the triple point is similar. However, by 30 μs the triple point in the nitrogen has clearly moved further upstream than its air counterpart. The established configuration is shown at 110 μs, with the shock stand off distance clearly further upstream in the nitrogen than in the air. This has the consequence of the impinging shock for nitrogen being further upstream than air. The established flow fields are very similar to their single frame schlieren counterparts. Lastly in the nitrogen, post bow shock luminescence is still visible despite the reduced exposure time.

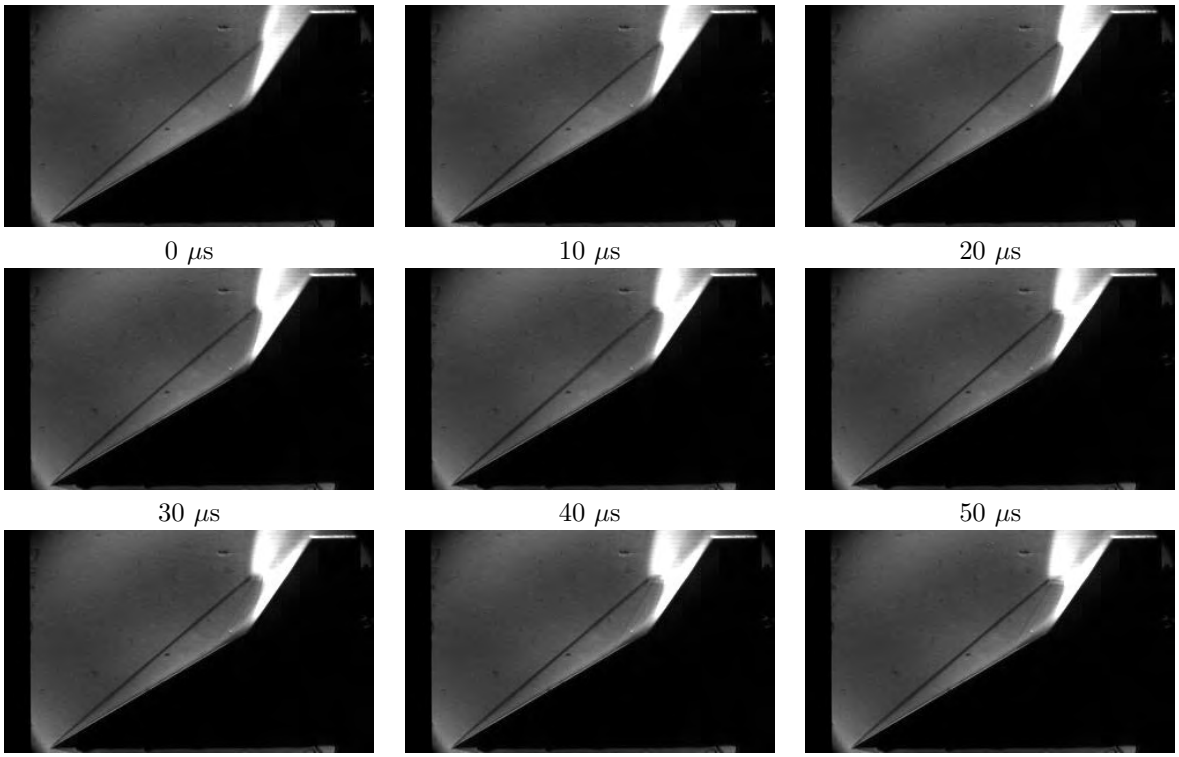

Figure 5.8: The establishment process of the triple point is shown for the M7_8 test condition in air. The interframe time is 10 μs, and the exposure time is 10 μs. Flow is from left to right.

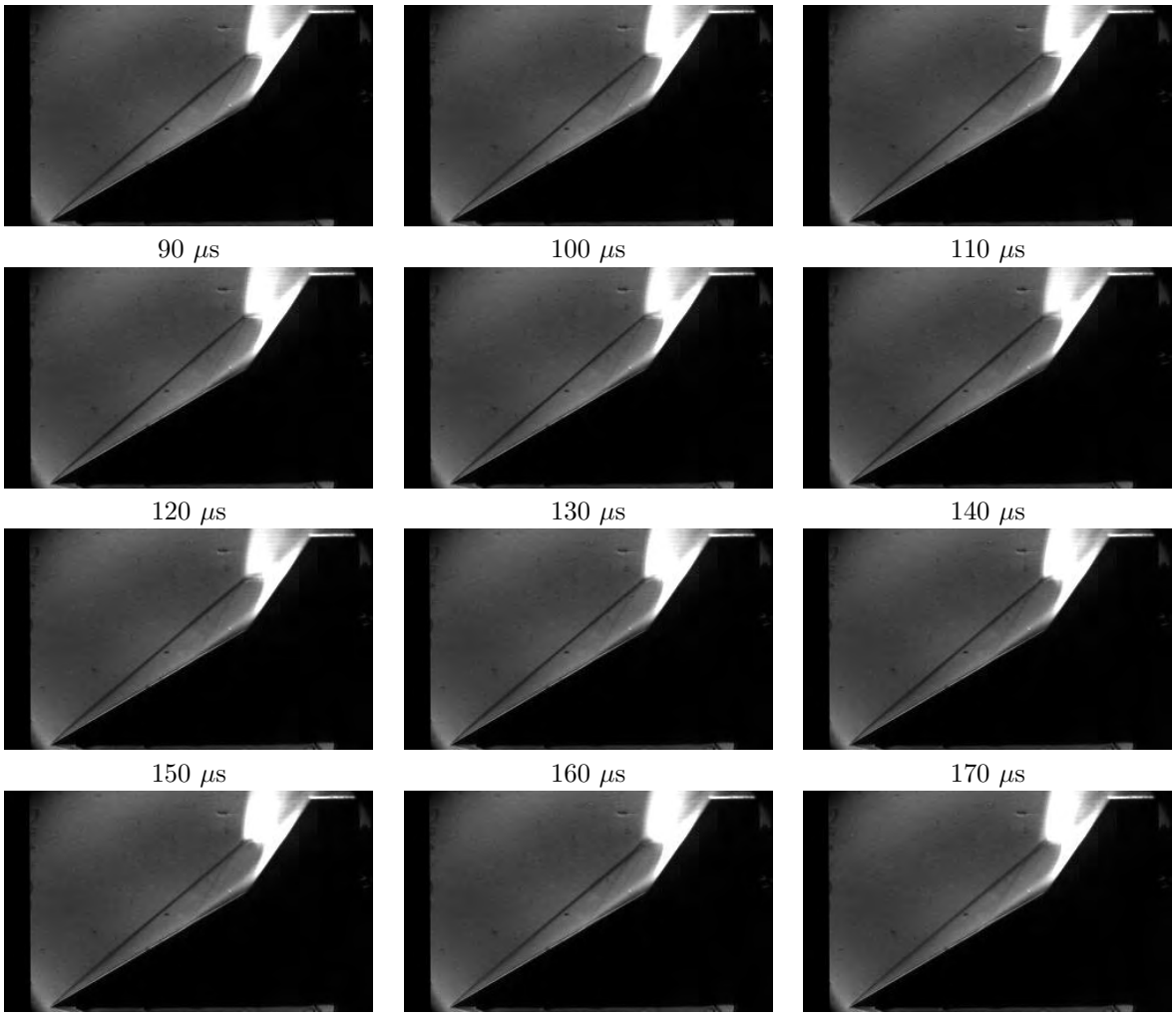

Figure 5.9: Movement in various parts of the flow field is shown for the M7_8 test condition in air. The interframe time is 10 μs, and the exposure time is 10 μs. Flow is from left to right.

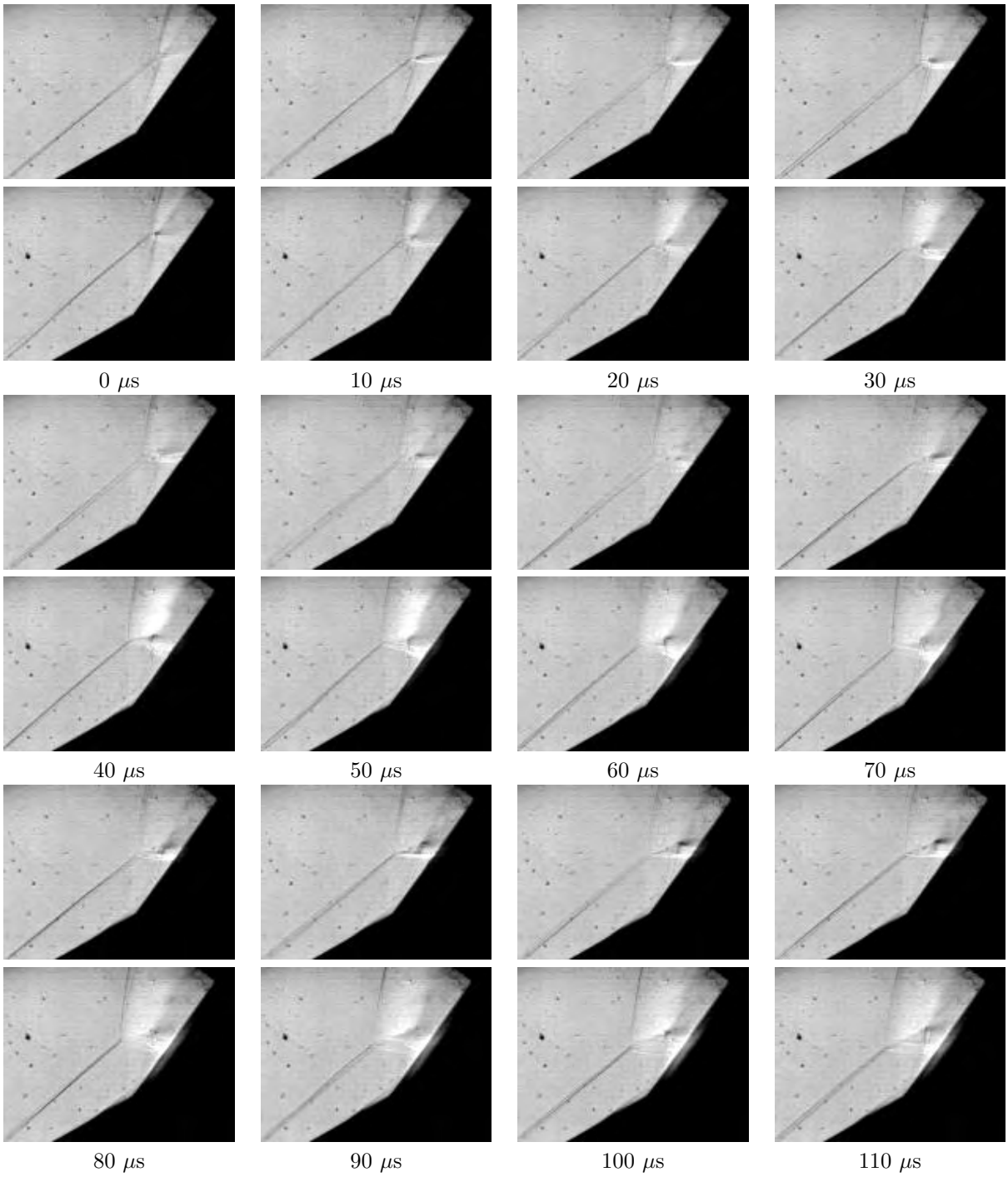

Figure 5.10: A comparison for the transient behavior of the M7_8 flowfield near the corner is shown for air (top) and nitrogen (bottom). The interframe time is 10μs and exposure time is 1μs. Flow is from left to right.

5.1.2 Double Cone Image Sequences

In this section the high speed imaging data are presented in a manner similar to the double wedge data. The establishment process is shown in one series of images, while the established behavior is shown in a second series of images.

The first test condition presented is the M7_2 test condition in air. The establishment is shown in Figure 5.11 and takes approximately 80 μs. In this series of images, establishment is seen to be oscillatory in nature, after which the triple point settles at its terminal location. The triple point is created by the separation shock from the start of the test gas. This is in contrast with the wedge model, where a finite amount of time is required for the separation shock to interact with the bow shock.

The established image series is shown for this test condition in Figure 5.12. Throughout this series the location of the separation shock appears to remain constant. As in the case of the single frame images, the dividing streamline appears to intersect the reattachment shock. Although there is oscillation in the location of these features, the interaction remains constant throughout the test gas. Triple point oscillation is observed, and thus the location of the impinging shock varies. No distinguishable differences are seen between nitrogen and air in this test condition.

The establishment process for the M4_3.6 test condition in air is shown in Figure 5.13 and takes 80 μs. The establishment behavior in this case is unique. From 0 μs to 50 μs there is upstream motion in the triple point, and then from 60 μs to 80μs the triple point travels back downstream to its final position. The first 50 μs is marked by the separation shock remaining in a constant location. Beginning at 60 μs there is upstream motion of the separation shock and a corresponding growth in the separated region. The separation region continues to grow until 110 μs. As in the case of the M7_2 test condition there is an interaction of the separation zone with the reattachment shock. In this case, however, there appears to be a departure from laminar behavior in the separation region.

The established behavior for this test condition is shown in Figure 5.14. An oscillatory behavior in the size of the separation zone and location of the separation shock is seen in this series of images. Approximately one oscillation cycle is shown in these images. The maximum separation zone size

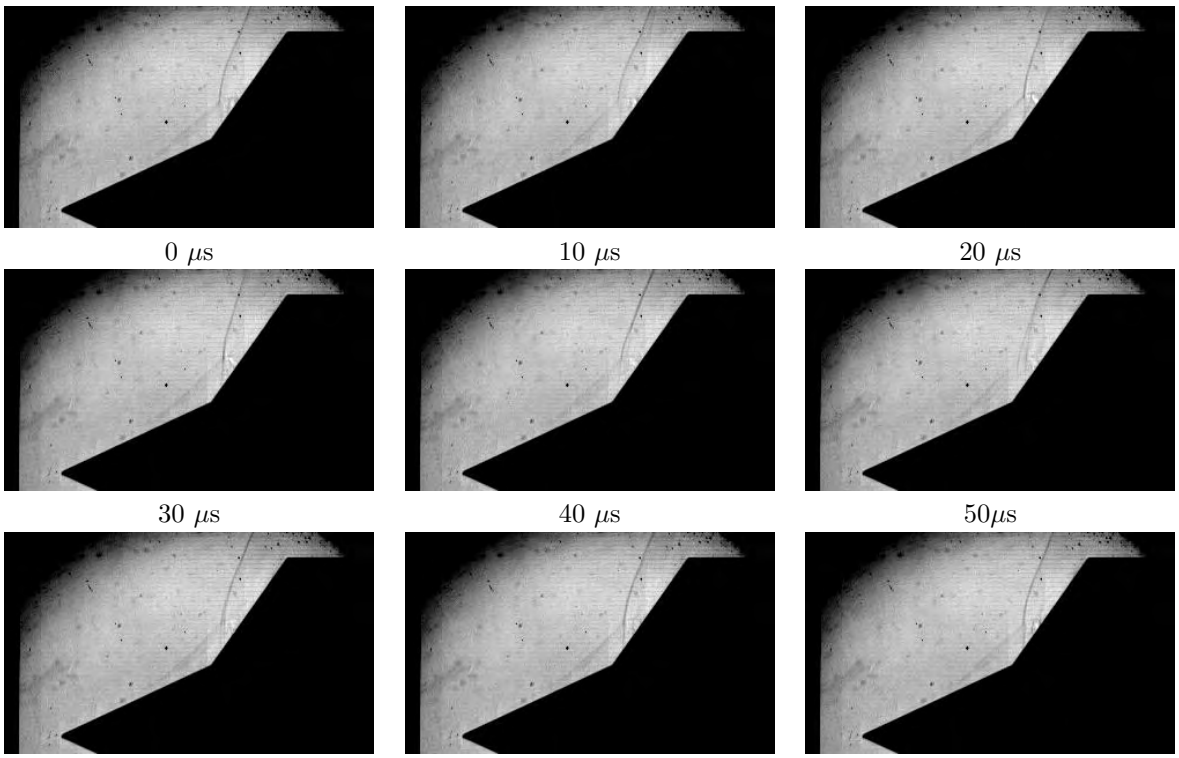

Figure 5.11: The establishment process of the triple point is shown in the double cone model for the M7_2 test condition in air. The interframe time is 10 μs and the exposure time is 1 μs. Flow is from left to right.

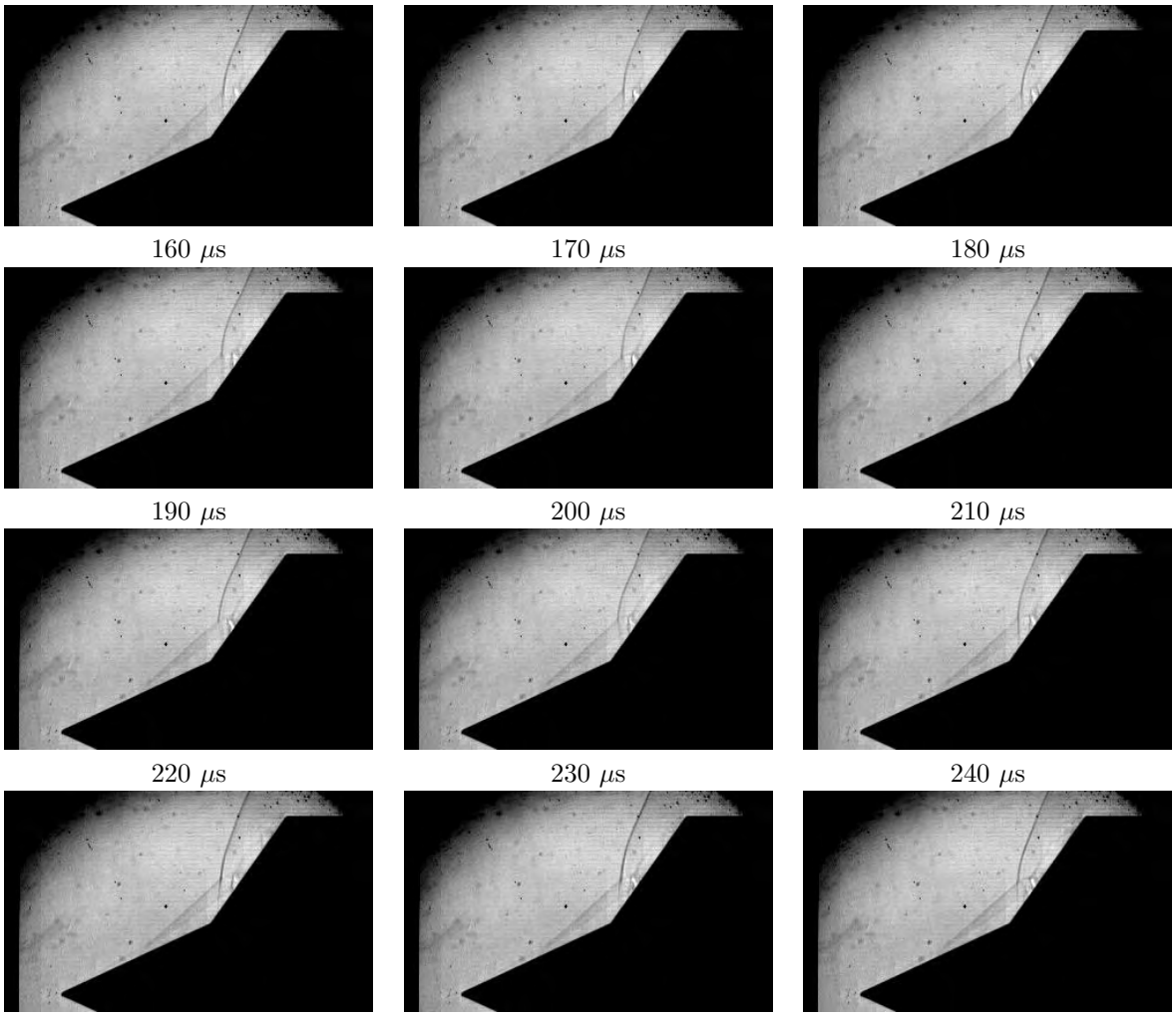

Figure 5.12: Movement in various parts of the flow field is shown for the M7_2 test condition in air. The interframe time is 10 μs, and the exposure time is 1 μs. Flow is from left to right.

(and forward most separation shock position) is seen at 370 μs. It reaches a minimum at 430 μs, followed by another maximum at 490 μs. This corresponds to an estimated oscillation frequency of 8.33 kHz. Triple point movement, again, corresponds with the location of the separation shock. The shear layer emanating form the triple point resides very close to the surface of the aft cone. Very similar behavior is seen for the nitrogen test condition including establishment and separation oscillation frequency.

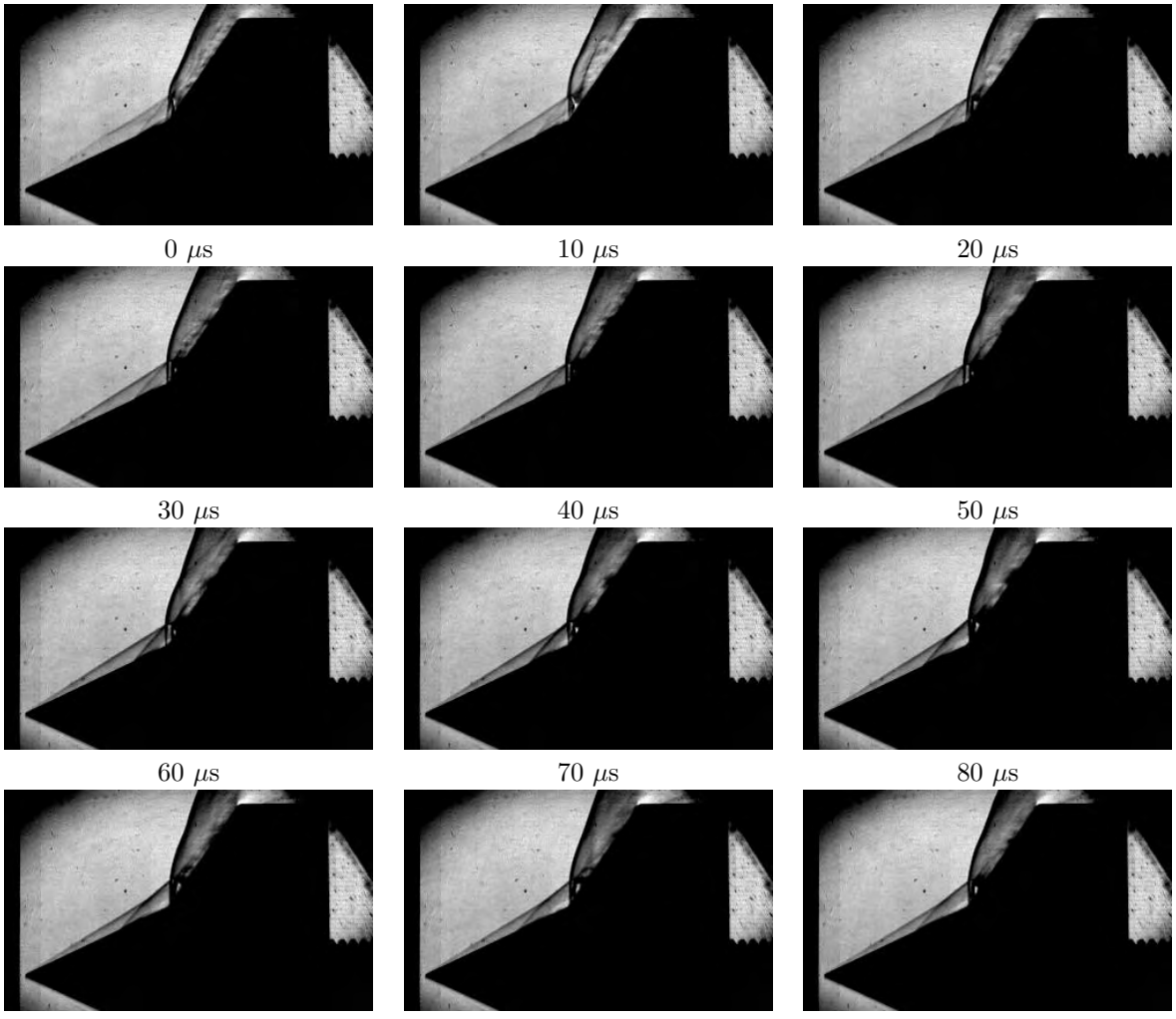

Figure 5.13: The establishment process of the triple point is shown for the M4_3.6 test condition in air. The interframe time is 10 μs, and the exposure time is 1 μs. Flow is from left to right.

The next series of images in Figures 5.15 show the triple point establishment for the M5_4 air test condition which occurs at 70 μs. The establishment process exhibits a sequence of events similar to those for the double wedge. This is the first case where the triple point only moves upstream until

Figure 5.14: Movement in various parts of the flow field is shown for the M4_3.6 test condition in air. The interframe time is 10 μs, and the exposure time is 1 μs. Flow is from left to right.

it settles in its established position. Similar to the M4_3.6 condition, the separation shock forms the triple point, and at the beginning of the test gas a separation zone has already been present. Another feature unique to this run condition is the formation of a second triple point above the primary triple point, which establishes on the same time scales as the primary triple point. This is seen to be formed by the first bow shock, and a wave which appears to originate from near the primary triple point's shear layer. A similar interaction is seen in Nompelis' dissertation [6]. This wave transverses through a supersonic region and interacts with the bow shock to create secondary triple point above the primary one.

A series of images after the establishment of the triple point is shown in Figure 5.16. In this series of images, an oscillation in the location of the separation shock can be seen. The magnitude of the oscillations is much smaller than for the M4_3.6 case. A minimum in upstream distance of the separation shock is detected at 190 μs. It reaches a maximum at 260 μs, and arrives back at the minimum at 320 μs. This corresponds to a frequency of approximately 7.69 kHz, which is the same order of magnitude as the M4_3.6 case. The secondary triple point up the main bow shock is seen to be a steady structure as well. This appears to be a weaker interaction than the primary triple point. The shear layer is also very close to the surface of the model in agreement with Nompelis [6], which isolates the supersonic jet to very near to the aft cone surface.

The final sequence of images in this section are for the establishment of the M7_8 condition, shown in Figure 5.17 which occurs over 60 μs. Signal levels are extremely low in this run condition due to a combination of the low freestream density and the axisymmetric geometry of the double cone, therefore the data taken with an exposure of 10 μs is presented. During the establishment process, the triple point moves upstream until the frame at 30 μs. It then regresses downstream until settling at 60 μs. Throughout this first sequence, the separation shock is moving upstream along the forward cone face. At earlier times in the establishment, the triple point is formed by the conical shock from the forward cone; however, starting at 40 μs it is the separation shock which interacts to form the triple point. Additionally, on the aft wedge, luminescent streamwise structures begin to appear on the aft body.

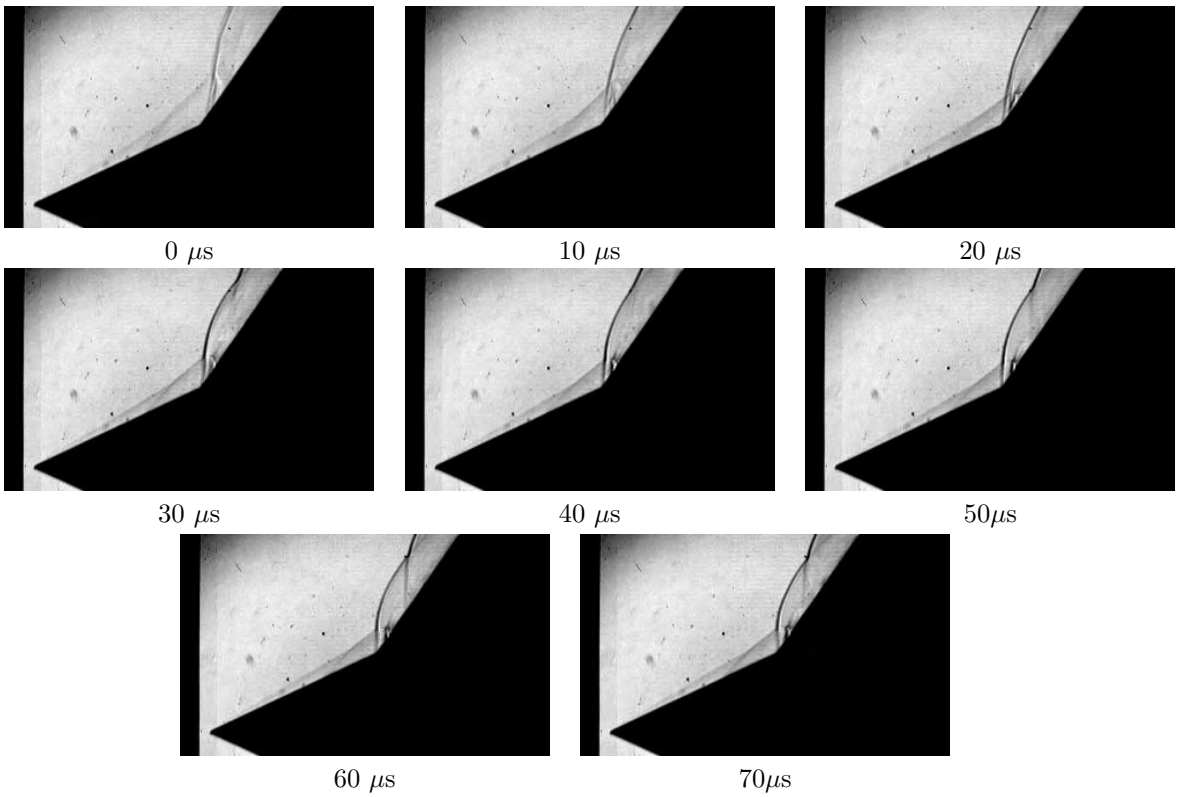

Figure 5.15: The establishment process of the triple point is shown for the M5_4 test condition in air. The interframe time is 10 μs and the exposure time is 1 μs. Flow is from left to right.

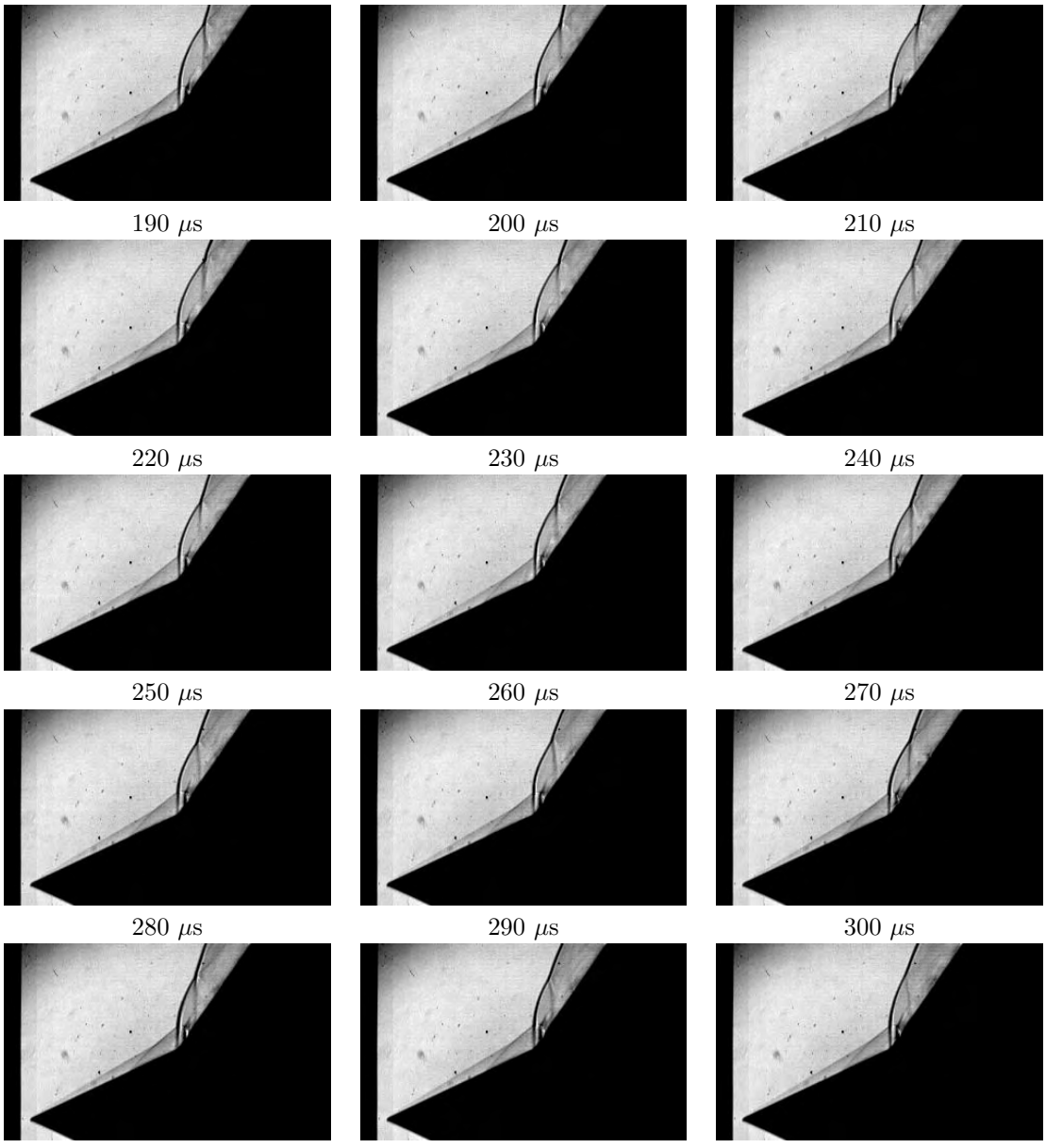

Figure 5.16: Movement in various parts of the flow field is shown for the M5_4 test condition in air. The interframe time is 10 μs and the exposure time is 1 μs. Flow is from left to right.

The continued behavior of the flow field is shown in Figure 5.18 The separation zone continues to grow until approximately 120 μs. Unlike the previous cases, distinct oscillations in the separation zone are not detected. Post bow shock luminescence is large, and aft body luminescence is visible in all frames. On the aft body, streaks are noticed which may be streamwise structures such as Görtler vortices. Minimal triple point movement is observed during the test time. In the case of the nitrogen, establishment time is 80 μs.

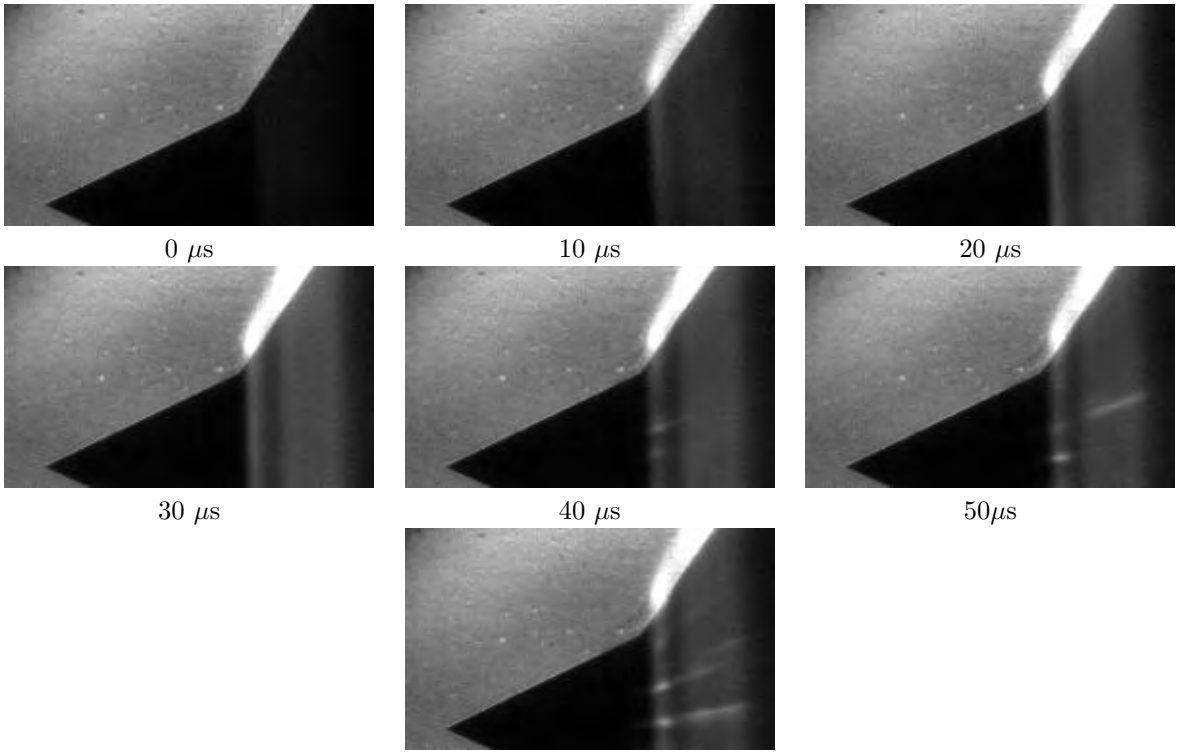

Figure 5.17: The establishment process of the triple point is shown for the M7_8 test condition in air. The interframe time is 10 μs and the exposure time is 10 μs. Flow is from left to right. The 10 μs exposure time is used due to low signal levels.

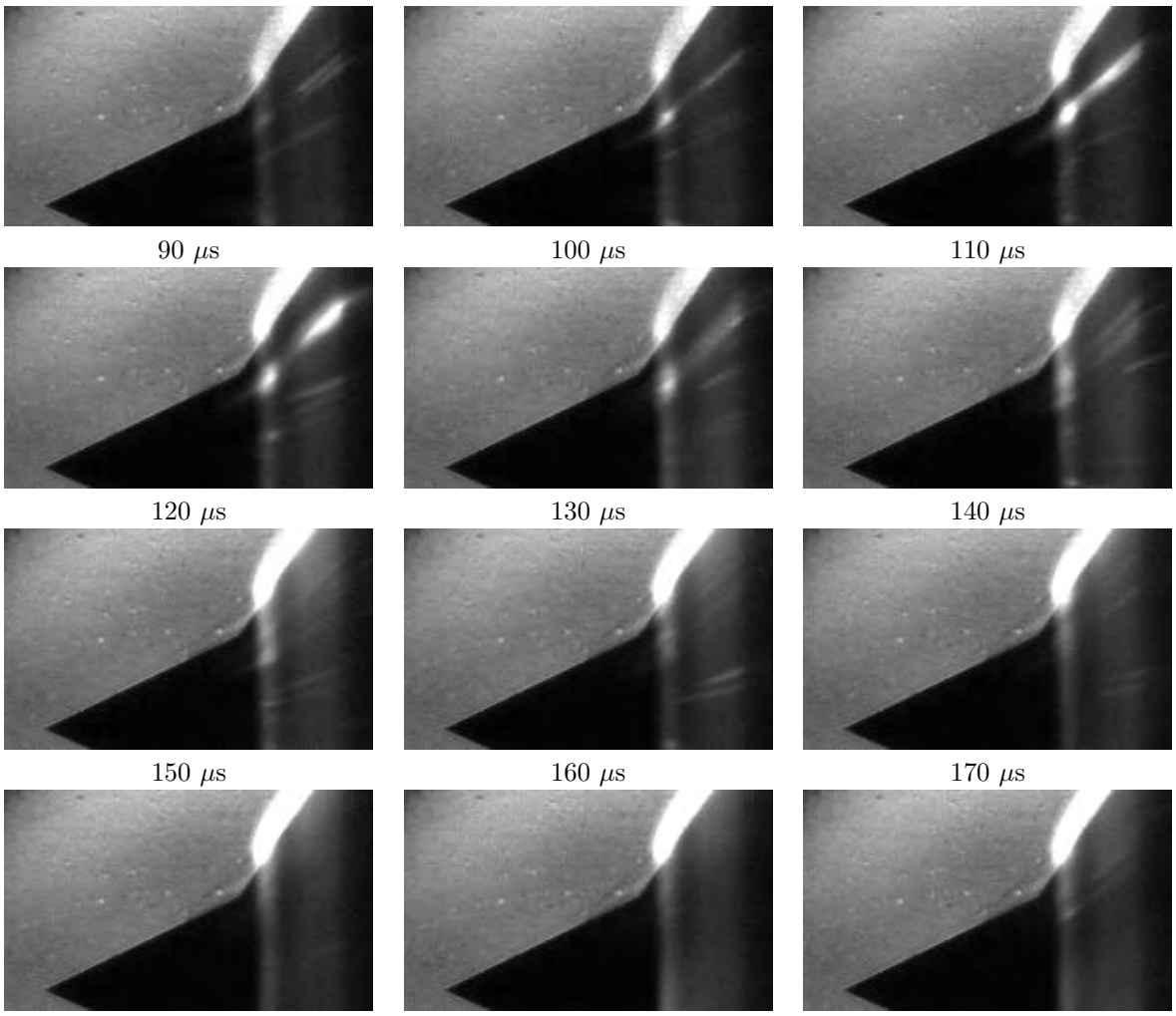

Figure 5.18: Movement in various parts of the flow field is shown for the M7_8 test condition in air. The interframe time is 10 μs, and the exposure time is 1 μs. Flow is from left to right.

5.2 Establishment Comparisons and Shock Tracking

In this section results of the high speed imaging analysis are presented. First, establishment times of the triple point are compared with establishment times from the heat transfer data presented in Chapter 4. These are plotted for select gauges on the double wedge in each test condition. Next, plots of the transient profile of the oblique shock, triple point, and bow shock are presented to visualize the trajectory of these flow features in time. Fast Fourier Transforms (FFTs) have been performed on these data to quantify oscillations in the shock frequency, and are compared with order of magnitude estimations of the frequency of post shock acoustic disturbances. Lastly, a series of high speed data was collected at compositions intermediate to nitrogen and air. Compositions include 30%, 50%, and 80% of the oxygen content of atmospheric air. These correspond to 0.3, 0.5 and 0.8 on Figure 2.12. To the author's knowledge, this is the first work investgating intermediate cases of nitrogen and air.

5.2.1 Comparison of Establishment Times

Establishment times from the heat transfer traces on the double wedge are presented in this section along with a comparison of the triple point establishment, as well as the prediction of laminar boundary layer establishment time from Gupta [42]. Properties behind the oblique shock are taken for the flat plate conditions. Heat transfer establishment times are taken to be the time it takes for the heating rate to reach the mean value in the established state. Some values are not reported when there is no effective establishment time, an example of which is Gauge A in Figure 4.1. These types of traces typically occur in the laminar flat plate region of the forward wedge.

Data are then normalized by dividing the time by the time it would take a freestream particle to traverse the surface of the model. This flow time is shown in Equation 5.1. L_1 is the length of the forward wedge face, L_2 is the length of the aft wedge face, and U_∞ is the freestream velocity.

$$t_{flow} = \frac{L_1 + L_2}{U_\infty} \tag{5.1}$$

Figures 5.19 - 5.22 present the aforementioned data sets for the four different test conditions in air and nitrogen. The total test time, in flow times, is listed in the caption for each figure. *BL Established* represents the time for a laminar boundary layer to establish on the forward wedge based off the work of Gupta [42]. This is plotted on the forward wedge, where this time scale is most representative of the flow physics. *Triple Point Established* represents the experimentally measured establishment times for the triple points from the high speed imaging data. This is plotted on the aft wedge, where this time scale is most representative of the flow physics.

In Figure 5.19 the data for the M7_2 case are presented. Forward wedge data are not plotted, as no observable establishment is present in the heat transfer traces. In this run condition, the predictions for boundary layer establishment are reasonably close to the triple point establishment time. Additionally, the measurements from the heat transfer traces near shock impingement agree well with the triple point behavior. They are slightly lower on either side of the impingement location. Differences in air and nitrogen are not observed.

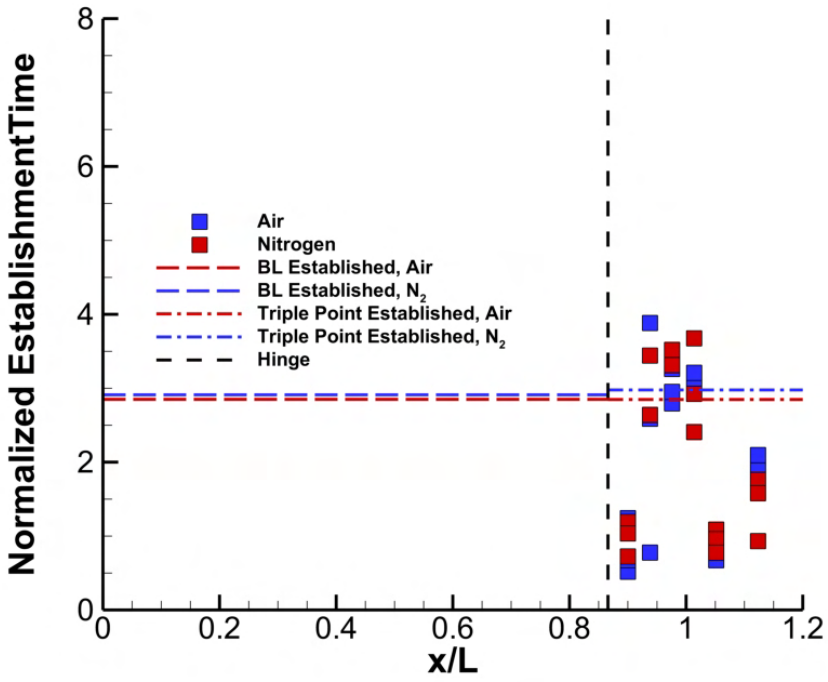

Figure 5.19: Establishment time in normalized units is presented for select heat transfer gauges in the M7_2 test condition. The total test time for this condition is 7.0 flow times.

The data for for the M4_3.6 test condition are presented in Figure 5.20. Predictions for the establishment of the laminar boundary layer and experimental measurements of the triple point establishment are considerably different, compared to the previous case. Data on the forward wedge, in general, have an establishment time of ∼2 times that of the laminar prediction. This is not unexpected, as heat transfer traces and imaging indicate a departure from laminar boundary layer behavior on the forward wedge. On the aft wedge, there is an increase in establishment time of the heat transfer data up to values of approximately the triple point establishment time. This occurs near to the location of shock impingement. Heat transfer and triple point data are in agreement, although heat transfer data are slightly higher. No differences between air and nitrogen are observed.

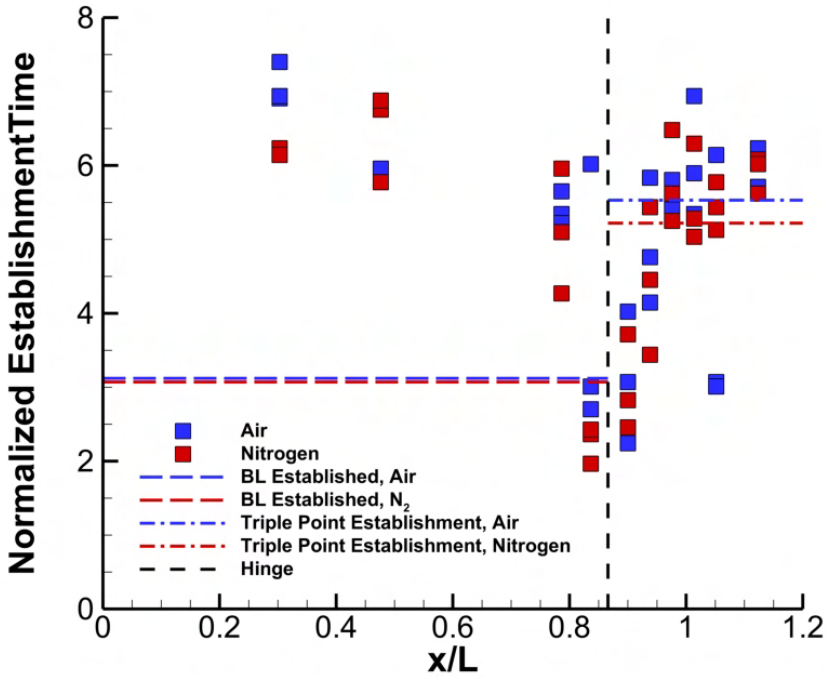

Figure 5.20: Establishment time in normalized units is presented for select heat transfer gauges in the M4_3 test condition. The total test time for this condition is 15.4 flow times.

Figure 5.21 presents the data for the M5_4 test condition. Laminar predictions for boundary layer establishment are slightly lower than the experimental triple point establishment results. This difference is not as dramatic as for the M4_3.6 test condition shown in Figure 5.20. Forward wedge data upstream, in the purely laminar region, are not shown due to a lack of distinct establishment.

Similar to the M4_3.6 test condition, on the forward wedge where the flow departs from laminar behavior the establishment time is higher than the laminar prediction. This is also the first distinct difference seen between air and nitrogen behavior. The establishment time of the air condition is significantly larger than for the nitrogen. This behavior may be coupled with the observations from Section 5.1.1, where the breakdown of the corner turning wave in air exists for approximately 160 μs longer than the turning wave in nitrogen. On the aft wedge, there is an observable increase in the establishment time which reaches levels distinctly above the triple point establishment time.

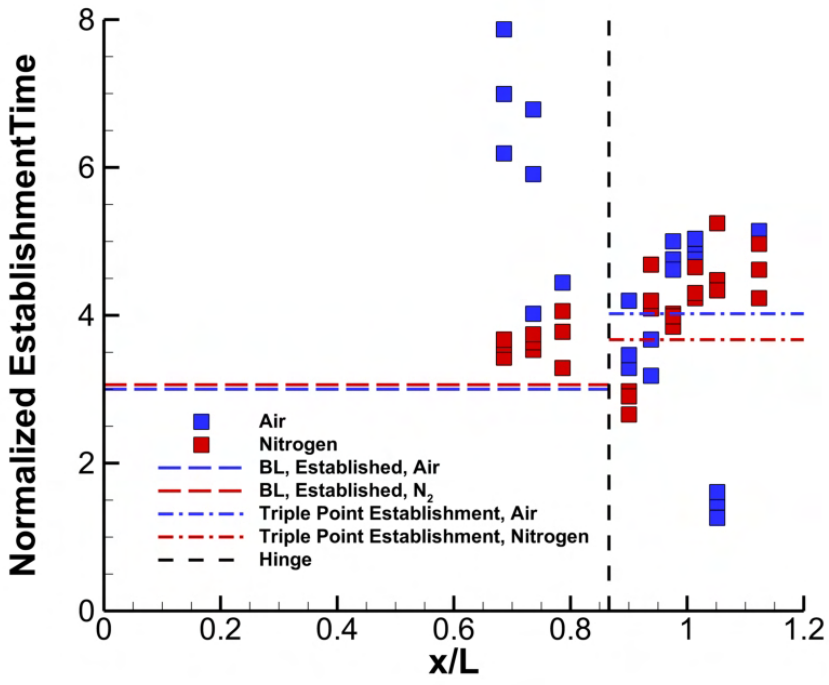

Figure 5.21: Establishment time in normalized units is presented for select heat transfer gauges in the M5_4 test condition. The total test time for this condition is 12.2 flow times.

Lastly, Figure 5.22 presents the data for the M7_8 test condition. As in previous cases, the experimental triple point establishment time is higher than the theoretical laminar boundary layer establishment time prediction. This is also the first condition where there is a distinct difference between these two metrics for air and nitrogen; air having a lower establishment time in both. Forward wedge data are only shown downstream of the separation shock, as no distinct establishment is observed in the purely laminar portion of the boundary layer. The establishment time is seen

to increase moving upstream. This is in agreement with the observations from Figures 5.8 and 5.9, where the separation shock moves upstream along the forward wedge face. On the aft there is scatter; however, data fall near the triple point establishment time. Only in the region very near to the shock impingement are there noticeable differences in the establishment times for air and nitrogen.

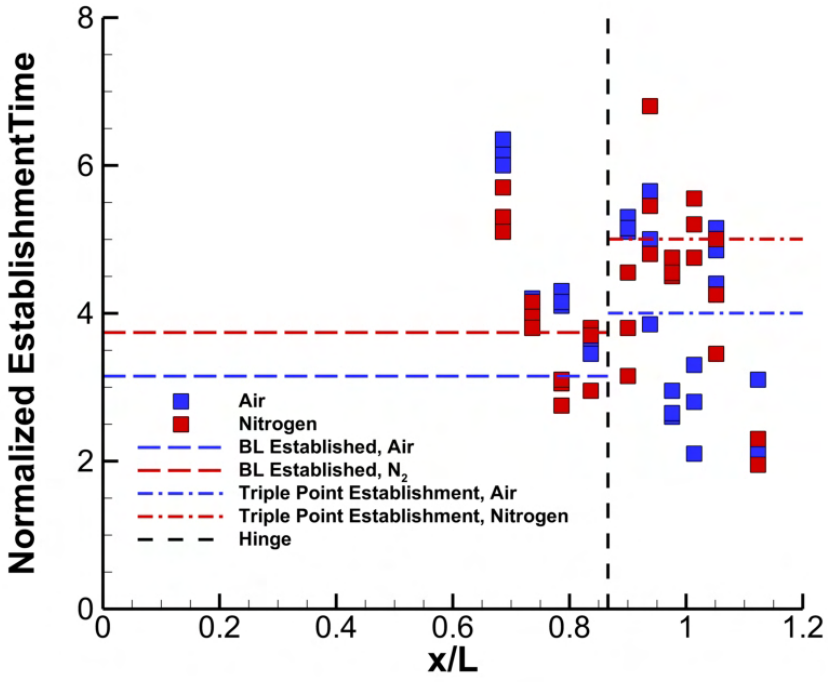

Figure 5.22: Establishment time in normalized units is presented for select heat transfer gauges in the M7_8 test condition. The total test time for this condition is 11.0 flow times.

5.2.2 Shock Tracking Results

In this section, the results from the shock tracking image analysis are presented. For each test condition, a single plot is presented with all of the shock surface tracks during the test gas. In order to properly visualize the shock behavior, surfaces are plotted on a color gradient from red to blue from the beginning to end of the test time. Results from the FFTs of the shock profiles are tabulated and compared with order of magnitude estimates for the frequency of post bow shock acoustic waves.

Double Wedge Results

The first test condition presented is the M7_2 condition. Data are presented in Figures 5.23(a) and (b). As observed in the high speed imaging in Figures 5.1 and 5.2, there is no distinct upstream motion of the shock during triple point establishment. Rather it is the separation shock which dictates the triple point interaction. Noticeable oscillations are apparent in the established profiles in the bow shock. There is less motion in the leading edge oblique shock. No distinct differences are observed between the profiles for nitrogen and air at this test condition.

Figure 5.24 presents the data for the the M4_3.6 test condition for nitrogen and air. Distinct upstream motion of the bow shock and triple point are observed during the establishment process. This case is unique in the fact that the established bow shock moves slightly upstream in time. This may, in part, be due to movement of the shock foot on the forward wedge, which interacts with the triple point shear layer. Although data are collected in what is assumed to be the steady time (determined from pitot traces), there may still be a transient present. A slight increase is seen in the oblique shock angle throughout the test gas. Differences between air and nitrogen are minimal.

The M5_4 test condition is presented in Figure 5.25. As in the case of the M4_3.6 condition, there is distinct upstream motion of the shock during the establishment. Upon establishment the bow shock oscillates about a mean position, rather than continuing to traverse upstream. Some movement is detected in the oblique shock, however this is not large in magnitude after establishment. As observed in the the single frame schlieren imaging, the bow shock for the nitrogen has a larger standoff distance than for air.

Lastly, the M7_8 test condition is presented in Figure 5.26. Similar to the previous two test conditions, forward motion is present during establishment, followed by oscillations around a mean position. There is a noticeably larger stand off distance in the nitrogen compared with the air. This is evidenced in the establishment, where the travel distance for the triple point structure is longer than for the air. Oscillations in the nitrogen bow shock appear to be larger than for the air. Minimal oscillations are observed in the oblique shock.

An additional investigation of the M7_8 test condition is presented in Figure 5.27, where mix-

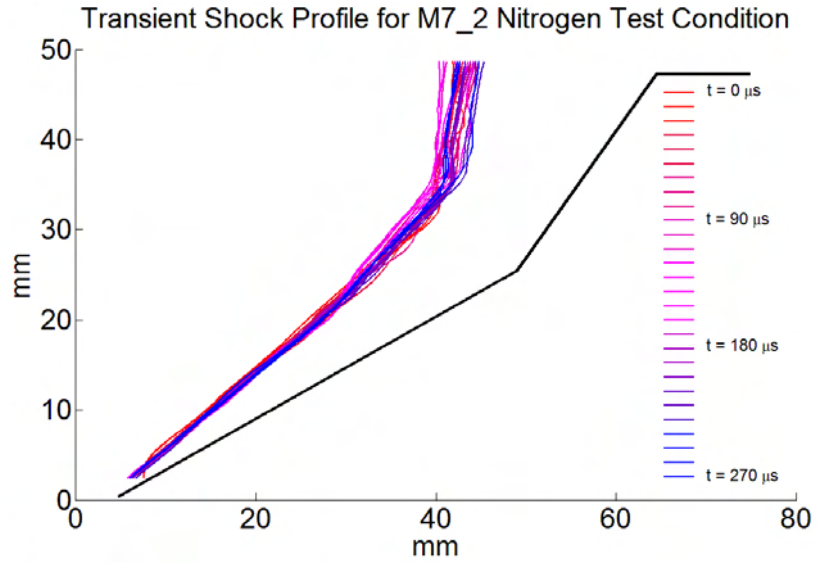

(a)

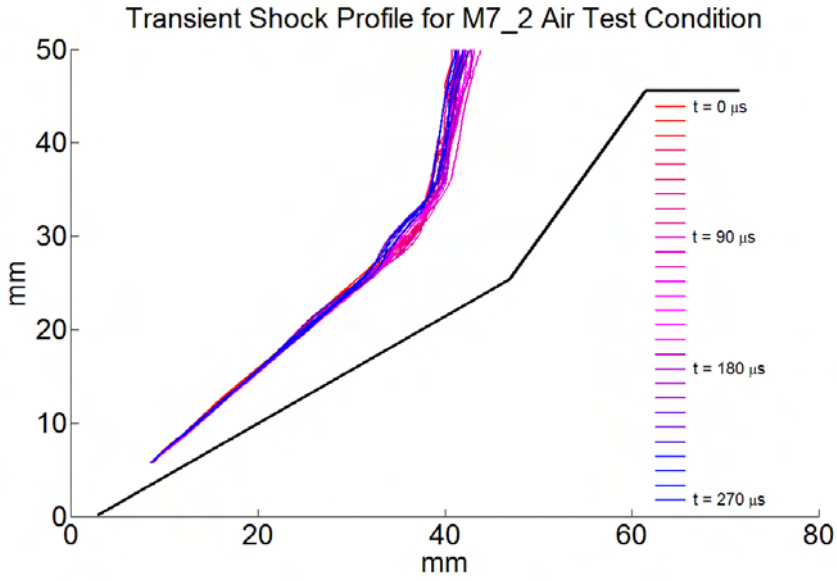

(b)

Figure 5.23: Transient double wedge shock profiles are shown for the M7_2 test condition in (a) nitrogen and (b) air. The color scheme transitions from red to blue with increasing time. Some wrinkling in the shock surface is observed due to low signal levels in the schlieren imaging inhibiting edge detection.

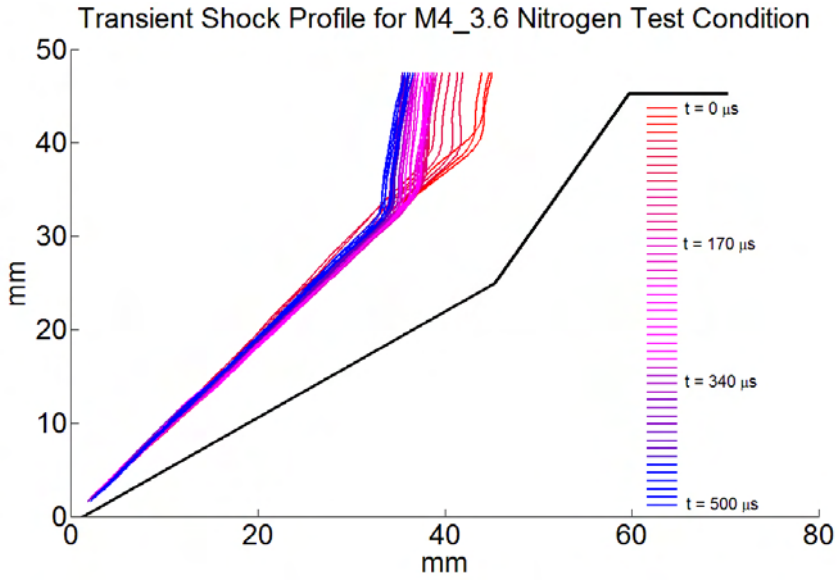

(a)

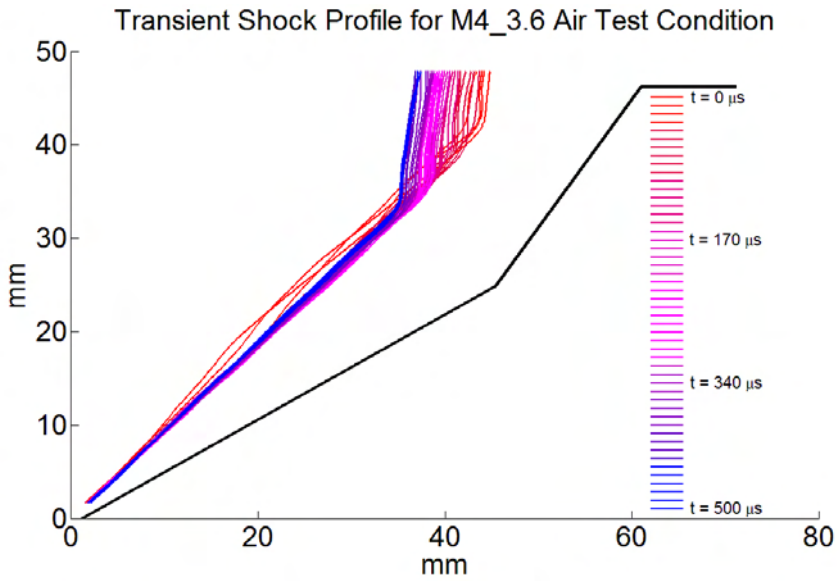

(b)

Figure 5.24: Transient double wedge shock profiles are shown for the M4_3 test condition in (a) nitrogen and (b) air. The color scheme transitions from red to blue with increasing time.

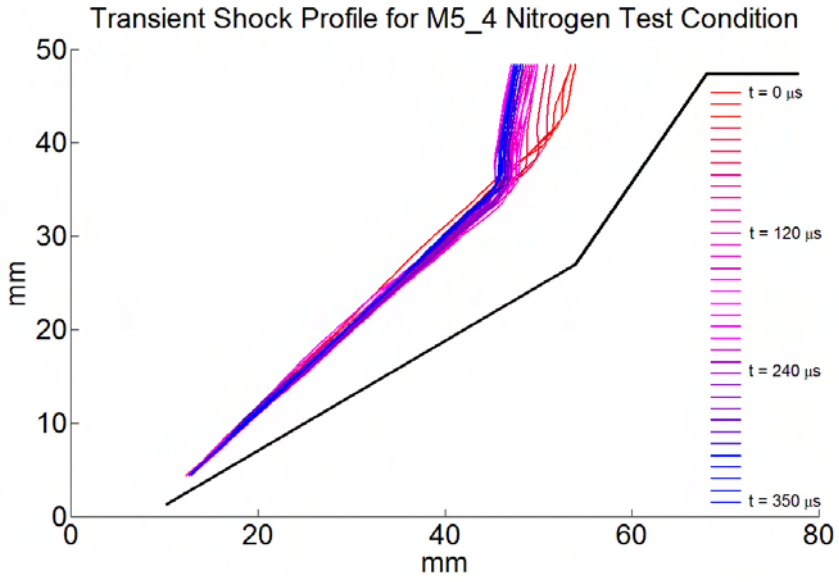

(a)

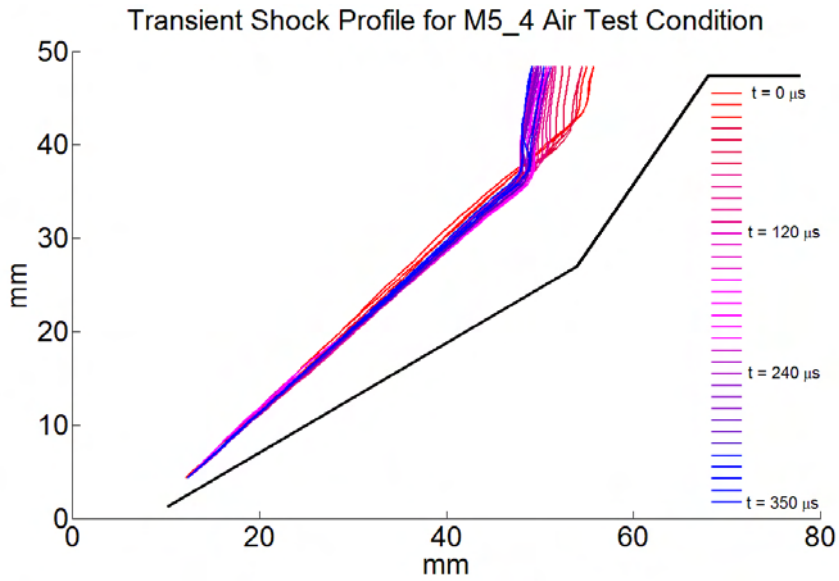

(b)

Figure 5.25: Transient double wedge shock profiles are shown for the M5_4 test condition in (a) nitrogen and (b) air. The color scheme transitions from red to blue with increasing time.

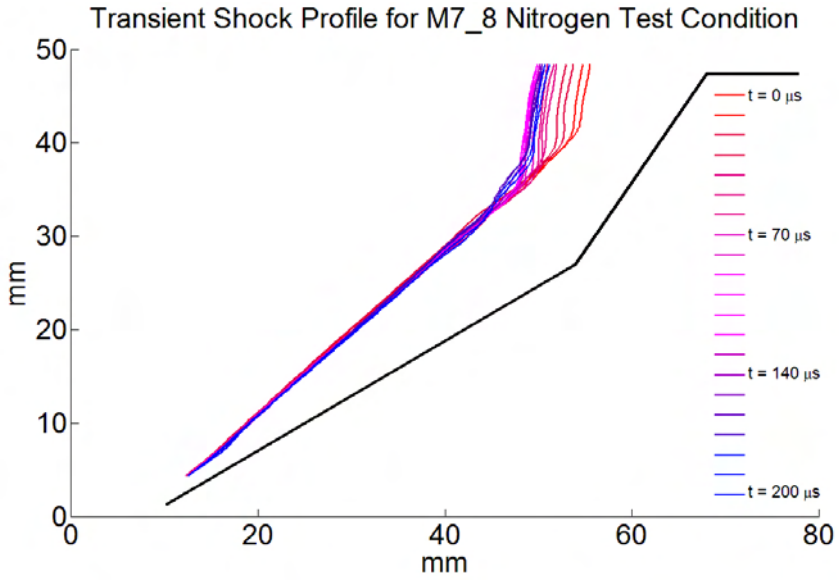

(a)

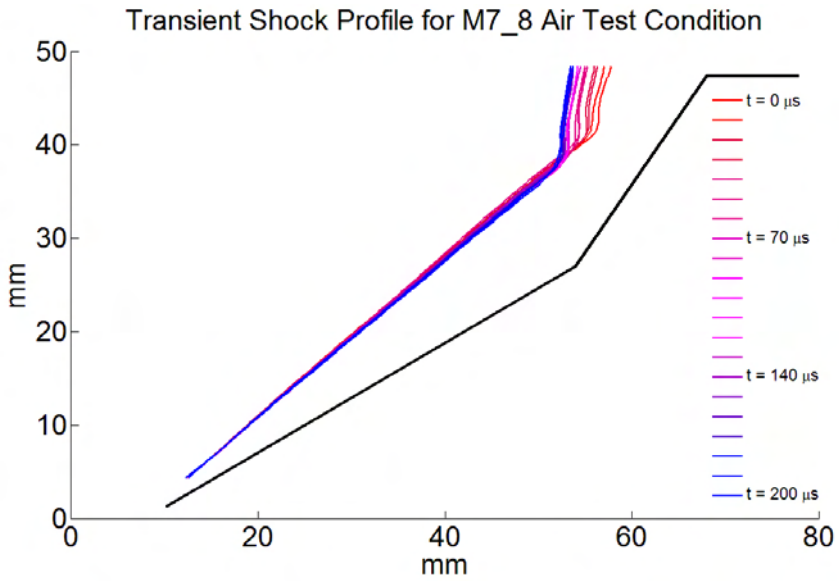

(b)

Figure 5.26: Transient double wedge shock profiles are shown for the M7_8 test condition in (a) nitrogen and (b) air. The color scheme transitions from red to blue with increasing time.

tures intermediate to nitrogen and air are present. These mixtures are 30%, 50%, and 80% of the atmospheric content of air based on Figure 2.12. A 0% mixture would be pure nitrogen, while a 100% would be atmospheric air. To maintain visual clarity, the establishment process is omitted. Shock surfaces are aligned based on the location of the double wedge model in the image. In all cases, the oblique shock location agrees very well. Interestingly, there is nearly no difference in shock location in the nitrogen, 30%, and 50% conditions. It is not until the 80% test condition, where the bow shock forms intermediate to the two extremes, that significant differences are seen. The freestream compositions and post shock equilibrium compositions for each mixture are listed in Table 5.1. Molecular oxygen may have a role in this behavior as it is the species that changes the most throuought these conditions; increasing by nearly 2 orders of magnitude from the 30% mixture to atmospheric air. With respect to the freestream, the O_2 content is increased only by a factor of 3. This indicates that as the O_2 content is increased, less is dissociated to create atomic oxygen and nitric oxide. Atomic nitrogen decreases by approximately 1 order of magnitude, most likely due to the creation of nitric oxide. Lastly, nitric oxide increases by a factor of 5.

To complement this, a second table with dissociation fractions, f (in percentage), is presented in Table 5.2. Dissociation fraction is defined as the ratio of number of diatomic molecules which dissociate, to the original number of diatomic molecules. In the pure nitrogen case, a 3.46% dissocation is seen. This falls to 1.79% in the 30% condition, and increases as the composition moves toward atmospheric air. Oxygen dissociation is at a much higher rate, starting at 99.5% and decreasing to 82.7%. As suggested previously, this indicates an increase in molecular oxygen behind the bow shock. Molecuar oxygen has the highest molecular weight of all post shock species. This, in part, contributes to the increasing density behind the bow shock, leading to a decrease in the bow shock standoff distance. For a given temperature and pressure, molecular oxygen will have the highest density of all post shock species. Equilibrium calculations of post shock species indicate an increasing post shock density with increasing freestream oxygen content, and shock standoff is known to be inversely proportional to post-shock density [74].

The results of the Fast Fourier Transforms of each test condition are shown in Table 5.3 The

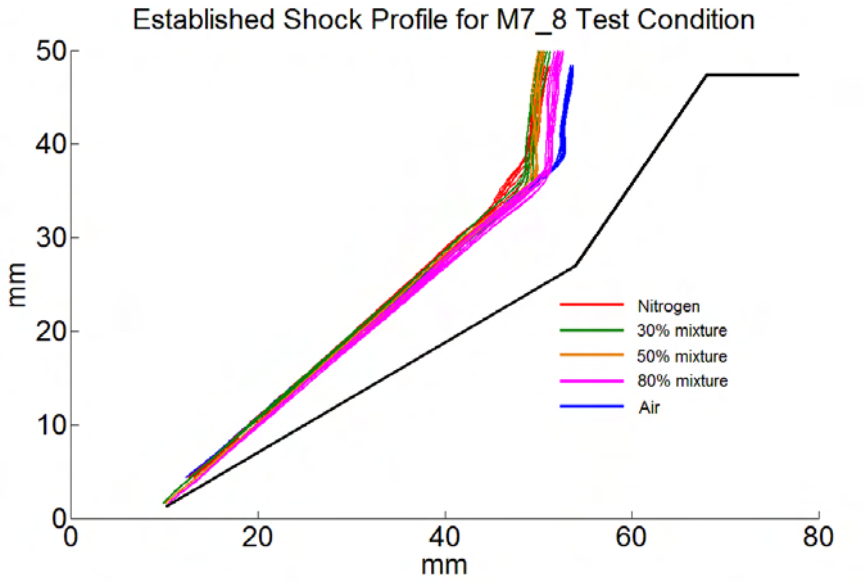

Figure 5.27: Double wedge shock profiles are shown for the M7_8 test condition in nitrogen and air, as well as intermediate mixtures of 30%, 50%, and 80%. Profiles are shown after triple point establishment.

Table 5.1: Freestream composition, and post normal shock equilibrium species concentration and temperature for nitrogen and air mixtures in the M7_8 test condition from Figure 2.12.

	Freestream		Post Shock					
Mixture	N_2	O_2	N_2	N	O_2	O	NO	T, K
Nitrogen	1.000	0.000	9.330E-1	6.697E-2	-	-	-	5178
30%	0.926	0.074	8.404E-1	2.329E-2	3.250E-4	1.286E-1	7.343E-3	4754
50%	0.883	0.117	7.821E-1	8.755E-3	1.978E-3	1.924E-1	1.473E-2	4425
80%	0.825	0.175	7.057E-1	2.025E-3	1.474E-2	2.480E-1	2.949E-2	3990
Air	0.790	0.210	6.659E-1	1.082E-3	3.152E-2	2.639E-1	3.751E-2	3902

Table 5.2: The dissociation fraction of the diatomic air molecules is presented as a percentage, for each of the M7_8 freestream compositions.

Mixture	f_{N_2}	f_{O_2}
Nitrogen	3.46	-
30%	1.79	99.5
50%	1.48	98.1
80%	2.18	90.4
Air	2.82	82.7

Table 5.3: Frequencies from the FFTs of the shock position data from the double wedge experiments. Estimates of post-bow shock acoustic wave frequency are also provided. All frequencies are in kHz.

Test Condition	N_2, Experiment			Prediction	Air, Experiment			Prediction
M7_2	9.38	18.8	25.0	4.21	25.0	43.8	-	4.01
M4_3.6	4.69	7.81	10.9	9.46	4.69	7.81	10.9	7.95
M5_4	6.25	25.0	40.6	6.19	6.25	25.0	40.6	6.29
M7_8	12.5	37.8	-	7.22	12.5	37.8	-	7.52

first 3 peaks in the data are taken (not all cases exhibit 3 peaks). Order of magnitude estimates in the oscillation frequencies are also presented. An acoustic wave is assumed to travel between the shock wave and the shear layer with a convection velocity equal to that of the post shock flow field. Frequencies are calculated by averaging the post shock equilibrium and frozen conditions, and taking an average length between the bow shock and the shear layer. There is inherent error in the experimental data as FFTs are computed with only 10-30 points. Generally, to an order of magnitude, the prediction of acoustic frequency agrees best with the lowest peak found. These waves may be the cause for this low frequency motion. Another source of motion, as noted by Lind and Lewis [48] may be the shear layers which shed vortices.

Double Cone Results

Data from the double cone tests are shown on the top half of the cone to better visualize shock behavior. A combination of low densities an the axisymmetric model can yield low signal levels in the schlieren imaging. In some of the test conditions, surface data are omitted below the triple point due to inadequate shock tracking.

The results of the double cone tests in the M7_2 condition are shown in Figure 5.28. Similar to this test condition on the double wedge, there is no forward movement observed during the establishment process of the bow shock. There is, however, upstream movement in the separation shock which interacts to form the triple point. This is in agreement with the imaging results. No differences are observed between nitrogen and air.

The results of the M4_3.6 test are shown in Figure 5.29. Upstream motion is seen during the establishment, and similar to this test condition on the double wedge, there is further upstream

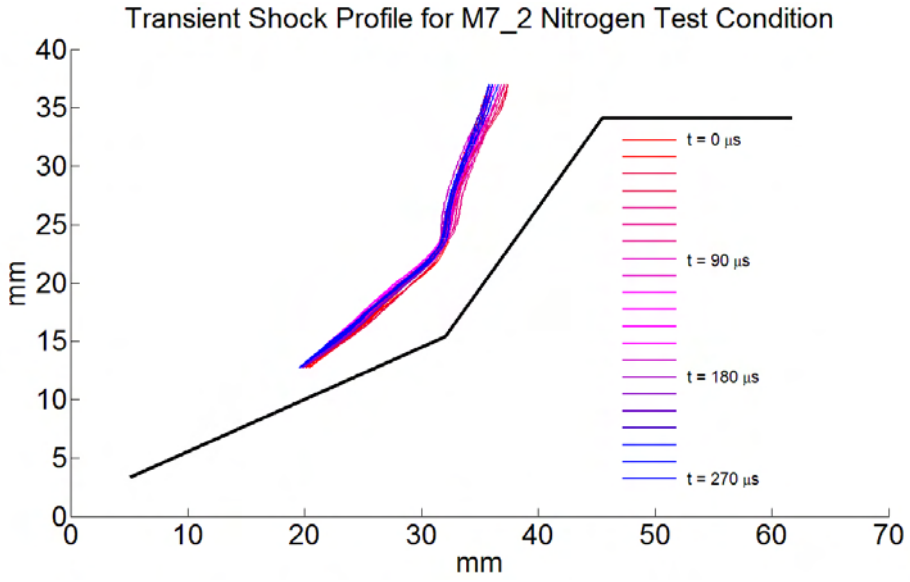

(a)

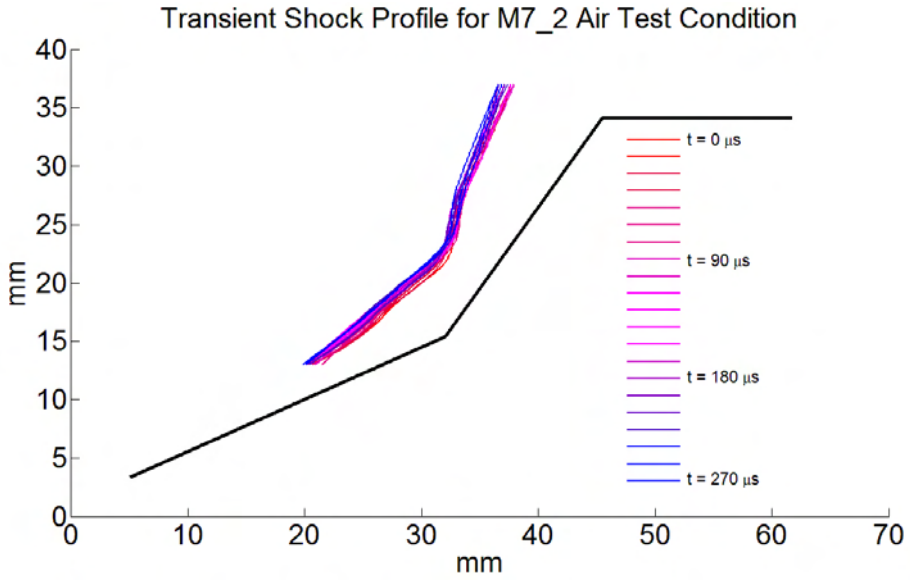

(b)

Figure 5.28: Transient double cone shock profiles are shown for the M7_2 test condition in (a) nitrogen and (b) air. The color scheme transitions from red to blue with increasing time.

motion of the bow shock. This is not seen in the conical shock. Midway between the the oblique shock and the bow shock, the result of the separation shock moving upstream can be visualized as the shock surfaces rising in the vertical direction. There are no distinct difference seen between the air and the nitrogen at this test condition.

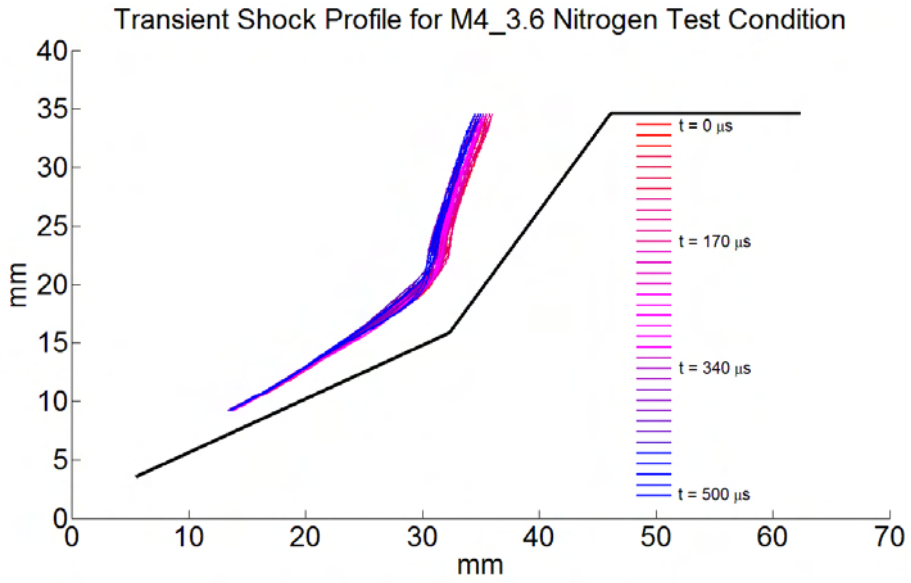

(a)

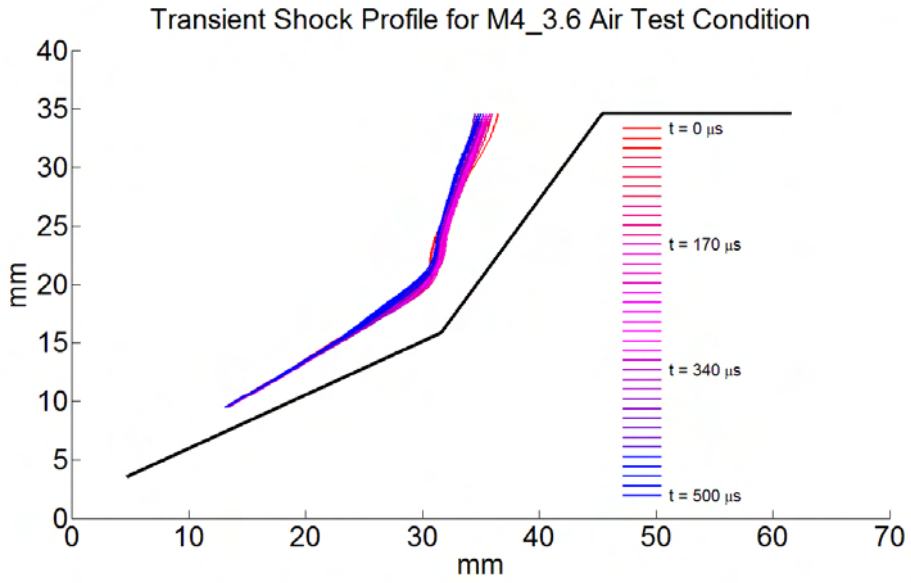

(b)

Figure 5.29: Transient double cone shock profiles are shown for the M4_3.6 test condition in (a) nitrogen and (b) air. The color scheme transitions from red to blue with increasing time.

Figure 5.30 presents the data for the M5_4 test condition in nitrogen and air. This is the

first case where different behavior is observed between test gases. In the case of the nitrogen, no upstream motion of the triple point is observed, where in the case of the air it is seen. Both cases exhibit minimal movement in the leading edge conical shock. There is a larger amount of oscillation noticeable in the nitrogen when compared with the air; however, there are no differences in the stand off distances of the bow shocks.

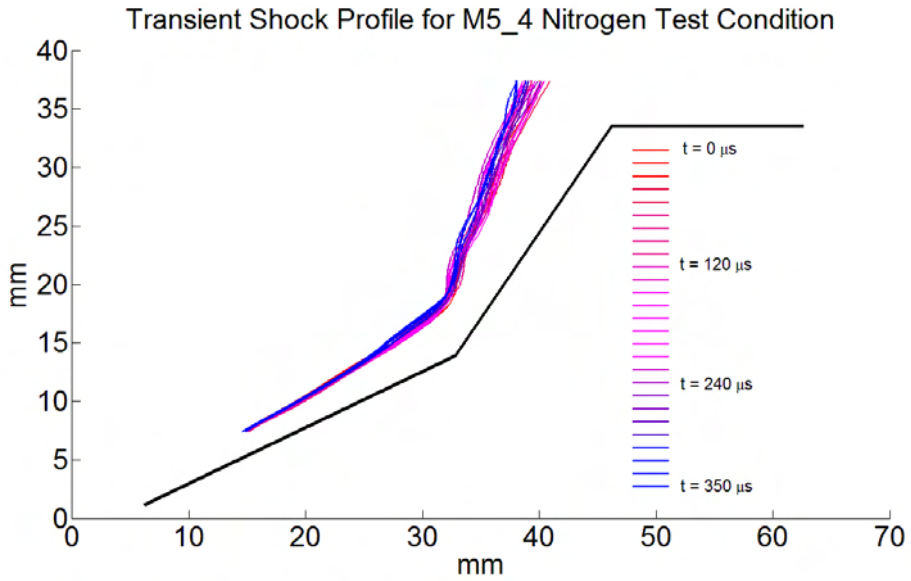

(a)

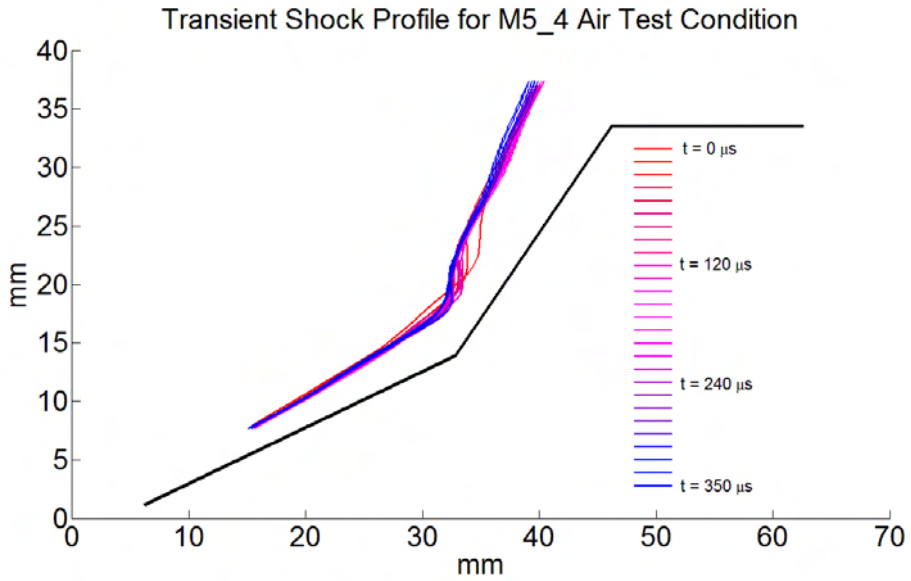

(b)

Figure 5.30: Transient double cone shock profiles are shown for the M5_4 test condition in (a) nitrogen and (b) air. The color scheme transitions from red to blue with increasing time.

Lastly, the M7_8 data are presented in Figure 5.31. This test condition has suffered from signal loss, thus the bottom portion of the data is not included. Distinct upstream shock motion is not observed during the establishment of the flow field. In the case of the nitrogen, oscillations are greater than those for the air condition. The air condition nearly maintains a constant bow shock position.

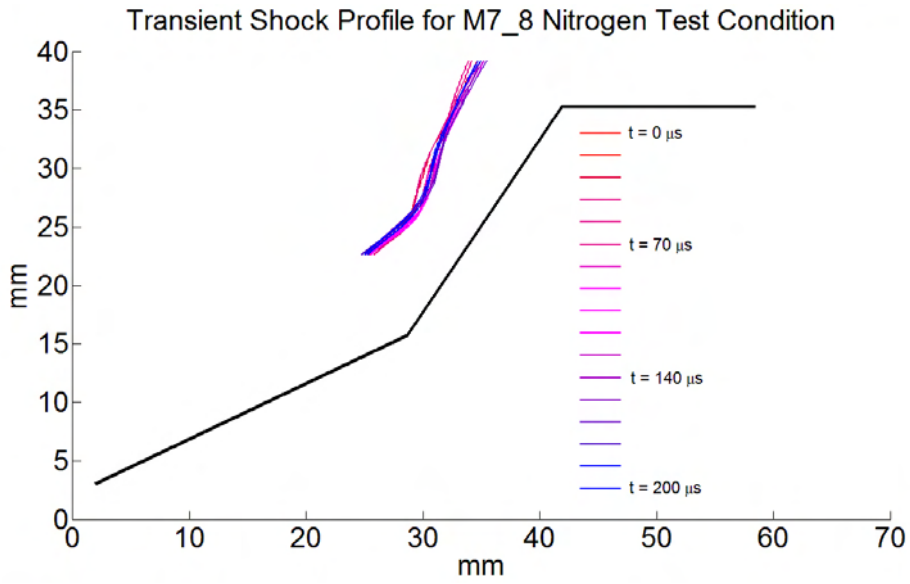

(a)

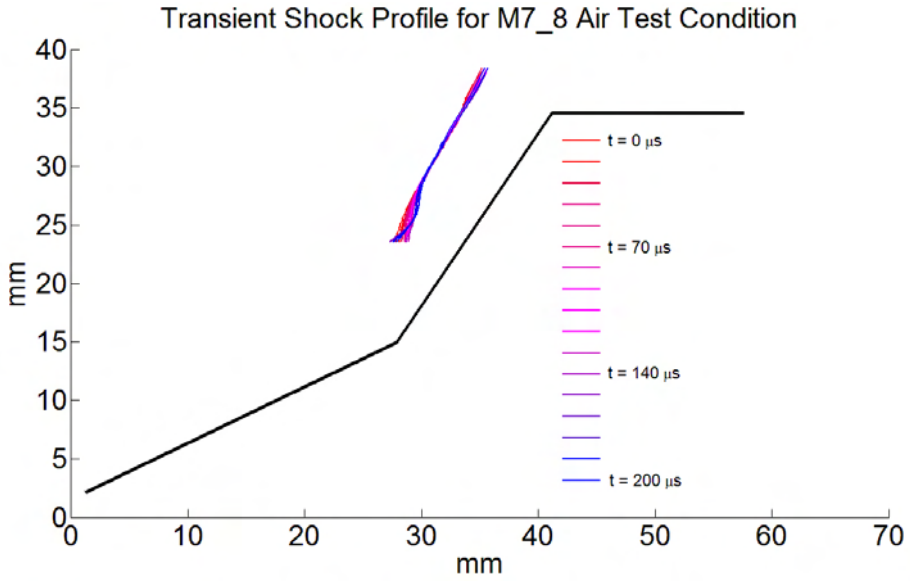

(b)

Figure 5.31: Transient double cone shock profiles are shown for the M7_8 test condition in (a) nitrogen and (b) air. The color scheme transitions from red to blue with increasing time.

Table 5.4: Frequencies from the FFTs of the shock position data from the double cone experiments. Estimates of post-bow shock acoustic wave frequency are also provided. All frequencies are in kHz.

Test Condition	N_2, Experiment			Prediction	Air, Experiment			Prediction
M7_2	12.5	21.9	31.3	95.0	12.5	21.9	31.3	103
M4_3.6	6.25	10.9	15.6	63.7	6.25	10.9	15.6	86.8
M5_4	7.03	14.1	18.8	140	7.03	14.1	18.8	167
M7_8	12.5	21.9	28.1	199	12.5	28.1	-	226

As in the case of the double wedge model, frequency data from the double cone are summarized in Table 5.4. Experimental data are presented for air and nitrogen, as well as acoustic estimates described previously. Measurement error is higher than the for double wedge flow, as some structures are difficult to visualize. Experimental measurements are on the order of the double wedge case. The most noticeable differences in this case are the acoustic estimates. In the current estimates they are approximately an order of magnitude larger than the experimental data. These high frequencies are a result of a smaller model (and thus smaller shock standoffs) and the conical flow physics (where pressure relief aids in reducing shock stand-off compared to a 2-D equivalent). Additionally error is introduced because properties are taken to be those immediately behind the waves. Unlike the 2-D planar case, flow properties are not constant behind conical shocks.

5.3 Conclusions

A set of high speed images has been presented in this section which visualizes the establishment process and established behavior of the four different test conditions on both the double wedge and double cone models in air and nitrogen. Data are collected at an interframe time of 10 μs with an exposure time of either 1 or 10 μs. Image data are presented for the air test conditions for each of the two models. In certain cases nitrogen data are presented along side the air data to illustrate differences between the two test gases. Considerable luminescence can be seen in the data sets which utilize a 10 μs exposure time. This is due to reasonably large post shock temperatures causing atomic and molecular emission. Triple point establishment times from all of the high speed image series are presented for air and nitrogen. These are seen to vary both between each of the four

test conditions, as well as between air and nitrogen tests (for the higher enthalpy test conditions). For a given test condition, in all cases where the difference between the establishment times is beyond the experimental error, the triple point establishment is always longer in nitrogen. This is most likely coupled to the increased shock standoff distance in nitrogen, compared with air.

A series of plots compares scaled triple point establishment times with establishment times from wedge heat transfer data. In general the triple point establishment time agrees well with the heat transfer establishment time near shock impingement/peak heating. This is no surprise, as the triple point dictates the location of shock impingement. Heat transfer establishment is not included on various upstream gauges, as a distinct establishment is not observed in the transient heat transfer traces, similar to Gauge A in Figure 4.1. In the three highest test conditions, several gauges near the hinge location (continuing to gauges further upstream in some cases), are seen to take a significantly longer time to establish than the predicted laminar establishment time (which is shown as a line upstream of the hinge). The middle two enthalpies exhibit a departure from laminar boundary layer behavior in both the high speed imaging as well as the thermocouple traces. It is marked by an increase in heat transfer above the initially observed value. In the case of the highest enthalpy, this is due to the separation zone formed in the vicinity of the hinge. Establishment is marked by a decrease in heat transfer below the initially observed value. In both cases establishment time is increased above the boundary layer establishment prediction. Similar to historical experimental data sets, establishment is found to take 2-8 flow times. This is still in agreement with historical values of 5.5-11 [13] and in disagreement with simulations which indicate establishment takes 100-200 flow times [44, 5].

Edge detection algorithms are used to extract the upstream shock position in each frame of the high speed images (for both the double cone and double wedge models). Plotting each of these surfaces during the test gas visualizes the establishment process as well as the oscillations of the shock structure during the established test time. Differences in profiles, as expected, only become apparent at the two highest enthalpies. A set of experiments unique to this work investigates the effect of various compositions between pure nitrogen and atmospheric air. Established shock shapes

are presented for compositions of nitrogen, 30%, 50%, and 80% of the molar concentration of oxygen in air, and atmopsheric air. As expected, and seen in the single frame schlieren, increasing the oxygen content moves the bow shock downstream. The pure nitrogen, 30%, and 50% mixutures all appear to align on the same profile. The 80% mixture sits approximately half way between these profiles and the atmospheric air profile. Post bow shock equilibrium compositions are presented, and indicate that molecular oxygen is the species which has the largest change after the 50% mixture. Thus, O_2 may be an important species in dictating shock stand off distance, as well as post shock behavior.

Fast Fourier Transforms of the transient profiles are taken to discover any underlying frequencies. These frequencies are compared with predicted frequencies of an acoustic wave traveling between the bow shock front and the shear layer. Agreement for the lowest experimental frequency from the wedge model is found to better than an order of magnitude (as this is the limit of the acoustic predictions). Predictions for the cone model disagree by approximately an order of magnitude. Additionally, these predictions are all above the Nyquist Frequency of the collected data (50 kHz), thus they could not be resolved and may be mapped back into lower frequencies due to aliasing. Thus, observed frequencies for the current cone data may either be a result of an under sampled high frequency signal, or they may have a physical basis and originate from another source (facility noise, shock boundary layer interactions near separation, etc...).

Chapter 6

Post-Shock Emission Spectroscopy Experiments as a Direct Measure of Flow Thermochemistry

In this section, the results from the NO emission spectroscopy results are presented. The NO γ band (A-X transition, $^2\Sigma^+ \rightarrow ^2\Pi_{1/2,3/2}$) is interrogated in the wavelength range of 220-255 nm (near ultra violet). The current experiments are influenced by the work of Sharma [57], where more in depth details of the setup up design can be found. The M7_8 air flow field is interrogated at four points behind the bow shock 6.1 mm above the location of the triple point. Points are taken at 0 mm (on the bow shock), 2 mm, 4 mm, and, 6mm behind the bow shock. These are chosen such that they are spread equally between the bow shock and the shear layer. Vertical location is chosen such that interrogation locations are away from shock interactions and other flow features. Figure 6.1 shows the points with reference to the M7_8 air flow field.

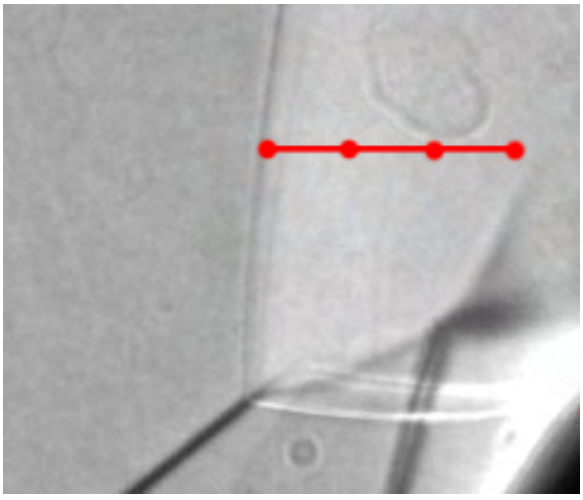

Figure 6.1: The points at which spectroscopic data are collected are shown. Flow is from left to right.

Three data sets are obtained at each location for a total of 12 data sets. A delay of 90 μs is added from the start of the test time to ensure the shock structures have established. Signal is collected

for 110 μs during the remainder of the test time. Raw (uncalibrated) signals from each location are presented in Figure 6.2. Each signal is the collection of binning 20 rows of the signal from the ICCD. Background images are binned in the same region and subtracted from the data.

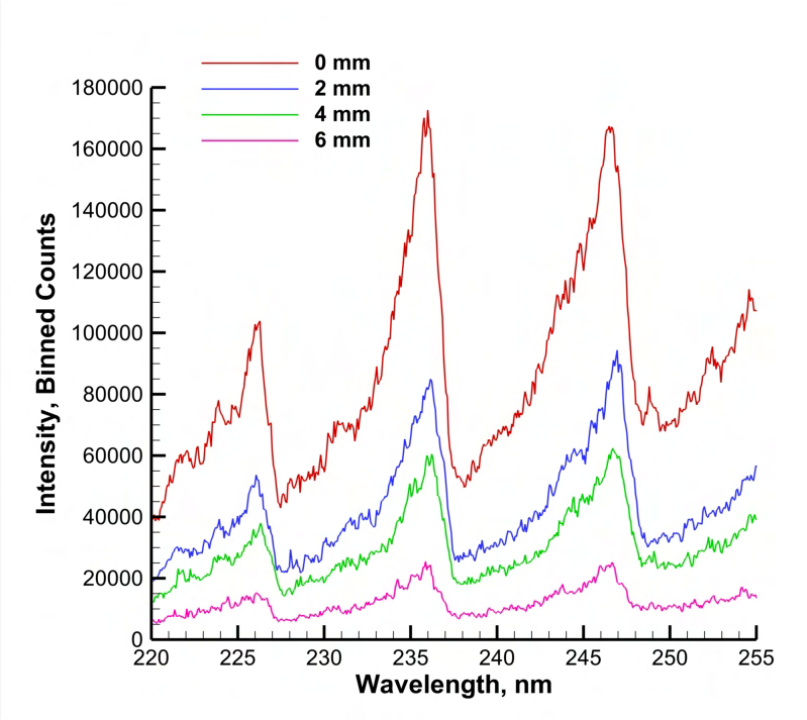

Figure 6.2: Binned spectra are shown for each of the four interrogation locations. 0mm is on the bow shock and positive is down stream of the bow shock.

A distinct decrease in raw signal intensity can be seen in Figure 6.2 as the spatial position moves downstream. Emission signal is positively correlated with both the number of molecules emitting, as well as the temperature. Behind a normal shock the NO levels are expected to increase toward the equilibrium composition [57] with increasing distance. Therefore, it is expected that temperature will decrease due to the overall decrease of signal levels.

After being calibrated for intensity the spectra are fitted to simulated spectra using two different codes. LIFBASE is a commercial (freeware) code which simulates several different bands (one of which is the NO γ band) for various diatomic molecules. A second, in house, code developed by Sharma [57], based on a code developed by Professor Nick Glumac at the University of Illinois, is used as well. LIFBASE is limited to calculating vibrational and rotational quantum numbers of ν_{max}=5 and J_{max}=80. The in house code has increased limits up to vibrational and rotational

quantum numbers of ν_{max}=20 and J_{max}=250. Sharma determined that there was a non-negligible population of the vibrational and rotational states above the LIFBASE limits for temperatures in his expected temperature range (similar to the current temperature range). Both codes use a single temperature for constructing the spectra, thus we assume that NO rotational and vibrational modes are in equilibrium with each other.

Fitting is done in the same method of Sharma, where for each temperature, a scaling factor is computed which minimizes the calculated residual. The residual is defined as the absolute difference between the simulated spectra and the experimental data at a given wavelength. Simulated results are interpolated to match experimental wavelengths. This is done for each temperature (in 20K increments) in the range of 5000K to 10000K. The NO vibrational temperature is taken to be the temperature with the minimum residual. Figure 6.3 shows a fit for the experimental data of Shot 1997 at +4 mm. The calculated temperature is 7280K.

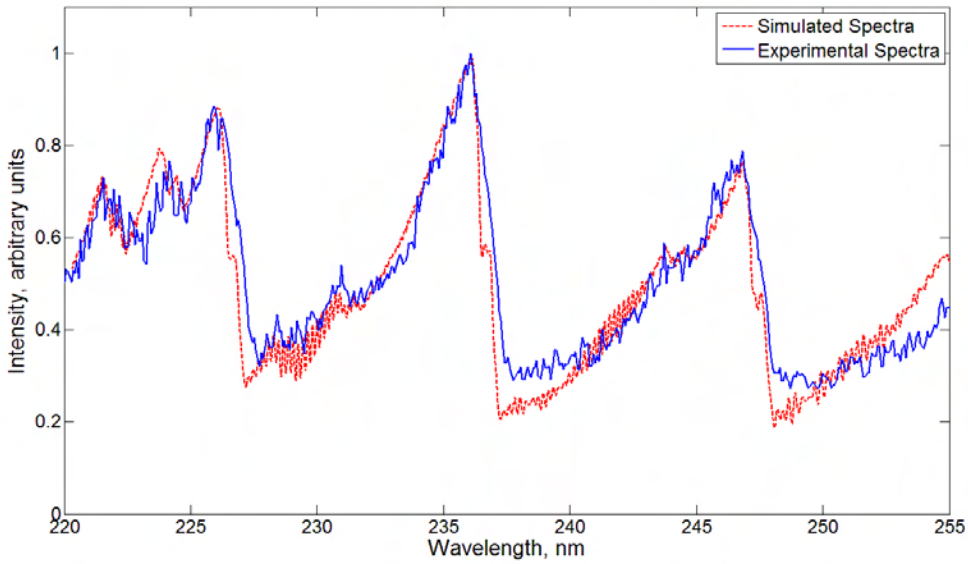

Figure 6.3: The simulated and experimental spectra are shown for the +4 mm position. The simulated temperature is 7280K.

This same procedure is performed with the in house code for each of the 12 (3 for each spatial position) data sets acquired and plotted in Figure 6.4 along with the predicted post-shock frozen temperature (7707 K) and equilibrium temperature (3902 K). Equilibrium temperatures are cal-

Table 6.1: Average NO vibrational temperatures from the fitted experimental data. Temperature fits for both the LIFBASE simulations and in house code simulations are shown along with the standard deviation, σ.

Location, mm	NO Temperature, K			
	LIFBASE		In House Code	
	T	σ	T	σ
0	8573	370	7713	301
2	8300	110	7527	110
4	7968	133	7227	129
6	8360	28	7647	42

culated using Cantera. A summary of the average temperatures at each location is presented in Table 6. The difference between the LIFBASE fitted temperatures and the in house code fitted temperatures are presented in this table.

In Figure 6.4, a distinct relaxation of temperature is observed moving downstream. This agrees with the observations of Sharma [57] for his similar Air-5 test condition. This trend, however, is not followed for the 6mm location. The deviation may be due to two factors. First, at this physical location in the flow, the shear layer is very close to the collection point. The shear layers, like the bow shock have a tendency to oscillate in location about a mean position. Fluctuations of $\sim$0.7 mm in the bow shock position are observed in the high speed imaging data. This, in turn, affects the shear layer location. Changes through the shear layer may affect the signal collected at this location if it enters the collection volume. An increase in temperature due to viscous heating was seen in a study of hypersonic shear layers by Massa and Austin [71]. Viscous dissipation was observed to cause an overshoot of temperature at the shear layer, and similar behavior may be happening in the current flow field. Second, the signal is much weaker than the other data collected (approximately one order of magnitude less than the strongest signal collected). A decrease in the signal to noise ratio may result in errors in the temperature fitting.

LIFBASE over predicts the temperatures by approximately 9-11% of the in house code prediction. As described before, this is due to the quantum number limits of LIFBASE. Non-trivial populations exist in the higher vibrational and rotational states and these must be accounted for to properly simulate the NO spectrum. The 0mm location agrees well with the predicted frozen temperature

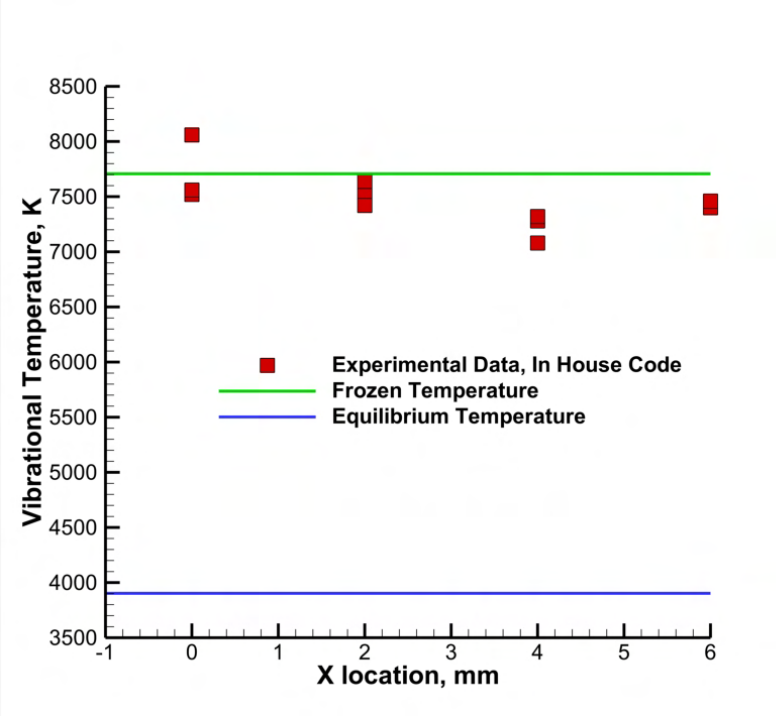

Figure 6.4: The temperature profile for the post shock NO flow field is shown. The bow shock is located at x = 0 mm and x increases moving downstream. Calculated frozen and equilibrium temperatures are shown. This data set is fitted with the in house code.

of 7707 K. Over the first four millimeters, the temperature decreases approximatley 6%. This indicates that this portion of the flow field exhibits a high degree of thermal non-equilibrium. A constant volume chemical kinetics prediction is carried out in Cantera for this test condition using the *reactor()* fucntion (a perfectly stirred reactor sub routine) in the Cantera package. Beginning with the frozen post shock values, the flow takes 72 μs to reach equilibrium, or 37mm of spatial distance (assuming a constant post shock velocity). Although vibrational relaxation and chemical relaxation are different processes, both the data and the prediction suggest that the post shock flow field is in a thermal and chemical non-equilibrium state.

A full error analysis is not considered for the current conditions due to the results of Sharma [57]. He observed that the majority of error (70-97%) is a combination of uncertainty in the location of imaging and Mach reflection location. This is due to a relatively high sensitivity of the NO temperature to streamwise position. Not surprisingly, the sensitivity is highest immediately behind the normal shock, which for the current work has the highest scatter, as seen in Table 6. In Sharma's

study, he was able to calculate the value of $\partial T/\partial x$ (the spatial derivative of NO temperature) from a simulation performed for his test condition. No such simulation exists for the current test condition and there are no current in house capabilities.

6.1 Conclusions

A brief spectroscopic investigation of the NO γ band has been presented. The post bow shock flow field is interrogated at four different locations in the streamwise direction. NO spectra in the wavelength range of 220 nm to 255 nm are obtained and temperature fit using an in house code to obtain vibrational temperatures. The peak temperatures obtained exhibit reasonable agreement with the predicted frozen post shock value and a decay in temperature is seen moving downstream. The furthest downstream point disagrees with this trend, however its vicinity to the shear layer and low signal level may be the cause for the disagreement with the upstream behavior. The experimental data indicate that the entire flowfield between the bow shock and the shear layers is in a state of thermal non-equilibrium. A constant volume chemical kinetics prediction also suggests that the flowfield is in a state of chemical non-equilibrium.

Chapter 7

Conclusions and Future Work

7.1 Conclusions

In this work, the flow physics of double wedge and double cone models in a hypervelocity environment have been investigated. A novel test campaign is created which spans the operable range of the Hypervelocity Expansion Tube. Freestream gas chemistry is varied between air and nitrogen to examine the effects of oxygen on the flowfield. In the highest enthalpy test condition, a brief study of mixtures intermediate to pure nitrogen and atmospheric air is carried out. To the author's knowledge, this is the first such set of tests ever conducted. Four different diagnostic techniques are used to extract information from the flow field: single frame high resolution schlieren photography, fast response coaxial thermocouple heat transfer gauges, high speed schlieren imaging, and nitric oxide emission spectroscopy. These four methods allow information to be gathered about the inviscid flow features, the viscous flow features, and the flow field thermochemistry.

Schlieren data are visually analyzed, and differences in the two test gases are seen at enthalpies as low as 3.6 MJ/kg. The higher Reynolds number data experience a boundary layer which departs from laminar behavior. Separation length scaling has been investigated, and a theoretical scaling parameter is applied to data in both air and nitrogen. The flow through the shocks is solved for with an equilibrium solver, and the current methods are verified by using a test condition similar to historical data with the double wedge model. In the case of the double cone, two types of interactions are seen: a typical laminar interaction, and a new interaction where the dividing streamline intersects the reattachment shock at an intermediate point. Double cone data are then scaled by solving for flow parameters immediately behind the conical shocks. Using this assumption the double cone

separation length data are seen to scale well across all test conditions, having a separation zone size that is less sensitive to pressure than the double wedge. The state of the incoming boundary layer is observed to have a significant effect on the scaled separation length data.

Heat transfer profiles on the wedge model are presented and compared with the schlieren images to assess the effects of different flow features, as well as gas composition, on heat transfer rates. In nearly all test conditions, there is an associated establishment time with the heat transfer traces. Averages are taken through this established test time. In the lowest enthalpy case, there is no appreciable difference observed for the heat transfer profiles in nitrogen and air. As expected, increasing differences in the profiles are seen as the enthalpy increases. A departure from laminar heating behavior for the two highest Reynolds numbers is seen, and is in agreement with observation from the schlieren images. Air heat transfer rates are always higher than for nitrogen when chemistry effects are present. This is in agreement with theoretical models for the behavior of the boundary layer when exothermic reactions are present [14] and experimental data [28]. The largest discrepancies generally occur on the aft wedge near the region of shock impingement and can differ greatly. In the M7_8 test condition the increase in peak heating for air over nitrogen is $\sim$50%. There is considerable scatter in these regions which is most likely due to variation in the flow field through shot to shot variation. Spatial heat transfer gradients are large, and thus small changes in shock impingement location can potentially alter heat transfer profiles. Unsteadiness may contribute to scatter in the data as aft wedge fluctuations are on the order of 10-20%.

A series of high speed images is collected over both the double wedge and double cone models. These give a direct measurement of triple point establishment times in all test conditions. These establishment times are compared with the expected establishment time from laminar flat plate predictions on the forward wedge, and the establishment times from select heat transfer gauges. The establishment time of the triple point (via high speed imaging) is representative of the inviscid time scales, while the establishment of the heat transfer (via surface heat transfer gauges) is representative of the viscous time scales. Heat transfer establishment times near shock impingement roughly correspond with triple point establishment times. Viscous effects (transition and separation zone

formation) are seen to increase the establishment time on the forward wedge above the predicted laminar flat plate establishment. Current establishment times (2-8 flow times) agree with historical experimental establishment times (5.5-11 flow times), and are in disagreement with predictions from numerical simulations (100-150 flow times). Currently a possible explanation for this disagreement is a loss in temporal accuracy due to the time integration scheme of the numerical simulations. Another potential cause for disagreement is that in the current experiments, the accelerator gas generates a flow over the model preceding the test gas. Thus at the start of the test gas there is a a flow which has been in the establishment process. More than likely, this would not account for the order of magnitude difference between experiments and the simulations.

Other transient features of the flow field are also revealed. Shock oscillation is observed and quantified using boundary tracking algorithms in the high speed image series. In each image series the location of the oblique shock and bow shock are tracked and recorded. These are plotted to aid in the visualization of the establishment process, as well as the established behavior of the shock structure. Fast Fourier Transforms are taken of a single vertical location of the bow shock location. Oscillation frequency is recorded and compared to predictions from acoustic wave theory. Agreement is reasonable in the double wedge case, however in the double cone case, predictions overestimate experimental values. This may be due to expected frequencies being above the Nyquist frequency of the experimental data. There is potential for these high frequencies to be mapped back into the the lower frequencies.

Lastly, the investigation of freestream compositions intermediate to pure nitrogen and atmospheric air is carried out. Compositions of 30%, 50%, and 80% of the molar concentration of oxygen in atmopsheric air are considered. The pure nitrogen, 30%, and 50% compositions are observed to lie on top of each other. The 80% composition lies approximately halfway between these cases and the atmospheric air case. Equilibrium calculations suggest that the concentration of molecular oxygen may have a role in shock standoff distance at these compositions.

The final part of this work aimed to investigate the ultraviolet nitric oxygen emission signal behind the bow shock in the highest enthalpy test condition. Four spatial locations are interrogated,

and at each of these locations emission data are calibrated and temperature fit to yield NO vibrational temperatures. As expected, a relaxation of temperature is seen behind the bow shock. The temperature profile does suggest that the flow is in thermal non-equilibrium from post-bow shock to the shear layer. A chemical kinetics simulation is carried out which also estimates that the flow field is in chemical non-equilibrium. Although not identical, these two phenomena are coupled, and both indicate that the state of the post shock flow field is in thermochemical non-equilibrium.

Chemistry effects are present in various parts of the flow field. These effects become more prominent with increasing flow enthalpy. As expected, they are strongest in regions of high temperature, including: post-bow shock regions, and areas of shock boundary layer interaction. Bow shocks are observed to have a larger standoff distance with nitrogen as a test gas, compared to air. Additionally, the establishment time for the nitrogen triple point is larger than that for air. Near regions of peak heating, air exhibits augmented heating compared to nitrogen. Boundary layers in dissociating flow fields exhibit thinning (as explained in Chapter 1) which leads to larger gradients at the wall, and in turn, increased wall heat transfer rates. A second potential cause of augmented heating is recombination at the wall. The recombination of dissociated air is an exothermic reaction, and can generate additional heat flux to the wall.

This work has resulted in several contributions to the existing body of literature. Coupling between the fluid mechanics and chemistry has been observed through various diagnostics, where direct measurements of the differences between air and nitrogen are made. An extensive investigation of flow establishment and flow steadiness has been performed, looking at the transient nature of various flow field features. Lastly, the database of hypersonic shock/boundary layer interactions has been extended with a comprehensive set of schlieren images, heat transfer data, high speed imaging, and emission spectroscopy data.

7.2 Future Work

The continued campaign of this work involves executing a series of test conditions which have been designed to mimic several test conditions used in the historic literature. The four diagnostics applied

here will be applied at these new test conditions. Comparisons between historic simulations and experimental data sets can then be made.

Spectroscopic measurements should be extended to other test conditions and species. The post-bow shock flow field M5_4 test condition may be able to be interrogated, as NO is expected behind the shock. While temperatures are lower than the M7_8 test condition, the established test time is approximately twice as long, and post shock NO number densities are estimated to be ∼8 times higher (due to a higher flow density). This results in 16 times the amount of emission due to time integration and number density and may be able to counter the reduced temperature. Additionally, a method for investigating the nitrogen flow field should be established. Options include obtaining emission data from atomic nitrogen (which is expected behind the bow shock) or the molecular nitrogen ion (N_2^+) which has been detected at a similar test condition [57].

The Cordin 535 rotating mirror camera which has recently been acquired will be able to collect extremely high speed/high resolution imaging data. Detailed, time-resolved images can be obtained in the vicinity of transient flow features such as: triple point establishment, boundary layer transition, separation zone establishment, shear layer behavior, and shock impingement.

Currently, computational efforts are underway at the Air Force Research Lab to simulate the M7_2 test condition over the double wedge. The computations use a Monte Carlo method which simulates particle packets, rather than assuming the fluid is a continuum. Due to immense computational load, the freestream density cannot be matched and is taken 20 times less than the M7_2 condition. In its current state, the HET cannot produce a flow with such a low density. One option to compare simulation and experiment is to match the Knudsen numbers. This would require a model $1/20^{th}$ the scale, or a combination of reduced flow density and reduced model size. Diagnostics would need to be adjusted to capture data over such a small model.

The double cone model has only been investigated with the single frame and high speed schlieren imaging. An effort to get heat transfer data over the model would be beneficial. Due to the small model size, this is not a trivial effort, and must be properly planned. Thermocouple gauges may be able to be instrumented on the model; however, due to their large size, the number may be severely

limited. Another potential option is creating a MACOR model (or a steel model with a MACOR insert) and using platinum thin film gauges. These gauges (as well as MACOR) are extremely delicate and may only survive for a limited number of tests.

There is currently a gap in the literature examining the effect of freestream chemistry on the location of peak heating. Nearly all studies generally use enthalpy as the parameter that is varied. Studies which do examine both air and nitrogen do not maintain constant freestream parameters. A comprehensive set of simulations of the current test conditions would greatly aid in determining the effect of freestream chemistry on the peak heating location and magnitude.

Finally, this study considered several combinations of models and test conditions which generated transitional/turbulent boundary layer behavior. The current interest for researchers performing simulations and generating models is purely laminar interactions. Laminar boundary layer/separation behavior is much more feasible for simulations, and eliminates any ambiguity due to turbulence modeling. Obtaining this data is possible via model size reduction, reducing freestream unit Reynolds number, or a combination of both.

Appendix A

Table of Experimental Tests

Table A.1: All experiments executed during this work are listed.

Shot #	Condition	Gas	Model	Diagnostic	Notes
879	M7_8	Air	Cone	Single Frame Schlieren	
880	M7_8	Air	Cone	Single Frame Schlieren	
881	M7_8	Air	Cone	Single Frame Schlieren	
882	M7_8	Air	Cone	Single Frame Schlieren	
883	M7_8	Air	Cone	Single Frame Schlieren	
884	M7_8	Air	Cone	Single Frame Schlieren	
902	M5_4	Air	Cone	Single Frame Schlieren	
903	M5_4	Air	Cone	Single Frame Schlieren	
904	M7_8	Air	Cone	Single Frame Schlieren	
906	M7_2	Air	Cone	Single Frame Schlieren	
907	M7_2	Air	Cone	Single Frame Schlieren	
915	M5_4	N2	Cone	Single Frame Schlieren	
916	M5_4	N2	Cone	Single Frame Schlieren	
917	M7_8	N2	Cone	Single Frame Schlieren	
918	M7_8	N2	Cone	Single Frame Schlieren	
919	M7_8	N2	Cone	Single Frame Schlieren	
920	M7_2	N2	Cone	Single Frame Schlieren	
922	M7_2	N2	Cone	Single Frame Schlieren	
923	M7_2	N2	Cone	Single Frame Schlieren	
942	M5_4	Air	Cone	Single Frame Schlieren	
943	M5_4	Air	Cone	Single Frame Schlieren	
946	M4_3.6	Air	Cone	Single Frame Schlieren	
947	M4_3.6	Air	Cone	Single Frame Schlieren	
953	M4_3.6	Air	Cone	Single Frame Schlieren	
954	M4_3.6	N2	Cone	Single Frame Schlieren	
955	M4_3.6	N2	Cone	Single Frame Schlieren	
956	M7_2	Air	Cone	Single Frame Schlieren	
957	M7_2	Air	Cone	Single Frame Schlieren	
967	M5_4	Air	Wedge	Single Frame Schlieren	
968	M5_4	Air	Wedge	Single Frame Schlieren	
969	M5_4	Air	Wedge	Single Frame Schlieren	

970	M5_4	N2	Wedge	Single Frame Schlieren	
971	M5_4	N2	Wedge	Single Frame Schlieren	
972	M5_4	N2	Wedge	Single Frame Schlieren	
973	M7_8	Air	Wedge	Single Frame Schlieren	
974	M7_8	Air	Wedge	Single Frame Schlieren	
975	M7_8	Air	Wedge	Single Frame Schlieren	
976	M7_8	N2	Wedge	Single Frame Schlieren	
977	M7_8	N2	Wedge	Single Frame Schlieren	
978	M7_8	N2	Wedge	Single Frame Schlieren	
981	M7_2	Air	Wedge	Single Frame Schlieren	
982	M7_2	Air	Wedge	Single Frame Schlieren	
983	M7_2	Air	Wedge	Single Frame Schlieren	
984	M7_2	N2	Wedge	Single Frame Schlieren	
985	M7_2	N2	Wedge	Single Frame Schlieren	
986	M7_2	N2	Wedge	Single Frame Schlieren	
987	M4_3.6	Air	Wedge	Single Frame Schlieren	
988	M4_3.6	Air	Wedge	Single Frame Schlieren	
989	M4_3.6	Air	Wedge	Single Frame Schlieren	
990	M4_3.6	N2	Wedge	Single Frame Schlieren	
991	M4_3.6	N2	Wedge	Single Frame Schlieren	
992	M4_3.6	N2	Wedge	Single Frame Schlieren	
993	M4_3.6	N2	Wedge	Single Frame Schlieren	
994	M4_3.6	N2	Wedge	Single Frame Schlieren	
995	M5_4	AIr	Wedge	Single Frame Schlieren	
996	M5_4	N2	Wedge	Single Frame Schlieren	
1005	M5_4	Air	Wedge	Thermocouples	Testing
1006	M5_4	Air	Wedge	Thermocouples	Testing
1007	M5_4	Air	Wedge	Thermocouples	Testing
1008	M5_4	Air	Wedge	Thermocouples	Testing
1009	M5_4	Air	Wedge	Thermocouples	Testing
1010	M5_4	Air	Wedge	Thermocouples	
1011	M5_4	Air	Wedge	Thermocouples	
1012	M5_4	Air	Wedge	Thermocouples	
1014	M5_4	Air	Wedge	Thermocouples	
1015	M5_4	Air	Wedge	Thermocouples	
1016	M5_4	Air	Wedge	Thermocouples	
1017	M5_4	Air	Wedge	Thermocouples	
1018	M5_4	Air	Wedge	Thermocouples	
1019	M5_4	Air	Wedge	Thermocouples	
1020	M5_4	Air	Wedge	Thermocouples	
1021	M5_4	Air	Wedge	Thermocouples	
1024	M5_4	N2	Wedge	Thermocouples	
1026	M5_4	N2	Wedge	Thermocouples	

1027	M5_4	N2	Wedge	Thermocouples
1028	M5_4	N2	Wedge	Thermocouples
1029	M5_4	N2	Wedge	Thermocouples
1030	M5_4	N2	Wedge	Thermocouples
1031	M7_8	Air	Wedge	Thermocouples
1032	M7_8	Air	Wedge	Thermocouples
1033	M7_8	Air	Wedge	Thermocouples
1034	M7_8	Air	Wedge	Thermocouples
1036	M7_8	Air	Wedge	Thermocouples
1037	M7_8	Air	Wedge	Thermocouples
1038	M7_8	Air	Wedge	Thermocouples
1043	M7_8	N2	Wedge	Thermocouples
1044	M7_8	N2	Wedge	Thermocouples
1045	M7_8	N2	Wedge	Thermocouples
1046	M7_8	N2	Wedge	Thermocouples
1047	M7_8	N2	Wedge	Thermocouples
1048	M7_8	N2	Wedge	Thermocouples
1049	M7_8	N2	Wedge	Thermocouples
1050	M7_8	N2	Wedge	Thermocouples
1053	M7_8	Air	Wedge	Thermocouples
1054	M7_8	Air	Wedge	Thermocouples
1055	M7_8	Air	Wedge	Thermocouples
1056	M7_8	N2	Wedge	Thermocouples
1058	M7_8	N2	Wedge	Thermocouples
1059	M7_8	N2	Wedge	Thermocouples
1067	M7_2	Air	Wedge	Thermocouples
1068	M7_2	Air	Wedge	Thermocouples
1069	M7_2	Air	Wedge	Thermocouples
1070	M7_2	Air	Wedge	Thermocouples
1071	M7_2	Air	Wedge	Thermocouples
1072	M7_2	Air	Wedge	Thermocouples
1078	M7_2	N2	Wedge	Thermocouples
1079	M7_2	N2	Wedge	Thermocouples
1080	M7_2	N2	Wedge	Thermocouples
1081	M7_2	N2	Wedge	Thermocouples
1082	M7_2	N2	Wedge	Thermocouples
1083	M7_2	N2	Wedge	Thermocouples
1084	M4_3.6	Air	Wedge	Thermocouples
1085	M4_3.6	Air	Wedge	Thermocouples
1086	M4_3.6	Air	Wedge	Thermocouples
1092	M4_3.6	Air	Wedge	Thermocouples
1093	M4_3.6	Air	Wedge	Thermocouples
1094	M4_3.6	Air	Wedge	Thermocouples

1095	M4_3.6	N2	Wedge	Thermocouples	
1096	M4_3.6	N2	Wedge	Thermocouples	
1097	M4_3.6	N2	Wedge	Thermocouples	
1098	M4_3.6	N2	Wedge	Thermocouples	
1099	M4_3.6	N2	Wedge	Thermocouples	
1100	M4_3.6	N2	Wedge	Thermocouples	
1103	M5_4	Air	Wedge	High Speed, SA-5	100 kHz, 10 μs exp.
1104	M5_4	Air	Wedge	High Speed, SA-5	100 kHz, 10 μs exp.
1105	M5_4	N2	Wedge	High Speed, SA-5	100 kHz, 10 μs exp.
1106	M5_4	N2	Wedge	High Speed, SA-5	100 kHz, 10 μs exp.
1107	M7_8	Air	Wedge	High Speed, SA-5	100 kHz, 10 μs exp.
1108	M7_8	Air	Wedge	High Speed, SA-5	100 kHz, 10 μs exp.
1109	M7_8	N2	Wedge	High Speed, SA-5	100 kHz, 10 μs exp.
1110	M7_8	N2	Wedge	High Speed, SA-5	100 kHz, 10 μs exp.
1111	M5_4	Air	Cone	High Speed, SA-5	100 kHz, 10 μs exp.
1112	M5_4	Air	Cone	High Speed, SA-5	75 kHz, 10 μs exp.
1113	M5_4	N2	Cone	High Speed, SA-5	75 kHz, 10 μs exp.
1114	M5_4	N2	Cone	High Speed, SA-5	100 kHz, 10 μs exp.
1117	M7_8	Air	Cone	High Speed, SA-5	100 kHz, 10 μs exp.
1118	M7_8	Air	Cone	High Speed, SA-5	75 kHz, 10 μs exp.
1119	M7_8	N2	Cone	High Speed, SA-5	75 kHz, 10 μs exp.
1120	M7_8	N2	Cone	High Speed, SA-5	100 kHz, 10 μs exp.
1140	M7_2	Air	Cone	High Speed, SA-5	75 kHz, 10 μs exp.
1143	M7_2	Air	Cone	High Speed, SA-5	75 kHz, 10 μs exp.
1144	M7_2	N2	Cone	High Speed, SA-5	75 kHz, 10 μs exp.
1145	M7_2	Air	Cone	High Speed, SA-5	100 kHz, 10 μs exp.
1147	M7_2	N2	Cone	High Speed, SA-5	100 kHz, 10 μs exp.
1148	M4_3.6	Air	Cone	High Speed, SA-5	100 kHz, 10 μs exp.
1149	M4_3.6	N2	Cone	High Speed, SA-5	100 kHz, 10 μs exp.
1153	M4_3.6	Air	Cone	High Speed, SA-5	75 kHz, 10 μs exp.
1154	M4_3.6	N2	Cone	High Speed, SA-5	75 kHz, 10 μs exp.
1156	M5_4	Air	Cone	High Speed, SA-5	100 kHz, 10 μs exp.
1157	M5_4	N2	Cone	High Speed, SA-5	100 kHz, 10 μs exp.
1158	M7_8	Air	Cone	High Speed, SA-5	100 kHz, 10 μs exp.
1159	M7_8	N2	Cone	High Speed, SA-5	100 kHz, 10 μs exp.
1160	M7_2	Air	Wedge	High Speed, SA-5	100 kHz, 10 μs exp.
1162	M7_2	N2	Wedge	High Speed, SA-5	100 kHz, 10 μs exp.
1163	M5_4	Air	Wedge	High Speed, SA-5	100 kHz, 10 μs exp.
1164	M5_4	N2	Wedge	High Speed, SA-5	100 kHz, 10 μs exp.
1165	M7_8	Air	Wedge	High Speed, SA-5	100 kHz, 10 μs exp.
1166	M7_8	N2	Wedge	High Speed, SA-5	100 kHz, 10 μs exp.
1167	M4_3.6	Air	Wedge	High Speed, SA-5	100 kHz, 10 μs exp.
1168	M4_3.6	Air	Wedge	High Speed, SA-5	100 kHz, 10 μs exp.

1169	M4_3.6	N2	Wedge	High Speed, SA-5	100 kHz, 10 μs exp.
1170	M4_3.6	N2	Wedge	High Speed, SA-5	100 kHz, 10 μs exp.
1171	M7_8	30%	Wedge	High Speed, SA-5	100 kHz, 10 μs exp.
1172	M7_8	30%	Wedge	High Speed, SA-5	100 kHz, 10 μs exp.
1173	M7_8	30%	Wedge	High Speed, SA-5	100 kHz, 10 μs exp.
1174	M7_8	80%	Wedge	High Speed, SA-5	100 kHz, 10 μs exp.
1175	M7_8	80%	Wedge	High Speed, SA-5	100 kHz, 10 μs exp.
1176	M7_8	50%	Wedge	High Speed, SA-5	100 kHz, 10 μs exp.
1177	M7_8	50%	Wedge	High Speed, SA-5	100 kHz, 10 μs exp.
1191	M7_8	Air	Wedge	NO Emission Spec.	2 mm, 80 μs exp
1192	M7_8	Air	Wedge	NO Emission Spec.	2 mm, 110 μs exp
1193	M7_8	Air	Wedge	NO Emission Spec.	2 mm, 110 μs exp
1194	M7_8	Air	Wedge	NO Emission Spec.	2 mm, 110 μs exp
1195	M7_8	Air	Wedge	NO Emission Spec.	2 mm, 110 μs exp
1196	M7_8	Air	Wedge	NO Emission Spec.	4 mm, 110 μs exp
1197	M7_8	Air	Wedge	NO Emission Spec.	4 mm, 110 μs exp
1198	M7_8	Air	Wedge	NO Emission Spec.	4 mm, 110 μs exp
1199	M7_8	Air	Wedge	NO Emission Spec.	6 mm, 110 μs exp
1200	M7_8	Air	Wedge	NO Emission Spec.	6 mm, 110 μs exp
1201	M7_8	Air	Wedge	NO Emission Spec.	6 mm, 110 μs exp
1202	M7_8	Air	Wedge	NO Emission Spec.	0 mm, 110 μs exp
1203	M7_8	Air	Wedge	NO Emission Spec.	0 mm, 110 μs exp
1204	M7_8	Air	Wedge	NO Emission Spec.	0 mm, 110 μs exp

Appendix B

Machine Drawings

B.1 Double Cone Drawings

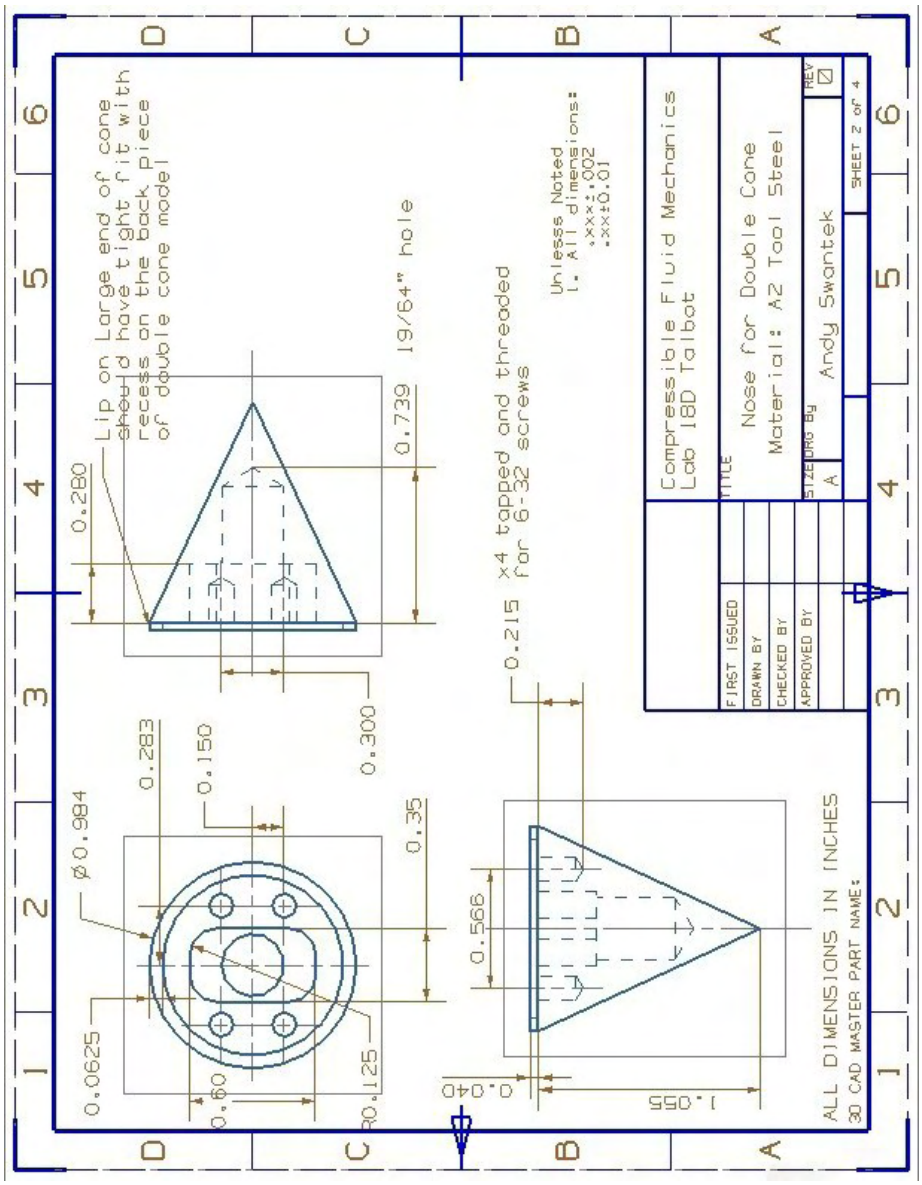

Figure B.1: Machine drawings for the forward piece of the double cone model.

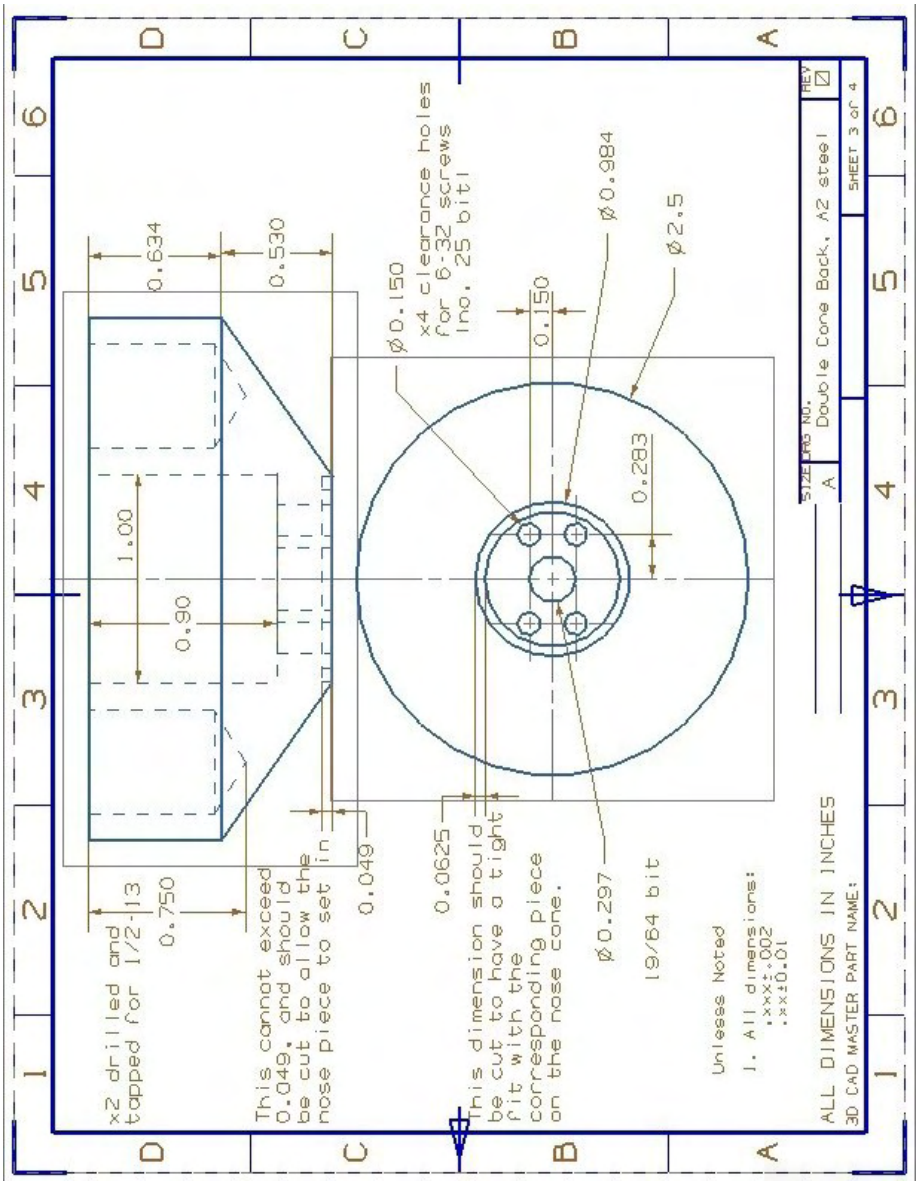

Figure B.2: Machine drawings for the aft piece of the double cone model.

B.2 Double Wedge Drawings

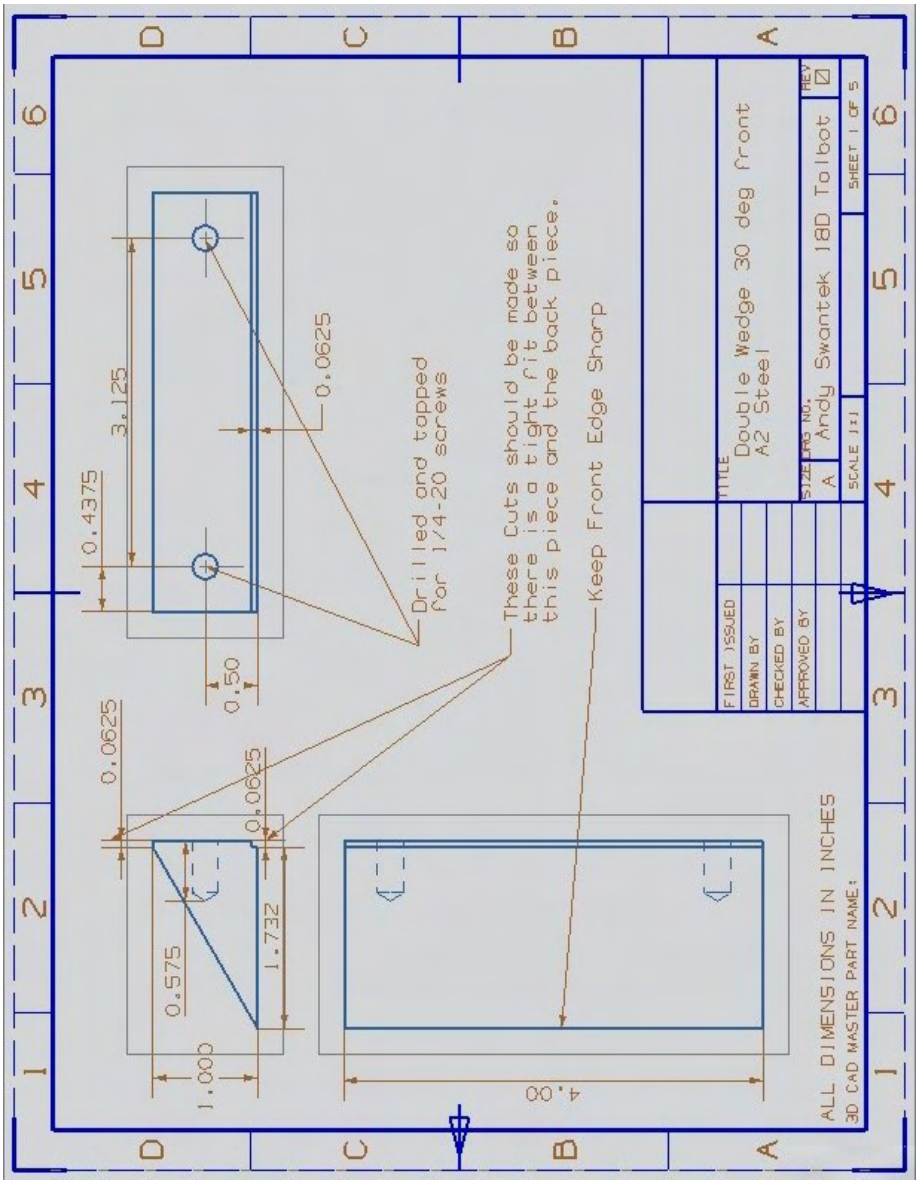

Figure B.3: Machine drawings for the forward piece of the double wedge model.

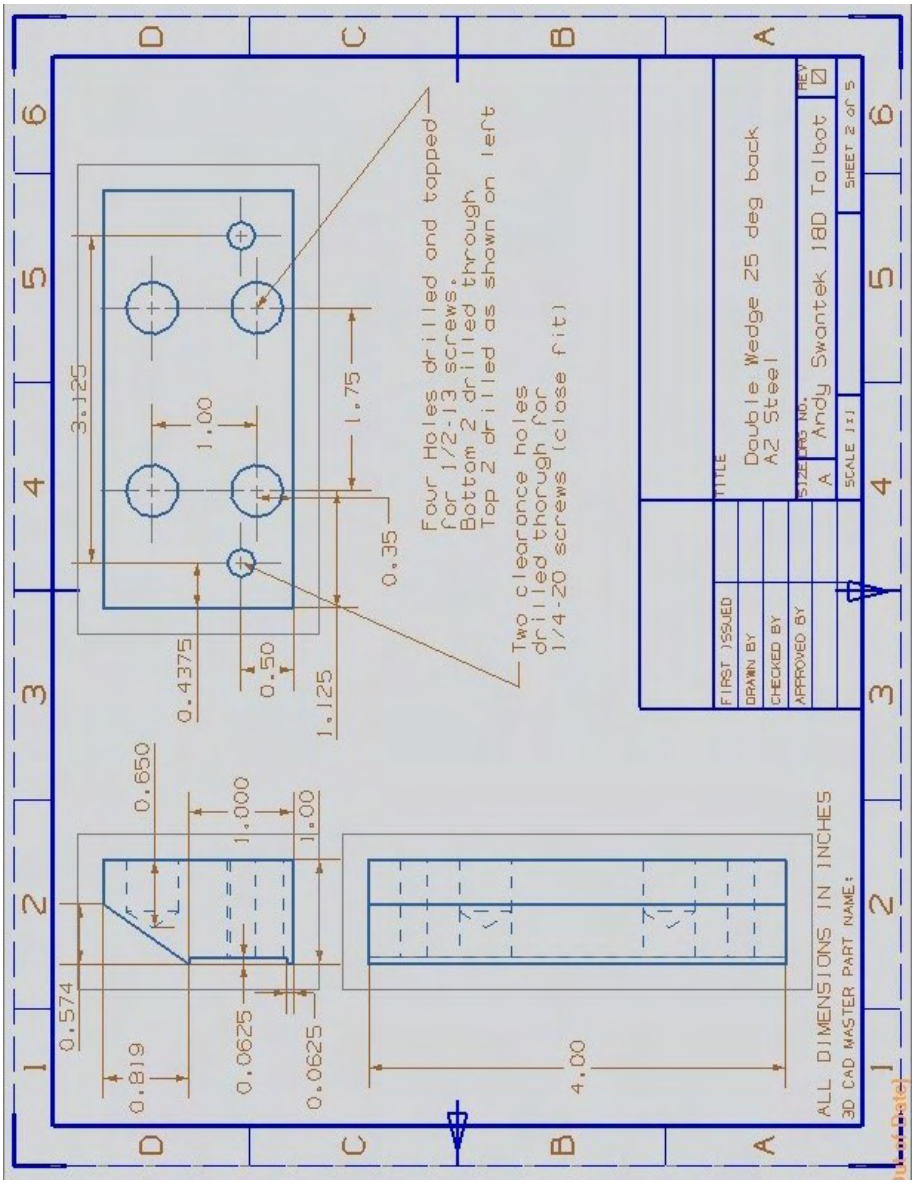

Figure B.4: Machine drawings for the aft piece of the double wedge model.

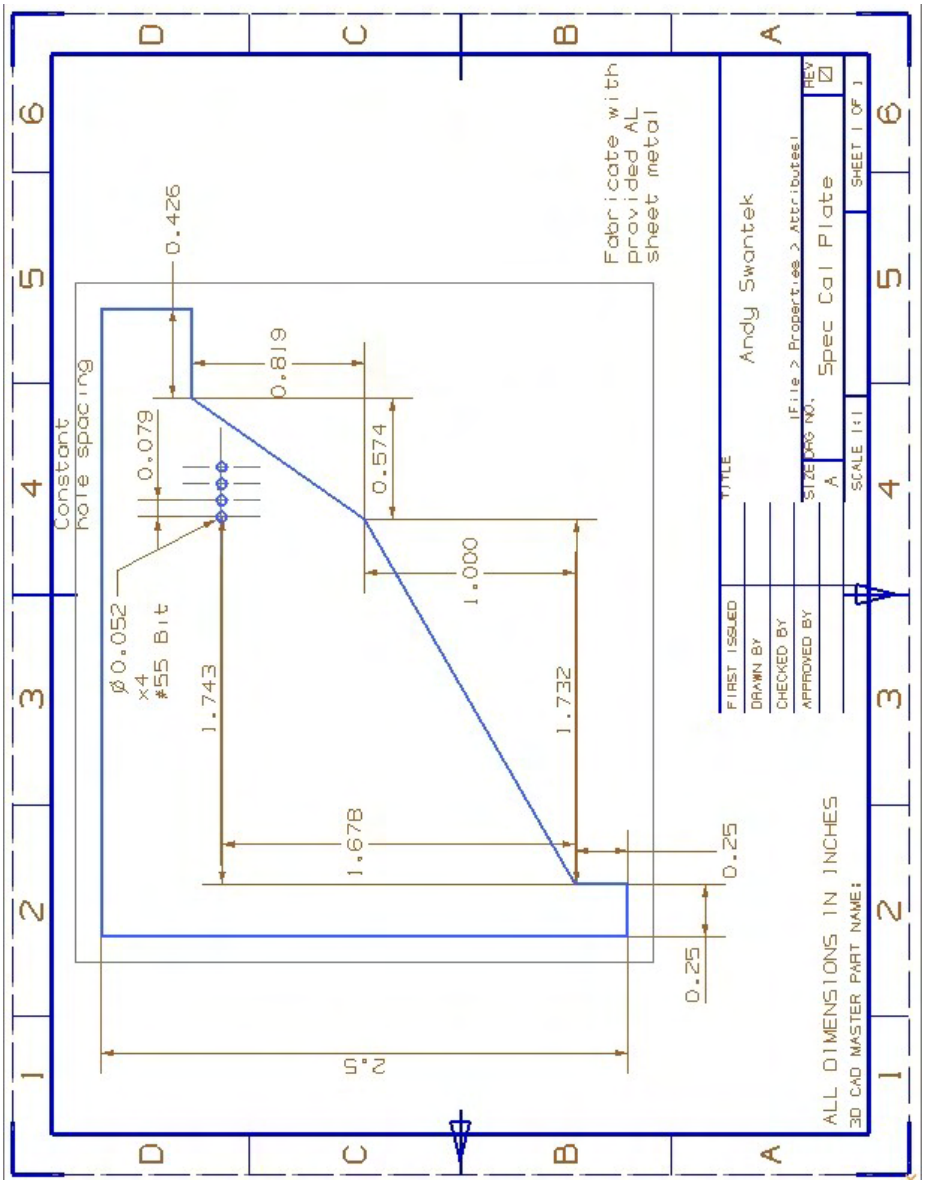

Figure B.5: Machine drawings for the aft piece of the double wedge model.

Appendix C

Method of Characteristics Predictions

The method of characteristics (MOC) is a useful tool for analyzing two-dimensional flows, especially those in which characteristics will inherently interact. In an effort to understand the wave patterns from the surfaces investigated, a two dimensional MOC code is written to predict wave behavior as well as shock location and shape. The code is entirely inviscid, as such, no effects of the boundary layer are considered. This section outlines two different methods for calculating the shock location and shape: an insentropic method, and a non-isentropic method. Originally written for the models of Flaherty [75], it can be used in future studies of double wedge models with curvature.

C.1 State calculations

The code reads in a data file containing the x and y locations of the surface of the model, and takes user inputs for the freestream Mach number, temperature and pressure. Surface Mach number, pressure, and temperature are solved for using isentropic turning theory. The relative turning angle of each segment is numerically calculated, and by implicitly solving the Prandtl-Meyer function (Equation C.1) with a Newton-Rhapson Method, the surface Mach number is obtained.

$$\nu = \left(\frac{\gamma+1}{\gamma-1}\right)^{1/2} tan^{-1}\left[\frac{\gamma-1}{\gamma+1}\left(M^2-1\right)\right]^{1/2} - tan^{-1}\left(M^2-1\right)^{1/2} \tag{C.1}$$

ν is the Prantl-Meyer angle, γ is the ratio of specific heats, and M is the Mach number. With the Mach number being known, the isentropic flow relations can thus be used to calculate the corresponding pressures, temperatures, and velocities. Each ramp is divided up into 10,000 equally spaced points to create adequate resolution of the local turning angle.

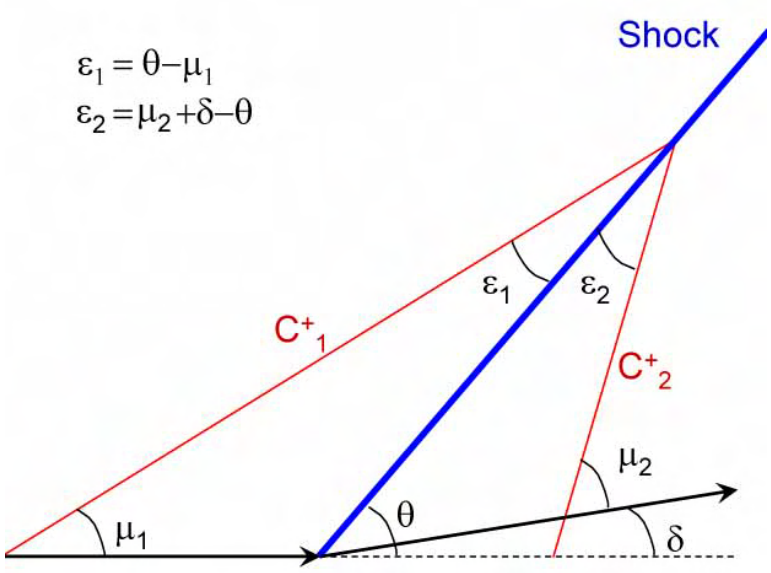

Figure C.1: A depiction of the interaction of two C^+ characteristics, which form a shock. Flow is from left to right.

C.2 Methodology

C.2.1 Isentropic

Along a curved ramp, C^+ characteristics will be the mechanism for turning the flow and increasing the temperature and pressure. At the intersection of the first two body C^+ characteristics a shock will necessarily form. Thompson [76] outlines a procedure to predict the shape of this location for weak waves. Figure C.1 illustrates two C^+ characteristics interacting.

Thompson shows that for weak waves (i.e. small turning angles) that $\epsilon_1 \approx \epsilon_2$ and that the error involved in this approximation is proportional to the square of the turning angle, δ^2. We thus implement this procedure in MATLAB and solve the flow field, progressing downstream. The shock will be formed by the intersection of the C^+ characteristics from the freestream and the C^+ characteristics from the body. The entire shock structure is found by extending the line from the previous characteristic interaction until it intersects the next C^+ characteristic from the body. A schematic for this is shown in Figure C.2.

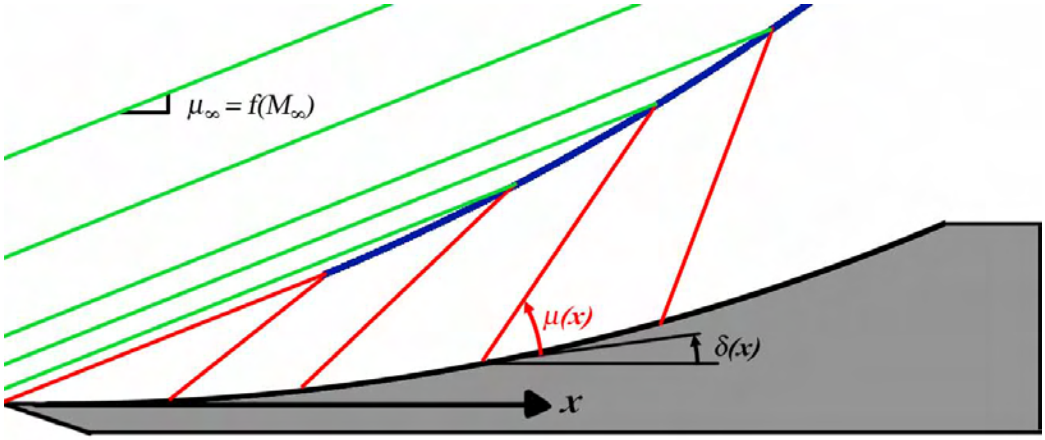

Figure C.2: A schematic of the flowfield and the different C^+ characteristics in it. Flow is from left to right. Green characteristics are from the freestream, red characteristics are from the body. The blue line is the shock wave.

C.2.2 Non-isentropic

The procedure is nearly the same for that of the isentropic case, however, the shockwave angle is solved for by implementing the oblique shock relation given by Equation C.2.

$$tan\left(\delta\right) = 2cot\left(\theta\right)\left(\frac{M_1^2 sin^2\theta - 1}{M_1^2\left(\gamma + cos2\theta\right) + 2}\right) \tag{C.2}$$

The turning angle used is that of the absolute turning angle with respect to the freestream. Physically this assumption means that information from the surface is transferred along the characteristic until it intersects the shock. Figures C.3(a) and (b) illustrate deviations resulting from the isentropic assumption versus the non-isentropic assumption.

Figures C.3(a) and (b) clearly indicate that non-isentropic wave behavior becomes important for reasonably small turning angles. Thus, we expect to observe differences in the calculation of the shock shape between the two different methods.

C.3 Ramp results

Figures C.4(a) and (b) show the resultant shock shape over a curved ramp model for Mach number of 5.12 and 7.42 respectively. The surface is shown by the bold black line, characteristics from the

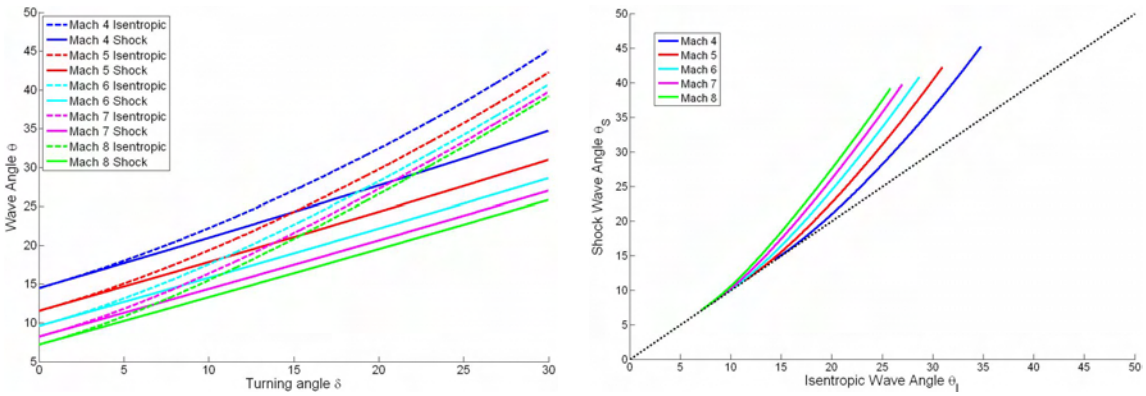

(a) (b)

Figure C.3: (a) For varying Mach numbers typical of HET operation the isentropic wave angle, θ_I, and the non-isentropic wave angle, θ_S, are plotted as functions of the turning angle. (b) The non-isentropic wave angle is also plotted as function of the isentropic wave angle. The dotted line has a slope of 1 to illustrate deviations.

surface are shown by the red lines, the isentropic wave is illustrated by the green line, and the non-isentropic wave is illustrated by the blue line.

Figures C.5(a) and (b) show the resultant shock shape over the Donovan ramp model for Mach numbers of 5.12 and 7.42 respectively. The color scheme is the same as in Figure C.4.

For both models, we observe that near the beginning of the shock formation the isentropic and non-isentropic solutions exhibity good agreement, as we would expect for these low turning angles. With increasing turning angle the non-isentropic wave deviates, and as we would expect from Figure C.3(a) is larger than the isentropic turning angle. Thus, the more realistic entropy increase due to non-isentropic waves tends to increase the distance between the wave and the body.

C.4 Convergence

While 10000 points are used for each model, the number of characteristics, N, used to compute shock location can be varied (i.e. only certain elements may have a characteristic). A convergence study is performed for the $M = 5.12$, curved ramp case. The metric by which convergence is assessed is the location of the shock formation. This plot is presented in Figure C.6.

We see that the code converges for approximately 100 characteristics, thus showing that for large enough N, the shock wave will be independent of the number of characteristics.

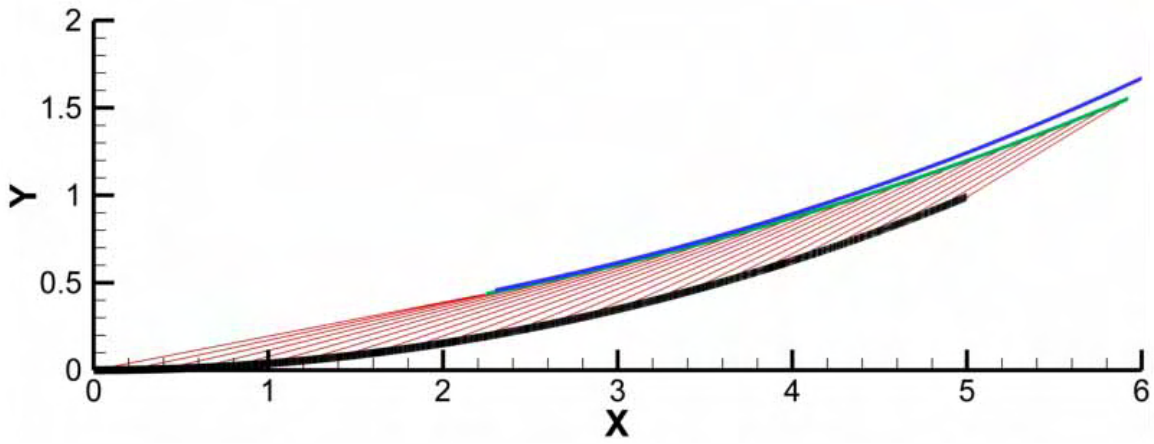

(a)

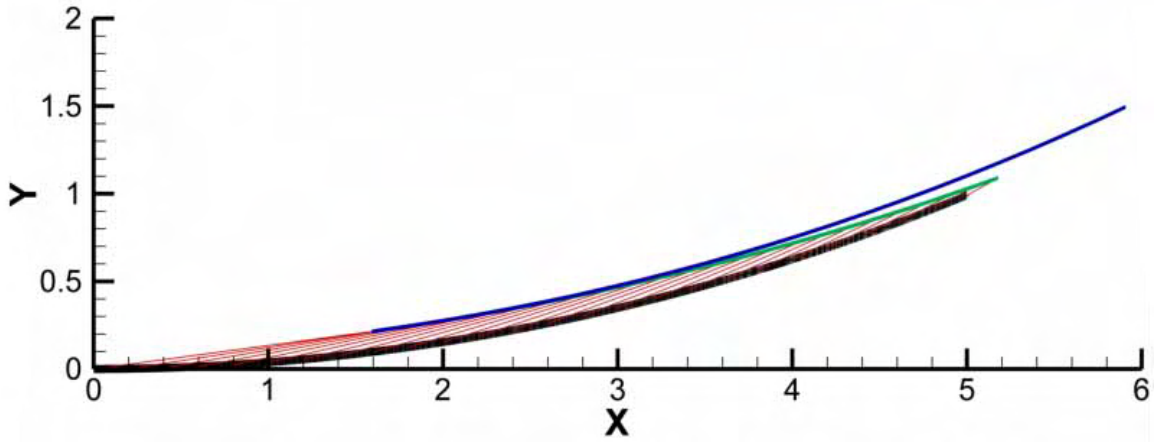

(b)

Figure C.4: Shock wave behavior for the curved ramp model at Mach numbers of (a) 5.12 and (b) 7.42. x and y units are in inches. The isentropic case is represented by the green line and the non-isentropic by the blue line.

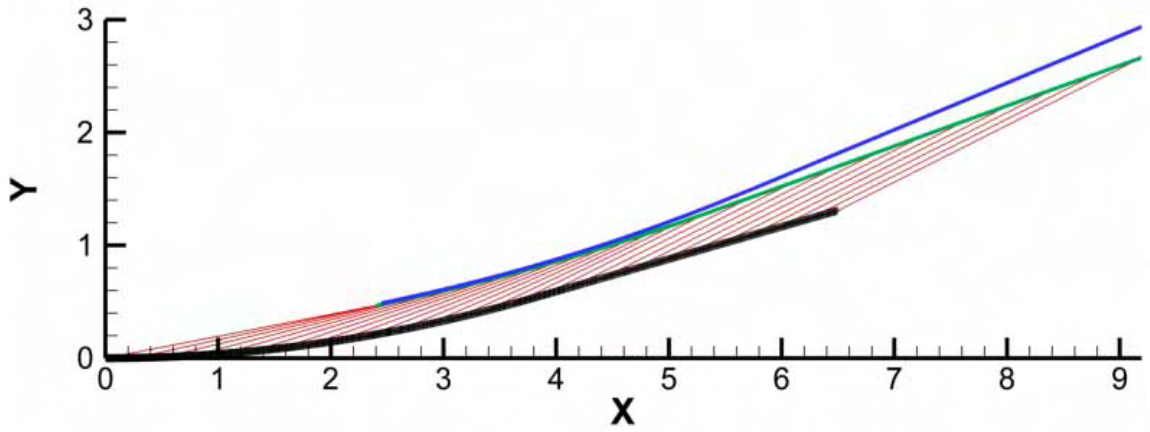

(a)

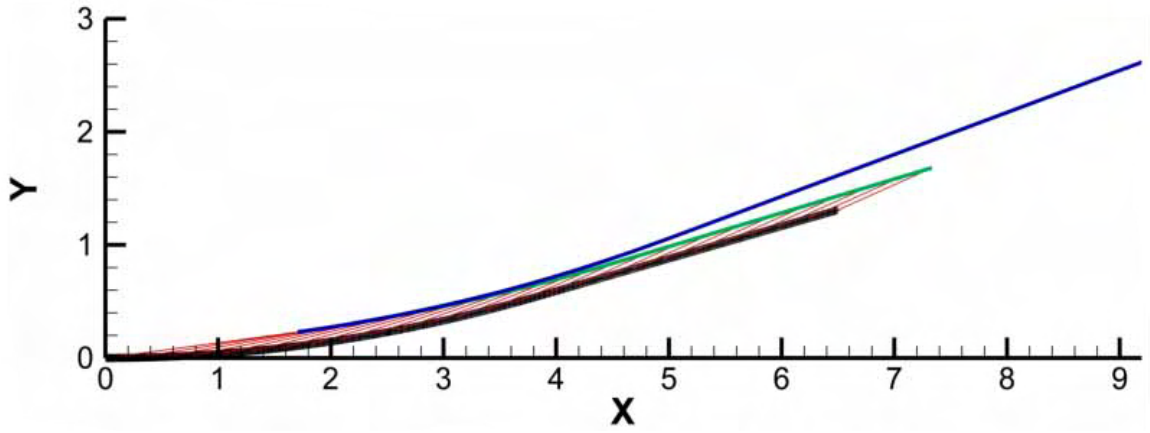

(b)

Figure C.5: Shock wave behavior for the Donovan ramp model at Mach numbers of (a) 5.12 and (b) 7.42. x and y units are in inches. The isentropic case is represented by the green line and the non-isentropic by the blue line.

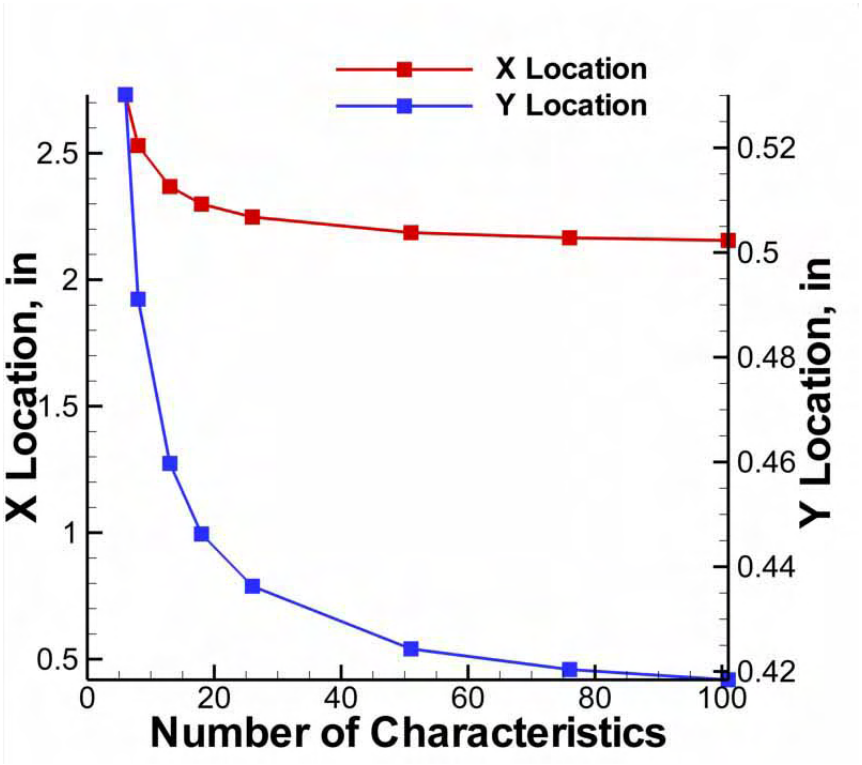

Figure C.6: The x and y locations of the shock formation are plotted versus the number of characteristics used on the curved ramp model at M = 5.12.

Appendix D

Raw Single Frame Schlieren Data

D.1 Double Wedge Raw Data

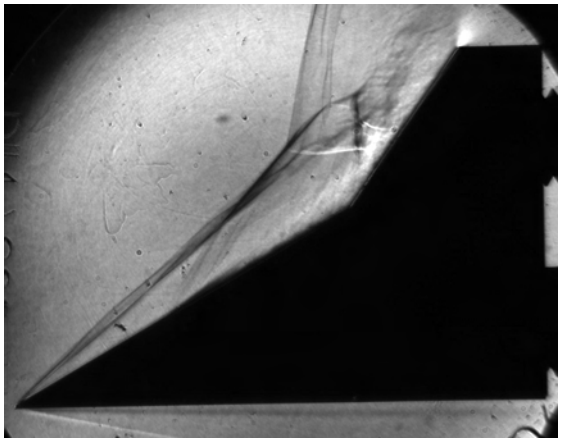

Shot 984 N_2

Shot 981 Air

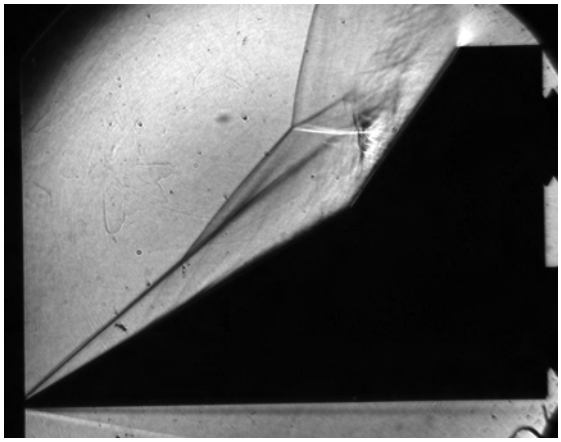

Shot 985 N_2

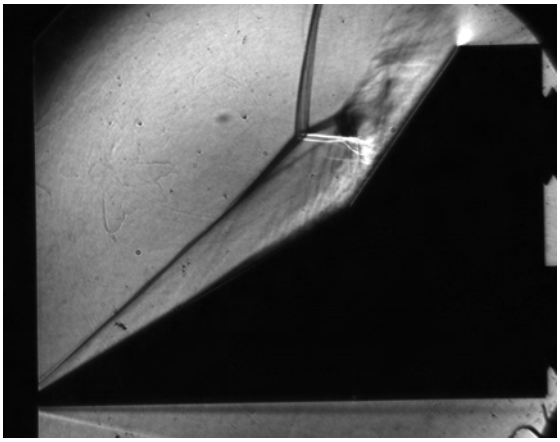

Shot 982 Air

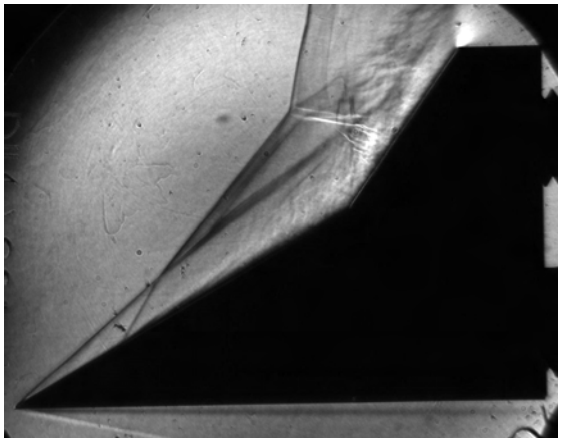

Shot 986 N_2

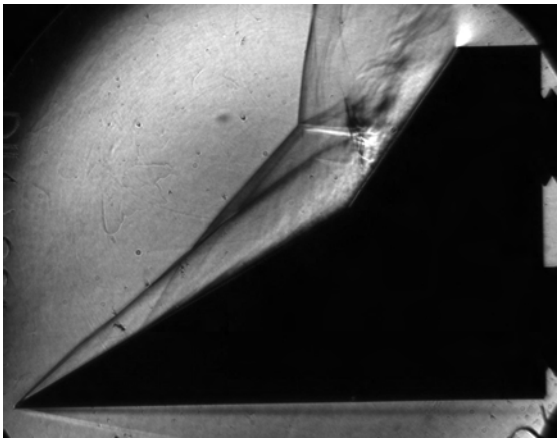

Shot 983 Air

Figure D.1: Raw data for the M7_2 condition is shown. Nitrogen is presented in the left column, air is presented in the right.

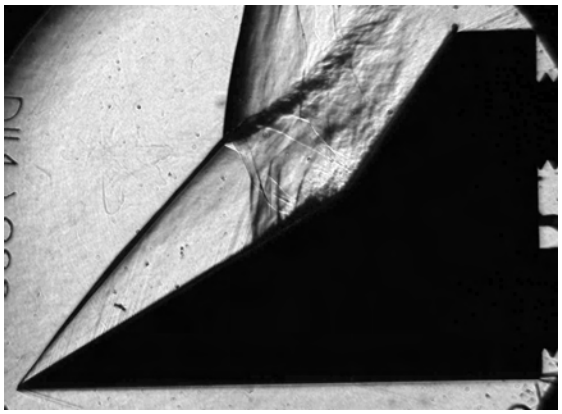

Shot 990 N_2

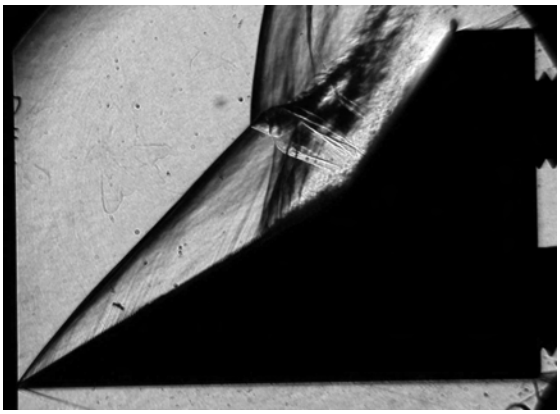

Shot 987 Air

Shot 991 N_2

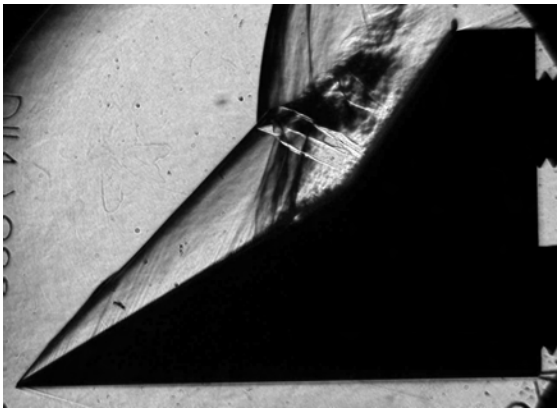

Shot 988 Air

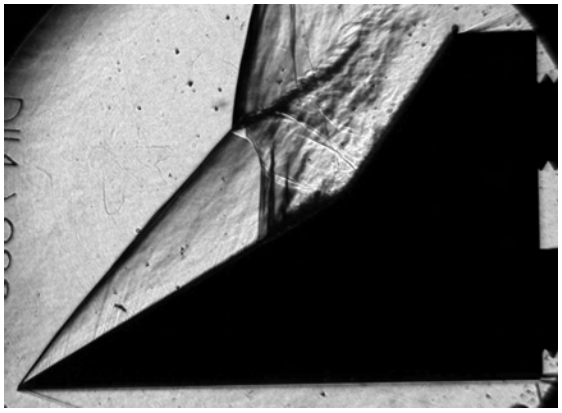

Shot 992 N_2

Shot 989 Air

Figure D.2: Raw data for the M4_3 condition is shown. Nitrogen is presented in the left column, air is presented in the right.

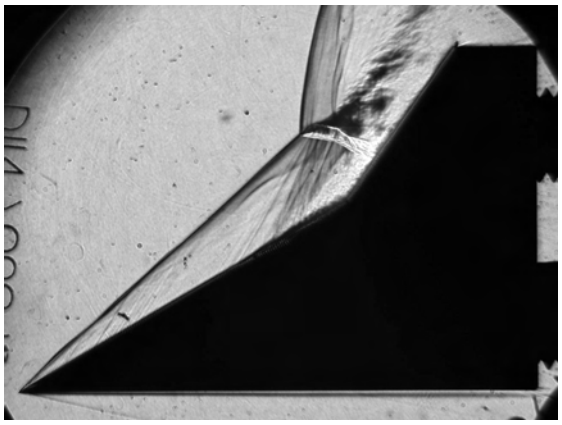

Shot 970 N_2

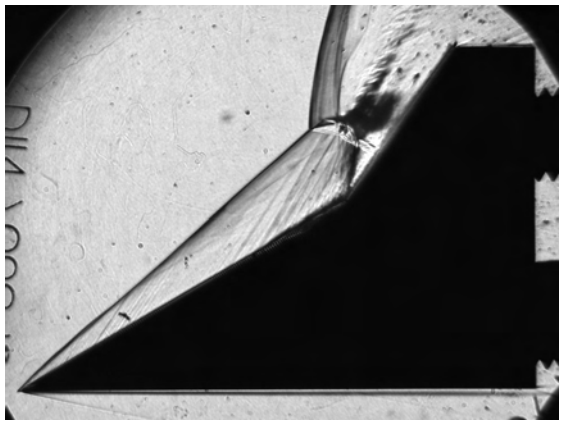

Shot 987 Air

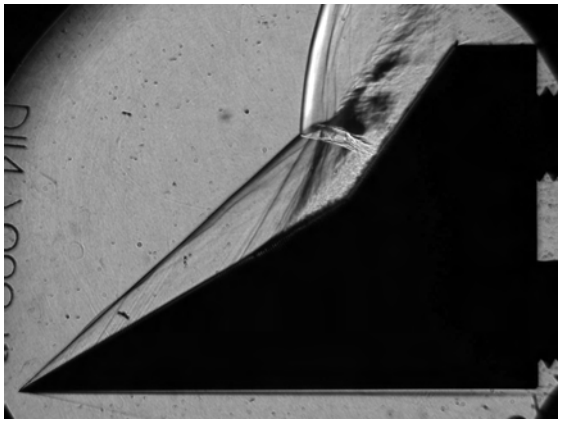

Shot 971 N_2

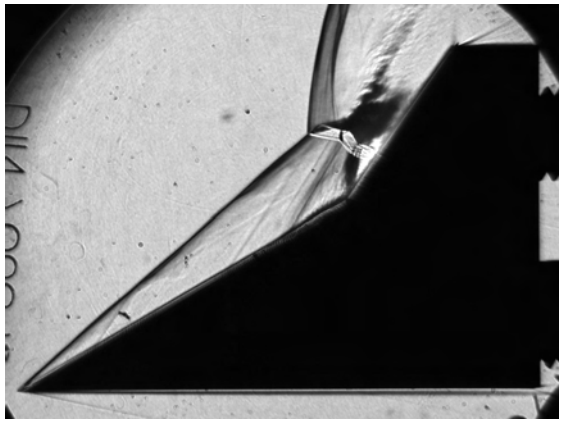

Shot 988 Air

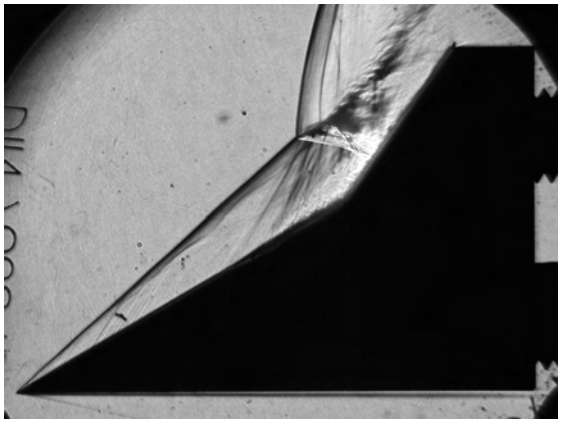

Shot 972 N_2

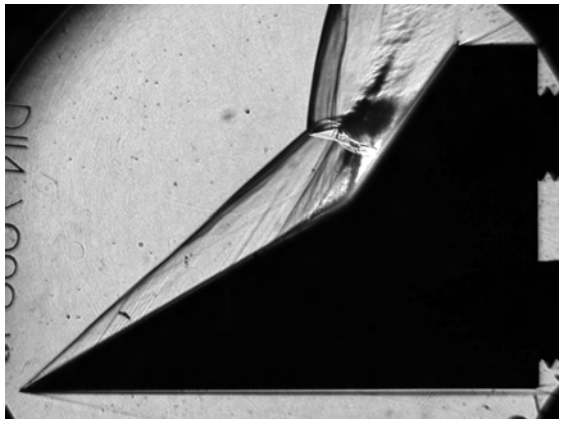

Shot 989 Air

Figure D.3: Raw data for the M5_4 condition is shown. Nitrogen is presented in the left column, air is presented in the right.

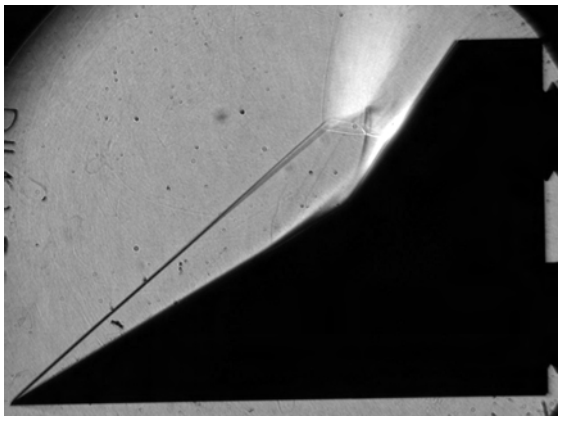

Shot 976 N_2

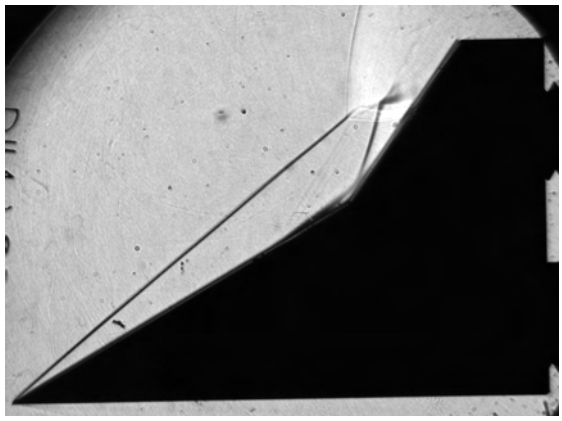

Shot 973 Air

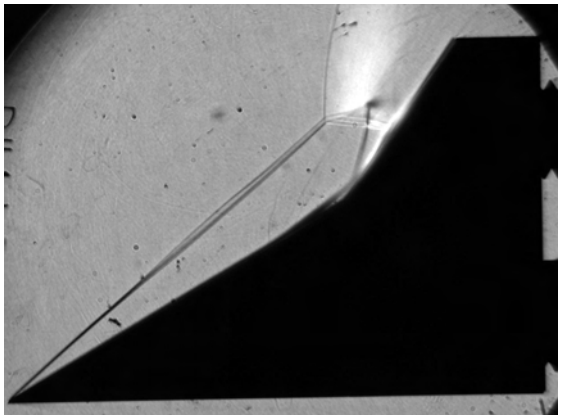

Shot 977 N_2

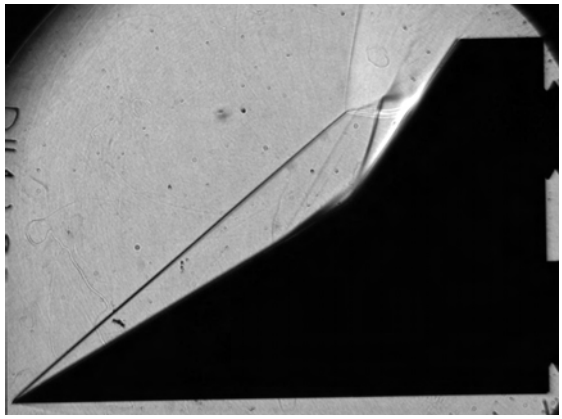

Shot 974 Air

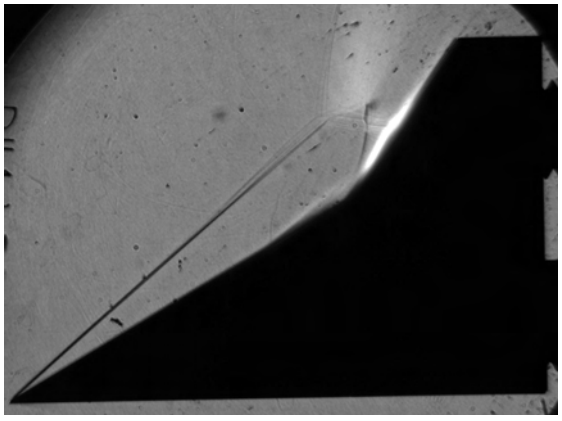

Shot 978 N_2

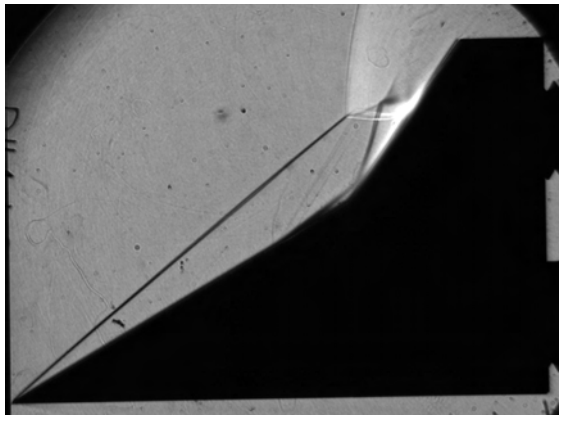

Shot 975 Air

Figure D.4: Raw data for the M7_8 condition is shown. Nitrogen is presented in the left column, air is presented in the right.

D.2 Double Cone Raw Data

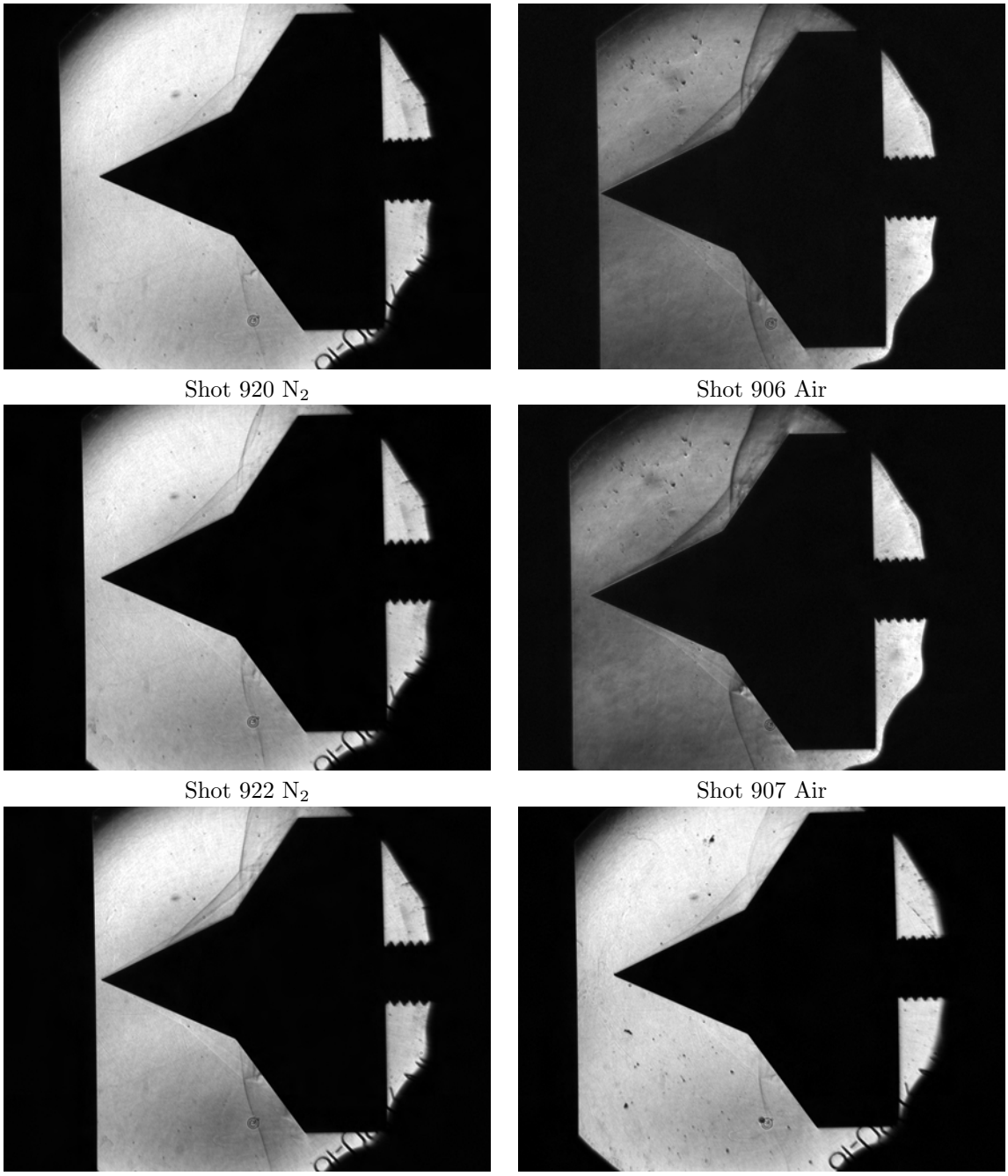

Shot 920 N_2 | Shot 906 Air

Shot 922 N_2 | Shot 907 Air

Shot 923 N_2 | Shot 956 Air

Figure D.5: Raw data for the M7_2 condition is shown. Nitrogen is presented in the left column, air is presented in the right.

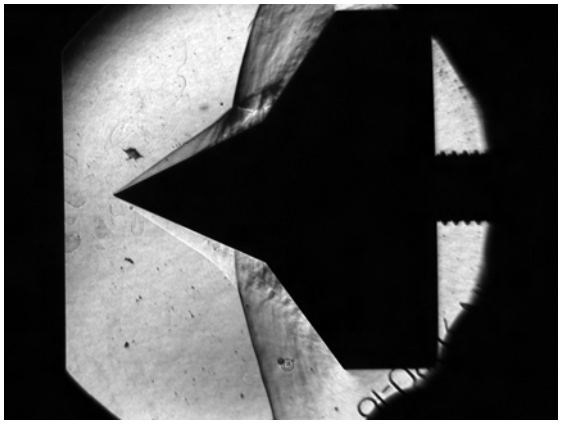

Shot 954 N_2

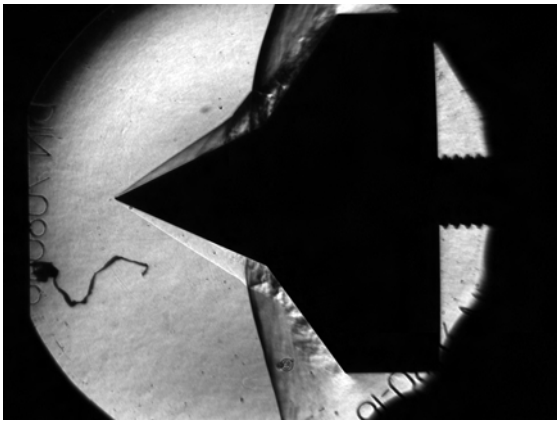

Shot 946 Air

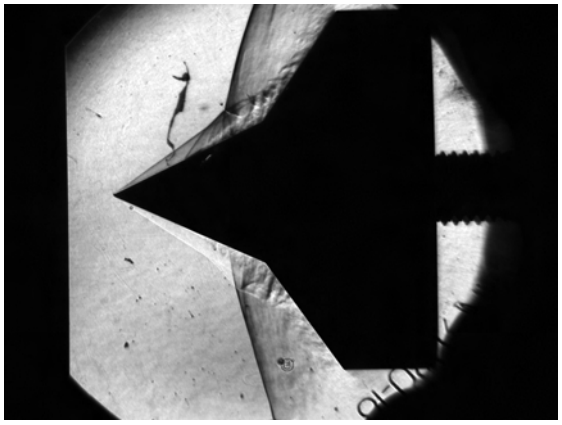

Shot 955 N_2

Shot 947 Air

Figure D.6: Raw data for the M4_3 condition is shown. Nitrogen is presented in the left column, air is presented in the right.

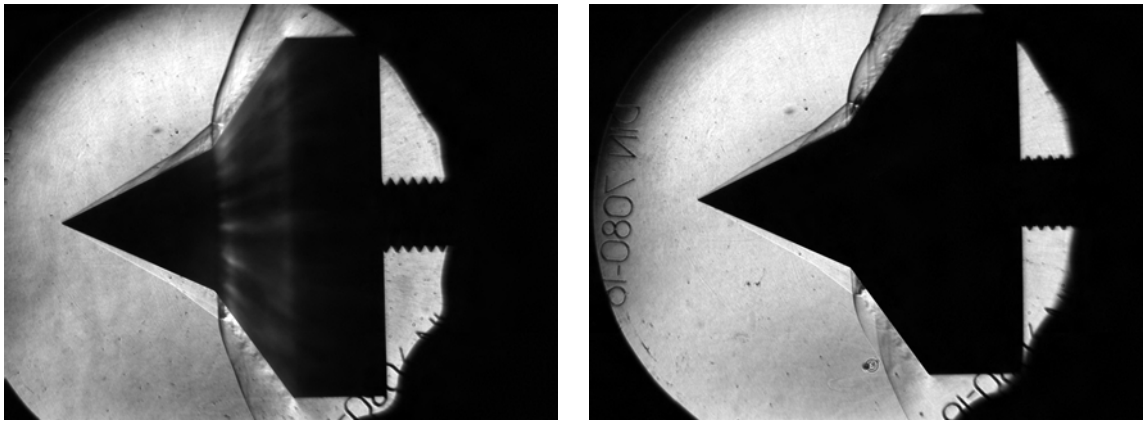

Shot 915 N_2 Shot 987 Air

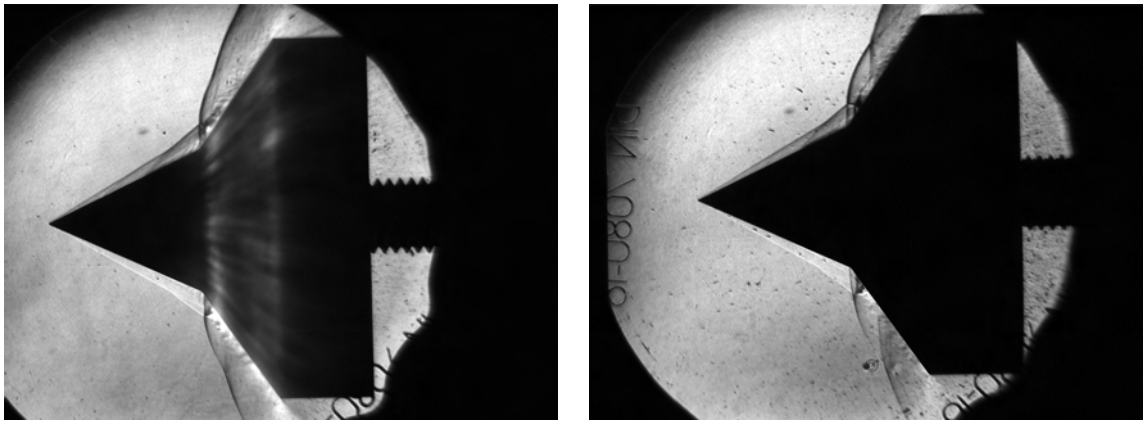

Shot 916 N_2 Shot 988 Air

Figure D.7: Raw data for the M5_4 condition is shown. Nitrogen is presented in the left column, air is presented in the right.

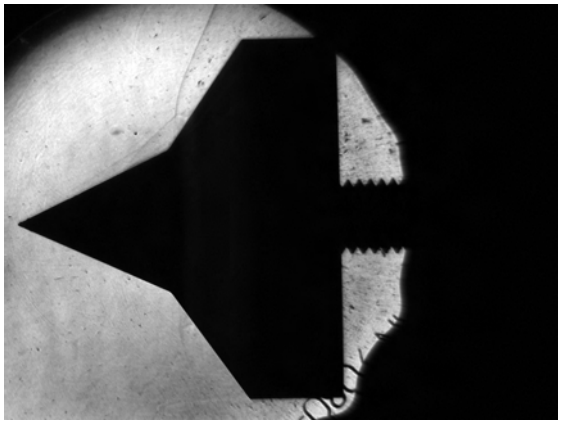

Shot 976 N_2

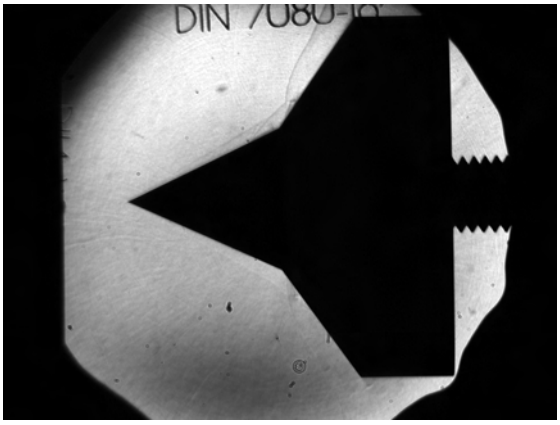

Shot 973 Air

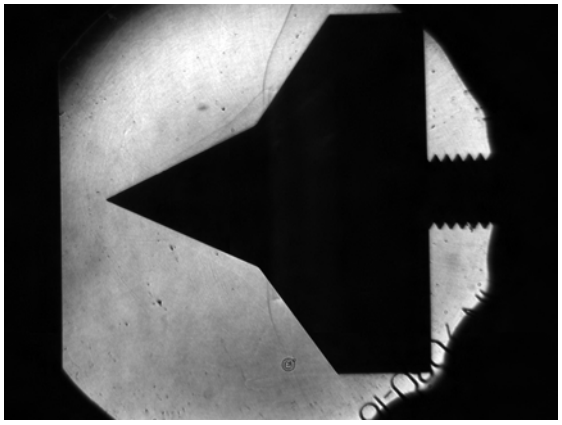

Shot 977 N_2

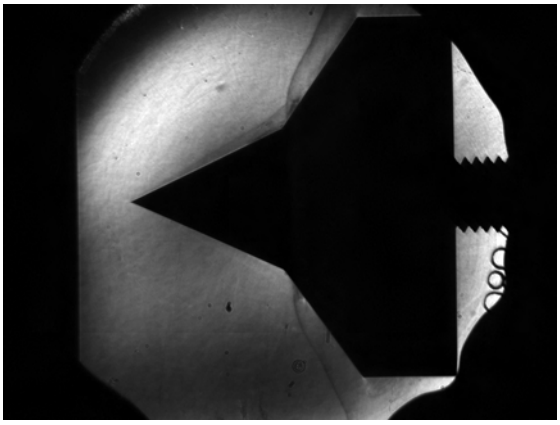

Shot 974 Air

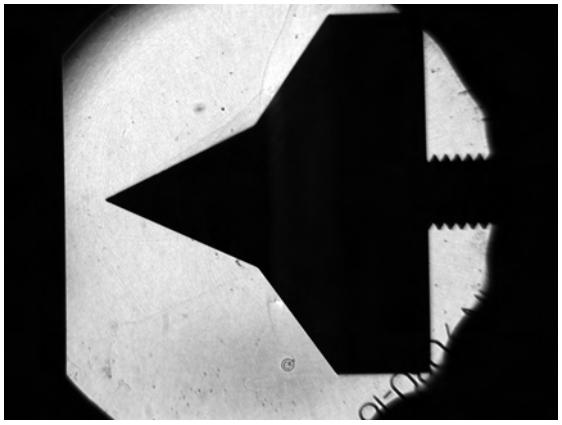

Shot 978 N_2

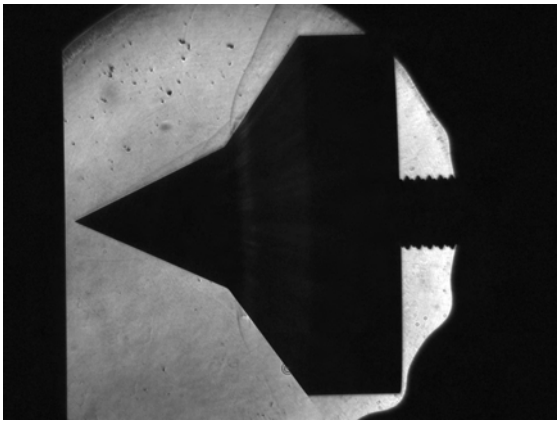

Shot 975 Air

Figure D.8: Raw data for the M7_8 condition is shown. Nitrogen is presented in the left column, air is presented in the right.

Appendix E

Additional High Speed Nitrogen Data

E.1 Double Wedge Data

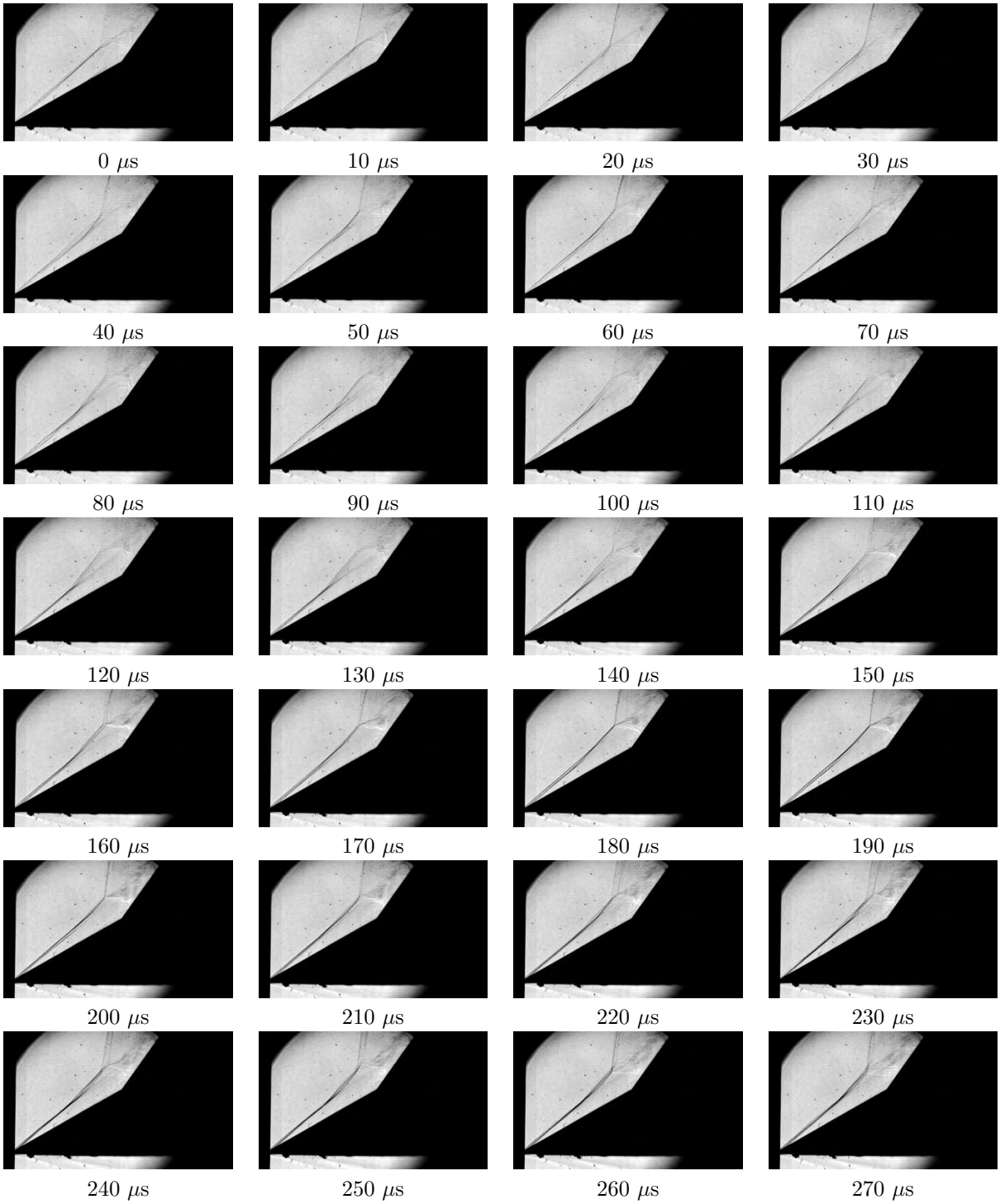

Figure E.1: High speed imaging for the M7_2 nitrogen flow field is shown. The interframe time is 10μs and exposure time is 1μs. Flow is from left to right.

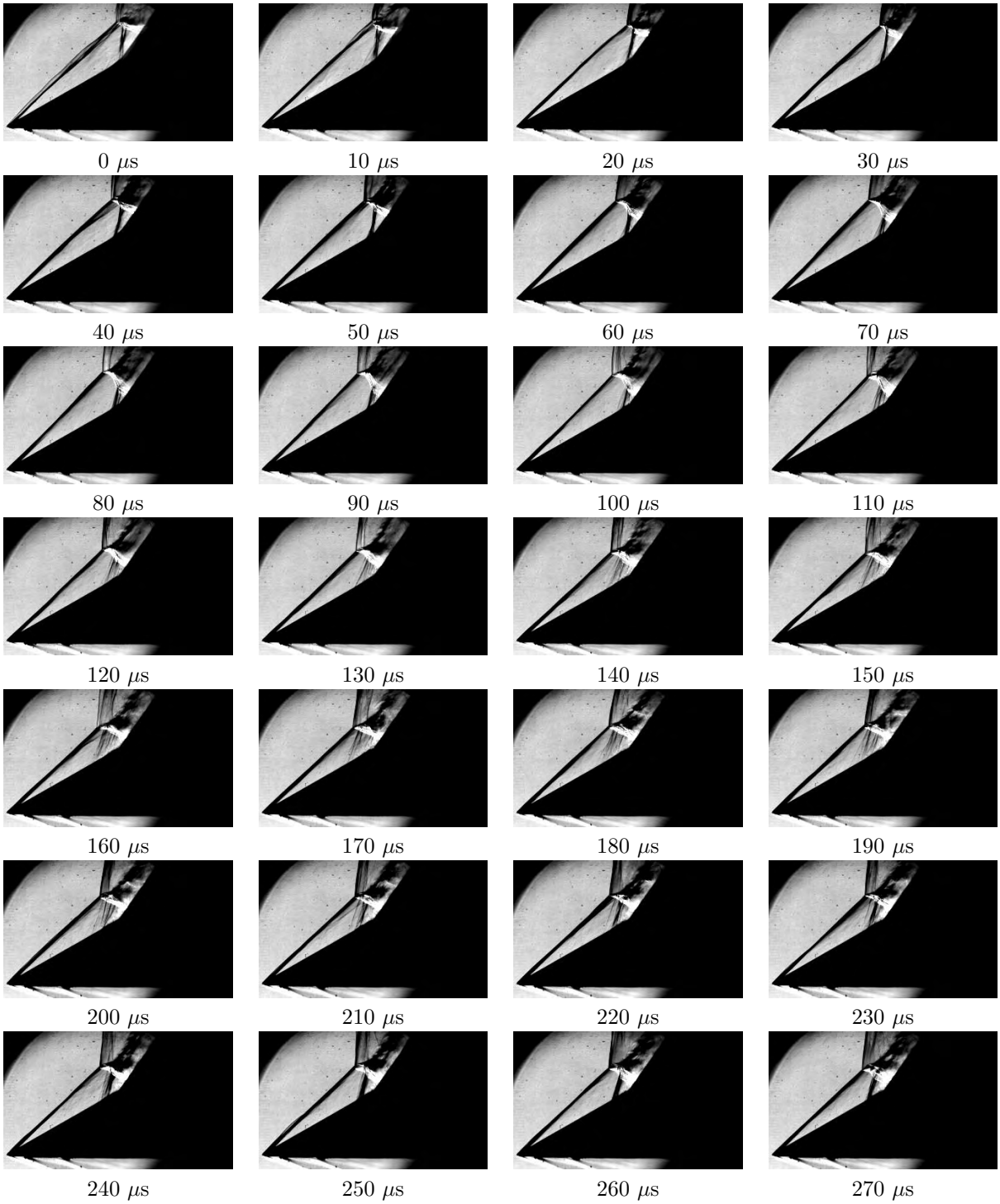

Figure E.2: The first half of the high speed imaging for the M4_3 nitrogen flow field is shown. The interframe time is 10μs and exposure time is 1μs. Flow is from left to right.

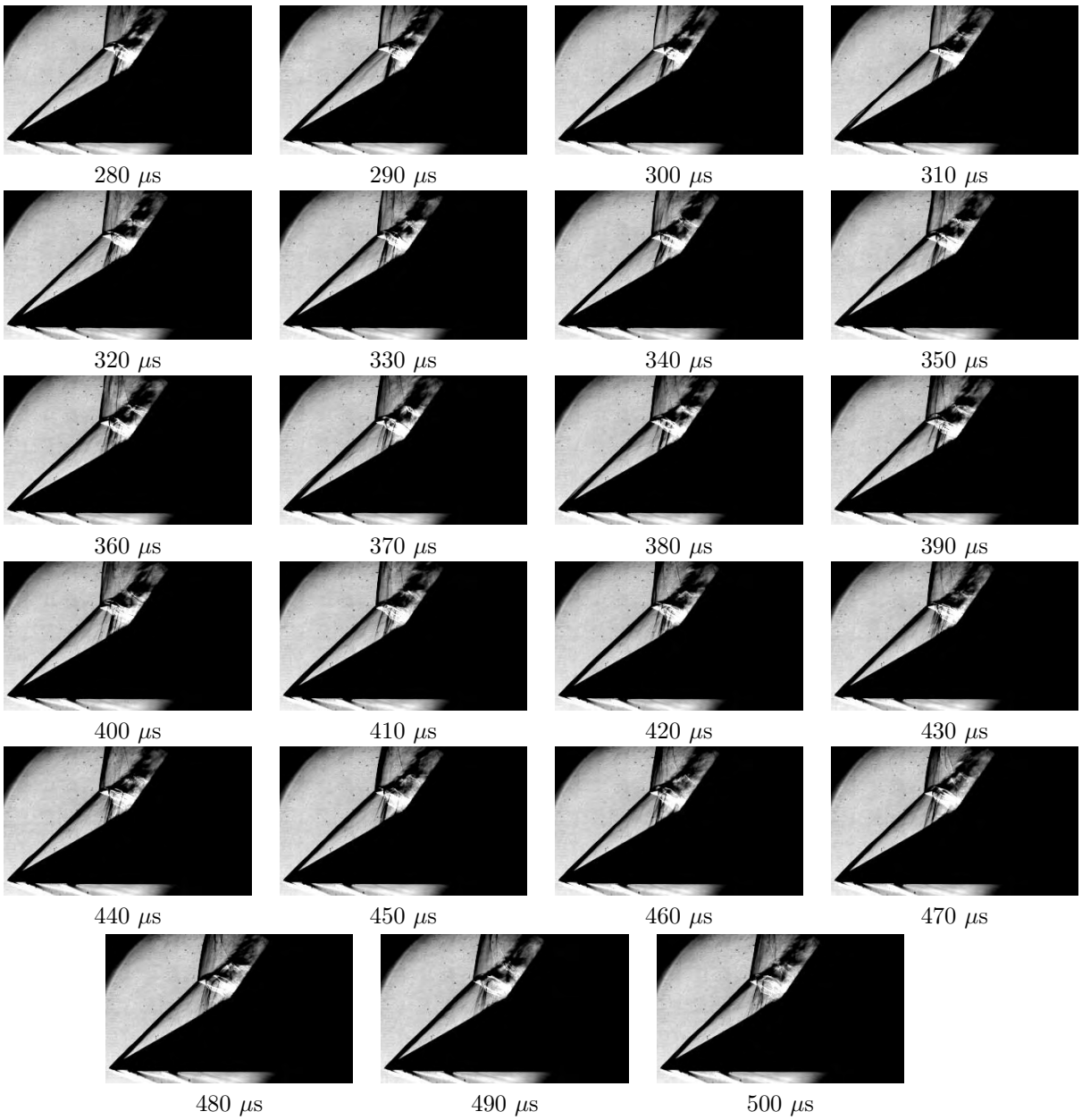

Figure E.3: The second half of the high speed imaging for the M4_3 nitrogen flow field is shown. The interframe time is 10μs and exposure time is 1μs. Flow is from left to right.

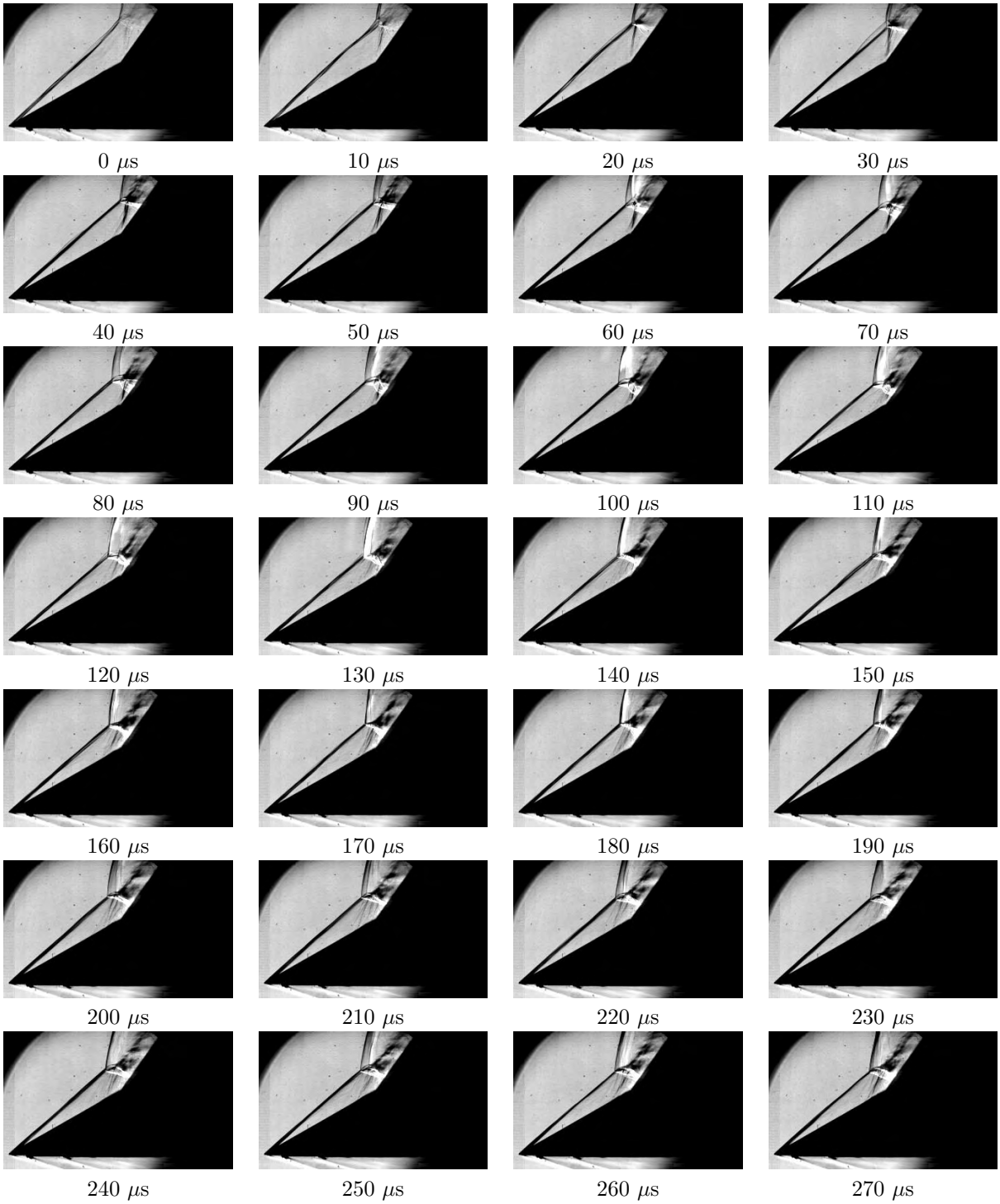

Figure E.4: The first half of the high speed imaging for the M5_4 nitrogen flow field is shown. The interframe time is 10μs and exposure time is 1μs. Flow is from left to right.

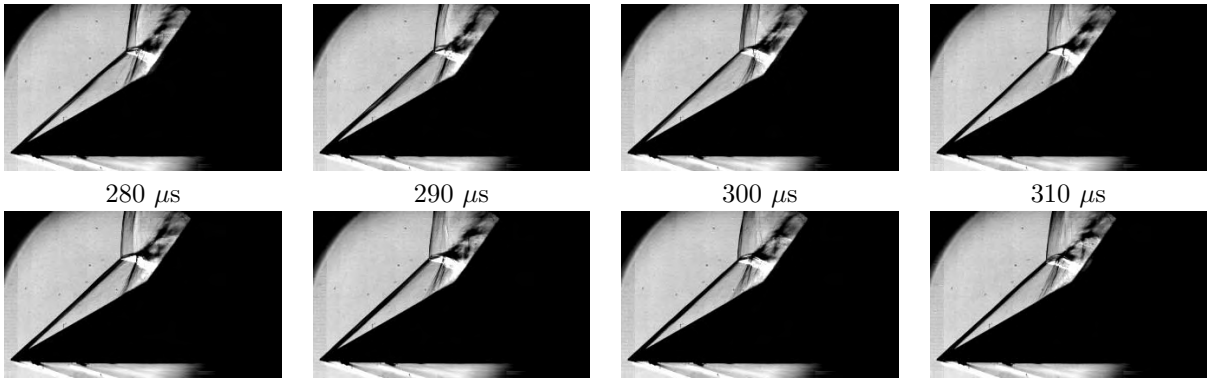

Figure E.5: The second half of the high speed imaging for the M5_4 nitrogen flow field is shown. The interframe time is 10μs and exposure time is 1μs. Flow is from left to right.

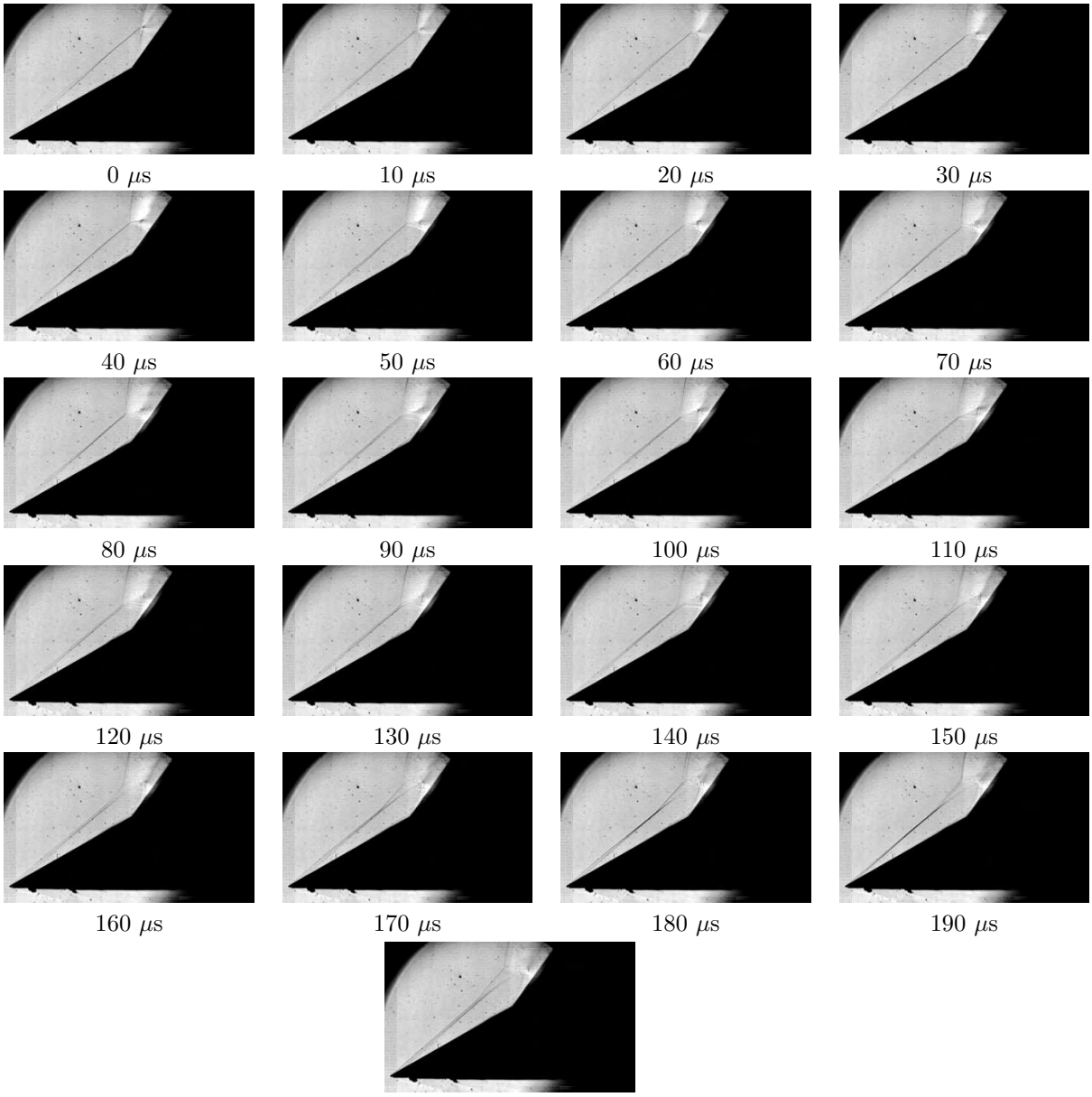

Figure E.6: High speed imaging for the M7_8 nitrogen flow field is shown. The interframe time is 10μs and exposure time is 1μs. Flow is from left to right.

E.2 Double Cone Data

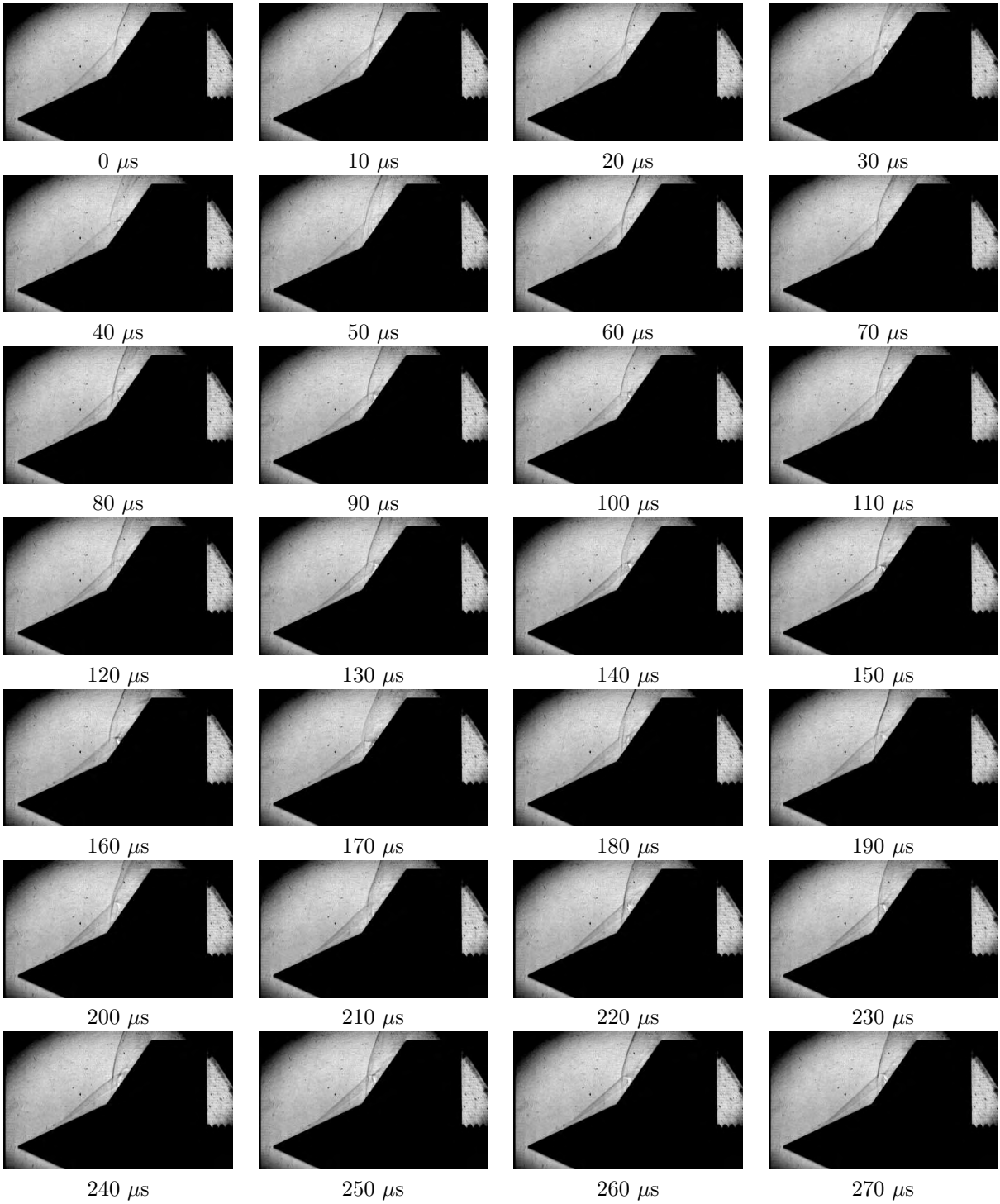

Figure E.7: High speed imaging for the M7_2 nitrogen flow field is shown. The interframe time is 10μs and exposure time is 1μs. Flow is from left to right.

Figure E.8: The first half of the high speed imaging for the M4_3 nitrogen flow field on the double wedge is shown. The interframe time is 10μs and exposure time is 1μs. Flow is from left to right.

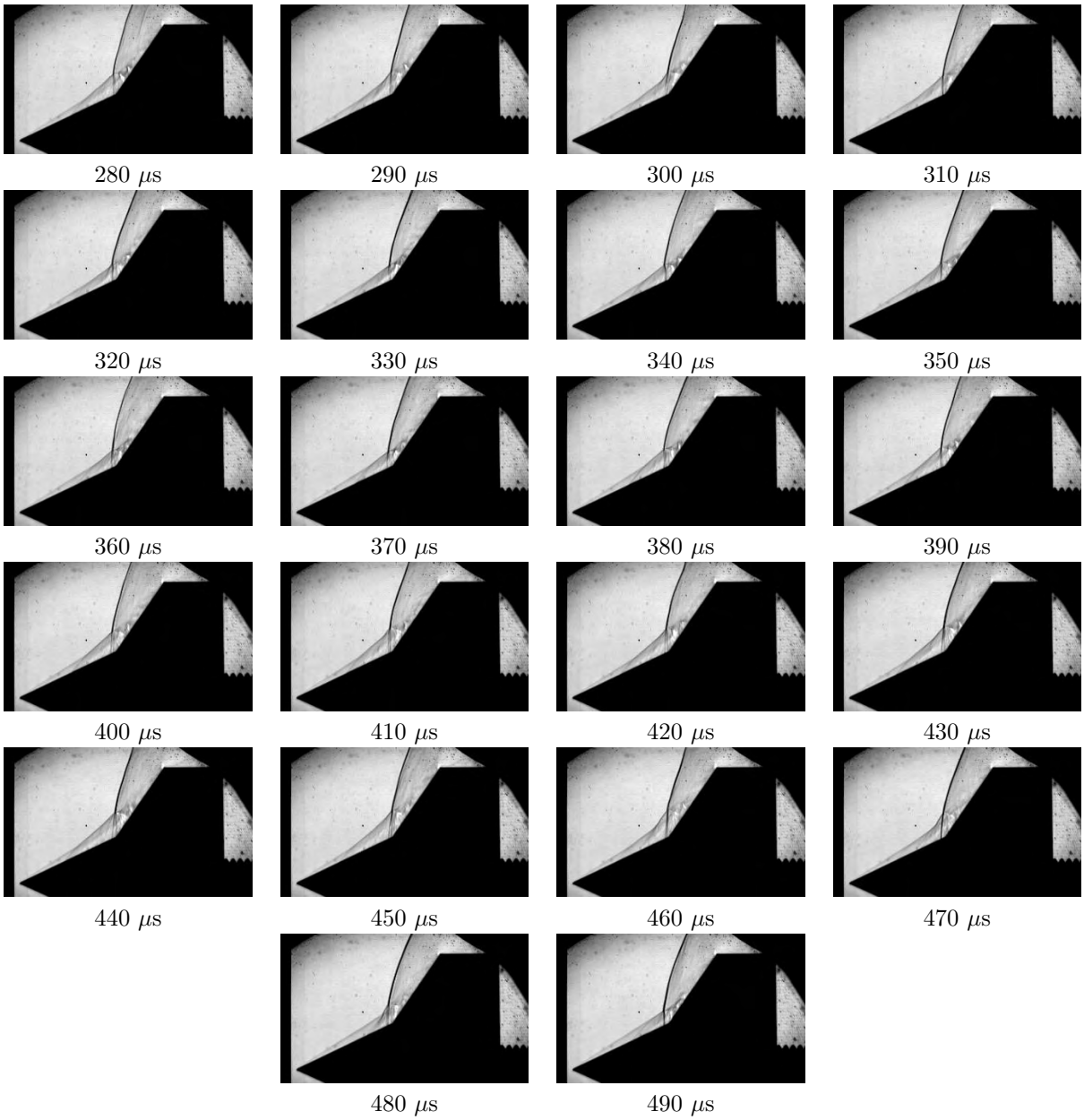

Figure E.9: The second half of the high speed imaging for the M4_3 nitrogen flow field on the double wedge is shown. The interframe time is 10μs is and exposure time is 1μs. Flow is from left to right.

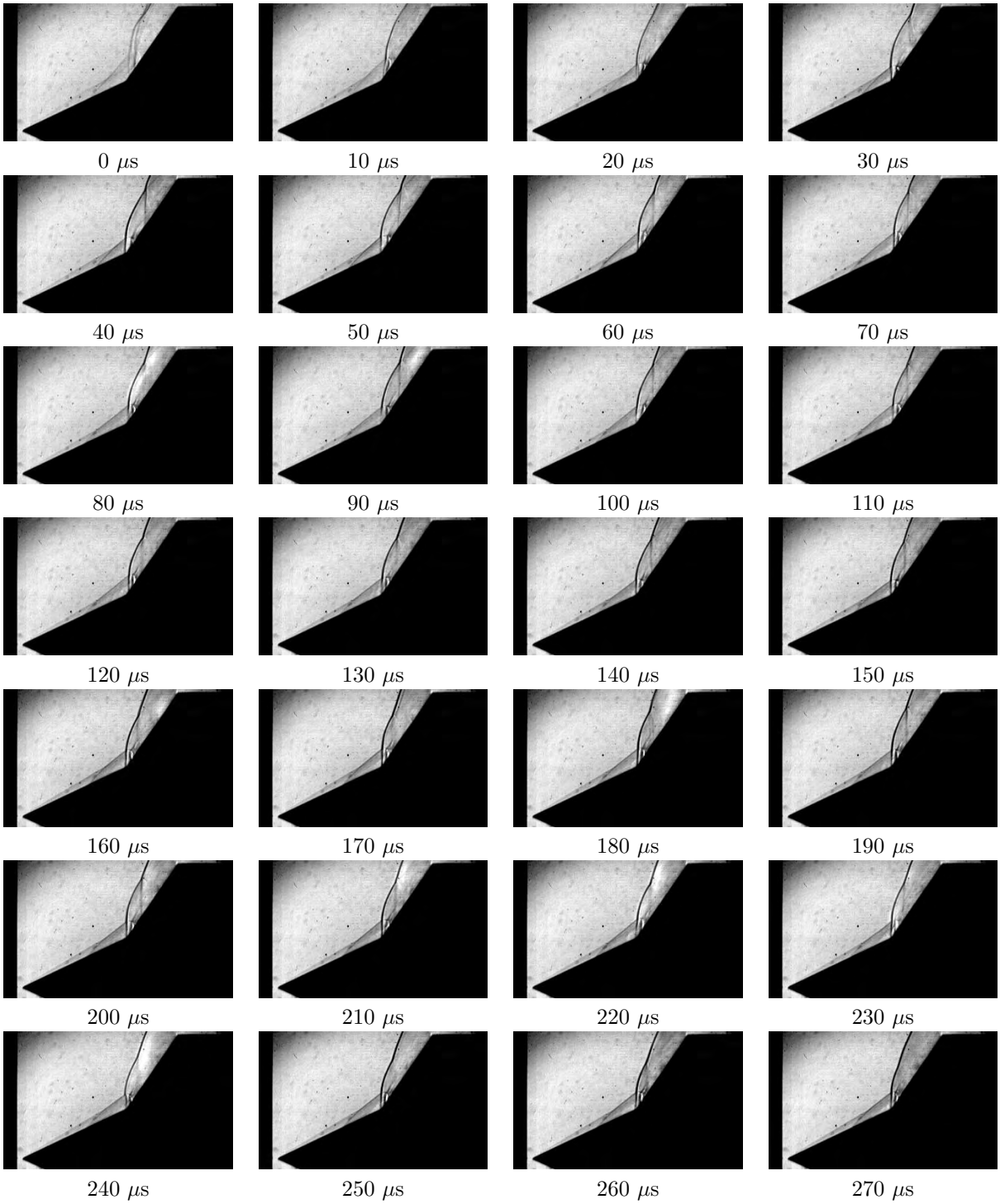

Figure E.10: The first half of the high speed imaging for the M5_4 nitrogen flow field is shown. The interframe time is 10μs and exposure time is 1μs. Flow is from left to right.

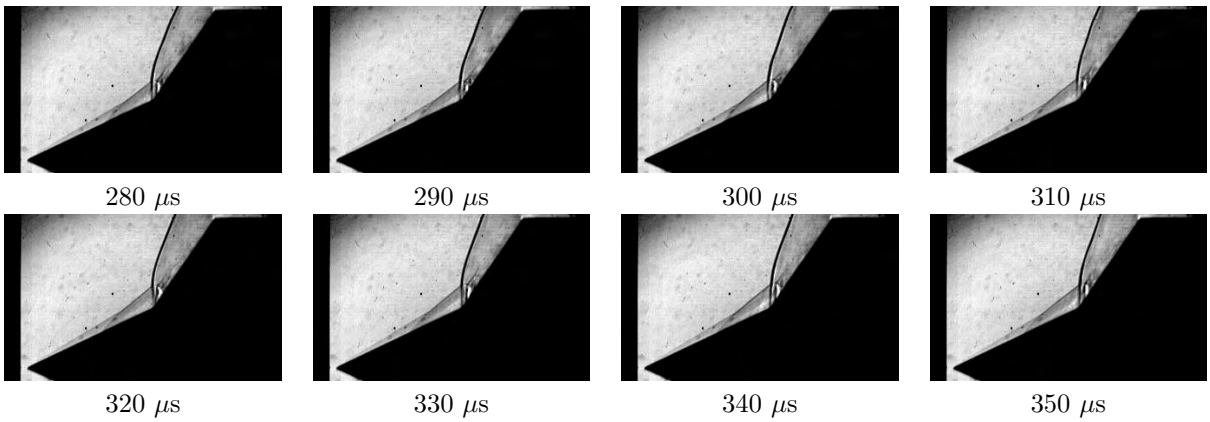

Figure E.11: The second half of the high speed imaging for the M5_4 nitrogen flow field is shown. The interframe time is 10μs and exposure time is 1μs. Flow is from left to right.

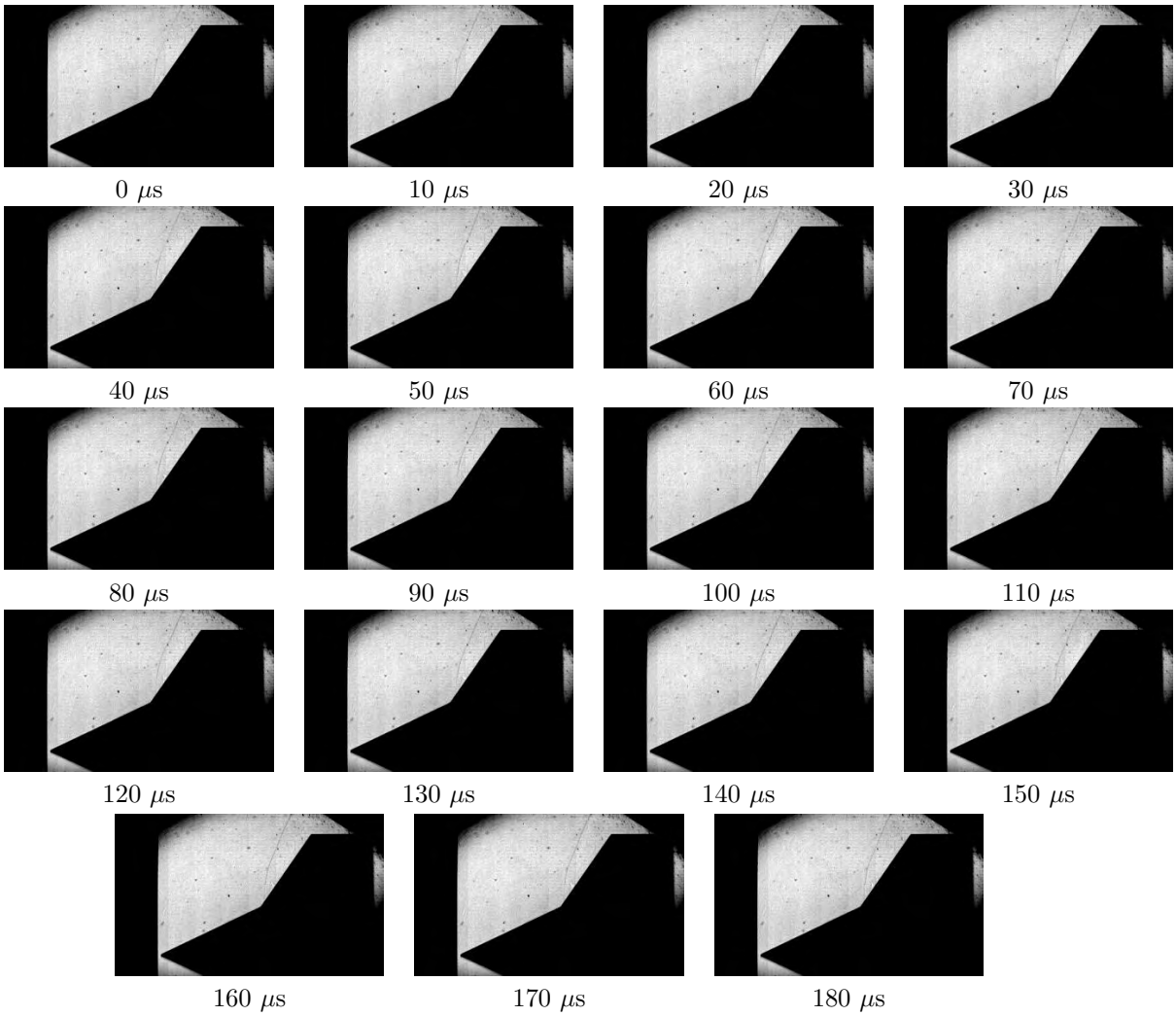

Figure E.12: High speed imaging for the M7_8 nitrogen flow field is shown. The interframe time is 10μs and exposure time is 1μs. Flow is from left to right.

Appendix F

Table of Triple Point Data

Table F.1: Results of the polar calculations for the triple wedge model. θ-δ is the oblique shock angle minus the first wedge turning angle.

			θ-δ, deg	Bow Shock Angle, deg			Transmitted Shock Angle, deg			Shear Layer Angle, deg		
Shot #	Gas	Test Condition	Measured	Measured	Calculated	% Diff	Measured	Calculated	% Diff	Measured	Calculated	% Diff
973	Air	M7.8	9.7	87.6	86.64	**-1.11**	25.0	25.04	**0.15**	19.1	15.69	**-21.74**
974	Air	M7.8	10.1	86.6	86.53	**-0.08**	21.3	25.17	**15.37**	14.2	16.16	**12.12**
975	Air	M7.8	9.7	87.4	86.64	**-0.88**	22.6	25.04	**9.73**	16.5	15.69	**-5.17**
976	N2	M7.8	11.1	87.2	86.21	**-1.15**	21.3	25.04	**14.93**	16.5	17.19	**4.00**
977	N2	M7.8	10.8	87.4	86.30	**-1.28**	23.3	24.96	**6.65**	16.2	16.84	**3.80**
978	N2	M7.8	11.0	86.8	86.24	**-0.65**	20.3	25.01	**18.84**	16.6	17.07	**2.77**
967	Air	M5.4	11.7	88.3	86.31	**-2.30**	20.3	20.11	**-0.96**	12.8	15.30	**16.35**
968	Air	M5.4	11.4	86.9	86.41	**-0.56**	19.4	20.02	**3.08**	14.2	14.93	**4.86**
969	Air	M5.4	12	88.2	86.21	**-2.30**	17.3	20.19	**14.33**	13.9	15.68	**11.33**
995	Air	M5.4	11.9	88.9	86.25	**-3.08**	19.9	20.17	**1.32**	14.4	15.55	**7.41**
970	N2	M5.4	12.6	88.3	85.97	**-2.71**	19.5	19.95	**2.26**	15.9	16.32	**2.56**
971	N2	M5.4	12.4	87.8	86.04	**-2.05**	19.8	19.90	**0.52**	15.3	16.07	**4.79**
972	N2	M5.4	12.4	87.1	86.04	**-1.23**	19.8	19.90	**0.52**	17.1	16.07	**-6.41**
996	N2	M5.4	12.3	88.3	86.07	**-2.59**	19.9	19.88	**-0.11**	13.9	15.95	**12.83**
987	Air	M 4.3.6	17.1	86.7	84.68	**-2.39**	8.1	15.65	**48.25**	26.2	19.52	**-34.24**
988	Air	M 4.3.6	17.1	86.1	84.68	**-1.68**	9.8	15.65	**37.39**	18.0	19.52	**7.78**
989	Air	M 4.3.6	17.3	86.1	84.59	**-1.78**	9.2	15.65	**41.22**	17.9	19.77	**9.48**
990	N2	M 4.3.6	20.1	85.0	83.31	**-2.03**	8.3	14.79	**43.88**	26.4	23.22	**-13.71**
991	N2	M 4.3.6	19.2	85.1	83.72	**-1.65**	7.1	15.02	**52.72**	16.0	22.09	**27.58**
992	N2	M 4.3.6	20.1	85.6	83.31	**-2.75**	6.9	14.79	**53.35**	19.0	23.22	**18.16**
993	N2	M 4.3.6	21.5	86.5	82.65	**-4.66**	3.8	14.27	**73.37**	23.1	24.94	**7.39**
994	N2	M 4.3.6	21.9	85.3	82.46	**-3.45**	7.2	14.08	**48.86**	26.7	25.43	**-4.99**
981	Air	M7.2	12.6	86.3	83.54	**-3.31**	23.8	23.37	**-1.84**	23.3	25.28	**7.82**
982	Air	M7.2	13.0	87.7	83.61	**-4.89**	22.3	23.42	**4.78**	22.2	25.06	**11.40**
983	Air	M7.2	13.6	86.3	83.79	**-2.99**	22.1	23.53	**6.09**	22.3	24.50	**8.98**
984	N2	M7.2	13.0	82.1	83.46	**1.63**	22.2	23.31	**4.76**	25.5	25.50	**-0.01**
985	N2	M7.2	14.3	85.1	83.83	**-1.52**	21.0	23.55	**10.83**	24.5	24.39	**-0.46**
986	N2	M7.2	16.2	82.1	82.85	**0.90**	21.0	22.76	**7.72**	29.2	27.26	**-7.10**

References

[1] Bertin, J. and Cummings, R., "Fifty years of hypersonics: where we've been, where we're going." *Progress in Aerospace Sciences*, Vol. 39, 2003, pp. 511–536.

[2] Holden, M., "Historical review of experimental studies and prediction methods to describe laminar and turbulent shock wave/boundary layer interactions in hypersonic flows," *Proceedings of the 44th AIAA Aerospace Sciences Meeting*, Reno, NV, USA, 2006.

[3] Holden, M., Wadhams, T., and MacLean, M., "A review of experimental studies with the double cone and hollow cylinder/flare configurations in the LENS hypervelocity tunnels and comparisons with Navier-Stokes and DSMC computations," *Proceedings of the 48th AIAA Aerospace Sciences Meeting*, Orlando, FL, 2010.

[4] Nompelis, I., Candler, G. V., MacLean, M., Wadhams, T. P., and Holden, M. S., "Numerical Investigation of Double-Cone Flow Experiments with High Enthalpy Effects," *Proceedings of the 48rd AIAA Aerospace Sciences Meeting*, Orlando, FL, 2010.

[5] Gaitonde, D., Canupp, P., and Holden, M., "Heat transfer predictions in a laminar hypersonic viscous/inviscid interaction," *Journal of Thermophysics and Heat Transfer*, Vol. 16, No. 4, 2002, pp. 481–89.

[6] Nompelis, I., *Computational study of hypersonic double-cone experiments for code validation*, Ph.D. thesis, The University of Minnesota, St. Paul, Minnesota, 2004.

[7] Olejniczak, J., Candler, G. V., and Hornung, H. G., "Computation of double-cone experiments in high enthalpy nitrogen," *Proecedings of the AIAA Thermophysics Conference*, Atlanta, GA, 1997.

[8] Davis, J., *High-enthalpy shock/boundary-layer interaction on a double wedge*, Ph.D. thesis, California Institute of Technology, Pasadena, CA, 1999.

[9] Rayner, J., *Boundary layer separation and thermal chocking*, Ph.D. thesis, Australian National University, Canberra, Australia, 1973.

[10] Mallinson, S., *Shock wave/boundary layer interaction at a compression corner in hypervelocity flows*, Ph.D. thesis, University of New South Wales, Canberra, Australia, 1994.

[11] Mallinson, S., Gai, S., and Mudford, N., "High enthalpy, hypersonic compression corner flow," *AIAA Journal*, Vol. 34, No. 6, 1996, pp. 1130–1137.

[12] Mallinson, S., Gai, S., and Mudford, N., "Establishment of steady separated flow over a compression-corner," *Shock Waves*, , No. 7, 1997, pp. 249–253.

[13] Mallinson, S., Gai, S., and Mudford, N., "Establishment of steady separated flow over a copression-corner," *Journal of Fluid Mechanics*, Vol. 342, 1997, pp. 1–35.

[14] Mallinson, S., Gai, S., and Mudford, N., "Upstream influence and peak heating in hypervelocity shock wave/boundary-layer interaction," *Journal of Propulsion and Power*, Vol. 12, No. 5, 1996, pp. 984–990.

[15] Grumet, A., Jr., J. A., and Lewis, M., "Numerical study of the effects of wall catalysis on shock wave/boundary layer interaction," *Journal of Thermophysics and Heat Transfer*, Vol. 8, No. 1, 1994, pp. 40–47.

[16] Olejniczak, J. and Candler, G. V., "Computation of hypersonic shock interaction flow fields," *Proceedings of the 7th AIAA/ASME Joint Thermophysics and Heat Transfer Conference*, Albuqureque, NM, 1999.

[17] Olejniczak, J., Candler, G. V., Wright, M. J., Hornung, H. G., and Leyva, I., "High enthalpy double-wedge experiments," *Proecedings of the AIAA Advanced Measurement and Ground Testing Technology Conference*, New Orleans, LA, 1996.

[18] Olejniczak, J., Candler, G. V., Wright, M. J., Leyva, I., and Hornung, H. G., "Experimental and Computational Study of High Enthalpy Double-Wedge Flows," *J. Thermophys. and Heat Transfer*, Vol. 13, No. 4, 1999, pp. 431–40.

[19] Marrone, P. and Treanor, C., "Chemical relaxation with preferential dissociation from excited vibration levels," *Physics of Fluids*, Vol. 6, No. 9, 1963, pp. 1215–1221.

[20] Park, C., "Assessment of two-temperature kinetic model for dissociating and weakly ionizing nitrogen," *AIAA Paper 86-1347*, 1986.

[21] Davis, J. and Sturtevant, B., "Separation Length in high-enthalpy shock/boundary layer interaction," *Phys. Fluids*, Vol. 12, No. 10, 2000, pp. 2661–87.

[22] Olejnizcak, J., *Computational and experimental study of nonequilibrium chemistry in hypersonic flows*, Ph.D. thesis, University of Minnesota, St. Paul, MN, 1997.

[23] Candler, G., *The computation of weakly ionized hypersonic flows in thermo-chemical nonequilibrium*, Ph.D. thesis, Stanford University, Stanford, CA, 1988.

[24] Hashimoto, T., "Experimental investigation of hypersonic flow induced separation over double wedges," *Journal of Thermal Science*, Vol. 18, No. 3, 2009, pp. 220–5.

[25] Edney, B., "Effects of Shock impingement on the heat transfer around blunt bodies," *AIAA Journal*, Vol. 6, No. 1, 1968, pp. 15–21.

[26] Maull, D., "Hypersonic flow over axially symmetric spiked bodies," *Journal of Fluid Mechanics*, Vol. 8, No. 4, 1960, pp. 584–592.

[27] Mair, W., "Experiments on separation of boundary layers on probes in front of blunt-nosed bodies in supersonic air stream," *Philosophical Magazine*, Vol. 43, No. 342, 1952, pp. 695–716.

[28] Holden, M., "Real gas effects on regions of viscous-inviscid interaction in hypersonic flows," *AIAA Paper 97-2056*, 1997.

[29] Wright, M., Sinha, K., Olejniczak, J., Candler, G., Magruder, T., and Smits, A., "Numerical and experimental investigation of double-cone shock interactions," *AIAA Journal*, Vol. 28, No. 12, 2000, pp. 2268–2276.

[30] Hefner, K., Chpoun, A., and Lengrand, J., "Experimental study of transitional axisymmetric shock=boundary layer interactions and M=5," *AIAA Paper 93-3131*, 1993.

[31] Nompelis, I., Candler, G., Holden, M., and Wadhams, T. P., "Real Gas Effects on Hypersonic Shock Wave Laminar Boundary Layer Interactions," *Proceedings of the 41th AIAA Aerospace Sciences Meeting*, Reno,NV, 2003.

[32] Nompelis, I., Candler, G., Holden, M., and Wadhams, T. P., "Computational investigation of hypersonic viscous/inviscid interactions in high enthalpy flows," *Proceedings of the 36th AIAA Thermophysics Conference*, Orlando, FL, 2003.

[33] Nompelis, I., Candler, G. V., and Holden, M. S., "Effect of Vibrational Nonequilibrium on Hypersonic Double-Cone Experiments," *AIAA Journal*, Vol. 41, No. 11, 2003, pp. 2162–9.

[34] Nompelis, I., Candler, G. V., MacLean, M., Wadhams, T. P., and Holden, M. S., "Numerical Investigation of High Enthalpy Chemistry on Hypersonic Double-Cone Experiments," *Proceedings of the 43rd AIAA Aerospace Sciences Meeting*, Reno, NV, 2005.

[35] Nompelis, I. and Candler, G., "Investigation of hypersonic double-cone flow experiments at high enthalpy in the LENS facility," *Proceedings of the 45nd AIAA Aerospace Sciences Meeting*, Reno, NV, 2007.

[36] Parker, T. and Wakemman, T., "Measuring Nitric Oxide Freestream Velocity Using Quantum Cascade Lasers at CUBRC," *Proceedings of the 45th AIAA Aerospace Sciences Meeting*, Reno, NV, USA, 2007.

[37] Candler, G., Doraiswamy, S., and Kelley, J., "The Potential Role of Electronically-Excited States in Recombining Flows," *Proceedings of the 48th AIAA Aerospace Sciences Meeting*, Orlando, FL, USA, 2010.

[38] Reimann, B. and Hannermann, V., "Numerical investigation of double-cone and cylinder experiments in high enthalpy flows using the DLR TAU code," *Proceedings of the 48th AIAA Aerospace Sciences Meeting*, Orlando, FL, USA, 2010.

[39] Knight, D. and Longo, J., "Shock interactions investigations associated with AVT-136," *Proceedings of the 48th AIAA Aerospace Sciences Meeting*, Orlando, FL, USA, 2010.

[40] Jones, W., Muylaert, J., Erbland, P., and Schmisseur, J., "Assessment of aerothermodynamic flight prediction tools through ground and flight experimentation," Tech. rep., North Atlantic Treaty Organization, November 2011, NATO RTO Technical Report TR-AVT-136.

[41] Davies, W. and Bernstein, J., "Heat transfer and transition to turbulence in the shock-induced boundary layer on a semi-infinite flat plate," *Journal of Fluid Mechanics*, Vol. 36, No. 87, 1969.

[42] Gupta, R., "An analysis of the relaxation of laminar boundary layer on a flat plate after passage of an interface with application to expansion-tube flows," Tech. rep., 1972, NASA TR R-397.

[43] Holden, M., "Establishment time of laminar separated flows," *AIAA Journal*, Vol. 9, 1971, pp. 2296.

[44] Druguet, M., Candler, G., and Nompelis, I., "Effects of numerics on Navier-Stokes computations," *AIAA Journal*, Vol. 43, No. 3, 2005, pp. 616–23.

[45] Jagadeesh, G., Hashimoto, T., Naitou, K., Sun, M., and Takayama, K., "Visualization of Unsteady Shock Oscillations in the High-Enthalpy Flow Field around Double Cones," *Journal of Visualization*, Vol. 6, No. 2, 2003, pp. 195–203.

[46] Marineau, E. and Hornung, H., "Study of bow-shock wave unsteadiness in hypervelocity flow from reservoir fluctuations," *Proceedings of the 48th AIAA Aerospace Sciences Meeting*, Orlando, FL, 2010.

[47] Lind, C. and Lewis, M., "Unsteady characteristics of a type IV shock interaction," *Journal of Aircraft*, Vol. 32, No. 6, 1995, pp. 1286–93.

[48] Lind, C. and Lewis, M., "Computational analysis of the unsteady type IV shock interaction of blunt body flows," *Journal of Propulsion and Power*, Vol. 12, No. 1, 1996, pp. 127–33.

[49] Sanderson, S., *Shock interaction in hypervelocity flow*, Ph.D. thesis, California Institute of Technology, Pasadena, CA, 1995.

[50] Sanderson, S., Hornung, H., and Sturtevant, G., "The influence of non-equilibrium dissociation on the flow produced by shock impingement on a blunt body," *Journal of Fluid Mechanics*, Vol. 516, 2004, pp. 1–37.

[51] Holden, M., Moselle, J., and Lee, J., "Studies on aerothermal loads generated in regions of shock/shock interaction in hypersonic flow," Tech. rep., 1991, NASA CR181893.

[52] Holden, M., Wieting, A., Moselle, J., and Class, C., "Studies on aerothermal loads generated in regions of shock/shock interaction in hypersonic flow," *Proceedings of the 26th AIAA Aerospace Sciences Meeting*, Reno, NV, 1988.

[53] Lu, F. and Marren, D., *Advanced Hypersonic Test Facilities*, AIAA Progress in Astronautics and Aeronautics Series, Reston, VA, 2002.

[54] Trimpi, R., "Preliminary theoretical study of the expansion tube, new device for producing high enthalpy short-duration hypersonic gas flows," Tech. rep., 1962, NASA TR R-133.

[55] Anderson, J., *Modern Compressible Flow: With Historical Perspective*, McGraw-Hill Science/Engineering/Math, 2002.

[56] Paull, A. and Stalker, R., "Test flow disturbances in an expansion tube," *Journal of Fluid Mechanics*, Vol. 245, No. Dec 1992, 1992, pp. 493–521.

[57] Sharma, M., *Post-shock thermochemistry in hypervelocity CO_2 and air flow*, Ph.D. thesis, University of Illinois, Urbana, IL, 2010.

[58] Dufrene, A., *Design and characterization of the hypervelocity expansion tube*, Master's thesis, University of Illinois, Urbana, IL, 2006.

[59] Dufrene, A., Sharma, M., and Austin, J. M., "Design and Characterization of a Hypervelocity Expansion Tube Facility," *Journal of Propulsion and Power*, Vol. 23, No. 6, Nov 2007, pp. 1185–1193.

[60] Sharma, M., *Further development and experimentation with the hypervelocity expansion tube*, Master's thesis, University of Illinois, Urbana, IL, 2007.

[61] Settles, G., *Schlieren and Shadowgraph Technique: Visualizing Phenomena in Transparent Media*, Springer-Verlag, Berlin, Germany, 2001.

[62] Flaherty, W., *Experimental surface heat flux measurements in hypervelocity flows*, Master's thesis, University of Illinois, Urbana, IL, 2010.

[63] Goodwin, D., "An open-source, extensible software suite for CVD process simulation," *Proc. of CVD XVI and EuroCVD Fourteen*, 2003, pp. 155–162.

[64] Glick, H., "Modified Crocco-Lees mixing theory for supersonic separated and reattaching flows," *Journal of Aerospace Sciences*, Vol. 29, 1962, pp. 1238.

[65] Sychev, V. V., "Asymptotic theory of separation flows," *Fluid Dynamics*, Vol. 17, 1982, pp. 1179.

[66] Roshko, A., "Free shear layers, base pressure and bluff-body drag," *Symposium on Developments in Fluid Dynamics and Aerospace Engineering*, Interline, Bangalore, 1995.

[67] Stewartson, K. and Williams, P., "Self-induced separation," *Proc. R. Soc. London, Ser. A*, Vol. 312, 1969, pp. 181.

[68] Sanderson, S., Austin, J., Liang, Z., , Shepard, F. P. J., and Hornung, H., "Reactant jetting in unstable detonation," *Progress in Aerospace Sciences*, Vol. 46, No. 2-3, 2010, pp. 116–131.

[69] Olejniczak, J., Wright, M. J., and Candler, G. V., "Numerical study of shock interactions on double-wedge geometries," *Proceedings of the 34th AIAA Aerospace Sciences Meeting*, Reno, NV, 1996.

[70] Browne, S., Ziegler, J., and Shepherd, J. E., "Numerical Solution Methods for Shock and Detonation Jump Conditions," Tech. rep., California Institute of Technology, Pasanda, Ca, August 2008, GALCIT Report FM2006.006.

[71] Massa, L., Austin, J., and Jackson, T., "Triple-point shear layers in gaseous detonation waves," *Journal of Fluid Mechanics*, Vol. 586, 2007, pp. 205–248.

[72] Hayne, M., Mei, D., Gai, S., and McIntyre, T., "Boundary layers on a flat plate at sub- and superorbital speeds," *Journal of Thermophysics and Heat Transfer*, Vol. 21, No. 4, 2007, pp. 772–779.

[73] Knight, D., Longo, J., Drikakis, D., Gaitonde, D., Lani, A., Nompelis, I., Reimann, B., and Walpot, L., "Assessment of CFD capability for prediction of hypersonic shock interactions," *Progress in Aerospace Sciences*, Vol. 48-49, 2012, pp. 8–26.

[74] Wen, C. and Hornung, H., "Non-equilibrium dissociating flow over spheres," *Journal of Fluid Mechanics*, Vol. 299, 1995, pp. 389–405.

[75] Flaherty, W., Crafton, J., Elliott, G., and Austin, J., "Application of fast pressure sensitive paint in hypervelocity flow," *Proceedings of the 49th AIAA Aerospace Sciences Meeting*, Orlando, FL, 2011.

[76] Thompson, P., *Compressible Fluid Dynamics*, McGraw-Hill Inc., 1972.